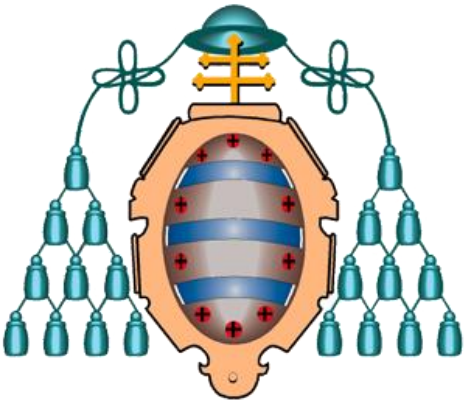

UNIVERSIDAD DE OVIEDO

Programa de doctorado en Ciencia y Tecnología de Materiales

FUNCIONALIZACIÓN COVALENTE DE NANOTUBOS DE CARBONO Y GRAFENO PARA SU APLICACIÓN EN CATÁLISIS

Tesis doctoral

Matías Blanco Fernández

Septiembre 2015

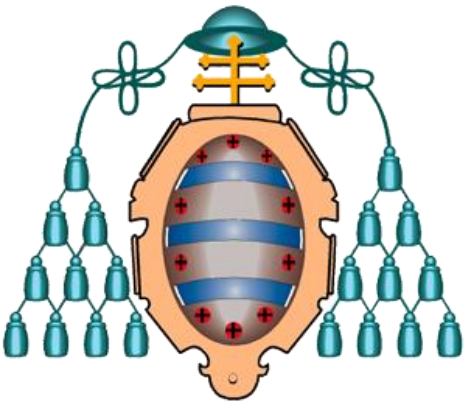

UNIVERSIDAD DE OVIEDO

Programa de doctorado en Ciencia y Tecnología de Materiales

FUNCIONALIZACIÓN COVALENTE DE NANOTUBOS DE CARBONO Y GRAFENO PARA SU APLICACIÓN EN CATÁLISIS

Tesis doctoral

Rosa Menéndez

Patricia Álvarez

ÍNDICE

Agradecimientos……III

Resumen……VII

Abstract……..IX

Listado de Figuras y Tablas……...XI

1. Introducción……..1

1.1 Catálisis.....3
1.2. Nanomateriales de carbono…….....6
1.2.1 Descripción.……7
1.2.2 Propiedades…….9
1.2.3 Funcionalización de los nanomateriales.....10
1.3 Nanomateriales de carbono en catálisis..……17
1.3.1 Materiales prístinos y oxidados…….17
1.3.2 Sistemas híbridos nanomaterial-metal……21
1.4 Carbenos N-heterocíclicos..……..……27
1.4.1 Generalidades de los carbenos……..28
1.4.2. Reacciones de transferencia de hidrógeno…….....31

2. Objetivos y organización de la memoria……33

3. Experimental.....39

3.1 Materiales de partida……41
3.2 Purificación, oxidación y reducción térmica de los nanomateriales de carbono...…….…..43
3.2.1 Purificación de nanotubos de carbono…….…43
3.2.2 Oxidación suave de nanotubos de carbono……....43
3.2.3 Oxidación moderada de nanotubos de carbono.……....44
3.2.4 Oxidación fuerte de nanotubos de carbono……....45
3.2.5 Oxidación de grafito. Obtención de óxido de grafeno……...45
3.2.6 Reducción térmica de nanomateriales de carbono…….46
3.3 Funcionalización de nanomateriales de carbono……..47
3.3.1 Funcionalización a través de grupos carboxilo...……..48
3.3.2 Funcionalización a través de grupos hidroxilo…….……49

3.3.3 Síntesis de complejos NHC de iridio soportados…….50
3.3.4 Síntesis de complejos NHC de iridio homogéneos……...51
3.4 Técnicas de caracterización……..54
3.4.1 Caracterización de sistemas homogéneos…….54
3.4.2 Microscopía..…….57
3.4.3 Espectroscopía..……60
3.4.4 Análisis térmico…….65
3.4.5 Otras técnicas……....67
3.5 Experimentos de adsorción.....72
3.6 Experimentos catalíticos……...74

4. Resultados……..77

4.1 Artículo I..……81
4.2 Artículo II..…….115
4.3 Artículo III..……161
4.4 Artículo IV..……...191
4.5 Artículo V..…….229

5. Conclusiones……267

Bibliografía……...277

Anexo……...289

AGRADECIMIENTOS

Me gustaría empezar agradeciendo a las directoras de este trabajo, Prof. Rosa Menéndez y Dra. Patricia Álvarez, todo el esfuerzo dedicado para acabar esta Tesis, todos los consejos dados y todo lo aprendido. No ha sido fácil, ha habido que morder y ha habido risas, y todo lo agradezco sinceramente.

Agradecer al Consejo Superior de Investigaciones Científicas (CSIC) que me permitiese realizar mi trabajo en el Instituto Nacional del Carbón (INCAR), al Ministerio de Economía y Competitividad la financiación mediante el proyecto CONSOLIDER-INGENIO Multicat 2010 (CSD2009-00050) en el que se enmarca esta Tesis, y al Ministerio de Educación por la concesión de una beca FPU (AP2010-0025) para mi sustento estos años.

Siguiendo con el proyecto, agradecer a su coordinador, Prof. Avelino Corma el poder haber compartido su genialidad, así como el permitirme realizar dos estancias en centros participantes del proyecto. La primera, en la Universidad de Zaragoza, quiero agradecer al grupo del Prof. Luis A. Oro el dejarme participar en su actividad durante dos meses, en especial a los doctores Jesús Pérez Torrente y Vicky Jiménez por el cariño, lo aprendido y producido, a Javier Fernández por su trabajo en catálisis, y a Dani Gómez por lo soportado. La segunda, en el propio Instituto de Tecnología Química de Valencia en el grupo del Prof. Corma, quiero agradecer al doctor Urbano Díaz de nuevo su paciencia, forma de ser y disponibilidad.

También quisiera agradecer al Prof. Maurizio Prato el haberme posibilitado realizar una nueva estancia, pero esta vez en el extranjero, en su grupo de la Università di Trieste en Italia. También al Dr. Alejandro Criado por toda la química y el italiano (incluidas costumbres) enseñados, y a todos mis compañeros del grupo Prato por acogerme tan bien estando fuera de casa, el hacer que me sintiese querido e integrado, en especial a Arturo Juzgado y Andrea La Rosa, a quienes puedo llamar amigos.

Volviendo a casa, quiero agradecer a todos los compañeros del INCAR los años pasados codo con codo, empezando por el trato cercano y los buenos consejos de los doctores Marcos Granda, Clara Blanco y Ricardo Santamaría. A Luis el bibliotecario y sus búsquedas *in extremis*. A todos los técnicos que tanto sufren al pedirles análisis y ensayos (Dolores, Jose, Aurea, Carlos y Zakariae, estos técnicos de la Universidad…) como a los compañeros de otros grupos y del propio. También acordarme de los que pasaron un breve tiempo con nosotros, como Flo, Yu Jin, Jorge y Javier, que algo me enseñaron y algo compartieron conmigo. Tanto a los que acabaron antes que yo, Silvia, Noel, Belén, Cristina, Nati,…, que me enseñaron a trabajar como trabajo; y de los chicos de prácticas, Lorena, Gabi, Adrián, Nuria, Alejandro, Pablo, Elisa, Andrea, Elena…, con los que aprendí a enseñar mi trabajo; a los que acaban a la vez, Patri Díaz, Uriel, con el que tanto me he pegado y tantas veces nos hemos pedido perdón; como a los que seguirán después de mí, Ana, Laura, Rubén; y los que espero que nunca se vayan, Patri Blanco, Zoraida, y Dani; gracias a todos por hacerlo más fácil y hacerme reir en momentos donde lo necesitaba, por la terapia para hacerme mejor persona, por ayudarme, por hacer vuestro trabajo para que yo haga el mío, por discutir las cosas,… Incluso por sacarme de quicio. Gracias.

No me quiero olvidar de Carmen y su madre Manuela. 5 años dándome de comer se merece unas líneas para ellas solas.

A todos mis amigos que se interesan por mi trabajo sin llegar a entenderlo, solo por el hecho de interesarse por mí, gracias una vez más (o puede que la primera quizá), pero esta vez por escrito. Habéis tenido que aguantar mucho, y más que os quedará, y aun así estáis ahí.

Son muchos años, muchos momentos con muchas personas, muy difíciles de agradecer en 3 hojas. Simplemente, gracias.

Papa, Mama, Alberto, Güelita, espero que estéis orgullosos. No puedo escribiros mi agradecimiento porque no es ni un ápice de lo que os debo.

Y Tú Pequeña… esto ha sido por ti. Gracias.

RESUMEN

Los nanotubos de carbono y el grafeno son dos nanomateriales de reciente descubrimiento que encuentran aplicación en numerosos campos. Sus excelentes propiedades mecánicas, eléctricas, térmicas y químicas hacen que sean útiles para la fabricación desde dispositivos electrónicos a sistemas de liberación de fármacos. Además, muchos sistemas catalíticos emplean en alguna fase del proceso nanotubos de carbono o grafeno.

En esta Tesis Doctoral se ha estudiado la integración de nanotubos de carbono y óxido de grafeno en sistemas catalíticos conocidos, como son los procesos de reducción de sustratos insaturados por medio de transferencia de hidrógeno catalizados por complejos de tipo carbeno N-Heterocíclicos de iridio. Se describen las estrategias empleadas para la preparación de soportes, el diseño de las rutas de funcionalización de las nanoestructuras con los complejos metálicos y la actividad catalítica de los materiales híbridos finales. Para tal fin, nanotubos de carbono y grafito fueron oxidados para el desarrollo de grupos funcionales oxigenados que permitiesen la funcionalización de los nanomateriales con los complejos. A lo largo del Trabajo se hizo especial esfuerzo en realizar la caracterización de todas las muestras involucradas

La funcionalización de nanotubos de carbono oxidados a través de sus grupos carboxilo permitió generar catalizadores soportados con mejor actividad catalítica que sus correspondientes sistemas homogéneos, presentando además una excelente

ciclabilidad y estabilidad al aire, en claro contraste con los sistemas análogos no soportados. La química superficial del soporte controla la actividad catalítica del sistema final, siendo necesaria una determinada cantidad y tipo de grupos funcionales oxigenados.

Para la generación de catalizadores de óxido de grafeno se diseñó una estrategia de funcionalización novedosa, consistente en su modificación selectiva con conectores orgánicos a través de los grupos hidroxilo superficiales. También se emplearon materiales en los que habían sido eliminados los grupos carboxilo mediante reducción térmica. Estos últimos materiales fueron los que presentaron mejor actividad catalítica, superior a los sistemas homogéneos y con buena ciclabilidad y estabilidad al aire.

El estudio del entorno local del complejo de iridio reveló la existencia de un enlace directo entre el metal y el soporte, lo que influye en la actividad catalítica del sistema. Se vio que la presencia de defectos estructurales en las redes aromáticas afecta negativamente a la actividad de los catalizadores, siendo la proporción de grupos funcionales oxigenados del soporte determinante para las uniones estabilizantes con el centro metálico.

ABSTRACT

Carbon nanotubes and graphene are recently discovered carbon nanomaterials which find application in a great number of fields. Their excellent mechanical, electrical, thermal and chemical properties make them useful for a wide range of new developments which move from electronic devices to drug-delivery systems. In addition, catalytic systems usually employ carbon nanotubes and graphene in any of the stages of the catalytic process.

In this Thesis, the integration of carbon nanotubes and graphene in well-known homogeneous catalytic systems, i.e., unsaturated-substrates reduction reactions by means of hydrogen transfer processes catalyzed with iridium N-heterocyclic carbene complexes is studied. This Memory describes the employed strategies for the preparation of the supports, the design of the nanostructure functionalization routes with the metallic complexes and the study of the catalytic activity of the final hybrid materials. Both types of materials were oxidized with the aim of developing oxygen functional groups which allow nanomaterial functionalization methods to be applied with the complexes. A special effort was made to accomplish a complete and exhaustive characterization of the involved samples.

Oxidized carbon nanotubes functionalization through their carboxylic groups generated supported catalysts with enhanced catalytic activity compared to their corresponding homogeneous systems. Moreover, they also present an excellent

cyclability and air stability, in sharp contrast with their analogous non-supported catalysts.

The synthesis of hybrid catalysts supported on graphene oxide was based in a new functionalization strategy, which consists in the modification of the surface hydroxyl groups employing organic-based connectors. The selectivity of the reaction was checked by the functionalization of the corresponding thermally reduced materials which do not possess carboxylic acids. The later were those which presented the best catalytic activity, superior to the homogeneous systems too. In addition, both hybrid catalysts also present cyclability and air stability.

The study of the local environment of the iridium organometallic complexes revealed a direct bond between the metal and the supports, which affects the catalytic activity of the system. The presence of structural defects in the aromatic lattice was demonstrated to generate catalysts with poor activities. Partially reduced materials based catalysts achieved the best performances. Moreover, the correct type and amount of oxygen functional groups are necessary to obtain a good behavior in order to stablish stabilizing bonds between those groups and the metallic centre.

LISTADO DE FIGURAS Y TABLAS

Listado de figuras

Figura	Título	Página
Figura 1.1	Diagrama de energía de una reacción química con y sin catalizador	4
Figura 1.2	Lámina de grafeno	7
Figura 1.3	Tipos de nanotubos de carbono según el número de capas	9
Figura 1.4	Ejemplos de funcionalizaciones no covalentes	12
Figura 1.5	Funcionalización lateral de nanotubos y grafeno	13
Figura 1.6	Esquema de la degradación oxidativa de un nanotubo de carbono	15
Figura 1.7	Obtención de GO	16
Figura 1.8	Ejemplo de funcionalización mediada por ácidos en nanotubos de carbono	16
Figura 1.9	Reacción de complejación catalizada por grafeno	18
Figura 1.10	Actividad del GO como carbocatalizador	20
Figura 1.11	Reacción de Suzuki catalizada por el híbrido GO-Pd	22
Figura 1.12	Hidrogenación selectiva de cinamaldehído por un híbrido CNT-Pt	23
Figura 1.13	Epoxidación de olefinas catalizada por un híbrido complejo de Salen-GO	24
Figura 1.14	Metátesis de cierre de anillo catalizada por un híbrido nanotubo-complejo de rutenio	25
Figura 1.15	Esquema de una pila de combustible que utliza nanotubos de carbono.	26
Figura 1.16	Esquema de un fotocatalizador de grafeno.	27
Figura 1.17	Carbenos NHC	29
Figura 1.18	Catalizadores de Grubbs de: a) primera generación, b) segunda generación y c) tercera generación	30
Figura 1.19	Mecanismo de la reacción de transferencia de hidrógeno (S = sustrato, P = producto, [M] = centro metálico)	32
Figura 3.1	Productos de partida orgánico-organometálicos	42
Figura 3.2	Desorción de grupos oxigenados con sus temperaturas de descomposición	66
Figura 4.1	a) Esquema de funcionalización de los nanotubos de carbono oxidados con complejos NHC de iridio; b)	116

	síntesis de los complejos homogéneos; c) síntesis de los blancos de reacción	
Figura 4.2	Actividad catalítica	118
Figura 4.3	Propuesta de ciclo catalítico empleando soportes de carbono	119
Figura 4.4	Funcionalización covalente de los nanotubos con diferente grado de oxidación	162
Figura 4.5	Actividad catalítica	163
Figura 4.6	Ruta de funcionalización a través de los grupos OH	192
Figura 4.7	Actividad catalítica de los híbridos grafeno-NHC-iridio, muestras de control y complejo homogéneo **Ir-imidO**	194
Figura 4.8	Ruta de funcionalización	229
Figura 4.9	Actividad catalítica	230
Figura 4.10	Caracterización de los sistemas híbridos basados en nanotubos de carbono y materiales grafénicos iridio-NHC	232

Listado de tablas

Tabla 3.1 Caracterización de grupos funcionales oxigenados mediante XPS pag.63

1. INTRODUCCIÓN

INTRODUCCIÓN

1.1 CATÁLISIS

Una sustancia que incremente la velocidad de una reacción química sin modificar la variación de energía libre de la misma se denomina catalizador, y el proceso es referido como catálisis.[1] El funcionamiento de la catálisis se basa en que, para la formación de los productos, el catalizador forma con los reactivos un estado de transición diferente y de menor energía de activación (*Ea*) a la misma temperatura si se compara con el que formarían sin catalizador (Figura 1.1). Estas reacciones permiten que el proceso transcurra mediante un nuevo mecanismo de reacción más estabilizado, la barrera cinética se rebaje y aumente la velocidad global de la reacción. No obstante, en alguna etapa intermedia el catalizador se debe regenerar para no afectar al equilibrio químico de la reacción. Generalmente bastan pequeñas cantidades para aumentar la velocidad de una reacción. Por tanto, los catalizadores permiten reacciones que de otro modo estarían bloqueadas o ralentizadas por una barrera cinética, lo que se traduce en mayor velocidad, mejor selectividad o incluso que se produzca la reacción química a menor temperatura.

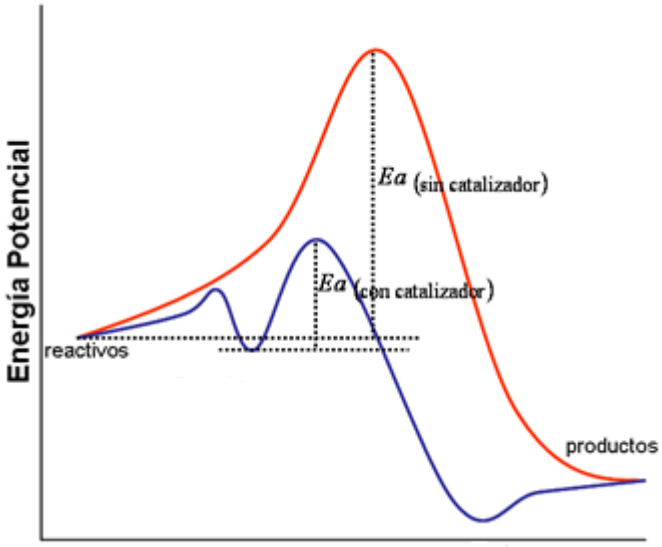

Figura 1.1. Diagrama de energía de una reacción química con y sin catalizador.

La unidad derivada del sistema internacional (SI) para medir la actividad catalítica de un catalizador es el katal, que es igual a moles producidos por segundo. No obstante, la actividad de un catalizador se describe generalmente mediante el *Turnover number*, o número de conversiones (TON) y la eficiencia catalítica mediante el *Turnover frecuency*, o frecuencia de conversiones (TOF), equivalente al número de conversiones por unidad de tiempo.[2]

Los diversos tipos de catalizadores existentes son tan variados como la cantidad de reacciones que son capaces de catalizar. De manera general, los ácidos próticos son probablemente los catalizadores más ampliamente usados, especialmente para muchas reacciones que involucran agua, incluyendo la hidrólisis y su inversa. Los metales de transición se utilizan para catálisis de procesos de óxidación-reducción, y si se complejan con ligandos orgánicos, se emplean para catalizar reacciones de síntesis orgánica. Los sólidos multifuncionales a menudo suelen ser catalíticamente activos, por ejemplo las zeolitas, la alúmina y los materiales de carbono. Debido a

esta gran variedad, una forma de clasificar los catalizadores es en catalizadores homogéneos y heterogéneos:

- **Catalizadores homogéneos**. Son aquellos que están disueltos junto con los reactivos en un disolvente común. La catálisis ácida es el claro ejemplo de sistema homogéneo. Otros ejemplos son los encimas en el campo de la biología, o la polimerización de Ziegler-Natta o el proceso Wacker de conversión de etileno a acetaldehído empleando catalizadores organometálicos.

- **Catalizadores heterogéneos**. Los catalizadores heterogéneos son aquellos que actúan en una fase diferente que los reactivos. Así, muchos de los catalizadores heterogéneos suelen ser sólidos que catalizan mezclas de reacción líquidas o gaseosas. Sin embargo, no todo el sólido es el sistema catalítico, ya que los catalizadores suelen estar soportados; esto es, los centros activos donde se desarrollan los procesos catalíticos están dispersos en una matriz. Para que se produzca la catálisis heterogénea se tienen que dar procesos de difusión desde el seno del medio de reacción hasta el catalizador, adsorción/absorción de los reactivos, reacción química en el centro activo, desorción de los productos y difusión de nuevo al seno del medio de reacción. Aunque parezca un fenómeno complejo, una vez que los reactivos han sido adsorbidos/absorbidos en el soporte, estos evolucionan hacia productos de una manera mucho más rápida comparada con el medio homogéneo. Además, los catalizadores soportados suelen ser más estables, y su recuperación y ciclabilidad son más sencillas, empleando en definitiva menos cantidad de catalizador.

  Aunque en la literatura se detalle la existencia de otros sistemas,[3] en este trabajo se considera como centro activo del proceso catalítico a un metal, el

cual será dispersado en una matriz. Ambos constituyen el propio catalizador heterogéneo.

La heterogenización de catalizadores se puede plantear desde dos puntos de vista. El catalizador puede ser sintetizado por completo de manera homogénea pero dejando un punto de anclaje para que en una última etapa sea inmovilizarlo sobre el soporte. Por otro lado, el catalizador puede ser construido desde cero sobre el soporte, modificándolo en etapas sucesivas. Para ello, se debe activar el soporte en una primera etapa, seguido de las correspondientes modificaciones orgánico-inorgánicas hasta conseguir sintetizar el catalizador final. En la literatura, aunque ambas aproximaciones se emplean, se considera que la segunda estrategia es más prometedora[4] pues permite controlar el proceso de modificación del soporte de una manera fácil y precisa, siendo además un proceso que evita las posibles etapas de descomposición de los ligandos del centro activo.

1.2 NANOMATERIALES DE CARBONO

El empleo de catalizadores heterogéneos donde se dispersan centros activos en una matriz ha sido ampliamente descrito. Desde sólidos inorgánicos como las sílices, las zeolitas o las alúminas,[5] hasta sólidos orgánicos como los polímeros[6] o los materiales de carbono[7] se han empleado ampliamente para la construcción de sistemas híbridos metal-soporte donde se consiguen mejorar las propiedades catalíticas del conjunto. El uso de un determinado soporte está muy ligado a las propiedades que este le puede ofrecer al metal. La estructura carbonosa de los materiales de carbono permite que los catalizadores tengan resistencia a medios oxidantes y/o corrosivos, un control preciso de la porosidad y gran facilidad en la recuperación del mismo debido a su insolubilidad en la mayoría de disolventes.[7] Los

nanotubos de carbono y el grafeno, nanomateriales de carbono de reciente descubrimiento, comparten las propiedades de los materiales clásicos. No obstante, sus pequeñas dimensiones hacen que los efectos cuánticos dominen en sus propiedades,[8] presentando además comportamientos que los materiales de carbono clásicos no poseen.

1.2.1 Descripción

El **grafeno** es un cristal bidimensional donde cada átomo de carbono se une a otros tres mediante orbitales híbridos sp^2, dejando un electrón libre en un orbital π distribuido por encima y por debajo del cristal. Así, los átomos se agrupan formando una estructura plana de tipo panal de abeja, de espesor monoatómico, y de superficie variable, idealmente infinita. Según la IUPAC, el término grafeno ha de aplicarse cuando se trate de las reacciones, relaciones estructurales y propiedades de una sola lámina individual de grafito.[9]

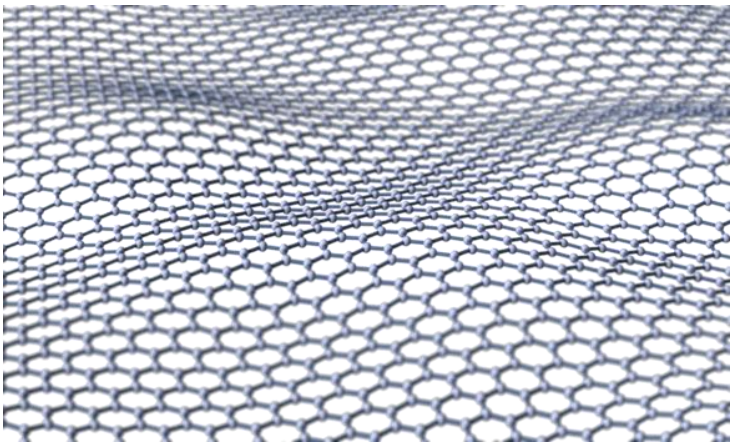

Figura 1.2. Lámina de grafeno

El grafeno fue aislado por primera vez en 2004 por Andrew Geim y Konstantin Novoselov,[10] y por su descubrimiento, fueron galardonados con el Premio Nobel de

Física en el año 2010. No obstante, se conocía la existencia del grafeno tiempo atrás, aunque se pensaba que la monolámina bidimensional no era termodinámicamente estable.

Los **nanotubos de carbono** (CNT**,** del inglés Carbon NanoTube)**,** descubiertos por Sumio Iijima en el año 1991, se pueden describir como una lámina de grafeno enrollada sobre sí misma en forma de cilindro de diámetro nanométrico y de longitud variable.[11] En los nanotubos de carbono, los átomos deben usar una hibridación superior a la sp^2 para obtener la forma tubular y poder plegar la lámina de grafeno.[12] Desde el punto de vista estructural, los nanotubos de carbono se pueden clasificar según el número de capas[13] que presentan (figura 1.3):

- Los nanotubos de carbono de pared sencilla (SWCNT de las siglas en inglés *Single – Walled Carbon NanoTubes*) constituidos por una única lámina de grafeno enrollada formando un cilindro.

- Los nanotubos de carbono de pared múltiple (MWCNT de la siglas en inglés *Multi – Walled Carbon NanoTubes*) formados por capas concéntricas separadas una distancia aproximada a la distancia interplanar de las láminas de grafito.

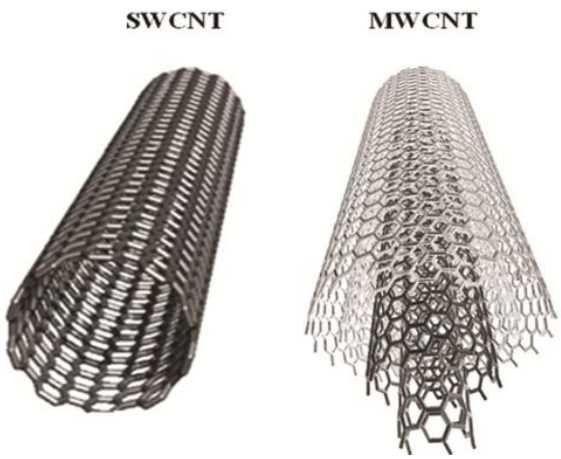

Figura 1.3. Tipos de nanotubos de carbono según el número de capas

1.2.2 Propiedades

Los nanotubos de carbono y el grafeno comparten muchas propiedades ya que ambos están formados por enlaces C-C de tipo sp^2 de anillos hexagonales en estructura de panal de abeja, donde al menos una dimensión está confinada. Las propiedades de ambos están muy ligadas a la calidad estructural de las láminas de grafeno, bien se presenten abiertas o enrolladas.

Así, si las láminas son perfectas, los dos materiales presentan excelentes propiedades eléctricas,[14] donde la conductividad es 1000 veces mayor que la actual del cobre, debido a que los electrones se mueven a lo largo de los enlaces con una conducción de tipo balístico (sin dispersión de energía y sin efecto Joule). La unión entre los átomos de carbono también hace que las propiedades térmicas sean 1000 veces superiores a las del cobre,[15] y que además sean los materiales con mayor módulo elástico y resistencia a tracción conocidos (200 veces superiores al acero).[16] Además, son materiales que pueden resistir la radiación ionizante sin modificarse y son impermeables a todos los gases. No obstante, si las láminas grafénicas en ambos

tipos de estructura presentan defectos, los materiales desarrollan porosidad, que en el caso de los nanotubos puede ser intrínseca por su propia estructura tubular, o extrínseca en función de su disposición tridimensional. Dichos defectos suelen estar decorados con grupos funcionales oxigenados (ácidos carboxílicos en bordes y puntas, y epoxy e hidroxilos en planos basales)[17], los cuales modifican la química superficial y el carácter anfifílico. Finalmente, son luminiscentes, bactericidas,[18] y biocompatibles.

Las propiedades que los nanotubos de carbono y el grafeno poseen permiten el desarrollo de excelentes catalizadores heterogéneos basados en sistemas híbridos nanomaterial-centro activo, con una gran resistencia mecánica y química que evita su disgregación en el medio de reacción. La porosidad controlada y la precisa detección del sistema catalítico gracias a las propiedades del soporte ofrecen ventajas que los catalizadores homogéneos no poseen. Además, la química superficial que ambos presentan puede afectar a la actividad catalítica, junto con la capacidad casi ilimitada de diseñar y sintetizar la especie catalítica, a través el empleo de reacciones clásicas y específicas de nanomateriales con los grupos funcionales.

1.2.3 Funcionalización de nanomateriales

El rango de reacciones que nanotubos de carbono y grafeno son capaces de catalizar por sí solos es muy limitado. Si bien se conocen algunos ejemplos, que se discutirán más adelante, para el desarrollo de catalizadores soportados los nanomateriales de carbono requieren tratamientos de funcionalización, ya que la actividad de un catalizador depende de la naturaleza, accesibilidad y concentración de sus centros activos, con lo que los materiales funcionalizados serán más eficientes que aquellos catalizadores con muy pocos centros activos.

En la literatura existen numerosos trabajos y revisiones sobre las distintas estrategias de modificación de nanotubos de carbono y grafeno. Este trabajo se centra en la inmovilización de catalizadores, con lo que se revisarán las estrategias de desarrollo de grupos funcionales para desembocar en un material híbrido nanomaterial de carbono-catalizador. Existen dos grandes aproximaciones para poder funcionalizar nanomateriales de carbono con las especies orgánicas e inorgánicas necesarias para construir el catalizador. Las estrategias se basan en el tipo de unión entre el catalizador y el material carbonoso. Estas son la funcionalización covalente y la no covalente.

1.2.3.1 Funcionalización no covalente.

La funcionalización no covalente se basa en el establecimiento de uniones diferentes al enlace covalente entre el modificador orgánico/inorgánico y el nanomaterial de carbono. Las ventajas que supone este método es que la estructura del material, y por tanto sus propiedades, sobre todo electrónicas, no tienen por qué verse modificadas al decorar el nanotubo o grafeno con un compuesto determinado. Las interacciones que se pueden emplear en la funcionalización no covalente son de muy diversa naturaleza. Puede establecerse un enlace iónico en las condiciones adecuadas entre los grupos funcionales del material y el modificador (síntesis hidrotermales, procesos sol-gel, procedimientos de nucleación y crecimiento electroquímico, etc.), que lo dejará fijado siempre y cuando las condiciones de pH no varíen. Por otro lado, existen uniones de tipo físico, como el enrollamiento de un polímero sobre la superficie de los materiales generando un nanocomposite, o la generación de uniones mediantes fuerzas de Van der Waals tipo apilamiento-π entre una molécula, generalmente de tipo aromática basada en hidrocarburos policíclicos

condensados funcionalizados, y la nube aromática de los nanomateriales de carbono. No obstante, en todos los casos la unión no es tan fuerte como el enlace covalente, con lo que los fenómenos de lixiviado del catalizador son frecuentes.

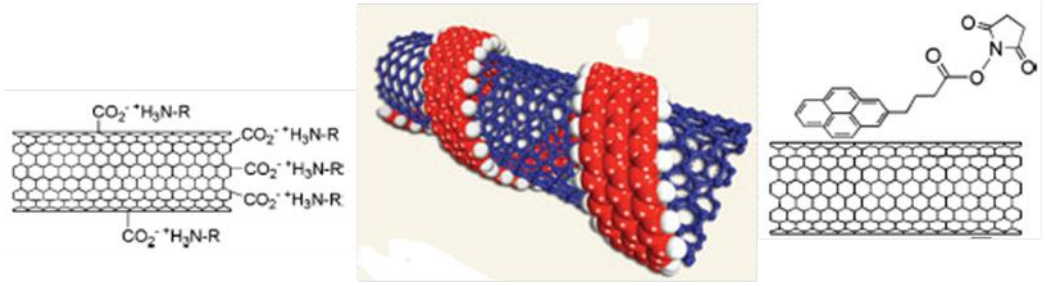

Figura 1.4. Ejemplos de funcionalizaciones no covalentes[19]

1.2.3.2 Funcionalización covalente

En esta estrategia se modifica la superficie carbonosa del material con enlaces covalentes con el futuro catalizador. La modificación covalente es un método empleado muy frecuentemente en la funcionalización de nanomateriales de carbono ya que se establecen fuertes uniones entre el material y el modificador. Además, el hecho de aplicar reacciones orgánicas e inorgánicas permite trasladar los conceptos y métodos de la química homogénea para la modificación de nanoestructuras. No obstante, la formación de enlaces directamente en la estructura carbonosa del nanomaterial suele suponer la pérdida de propiedades electrónicas al verse interrumpida la red sp^2 por un nuevo enlace, lo que se asocia con la generación de un defecto estructural.

La modificación covalente se puede también plantear mediante dos aproximaciones. La primera considera el **sistema π**, rico en densidad electrónica presente en nanotubos y grafenos, como reactivo de la reacción química, de manera que se añadirán sustratos capaces de reaccionar con los carbonos sp^2 de los

materiales. La figura 1.5 resume las diferentes posibilidades de reacción para la funcionalización lateral de nanotubos y grafenos.

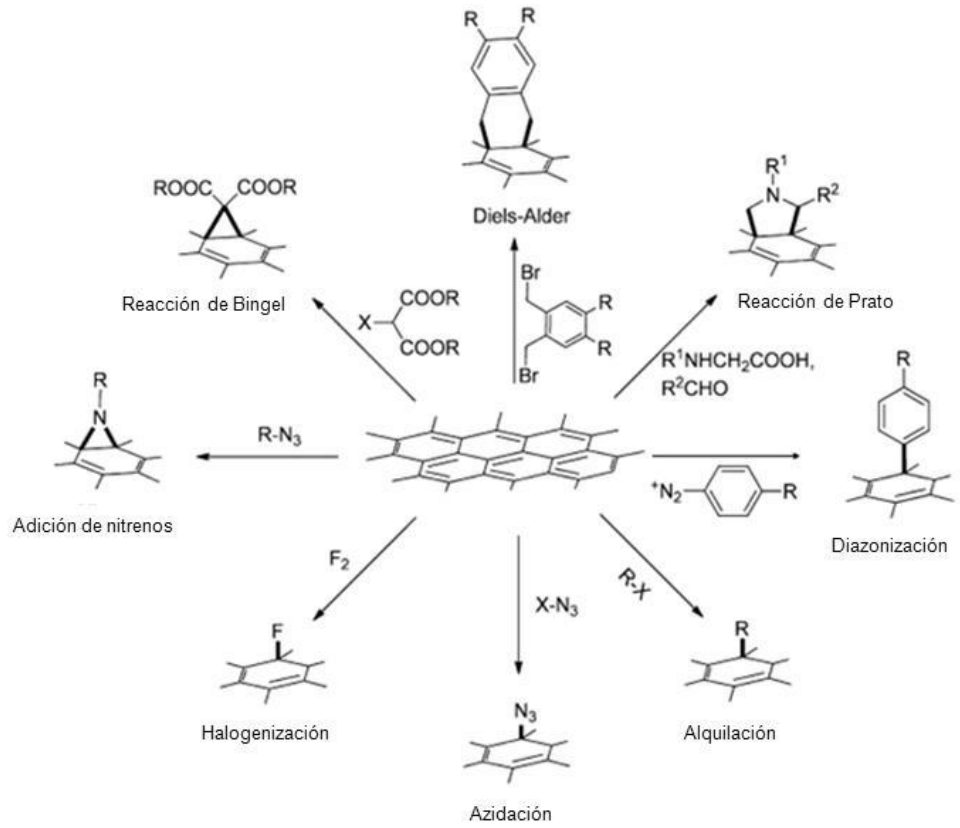

Figura 1.5. Funcionalización lateral de nanotubos y grafeno.[20]

En primera aproximación, considerando la pared del material como un nucleófilo, esta se puede halogenar en presencia de ácidos de Lewis,[21] o bien alquilarse y/o azidarse en reacciones de tipo S_N2. El grupo R puede ser parte del catalizador que se desea introducir, o bien un grupo funcional que permita la realización de reacciones sucesivas, como sustituciones en el caso del halógeno, o reacciones *click 2+3* en el caso de la azida.

Por otro lado, el esqueleto aromático de los materiales permite la conducción de electrones a lo largo de su estructura, con lo que se pueden comportar como

excelentes sustratos para realizar reacciones de cicloadición, como es la reacción Diels-Alder y la cicloadición 1,3-dipolar, conocida como la reacción de Prato. En estas reacciones, los estados de transición se forman por compartición de electrones π. Para que se puedan cumplir estos estados de transición cíclicos característicos, los nanomateriales son los que aportan el mayor número de electrones π gracias a la presencia de sus nubes electrónicas deslocalizadas. Finalmente, ese rico contenido en densidad electrónica los convierte en excelentes candidatos para realizar adiciones radicalarias. La adición de nitrenos o la química de sales de diazonio son ejemplos ampliamente usados donde se genera un radical que es atrapado por la nube aromática de los nanomateriales.

El segundo gran bloque de ejemplos descritos en la literatura hace uso la **química superficial oxigenada**. Al oxidar los materiales carbonosos, aparecen grupos funcionales oxigenados de tipo hidroxilo o epoxido en los planos basales, y carbonilo, fenol, lactona, quinona y carboxilo en sus bordes.

La oxidación de nanomateriales de carbono es un proceso común entre los métodos de obtención y purificación. En el caso de los nanotubos de carbono, tras los procesos de síntesis, los nanotubos se obtienen dentro de un conglomerado de impurezas. En la bibliografía se detallan diferentes métodos de purificación, como tratamiento térmico en atmósfera inerte u oxidante, purificación magnética, microfiltración y procesos electroquímicos.[22] De todos ellos, los métodos más aceptados y sencillos son tratamientos ácidos suaves para la disolución de los metales, y tratamientos ácidos muy oxidantes para la disolución de las partículas de carbono.[23] Sin embargo, este último tratamiento modifica superficialmente al nanotubo, ya que las paredes también se oxidan. La oxidación comienza en los extremos del nanotubo, degradando las puntas para dejar los extremos abiertos

decorados con funciones oxigenadas. Si el tratamiento prosigue, las paredes también son atacadas.

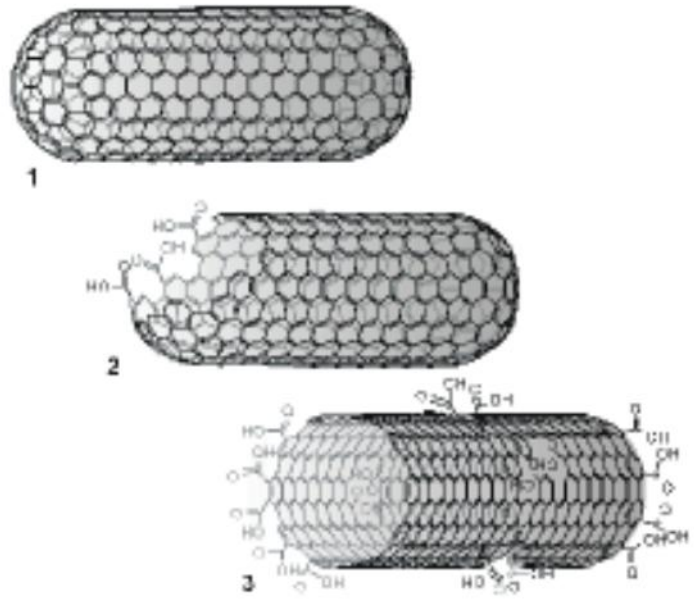

Figura 1.6. Esquema de la degradación oxidativa de un nanotubo de carbono

En el caso del grafeno, la oxidación es una estrategia ampliamente empleada en su metodología de obtención. El tratamiento de grafito con agentes muy oxidantes en medio ácido fuerte distorsiona la red sp^2 de las láminas grafénicas al captar oxígeno en forma de grupos funcionales, con lo que la distancia interlaminar aumenta.[24] Este procedimiento genera óxido de grafito. La mayor separación entre láminas facilita su exfoliación mediante tratamientos con agitación o ultrasonidos, obteniendo finalmente **óxido de grafeno** (GO), un derivado del grafeno, un material laminar plano de carbono cuya superficie está decorada con grupos funcionales oxigenados, presentando además defectos estructurales (vacantes, pares pentágono-heptagono, etc.).

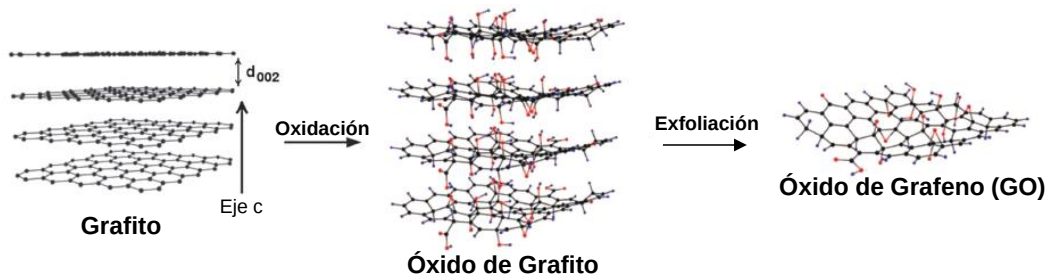

Figura 1.7. Obtención de GO[25]

Así, la rica química superficial oxigenada de los nanomateriales de carbono oxidados permite:

- La aplicación de tradicionales reacciones de esterificación y amidación sobre ácidos carboxílicos. Si bien existen ejemplos de esterificación directa en medio básico,[26] los grupos ácido superficiales suelen ser activados mediante la formación de cloruros de ácido con cloruro de tionilo[27] o de oxalilo,[28] o bien con el empleo de agentes de acoplamiento de aminoácidos de tipo carbodiimida, comúnmente empleados en la síntesis de proteínas.[29]

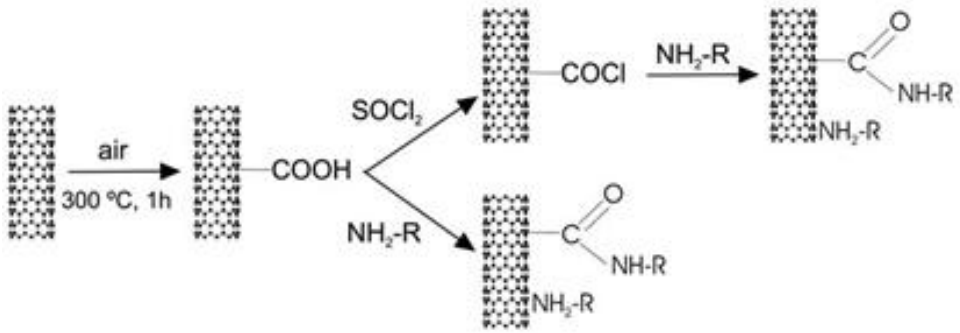

Figura 1.8. Ejemplo de funcionalización mediada por ácidos en nanotubos de carbono.[30]

- Los grupos epóxido pueden ser abiertos y posteriormente funcionalizados empleando suaves condiciones que permitirán una posterior modificación.

- Los grupos hidroxilo tradicionalmente se han empleado para la inmovilización de especies orgánicas e inorgánicas. Muchos autores inmovilizan silanos más o menos derivatizados aprovechando la afinidad que presenta el silicio por los grupos OH.[31]

1.3 NANOMATERIALES DE CARBONO EN CATÁLISIS

Desde sus respectivos descubrimientos, tanto nanotubos de carbono como el grafeno han sido empleados en sistemas catalíticos bien en su estado prístino, o bien purificados y oxidados, especialmente el GO, y finalmente funcionalizados con grupos biológicos, orgánicos e inorgánicos. Las excelentes propiedades que ambos materiales son capaces de aportar al sistema catalítico (apartado 1.2.2), así como las posibilidades de diseño y desarrollo de sistemas nanomaterial-catalizador a través de su funcionalización (apartado 1.2.3) los convierte en candidatos ideales para su empleo como catalizadores. Ambos materiales han sido usados en sistemas químicos, electroquímicos e incluso fotoquímicos, obteniendo mejores resultados que sistemas convencionales. A lo largo de esta sección se revisarán las aplicaciones que nanotubos de carbono y grafeno tienen en catálisis.

1.3.1 Materiales prístinos y oxidados

Como materiales prístinos, tanto nanotubos de carbono como el grafeno tienen un abanico de reacciones capaces de catalizar muy limitado. La ausencia de defectos limita los centros activos, siendo estos únicamente los carbonos insaturados. No obstante, se espera que las reacciones en las que el sistema π del grafito intervenga,

como son las alquilaciones-acilaciones de Friedel-Crafts, reacciones de óxido-reducción de contaminantes o reacciones de cicloadición[32] también sean activas en nanomateriales de carbono. Además, el sistema π deslocalizado les permite catalizar algunas reacciones particulares, como reacciones de complejación,[33] donde el material actúa como intermedio en la síntesis de complejos organometálicos de tipo η_6-areno de cromo. Asimismo, el sistema π de nanotubos de carbono es capaz de facilitar tanto reacciones de oxidación como de deshidrogenación oxidativa y craqueo de parafinas.[34]

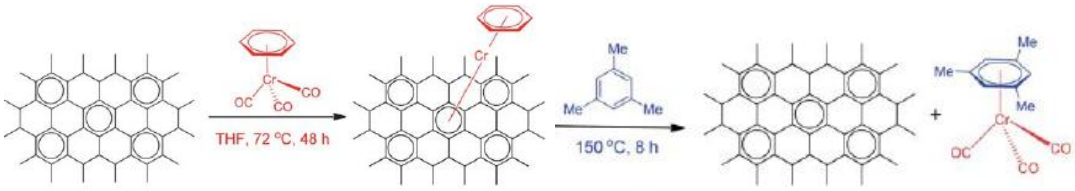

Figura 1.9. Reacción de complejación catalizada por grafeno.[33]

Como se comentó anteriormente, el limitado rango de reacciones donde los nanomateriales de carbono son útiles se expande si se desarrolla algún tipo de funcionalización, de tal manera que se introduzcan nuevos centros activos. La propia química superficial oxigenada que decora la estructura del GO es capaz de actuar como carbocatalizador, esto es, catalizador basado en carbono libre de metal, donde los centros activos serán los diferentes grupos funcionales:

- Los grupos funcionales de tipo ácido carboxilo hacen que se comporte como un ácido sólido, con lo que se pueden catalizar reacciones del tipo adiciones de Michael de sustratos insaturados a índoles. El sistema presentó además una alta reciclabilidad, mucho mayor que el catalizador comercial tradicional.[35] Su actividad como ácido sólido también se comprobó en reacciones de polimerización de apertura de anillo para generar poliésteres o poliamidas.[36]

- Puede usarse como oxidante que cumple con los preceptos de la química verde en oxidaciones de enlaces C-H para convertir arilmetanos, derivados del estilbeno o alquinos terminales en sus correspondientes cetonas, empleando para ello condiciones moderadas comparadas con métodos convencionales.[37]

- El GO es capaz de activar oxígeno para promover la oxidación selectiva de alcoholes a sus correspondientes aldehídos y cetonas, sin romper enlaces C-C como es el caso de oxidantes inorgánicos ni llegar al máximo grado de oxidación. Las reacciones presentan altas conversiones, teniendo el catalizador basado en grafeno una actividad más alta comparado con sistemas clásicos como carbones activados o pares alumina/rutenio. Asimismo, tioles pueden ser transformados en sus correspondientes disulfuros mediante reacciones sencillas catalizadas por GO.

- La introducción de nitrógeno en la red, por ejemplo, mediante reducción química del GO, permite tener actividad en la reacción de reducción de oxígeno de las pilas de combustible, o incluso la oxidación aeróbica selectiva de alcoholes bencílicos.[38]

- Los bordes de las láminas también pueden actuar como centro activo ya que algunas moléculas, como el nitrobenceno, puedan ser hidrogenadas en una reacción que cataliza el propio GO.[39]

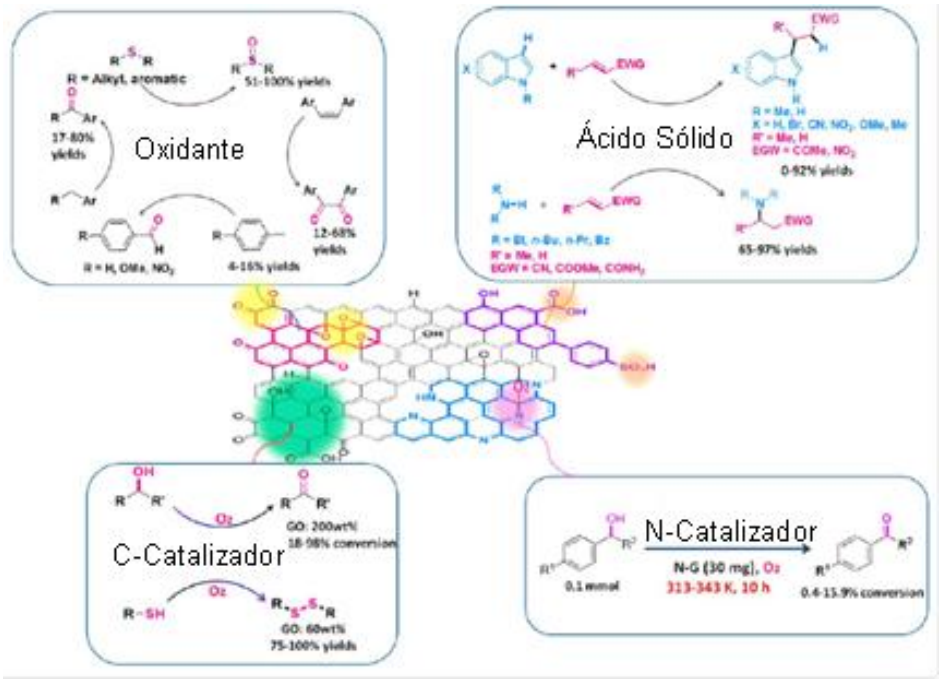

Figura 1.10. Actividad del GO como carbocatalizador.[40]

Los nanotubos de carbono purificados y oxidados tras los procesos de síntesis deberían presentar la misma actividad carbocatalítica que presenta el GO al poseer una estructura carbonosa decorada con defectos y grupos funcionales oxigenados similares. No obstante, la obtención del GO, o incluso polímeros con centros activos ácidos y básicos, es mucho más sencilla, con lo que no ha habido una aplicación de este material como carbocatalizador tan extensa comparado con la utilización del GO.[41]

1.3.2 Sistemas híbridos nanomaterial-metal

La reducción en la carga metálica, la fácil accesibilidad y localización del centro activo, así como la robustez y sencilla recuperación del catalizador hacen del empleo de sistemas nanomaterial de carbono-metal un recurso muy utilizado en el diseño de catalizadores heterogéneos. De nuevo, las propiedades que el nanosoporte puede ofrecer al centro activo juegan un papel clave a la hora de mejorar los resultados comparando con sistemas clásicos convencionales. Por tanto, se deben realizar uniones entre el metal y el material para que el segundo asista en los procesos catalíticos, convirtiéndose así en un soporte pro-activo que consiga mejores resultados en términos de actividad y estabilidad.

Una de las estrategias mas sencillas para el desarollo del híbrido nanomaterial-metal consiste en la dispersión e inmovilización de **nanopartículas metálicas** sobre soportes carbonosos nanoestructurados. De esta manera se generan sistemas catalíticamente activos. Numerosos ejemplos de reacciones de formación de enlaces C-C mediante acoplamientos cruzados (reacciones de Heck, Suzuki, Miyaura, etc.) han sido descritos con sistemas GO-Pd. Las nanopartículas se unen al material a través de los grupos funcionales oxigenados, evitando su agregación y lixiviado en el medio de reacción. De esta manera, se consigue aumentar la actividad del catalizador comparado con el sistema homogéneo (TOF de hasta 108000 h^{-1}), y además la recuperación y ciclabilidad del mismo se vuelven sencillos.[42] Por otro lado, se diseñaron híbridos material grafénico-Fe para facilitar reacciones de hidrogenación de sustratos alifáticos insaturados, donde la separación y posterior recuperación del catalizador se realizó de forma magnética. Sin embargo, las partículas se mantienen unidas al soporte ya que no se observó pérdida de actividad al someter a los catalizadores a un segundo ciclo.[43]

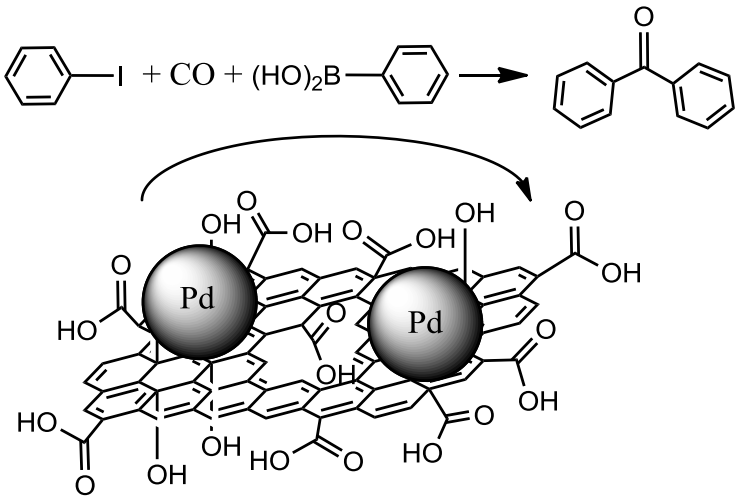

Figura 1.11. Reacción de Suzuki catalizada por el híbrido GO-Pd [44]

Nanotubos de carbono purificados que han desarrollado una química superficial similar al GO también han sido usados para el soporte de nanopartículas de tamaños inferiores a los 10 nm. Mediante impregnación de precursores de Rh se consiguió enlazar nanopartículas a los grupos funcionales oxigenados, y se demostró que los nuevos catalizadores consiguieron mayores selectividades en la reacción de hidroformilación de etileno comparado con un sistema Rh-SiO_2.[45] También mediante impregnación de un precursor de platino sobre nanotubos oxidados, la reacción de oxidación de metanol alcanzó una conversión 400% superior a la conseguida por el sistema Pt-carbón Vulcan en la oxidación de metanol. Las modificaciones químicas de la pared de nanotubos de carbono, que no en grupos funcionales oxigenados, también permiten la síntesis de materiales híbridos basados en nanopartículas de Pt, las cuales son efectivas en la hidrogenación de cinamaldehído. En este caso, se obtuvo una gran selectividad en la reducción del doble enlace, dejando el aldehído intacto.[46]

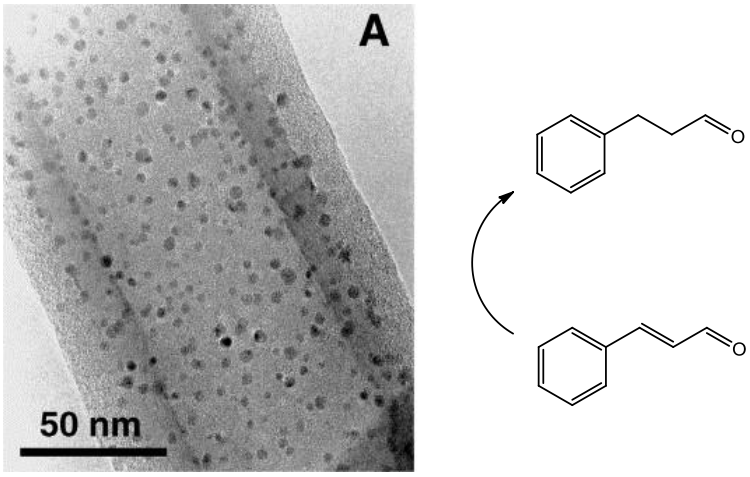

Figura 1.12. Hidrogenación selectiva de cinamaldehído por un híbrido CNT-Pt[46]

El uso de complejos organometálicos soportados sobre nanoestructuras de carbono para generar **catalizadores heterogéneos moleculares** está poco extendido, habiendo relativamente pocos ejemplos de sistemas híbridos nanomaterial de carbono-complejo organometálico. Se han descrito ejemplos de construcción del complejo de Salen de Cu (II) usando la química oxigenada del GO para la epoxidación de olefinas.[47] Sobre GO también se inmovilizaron complejos de rutenio que permitieron hidrogenar olefinas y cetonas, presentando mejor actividad y ciclabilidad que su correspondiente complejo en fase homogénea.[48] También hay ejemplos de uso de grafeno en lugar de GO, como la oxidación de pirogalol mediante un híbrido hemin-grafeno, donde el centro activo de una proteína se une al grafeno para tratar de replicar el comportamiento enzimático.[49]

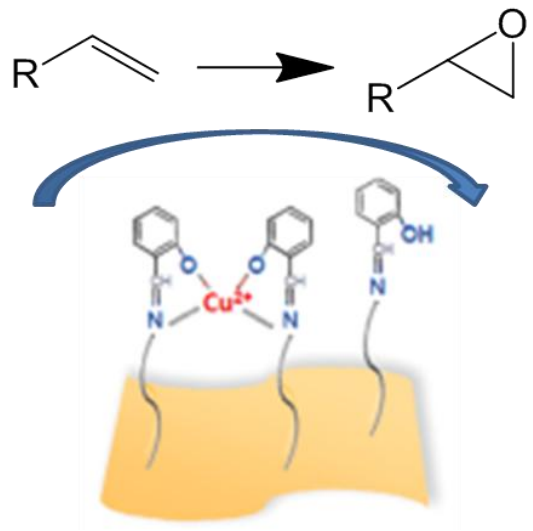

Figura 1.13. Epoxidación de olefinas catalizada por un híbrido complejo de Salen – GO[47]

Por su parte, se pueden encontrar varios ejemplos empleando como soporte nanotubos de carbono. Complejos de rodio[50] han sido inmovilizados sobre nanotubos modificados para reacciones de hidroformilación de propeno con excelentes resultados. Además, existen ejemplos de inmovilización del complejo de Wilkinson y de complejos quelatos sobre nanotubos de carbono para catalizar reacciones de hidrogenación de ciclohexeno, obteniendo mejores resultados comparado con catalizadores homogéneos y heterogeneizados sobre carbón activado análogos.[51] Por otro lado, se describió el anclaje de complejos de rutenio basados en los catalizadores de Grubbs en nanotubos de carbono para provocar la metátesis con cierre de anillo de olefinas. Los catalizadores presentaban una alta reciclabilidad.[52]

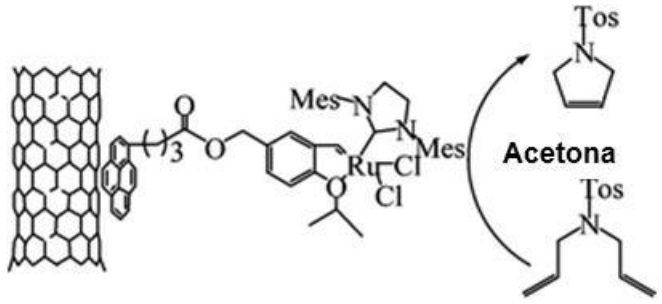

Figura 1.14. Metátesis de cierre de anillo catalizada por un híbrido nanotubo-complejo de rutenio[52]

Por otro lado, existen catalizadores basados en sistemas híbridos nanomaterial de carbono-metal que encuentran aplicación en campos diferentes de la catálisis molecular. En la literatura existen un gran número de trabajos cuyo objetivo se basa en el desarrollo de **pilas de combustible**, donde tradicionalmente se utilizan altas cargas de platino a altas temperaturas de trabajo. Ambos materiales, nanotubos y grafenos, han sido empleados para la construcción de las capas catalíticas de células en un intento de rebajar su temperatura de trabajo, su tamaño o sus cargas en metal. Con el uso de los sistemas híbridos basados en carbono, la estrategia más comúnmente empleada es la inmovilización de nanopartículas de metálicas sobre la superficie del nanomaterial, para después depositarlo como un film en el electrodo (cátodo o ánodo), de tal manera que se pueda aprovechar la electricidad de la evolución del hidrógeno a agua, de la reducción de oxígeno, o de la ruptura de agua o metanol a oxígeno, CO_2 e hidrógeno.[53]

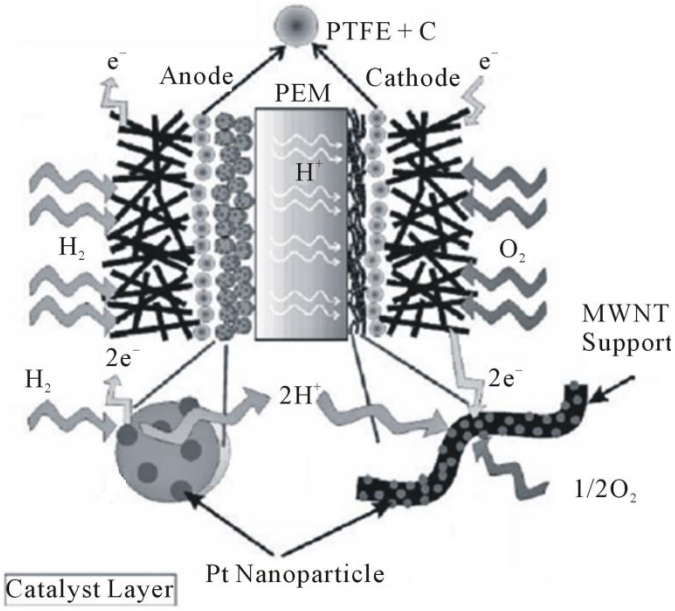

Figura 1.15. Esquema de una célula de combustible que utiliza nanotubos de carbono

La otra aplicación ampliamente estudiada es la combinación de nanoestructuras carbonosas como soporte de nanopartículas en el empleo de **fotocatalizadores**, sistemas capaces de convertir la energía lumínica en energía química. En este proceso, la luz activa el centro activo generando en sus estructuras electrónicas pares electrón-hueco. Durante la relajación, la energía absorbida es empleada en la generación de radicales muy reactivos, como por ejemplo radicales ·OH, los cuales seguirán procesos secundarios. Bajo estas premisas, los fotocatalizadores se pueden emplear en procesos de eliminación de contaminantes (orgánicos y biológicos) de aguas. El dióxido de titanio es el sistema más empleado ya que la energía necesaria para su activación se corresponde con la radiación UV solar. El papel de nanotubos o grafenos, además de soportar y localizar el titanio, reducir su carga y aportar porosidad al sistema, consiste en realizar transferencias electrónicas de manera que se rebaje la energía de la activación lumínica, pudiendo el titanio ser activado con radiación visible.[54]

Figura 1.16. Esquema de un fotocatalizador de grafeno[54]

1.4 CARBENOS N-HETEROCÍCLICOS

La primera vez que se aisló y caracterizó un carbeno N-heterocíclico (NHC) fue en 1991,[56] sin necesidad de reacciones de atrapamiento. Este hallazgo dio lugar a una nueva familia de compuestos orgánicos disponibles para la investigación. Con el tiempo, estas nuevas moléculas pasaron de ser curiosidades académicas a convertirse en una de las más empleadas herramientas en química orgánica, llegando a poder sustituir a las tradicionales fosfinas en las esferas de coordinación de los metales a la hora de sintetizar complejos organometálicos. Además, los complejos NHC poseen muchas aplicaciones en importantes procesos comerciales.

Los complejos NHC, como se describirá a lo largo de esta sección, son moléculas robustas y estables que generan catalizadores activos en un gran número de procesos químicos. Estas propiedades permiten que la generación de los sistemas híbridos complejo NHC-nanomaterial de carbono parcialmente oxidado sea posible, permitiendo además el traslado recíproco de propiedades entre soporte y metal, generando así nuevos y activos catalizadores moleculares.

1.4.1 Generalidades de los carbenos

Un carbeno es un compuesto orgánico neutro que posee un átomo de carbono divalente con 6 electrones en lugar de 8 en su capa de valencia. Para estabilizarse, emplea electrones disponibles de átomos vecinos, generalmente átomos dadores o átomos con orbitales disponibles, en función de las características electrónicas del carbeno. Por tanto, los carbenos suelen ser estabilizados con metales de transición, al tener orbitales de energía adecuada para enlazarse mediante enlaces carbeno – metal (orbitales vacíos) y retrodonaciones metal – carbeno (orbitales llenos). Si el carbeno tiene carácter electrófilo estamos ante un carbeno de Fisher, caracterizado por un estado electrónico fundamental singlete que se estabiliza al aceptar densidad electrónica desde orbitales ocupados del metal o de otros heteroátomos del bloque *p* dadores; por el contrario, si el carbeno tiene carácter nucleófilo (estado electrónico fundamental triplete) se genera un carbeno de Schrock, que se estabiliza por cesión de densidad electrónica a metales electrónicamente pobres, de principios de período.[55]

No obstante, existe un tercer tipo de carbenos diferente a los casos clásicos. En esta tercera clase, el carbeno posee un estado electrónico fundamental singlete, pero su naturaleza es nucleófila. Estamos ante los carbenos de Arduengo o **carbenos N-heterocíclicos** (NHC del inglés *N-heterocylic carbenes*).[56] Los carbenos NHC se estabilizan gracias a la densidad electrónica de tipo π de los heteroátomos vecinos, generalmente nitrógeno en uniones de tipo diamina, al orbital LUMO; simultáneamente, la electronegatividad de los heteroátomos vecinos rebaja la energía del HOMO por efecto inductivo al retirar carga. Además, su naturaleza cíclica ayuda a favorecer el estado singlete, ya que al doblarse los enlaces es más favorable que se produzca la hibridación sp^2 en el átomo carbénico.[57]

Los carbenos N-heterocíclicos más comúnmente utilizados son derivados de imidazol, pirazol o triazol, unidades parcialmente arómaticas que aportan otra fuente de estabilidad. No obstante, en la actualidad se conocen muchos derivados acíclicos, carbenos NHC en donde el segundo heteroátomo no es un átomo de nitrógeno en el anillo, carbenos con un solo átomo de nitrógeno como los pirrolidin-carbeno o incluso carbenos de anillo expandido.

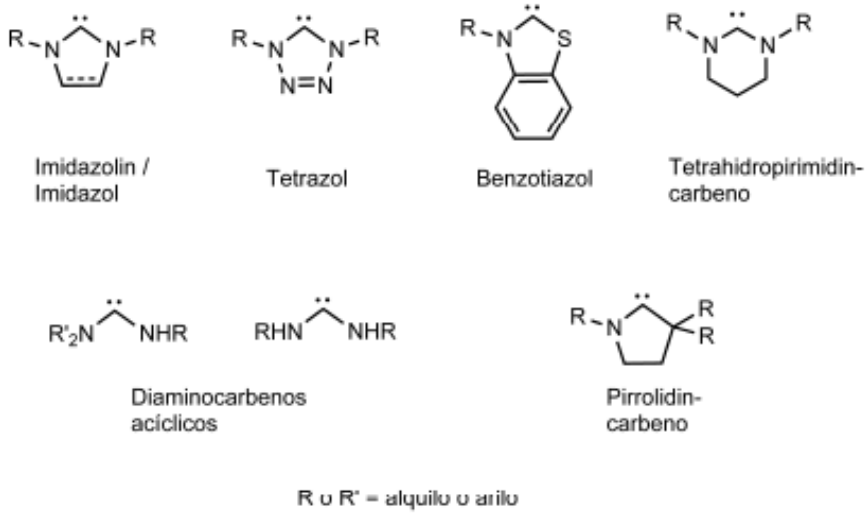

Figura 1.17. Carbenos NHC[58]

Las características nucleófilas del singlete del carbeno NHC le permiten actuar como unidad σ-dadora y enlazarse a un rango muy amplio de especies metálicas y no metálicas formando enlaces muy fuertes. Además, estas propiedades influencian en la estructura, estabilidad y reactividad de los aductos que forman. Estas también se pueden ver modificadas por los sustituyentes de los nitrógenos (u otros heteroátomos) u otros grupos funcionales presentes en ellos.

Si sumamos la facilidad de síntesis, generalmente mediante una desprotonación del catión correspondiente, los complejos organometálicos de tipo NHC han atraído

mucha atención en los últimos años. Bibliotecas de diferentes compuestos son fácilmente sintetizables, para ser capaces de convertirse en catalizadores activos y estables de multitud de reacciones, como polimerizaciones, hidroaminaciones, acoplamientos cruzados C-C, transferencias de hidrógeno, activaciones de CO_2 o metátesis de olefinas, entre otras. Un ejemplo muy claro es la construcción del catalizador de Grubbs (premio Nobel de química en el año 2005) de segunda y tercera generación (catalizador Hoveyda-Grubbs),[59] donde se sustituye una fosfina por la unidad NHC, de manera que el catalizador se vuelve más activo, estable frente al aire y la temperatura, y es capaz de ampliar el rango de sustratos e incluso polimerizar olefinas mediante metátesis de apertura de anillo.

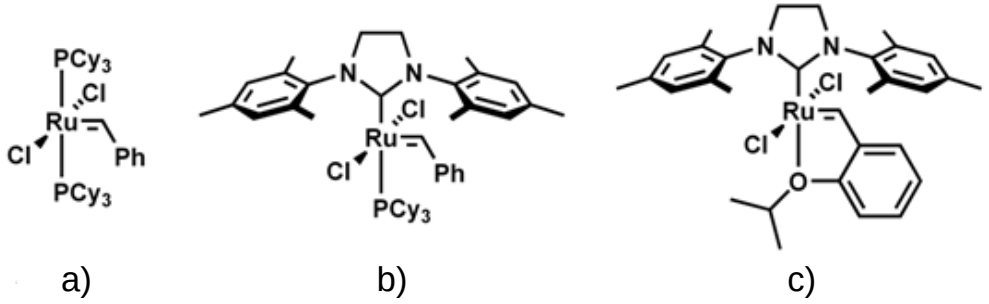

Figura 1.18. Catalizadores de Grubbs de: a) primera generación, b) segunda generación y c) tercera generación

Dentro de la amplia familia que suponen los complejos organometálicos NHC, cuando se emplea iridio como centro metálico se pueden obtener catalizadores activos de una gran variedad de reacciones, como procesos de hidrosililación, hidrogenación, hidroformilación, transferencia de hidrógeno e hidroboración. No obstante, una de las reacciones más estudiadas que emplea estos carbenos de iridio es la hidrogenación de compuestos orgánicos insaturados. Olefinas, aldehídos, cetonas e iminas alifáticas y aromáticas, simétricas o asimétricas e impedidas o no impedidas estéricamente pueden ser reducidas a sus correspondientes parafinas,

alcoholes y aminas en condiciones suaves de una manera rápida y sencilla. Además, la actividad de estos complejos es comparable a catalizadores más clásicos como los catalizadores de Wilkinson o de Crabtree, pero presentan mayor estabilidad térmica antes de su descomposición.

1.4.2 Transferencia de hidrógeno

Frente a la dificultosa, cara, peligrosa y poco selectiva hidrogenación tradicional empleando hidrógeno gas y un metal, un proceso mucho más refinado para llevar a cabo las reacciones de hidrogenación antes mencionadas es la transferencia de hidrógeno.[60] Consiste en el flujo de hidrógeno de un dador a través del iridio hasta un enlace múltiple, el cual se reduce. El dador de hidrógeno siempre es distinto del propio gas, y comúnmente se utiliza metanol, alcohol bencílico, 2-propanol, ácido fórmico y sus sales, y en ocasiones hidracina. Además, estas reacciones suelen realizarse en medio básico, el cual ayuda a la formación de especies de tipo metal-hidruro. La reacción de transferencia de hidrógeno se aplica tanto a nivel académico para llevar a cabo reducciones de sustratos insaturados de todo tipo en unas condiciones moderadas; como a nivel industrial, como en la licuefacción de carbón usando disolventes dadores del tipo tetralina.[61]

Respecto al mecanismo de la reacción de transferencia de hidrógeno, existen diferentes posibilidades en función del complejo que se emplee como catalizador. Sin embargo, catalizadores de iridio-NHC suelen seguir mecanismos de esfera interna, es decir, procesos en los que el sustrato se coordina directamente al metal. Generalmente, el sustrato coordinado se inserta en el enlace metal hidruro generando el producto final de la reducción, el cual será sustituido en la esfera de coordinación del metal por el dador de hidrógeno, que mediante una β-eliminación regenerará el

hidruro metálico. En este tipo de mecanismo, llamado mecanismo monohidruro, el protón que genera la especie catalíticamente activa, es decir, el hidruro metálico, corresponde al hidrógeno α del dador, el cual es transferido al carbono carbonílico del sustrato.[62]

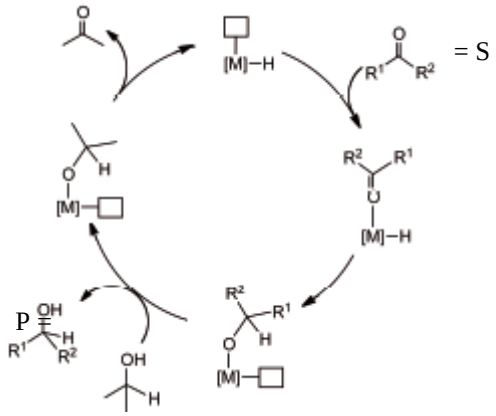

Figura 1.19. Mecanismo de la reacción de transferencia de hidrógeno (S = sustrato, P = producto, [M] = centro metálico).

2. OBJETIVOS Y ORGANIZACIÓN DE LA MEMORIA

OBJETIVOS Y ORGANIZACIÓN DE LA MEMORIA

2.1 OBJETIVOS

Conforme a las líneas descritas en el capítulo anterior, la presente memoria tiene por objetivo la síntesis y caracterización de sistemas híbridos nanomaterial de carbono (nanotubos de carbono o materiales grafénicos)-complejo organometálico de iridio para su aplicación como catalizador en reacciones de reducción mediante transferencia de hidrógeno. Este objetivo se enmarca dentro del proyecto CONSOLIDER MULTICAT 2010, donde la actividad del Grupo de Investigación se centra en el desarrollo de soportes proactivos de catalizadores basados en carbones activados, nanotubos de carbono y materiales grafénicos. Para alcanzar el objetivo general, se plantean los siguientes objetivos específicos:

1. **Obtención de nanomateriales de carbono** modificados con grupos funcionales oxigenados. Se eligen estrategias de modificación, bien con diferentes tratamientos oxidantes o empleando reducciones térmicas, para variar el tipo y la cantidad de los mismos en la superficie de los materiales.

2. **Diseño de estrategias de funcionalización covalente** a través de los grupos funcionales oxigenados. Se eligen reacciones selectivas a los diferentes grupos funcionales (carboxilos e hidroxilos) presentes en la

superficie de los nanomateriales de carbono para la introducción de ligandos precursores de los complejos organometálicos.

3. Aplicación de los nanomateriales de carbono funcionalizados como **soporte proactivo de catalizadores** para reacciones de reducción mediante transferencia de hidrógeno.

2.2 ORGANIZACIÓN DE LA MEMORIA

La presente Memoria, realizada como "compendio de publicaciones", describe la preparación, caracterización y aplicación de nanotubos de carbono y óxido de grafeno como soporte de catalizadores moleculares, en este caso complejos organometálicos NHC de iridio. La organización de los contenidos es la siguiente:

En la **Introducción**, Capítulo 1, se expone una visión general de los conceptos básicos de catálisis, así como el papel que desempeñan los nanomateriales de carbono, concretamente nanotubos de carbono y materiales grafénicos, como parte de sistemas catalíticos en diversos procesos. También se describen sus propiedades generales, factores por los cuales son seleccionados como soporte de catalizadores. Finalmente se introducen los complejos de tipo carbeno N-heterocíclicos de iridio, y su actuación en reacciones de reducción por medio de procesos de transferencia de hidrógeno, ya que la actividad catalítica de dichos complejos soportados sobre los nanomateriales de carbono es el eje central de las aportaciones del Trabajo.

En este Capítulo 2 se especifican los **Objetivos del Trabajo**, tras dar a conocer las ideas generales sobre las que versa la presente Memoria, así como exponer la organización de la misma.

El apartado **Experimental,** Capítulo 3, resume los procedimientos de preparación de los nanomateriales, las rutas de funcionalización aplicadas para la generación de los materiales híbridos nanomaterial-complejo organometálico, así como las técnicas analíticas empleadas en la caracterización y las metodologías seguidas en el estudio de la actividad catalítica.

La sección destinada a los **Resultados** obtenidos se ha dividido en cuatro capítulos correspondientes a los cuatro artículos de los que consta esta Tesis Doctoral. Cada artículo viene precedido de un breve resumen que recoge los resultados más significativos y las conclusiones alcanzadas.

Finalmente, las **Conclusiones generales**, con las aportaciones realizadas, cierran la Memoria en el último Capítulo 5.

A continuación se detallan las referencias bibliográficas de los artículos que constituyen el Capítulo 4, así como el factor de impacto 2014 (FI_{2014}) de las revistas donde fueron publicados.

- Artículo I: M. Blanco *et al*. "Influence of the degree of aligment of CVD-grown carbon nanotubes on their functionalization and adsorption capacity". Diamond and Related Materials **2013**, *37*, 1-7. FI_{2014}: 1.572

- Artículo II: M. Blanco *et al*. "Enhanced hydrogen transfer catalytic activity of iridium N-heterocyclic carbenes by covalent attachment to carbon nanotubes". ACS Catalysis **2013**, *3*, 1307-1317. FI_{2014}: 7.572

- Artículo III: M. Blanco *et al.* "Covalent immobilization of iridium-NHC catalysts on carbon nanotubes with increasing oxidation degree". *Artículo enviado a RSC Catalysis, Science and Technology*

- Artículo IV: M. Blanco *et al.* "Graphene–NHC–iridium hybrid catalysts built through –OH covalent linkage". Carbon **2015**, *83*, 21-31. FI_{2014}: 6.196

- Artículo V: M. Blanco *et al.* "Effect of structural differences of carbon nanotubes and graphene based iridium-NHC materials on the hydrogen transfer catalytic activity". *Carbon 2015, en prensa.*

3. EXPERIMENTAL

EXPERIMENTAL

3.1 MATERIALES DE PARTIDA

Todos los productos químicos, calidad *ACS Reagent* o superior, empleados para la realización del trabajo experimental, fueron adquiridos en la compañía *Sigma-Aldrich*, y se aplicaron directamente, salvo el N-metilimidazol y la ciclohexanona, que fueron destilados previo uso.

Los ácidos inorgánicos fueron suministrados por la empresa *Scharlau*, y se usaron sin purificación adicional. Los disolventes se destilaron previo uso empleando agentes desecantes adecuados, u obtenidos de un sistema de purificación de disolventes (*Innovative Technologies*). Por su parte, los disolventes deuterados D_2O, acetona-d_6 y $CDCl_3$ procedieron de *Eurosi-Top*, y no se les aplicó ninguna purificación adicional. El agua, de calidad Milli-Q, tuvo una conductividad de 18.2 MΩ · cm a una temperatura de 25 ºC.

Los nanotubos de carbono de pared múltiple (MWCNT) tipo ovillo proceden de la empresa *Sigma-Aldrich*. El fabricante especificó diámetros externos de 10-15 nm, internos de 2-6 nm y longitudes de 0.1-10 µm. Los nanotubos de carbono de pared múltiple tipo césped (I-NT) fueron suministrados por el Instituto Tecnológico de Materiales (ITMA). Se sintetizaron por CVD térmico utilizando un equipo *ET3000* de *First Nano* sobre obleas de silicio. Se depositaron capas finas de SiO_2, Al_2O_3

porosa y hierro. Tras un tratamiento térmico a 600 ºC, se generaron aglomerados de tamaño nanométrico que se usaron como soporte para el crecimiento de los nanotubos. El soporte se introdujo en el reactor de cuarzo, que se calentó a 750 ºC bajo una atmósfera de argón, pasando una corriente de etileno durante 1 hora. Se bajó la temperatura hasta 300 ºC en atmósfera de argón e hidrógeno, y finalmente se enfrió hasta temperatura ambiente en argón.

Sigma Aldrich suministró el grafito comercial (grafito C) empleado en la preparación de materiales grafénicos. Se presenta en forma de grafito en polvo, con un tamaño de partícula inferior a 70 μm.

Las sales de imidazolio [MeImH$(CH_2)_3$OH]Cl (**1**)[63] y [MeImH(1-ciclohexil-2-ol)]I (**2**),[64] así como el complejo organometálico precursor de carbenos N-Heterocíclicos de iridio [{Ir(μ-OMe)(cod)}$_2$ (cod = ciclooctadieno)[65] fueron preparados acorde a los procedimientos publicados previamente.

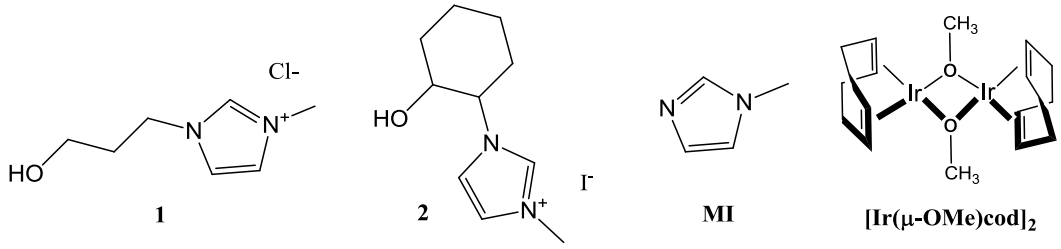

Figura 3.1. Productos de partida orgánico-organometálicos

3.2 PURIFICACIÓN, OXIDACIÓN Y REDUCCIÓN TÉRMICA DE LOS NANOMATERIALES DE CARBONO

3.2.1 Purificación de nanotubos de carbono

La purificación de los nanotubos de carbono se llevó a cabo mediante tratamiento con ácido clorhídrico. En un matraz tipo Erlenmeyer con agitación magnética se suspendieron 0,3 g de nanotubos en 70 mL de HCl. La suspensión se calentó a 60 ºC durante 15 min y se introdujo 2 h en un baño de ultrasonidos. Una vez finalizada la reacción, se diluyó añadiendo 200 mL de agua, y se centrifugó en una centrífuga *Consul 21* de *Orto Alresa* a 4700 rpm (3779 g de fuerza centrífuga relativa) durante 30 min, descartándose el sobrenadante y repitiéndose el proceso hasta pH neutro. El sólido resultante se secó en una estufa precalentada a 100 ºC, hasta peso constante. Los nanotubos obtenidos se etiquetaron como **C-NT-HCl** en los nanotubos tipo ovillo o **I-NT-HCl** para los nanotubos tipo césped.

3.2.2 Oxidación suave de nanotubos de carbono

En un matraz esférico equipado con un refrigerante de reflujo y con agitación magnética, se suspendieron 0,3 g de nanotubos de carbono purificados en una mezcla de 25 mL de NH_4OH (28%) y H_2O_2 (30%) en proporción 1:1. La mezcla se calentó a 80 ºC durante 5 horas. Finalizada la reacción se diluyó, añadiendo 200 mL de agua, y se centrifugó a 4700 rpm durante 30 min. Se descartó el sobrenadante y el procedimiento se repitió hasta pH neutro. El sólido obtenido se secó en una estufa precalentada a 100 ºC, hasta peso constante. Los nanotubos obtenidos se etiquetaron como **C-NT-LT** para los nanotubos tipo ovillo y **I-NT-LT** para los nanotubos tipo césped.

3.2.3 Oxidación moderada de nanotubos de carbono

Para realizar la oxidación moderada, se utilizó un proceso en dos etapas. En una primera etapa, se preparó una suspensión compuesta de 0,3 g de nanotubos purificados y 70 mL de una disolución de HNO_3 3 M. Dicha suspensión se calentó a 60 ºC durante 15 min, y se introdujo 2 h en un baño de ultrasonidos. Una vez finalizada la reacción, se diluyó añadiendo 200 mL de agua, y se centrifugó a 4700 rpm durante 30 min. El sobrenadante se descartó, y el procedimiento se repitió hasta pH neutro. El sólido obtenido se secó en una estufa precalentada a 100 ºC, hasta peso constante.

En la segunda etapa, se preparó una nueva suspensión del sólido anterior en 70 mL de H_2O_2 (30%), la cual se calentó a 60 ºC durante 15 min y se introdujo en un baño de ultrasonidos durante 2 h. Finalizada la reacción, se diluyó añadiendo 200 mL de agua. Posteriormente, se filtró a vacío sobre una placa filtrante tipo 4. El sólido fue lavado con abundante agua, y se secó en una estufa precalentada a 100 ºC hasta peso constante. Los nanotubos obtenidos se etiquetaron como **C-NT-MT** para los tipo ovillo o **I-NT-MT** para los tipo césped precursores.

3.2.4 Oxidación fuerte de nanotubos de carbono

En un matraz esférico equipado con un refrigerante de reflujo y con agitación magnética, 0,3 g de nanotubos de carbono purificados se suspendieron en una mezcla de 40 mL de H_2SO_4 (97%) y HNO_3 (65%) en proporción 3:1. Esta suspensión se introdujo 10 min en un baño de ultrasonidos, se calentó a 80 ºC durante 20 min y sin dejar que la mezcla se enfríe, se introdujo en el baño de

ultrasonidos 20 min adicionales. Tras la adición a esta mezcla de 200 mL de agua, se centrifugó a 4700 rpm durante 30 min. El sobrenadante se descartó, y el procedimiento se repitió hasta pH neutro. El sólido resultante se secó en una estufa precalentada a 100 ºC hasta peso constante. Los nanotubos obtenidos se etiquetaron como **C-NT-ST** para los tipo ovillo o **I-NT-ST** para los tipo césped.

3.2.5 Oxidación de grafito. Obtención de óxido de grafeno

El óxido de grafeno empleado en este trabajo (**GO-C**) se obtuvo mediante un procedimiento de dos etapas. La primera consiste en la oxidación del grafito empleando un método Hummers modificado, seguido de un tratamiento de exfoliación de 8 h mediante un baño de ultrasonidos. La primera etapa, oxidación del grafito, consistió en la suspensión de 7,5 g del grafito precursor en 360 mL H_2SO_4 concentrado bajo agitación mecánica constante. Se añadieron 7,5 g de $NaNO_3$ y mediante adición lenta, 45 g de $KMnO_4$, manteniendo la reacción a 35 ºC durante 3 h. Transcurrido ese tiempo, se añadieron lentamente 1,5 L de H_2O_2 con una concentración de 3 % peso en agua, permitiendo una 1 h adicional de reacción bajo agitación.

La eliminación de sales inorgánicas residuales y otras impurezas se realizó por centrifugación a 4000 rpm (3667g) en una centrífuga *GIROZEN 1580R*, descartando el sobrenadante y añadiendo 1 L de agua, repitiendo la operación hasta la obtención de pH neutro. De esta manera, se generó óxido de grafito que, dependiendo del procedimiento a utilizar para su exfoliación, se secó y molió (*Retsch MM2*, 10 min 60 Hz), o se mantuvo en suspensión para su exfoliación mediante de ultrasonidos. Tras el tratamiento con ultrasonidos, el producto resultante se centrifugó durante 30 min, reservando en este caso el sobrenadante y descartando el sólido, el cual

contiene fundamentalmente óxido de grafito no exfoliado. Así, se obtuvo **GO-C** en suspensión, cuyo secado y molienda para posteriores usos se realizó como el óxido de grafito precursor.

3.2.6 Reducción térmica de nanomateriales de carbono

Los nanomateriales de carbono **CNT-ST** y el óxido de grafito seco y molido (apartado 3.2.5) se redujeron parcialmente por vía térmica con el objetivo de eliminar grupos funcionales oxigenados superficiales generados en los procesos de oxidación. La estabilidad térmica de estos grupos está bien descrita en la bibliografía,[74] con lo que se seleccionó como temperatura de reducción 400 ºC al ser una temperatura suficientemente alta como para eliminar los ácidos carboxílicos pero lo suficientemente baja como para dejar inalterados los hidroxilos.

Así, los nanomateriales de carbono parcialmente reducidos a 400 ºC se obtuvieron por calentamiento en atmósfera inerte de nitrógeno (50 mL min^{-1}) de sus correspondientes materiales oxidados (nanotubos de carbono u óxido de grafito) secos. 1 g de material fue depositado en una navecilla cerámica e introducido en un horno horizontal eléctrico. Se seleccionó una rampa de calentamiento de 5 ºC min^{-1} y con un tiempo de residencia a la temperatura final de 1 h. De esta manera se obtuvieron respectivamente, **TR-CNT-ST** y **TRGO,** en función del tipo de material de partida empleado.

Destacar que en el tratamiento del óxido de grafito para la obtención del material grafénico parcialmente reducido se produce la simultánea exfoliación del material y reducción térmica parcial. Esto es debido a la rápida y brusca desorción de los grupos funcionales oxigenados lábiles en forma de CO y CO_2 provocada por el

tratamiento térmico, junto con el agua atrapada. Al generar una sobrepresión entre láminas del óxido de grafito, la súbita y explosiva salida de gases provoca la separación de las láminas del material, que al estar sometido a un tratamiento térmico a una temperatura determinada, prosigue la eliminación de grupos funcionales.[66]

3.3 FUNCIONALIZACIÓN DE LOS NANOMATERIALES DE CARBONO

3.3.1 Funcionalización a través de los grupos carboxilo

Uno de los grupos funcionales más reactivos que presentan los nanomateriales de carbono son los **ácidos carboxilos**. Al ser un grupo voluminoso estéricamente, los ácidos se localizan en bordes de plano y defectos estructurales. Son funciones responsables de la carga negativa superficial, y térmicamente lábiles, empezando a desorber como CO y CO_2 a temperaturas comprendidas entre 40 y 150 ºC. Su localización "externa" los vuelve muy reactivos, y al ser un grupo ácido son fácilmente manipulables con reacciones orgánicas de esterificación-amidación clásicas. En este trabajo, los ácidos carboxílicos superficiales se hicieron reaccionar con compuestos imidazólicos en dos etapas. El método de funcionalización consistió en el siguiente procedimiento:

0,1 g de nanomaterial de carbono fueron desgasificados mediante 4 ciclos de 10 min de vacío - 2 min de nitrógeno gas para asegurar la atmósfera inerte durante el proceso. A continuación, se añadieron 40 mL de $SOCl_2$, y la reacción se mantuvo a reflujo durante 24 h con agitación magnética. Tras ese tiempo, el $SOCl_2$ en exceso se eliminó mediante evaporación a presión reducida. El sólido se lavó 3 veces con 20

mL de tetrahidrofurano (THF), de manera que se suspendiese y decantase hasta obtener un líquido claro. Finalmente, el sólido se secó a vacío durante 2 h.

En la segunda etapa, el sólido anterior se suspendió en 20 mL de THF, a los cuales se añadieron 0,5 mmol de las sales de imidazolio **1**, **2** o de N-metilimidazol en cada caso (ver figura 3.1). La reacción se mantuvo a reflujo durante 24 h con agitación magnética. Transcurrido ese tiempo, el producto de reacción resultante se lavó mediante filtración en placa porosa tipo 4, 3 veces con 25 mL de THF, 3 veces con 25 mL de diclorometano (DCM) y 2 veces con 10 mL de éter etílico (Et_2O). Finalmente, se secó en una estufa precalentada a 100 ºC hasta peso constante.

Los materiales así obtenidos fueron etiquetados como **CNT-X-A** o **GOC-A** en función del nanomaterial de carbono empleado (nanotubos u óxido de grafeno), donde **X** es el grado de oxidación del nanomaterial de partida (HCl, LT, MT o ST) y **A** es el compuesto imidazólico empleado (sal 1, 2 o metilimidazol, MI)

3.3.2 Funcionalización a través de los grupos hidroxilo.

A diferencia de otros procedimientos tradicionalmente empleados en la bibliografía para la funcionalización de nanomateriales a través de los **grupos hidroxilo**, que suelen utilizar la química de derivados siloxanos, peligrosa y de difícil manejo, en este trabajo se optó por desarrollar un método de funcionalización empleando conectores basados puramente en carbono. El método consistió en el siguiente procedimiento en dos etapas:

0,1 g de nanomaterial de carbono fueron desgasificados siguiendo el procedimiento descrito en el apartado 3.3.1, y dispersados en 20 mL de DCM bajo

atmósfera inerte. Dicha suspensión se enfrió a 0 ºC con ayuda de un baño de hielo, y se añadieron 3,0 g (15 mmol) de *p*-nitrofenil cloroformiato y 2,1 mL (15 mmol) de trietilamina. La reacción se mantuvo 24 h con agitación magnética, dejando que la temperatura subiese lentamente de 0º C a temperatura ambiente. El sólido se filtró con ayuda de una placa porosa tipo 4 y se lavó 3 veces con 20 mL de DCM, para secarlo 2 horas bajo vacío. En el segundo paso, este sólido se dispersó en 20 mL de THF, y se añadieron 100 mg (0,56 mmol) de la sal de imidazolio **1** y trietilamina (0,2 mL). La mezcla se mantuvo reaccionando a reflujo con agitación magnética durante 24 h. Los productos se obtuvieron por filtrado en placa porosa tipo 4 y lavado 3 veces con 20 mL de THF, 3 veces con 20 mL de DCM y 2 veces con 10 mL de Et_2O. Finalmente, se secaron en una estufa precalentada a 100 ºC hasta peso constante.

Los materiales así obtenidos fueron etiquetados como **B-CNT-ST-1** o **B-GO-C-1**, donde *B* es el grado de reducción térmica aplicado (material oxidado o reducido a 400 ºC, **TR-**).

3.3.3 Síntesis de los complejos NHC de iridio soportados

El procedimiento más habitual y sencillo para la síntesis de los complejos NHC de iridio es la desprotonación del carbono C2 (carbono en posición α a los dos heteroátomos) del anillo heterocíclico por una base. La abstracción de ese protón genera el carbeno, que será atrapado por la unidad metálica dando lugar al complejo organometálico. Ambos procesos pueden ser simultáneos si el precursor posee ligandos básicos capaces de arrancar esos protones.

Siguiendo esta idea, los nanomateriales de carbono funcionalizados con sales de imidazolio fueron sometidos sistemáticamente a la síntesis de los complejos NHC de

iridio, empleando como complejo precursor $[\{Ir(\mu\text{-}OMe)(cod)\}]_2$. Este dímero es capaz de disociarse, de manera que sus grupos básicos metoxi desprotonorán los anillos de imidazolio generando el carbeno, que será atrapado y estabilizado por la unidad desnuda "[Ir(cod)]". Para ello, 0,1 g de los materiales funcionalizados empleando sus grupos carboxilos (apartado 3.3.1), como los funcionalizados en sus grupos hidroxilo (apartado 3.3.2), fueron desgasificados siguiendo el procedimiento descrito en la funcionalización a través de grupos carboxílicos (apartado 3.3.1) y puestos en suspensión de 25 mL de THF mediante agitación magnética vigorosa. A continuación se añadieron 100,0 mg (0,15 mmol) del complejo precursor de iridio $[\{Ir(\mu\text{-}OMe)(cod)\}]_2$. La reacción se mantuvo a reflujo durante 2 días. Transcurrido ese tiempo, el producto de reacción resultante se lavó 5 veces con 25 mL de THF mediante filtración en placa porosa, y 2 veces con 10 mL de Et_2O.

En la nomeclatura de las nuevas muestras obtenidas, se añadió el sufijo **–Ir** para indicar la presencia del complejo NHC de iridio en el material. De esta manera, se generan las muestras **B-CNT-X-A-Ir** o **B-GOC-A-Ir** siguiendo el esquema descrito en los apartados 3.3.1 y 3.3.2

A efectos comparativos, los materiales sin funcionalizar con las sales de imidazolio, es decir, los materiales de partida **CNT-ST, GO-C, TRCNT-ST** y **TRGO-C** se hicieron reaccionar con el complejo precursor de iridio del mismo que sus correspondientes materiales funcionalizados para la obtención de blancos de reacción. Los materiales obtenidos se etiquetaron como **CNT-ST-Ir, GO-C-Ir, TRCNT-ST-Ir** y **TRGO-C-Ir.**

3.3.4 Síntesis de complejos NHC de iridio homogéneos.

La síntesis y caracterización de los correspondientes complejos organometálicos NHC de iridio homogéneos se realizó con el objetivo de tener una comparativa homogénea a los complejos soportados. El diseño de sus estructuras se realizó de una forma lo más similar posible a la probable estructura del complejo enlazado covalentemente al nanomaterial. El procedimiento de nuevo es análogo al heterogéneo, pues consiste en la síntesis de la sal de imidazolio adecuada que será posteriormente desprotonada y pasará a formar parte de la esfera de coordinación del metal.

Todas las operaciones llevadas a cabo para la obtención de los complejos homogéneos NHC de iridio se realizaron bajo atmósfera inerte y en condiciones de sequedad siguiendo las técnicas Schlenck.

3.3.4.1 Síntesis de las sales de imidazolio precursoras

- Cloruro de 3-(3-Acetoxipropil)-1-metil-1H-imidazol-3-io (**3**):
  Para la síntesis de **3**, se mezcló 3-cloropropilacetato (1,54 mL, 12,5 mmol) con 1,0 mL (12,5 mmol) de N-metilimidazol en 15 mL de acetonitrilo (CH_3CN). La reacción se mantuvo a reflujo 72 h. El aceite incoloro formado se separó por decantación, y las impurezas generadas se lavaron con n-hexano. El producto final fue secado en vacío. Rdto: 83%. Análisis Calculado para $C_9H_{15}ClN_2O_2$: C, 49.93; H, 6.91; N, 12.81. Encontrado: C, 50.14; H 6.85; N, 12.90. ESI-HRMS (CH_3CN) m/z = 183.11 $[M]^+$. ^{1}H RMN (298 K, $CDCl_3$): δ = 9.03 (s, 1H, NC*H*N), 7.69 (d, *J* = 2.0, 1H, CH Im), 7.61

(d, *J* = 2.0, 1H, CH Im), 4.35 (t, *J* = 7.1, 2H, NCH_2), 4.14 (t, *J* = 5.9, 2H, OCH_2), 3.95 (s, 3H, NCH_3), 2.25 (m, 2H, CH_2), 2.04 (s, 3H, $OCCH_3$). $^{13}C\{^1H\}$ NMR (298 K, $CDCl_3$): δ 172.53 (C=O), 136.87 (NC*H*N), 125.03 (CH Im), 123.76 (CH Im), 61.96 (OCH_2), 47.96 (NCH_2), 36.52 (NCH_3), 30.25 (CH_2), 20.70 (OCH_3).

- Preparación de yoduro de 1-(2-Acetoxiciclohex-1-il)-3-metil-1H-imidazol-3-io (**4**):

  La síntesis de **4** se llevó a cabo en dos etapas. En la primera, se sintetizó el acetato de trans-2-(1H-imidazol-1-il)ciclohexilo mediante reacción de isopropenilacetato (6,0 mL, 54 mmol), con trans-2-(1-imidazolil)ciclohexanol (1,5 g, 9,0 mmol), catalizada por lipasa B extraída de *Cándida Antárctica* (150 mg) en 10 mL de cloroformo ($CHCl_3$). Rdto: 56%. ^{1}H-RMN (298 K, $CDCl_3$): *δ* = 7.50 (br, 1H, NC*H*N), 7.03 (t, *J* = 1.2, 1H, CH Im), 6.93 (t, *J* = 1.2, 1H, CH Im), 4.88 (m, 1H, NCH), 3.94 (m, 1H, OCH), 2.13 (m, 2H, CH_2), 1.87 (s, 3H, CH_3), 1.84 (m, 2H, CH_2), 1.50−1.35 (m, 4H, CH_2).

  En la segunda etapa, se añadió yoduro de metilo CH_3I (0,307 g, 2,16 mmol) a una solución del compuesto anterior (0,410 g, 1,97 mmol) en 15 mL de CH_3CN. La reacción se mantuvo a reflujo durante la noche. El disolvente se eliminó del medio de reacción a presión reducida, y el sólido de color blanco obtenido fue recristalizado en 2-propanol a 0 ºC. Rdto: 85%. ^{1}H-RMN (298 K, $CDCl_3$): *δ* 10.24 (s, 1H, NC*H*N), 7.38 (t, *J* = 1.8, 1H, CH Im), 7.33 (t, *J* = 1.8, 1H, CH Im), 4.95 (m, 1H, NCH), 4.52 (m, 1H, OCH), 4.15 (s, 3H, NCH_3), 2.40 (m, 1H, CH_2), 2.18 (m, 1H, CH_2), 1.98 (s, 3H, CH_3), 1.89 (m, 2H, CH_2), 1.62−1.40 (m, 4H, CH_2).

3.3.4.2 Procedimiento general para la síntesis de los complejos homogéneos NHC de iridio.

Los complejos NHC de iridio con funciones acetoxi fueron obtenidos por un procedimiento de dos etapas basado en la transmetalación a través de carbenos intermedios de plata. En la primera etapa, se formó el carbeno de plata mediante 48 h de reacción a reflujo y en oscuridad de una mezcla de Ag_2O (0,116 g, 0,5 mmol) con la sal de imidazolio **3** o **4** (0,611 mmol) en 20 mL de DCM. El exceso de Ag_2O se eliminó por filtrado, obteniendo una solución incolora del complejo NHC-plata.

En el segundo paso, se añadió una suspensión de $[\{Ir(\mu\text{-}Cl)(cod)\}_2]$ (0,205 g, 0,305 mmol) en 15 mL de acetona a una disolución concentrada del carbeno de plata en 1 mL de DCM. La mezcla se mantuvo reaccionando bajo agitación magnética 24 h a temperatura ambiente. Las sales AgX (X = Cl, I) se eliminaron por filtrado, y las soluciones de color naranja obtenidas fueron llevadas a sequedad a vacío. Las impurezas del residuo se lavaron con n-hexano, obteniendo sólidos de color amarillo, que fueron separados por decantación y secados a vacío.

- **[IrCl(cod)(MeIm(CH_2)$_3$OCOCH_3)] (5):** Rdto.: 61 %. Análisis calculado para $C_{17}H_{26}ClN_2O_2Ir$: C, 39.41; H, 5.06; N, 5.41. Encontrado: C, 39.50; H, 5.11; N, 5,53. ^{1}H NMR (298 K, $CDCl_3$): δ 6.85 (d, *J* = 2.0, 1H, CH Im), 6.82 (d, *J* = 2.0, 1H, CH Im), 4.59 (m, 2H CH_2N, 1H CH cod), 4.32 (m, 1H, CH cod), 4.16 (m, 2H, CH_2O), 3.95 (s, 3H, CH_3 Im) 2.98, 2.84 (m, 1H, CH cod), 2.33 (m, 2H, CH_2 cod), 2.21 (m, 2H CH_2, 2H CH_2 cod), 2.10 (s, 3H, OCH_3) 1.81-1.56 (m, 4H, CH_2 cod). $^{13}C\{^1H\}$ RMN (298 K, $CDCl_3$): δ = 180.89 (NCN), 171.12 (OCO), 121.94, 120.37 (CH Im), 84.89, 84.60 (CH cod), 61.73 (CH_2N), 51.89, 51.30 (CH cod), 47.55 (CH_2O), 37.48 (CH_3 Im), 34.01, 33.44 (CH_2 cod), 30.38 (CH_2),

30.03, 29.31 (CH_2 cod), 21.10 (OCH_3). MS (MALDI-ToF, matriz DIT, CH_2Cl_2) *m/z* = 519.4 [M + H], 483.2 [M – Cl].

- **[IrCl(cod)(MeIm(ciclohexil)OCOCH$_3$)] (6):** Rdto.: 55 %. Análisis calculado para $C_{20}H_{30}ClIrN_2O_2$: C, 43.04; H, 5.42; N, 5.02. Encontrado: C, 44.01; H, 5.98; N, 4.89. ^{1}H RMN (298 K, $CDCl_3$): δ 6.89 (d, *J* = 2.0, 1H, CH Im), 6.82 (d, *J* = 2.0, 1H, CH Im), 5.32 (m, 1H, CHO), 5.13 (m, 1H, CHN), 4.61 (br, 2H, CH cod), 3.96 (s, 3H, NCH_3), 3.34 (m, 1H, CH cod), 3.01 (m, 1H, CH cod), 2.25 (m, 4H CH_2, 4H cod), 1.90 (s, 3H, OCH_3), 1.81–1.42 (m, 4H CH_2, 4H cod). ^{13}C{^{1}H} RMN (298 K, $CDCl_3$): 180.64 (NCN), 170.22 (OCO), 122.17, 119.75 (CH Im), 84.28, 84.00 (CH cod), 73.11 (CHO), 62.77 (CHN), 51.61, 51.67 (CH cod), 37.61 (NCH_3), 33.86, 33.72, 33.56, 32.01 (CH_2), 29.88, 29.66, 24.90, 24.24 (CH_2 cod), 21.07 (OCH_3). MS (MALDI-ToF, matriz DIT, CH_2Cl_2) m/z = 558.3 [M], 523.3 [M – Cl].

3.4 TÉCNICAS DE CARACTERIZACIÓN

3.4.1 Caracterización de sistemas homogéneos

3.4.1.1 Resonancia magnética nuclear

La resonancia magnética nuclear (RMN) es una técnica que se basa en la excitación de spines de átomos con momento de spin nuclear distinto de 0, como son el ^{1}H, ^{2}D, ^{13}C, ^{19}F, ^{31}P, etc. Al aplicar un campo magnético, los spines se alinean con él, de manera que al emitir pulsos de radiación se puede cambiar el sentido de la

orientación del spin, y esa transición está cuantizada en el rango de las ondas de radio.

La particularidad de la técnica es que los entornos químicos de cada grupo de átomos equivalente, dentro de una molécula, afectan a su momento de spin. Los efectos inductivos basados en la diferente electronegatividad, y las diferentes formas resonantes que puede presentar una molécula, modifican la densidad de electrónica en el átomo magnéticamente activo, con lo que el apantallamiento electrónico sentido el spin se altera. Por tanto, la energía de la transición adquiere nuevos valores, con lo que mediante el uso de resonancia magnética nuclear se pueden resolver las estructuras de dichas moléculas.

Los espectros RMN se obtuvieron en espectrómetros *Bruker Advance 300* (^{1}H: 300,1276; ^{13}C: 75,4792 MHz) y *Bruker Advance 400* (^{1}H: 400,1625 MHz, ^{13}C: 100,6127 MHz). Los datos se indican en cada producto de la siguiente manera: Desplazamiento químico δ (ppm relativas a las señales del tetrametilsilano, usando como referencia las resonancias de los disolventes parcialmente deuterados), multiplicidad (s: singulete, d: doblete, t: triplete, q: quintuplete, dd: doble doblete, br: singulete ancho, m: multiplete), constantes de acoplamiento *J* (aportadas en Hz) e integración. La resolución de los espectros se consiguió mediante un uso combinado de los experimentos ^{1}H-^{1}H COSY, ^{13}C APT y ^{1}H-^{13}C-HSQC.

3.4.1.2 Espectrometría de masas

La espectrometría de masas es una técnica instrumental de análisis químico que permite la identificación y la determinación de la cantidad presente de sustancias

químicas por la simple medida de la relación masa-carga y de la concentración de iones en una fase gaseosa.

Existen numerosas combinaciones de fuentes de ionización de iones y de detectores, pero en esencia el fundamento de la separación de iones se basa en la aplicación de campos eléctricos y magnéticos que hacen que los iones se separen en función de su carga. Una vez separados, los iones de misma carga se separan en función del tiempo que tardan en recorrer la distancia entre la fuente de ionización y el detector, llamado tiempo de vuelo (TOF, del inglés *Time of Flight*) a diferentes velocidades, ya que al ser la carga constante, la energía cinética depende solo de la masa. Las fuentes de ionización más comúnmente empleadas pueden ser láseres de ionización-desorción asistidos por una matriz (MALDI, del inglés *Matrix-assisted Laser Desorption-Ionization*), plasmas (ver apartado 3.4.5.2) o formación de iones en electrosprais (ESI-MS, del inglés *ElectroSpray Ionization Mass Spectrometry*) por disociación-ionización de las sustancias a analizar.

En este trabajo, los espectros de masas empleados en la caracterización de las moléculas y los complejos homogéneos se obtuvieron en equipos MALDI-TOF mediante uso de un espectrómetro *Bruker MICROFLEX*, con *trans*-2-[3-(4-tert-butilfenil)-2-metilpropen-2-ilideno] malononitrilo (DCTB) o ditranol (DTB) como matrices.[67] Adicionalmente se obtuvieron espectros de masas en electroespray empleando un espectrómetro *Bruker MicroTOF-Q*, usando en su caso formiato de sodio como referencia.

3.4.2 Microscopía

3.4.2.1 Microscopía electrónica de barrido

La microscopía electrónica de barrido (SEM, del inglés *Scanning Electron Microscopy*) utiliza haces de electrones para barrer la superficie de la muestra y determinar su aspecto superficial. Un detector formado por lentes basadas en electroimanes mide la cantidad e intensidad de electrones que esta devuelve en forma de electrones secundarios (electrones arrancados de la muestra) o retrodispersados (electrones rebotados en la superficie). Su resolución está entre 4 y 20 nm, dependiendo del microscopio.

Las muestras se analizaron utilizando un microscopio *Merlin Zeiss* (*Carl Zeiss SMT*, operando a 30,0 kV) y detectores de electrones secundarios y retrodispersados. Para la preparación de las muestras, 5 mg fueron depositados sobre un adhesivo de carbono de doble capa, el cual se pegó a un soporte adecuado que se introdujo en la cámara del equipo.

3.4.2.2 Microscopía electrónica de transmisión

La caracterización ultraestructural de las muestras se realizó mediante microscopía electrónica de transmisión (TEM, del inglés *Transmission Electron Microscopy*). A diferencia de la técnica anterior, los equipos TEM operan a voltajes más altos sobre muestras mucho más finas. La detección se lleva a cabo sobre pantallas de fluorescencia gracias a los electrones transmitidos a lo largo de la sección de la muestra.

Las medidas se hicieron en un equipo *JEOL 2000 EX – II*, trabajando con un voltaje de aceleración de electrones de 160 KV (poder de resolución 3.4 Å entre líneas), y equipado con sistema de digitalización de imágenes *Micrograph GATAN*. Las imágenes de alta resolución fueron obtenidas en un instrumento *JEOL JEM 2100-F*, equipado con un cañón de emisión de campo de electrones, operando a un voltaje de 200 KV, que permite alcanzar una resolución de 1,9 Å entre puntos y 1,0 Å entre líneas. Además, el equipo cuenta con una microsonda de análisis de rayos X de energía dispersada (EDX, del inglés *Energy Dispersive X-Ray spectroscopy*) *Oxford* que permite identificar y cuantificar los elementos presentes en la región analizada, y una unidad de barrido por transmisión (STEM, del inglés *Scanning Transmission Electron Microscopy*) con detectores de campo claro (BF) y campo oscuro (DF) para la obtención de mapas de composición de las muestras. La digitalización de las imágenes se hizo mediante una cámara CCD *GATAN*.

La preparación de la muestra para realizar las medidas en ambos equipos se realizó por depósito de varias gotas de una suspensión agitada de concentración 0.1 mg mL^{-1} en etanol sobre una rejilla de carbono. Esta rejilla se secó al aire.

3.4.2.3 Microscopía de fuerza atómica

La microscopía de fuerza atómica (AFM, del inglés *Atomic Force Microscopy*) es una microscopía de proximidad, en la que el microscopio empleado es un instrumento mecano-óptico capaz de detectar fuerzas del orden de los pN.[68] La topografía de la muestra se registra con una sonda, generalmente una punta afilada de forma piramidal o cónica, que se acopla a un cantilever flexible de sólo unos 200 μm. En situaciones de alta cercanía entre la punta y la superficie (entre 5 y 15 nm en modo no contacto), se puede detectar la fuerza atómica en forma de flexión del

cantiléver mediante la ayuda un haz laser reflejado en su parte posterior. El desplazamiento tridimensional se realiza con un sistema auxiliar piezoeléctrico.

Para determinar la altura que indica el número de capas (cada capa de grafeno mide 0,335 nm, y de GO en torno a 1 nm)[69], el área de los nanomateriales y su topografía se empleó un equipo comercial *Cervantes AFM*, *Nanotec Electrónica*, operado en condiciones ambiente. Como cantiléver se usaron puntas comerciales *Nanosensor PPP-NCH*, *PointProbe*. Las medidas se llevaron a cabo en condiciones ambiente. Para el tratamiento de datos, el control del microscopio y la adquisición de las imágenes se empleó el software WSxM 5.1.

Las muestras se prepararon de la misma manera que la descrita en el apartado 3.4.2.2. Se depositaron, en función de su concentración, una o dos gotas de suspensión sobre una lámina de mica y se dejó secar al aire.

3.4.3 Espectroscopía

3.4.3.1 Espectroscopía infrarroja con transformada de Fourier

Las energías vibracionales de los enlaces que configuran los grupos funcionales de moléculas orgánicas, inorgánicas e incluso de la superficie de materiales carbonosos están cuantizadas. Los rangos en los que se localizan sus excitaciones y relajaciones se centran en el infrarrojo. Cada fonón, o modo de vibración, tiene una energía única y se presenta como un pico en el espectro de infrarrojo.

Los espectros de infrarrojo para la identificación de los grupos funcionales se obtuvieron en un espectrómetro *Nicolet 8700 FTIR*, utilizando los accesorios de

transmisión y de reflexión total atenuada, y un detector de sulfato de triglicina deuterada (Deuterated Triglycine sulfate, DFT). Para la obtención de los espectros se trabajó a una resolución 4 cm^{-1}, registrándose 128 barridos por muestra en el rango espectral situado entre los números de onda 600 y 4000 cm^{-1}, previa sustracción del blanco ambiental. Los espectros se convirtieron a la función Kubelka–Munk, eliminando el agua y el CO_2 por resta de sus correspondientes espectros.

Las muestras se presentaron en forma de pastilla de 1 cm^2 de superficie mediante mezcla física con bromuro potásico en relación 1:100 (0,3 g totales), prensadas con el molde adecuado a una presión de 5 ton cm^{-1}. El blanco se midió empleando sólo KBr en la pastilla.

3.4.3.2 Espectroscopía Raman

La espectroscopía Raman se basa en la dispersión inelástica de la luz por medio de la transmisión de la energía del electrón excitado a un fonón. Las vibraciones de los enlaces anteriormente comentadas en la sección 3.4.3.1 también hacen que los materiales de carbono sean activos para los fenómenos Raman, pues algunos enlaces siguen las reglas de selección de ambos procesos, como es el caso de los enlaces C-C. Así, los materiales con estructuras grafénicas presentan las bandas G (~1560 cm^{-1}, típica del grafito), correspondiente a la vibración tangencial en el plano de los atómos de carbono con hibridación sp^2 del esqueleto carbonoso; y D (~1350 cm^{-1}, típica del diamante), correspondiente a la vibración doble resonante fuera de plano realizada por un fonón, y que se asocia a los enlaces sp^3 causados por defectos estructurales, los cuales permiten la propia curvatura de nanotubos de carbono. Si esta vibración es realizada por dos fonones, aparece la banda 2D o G' (~2700 cm^{-1}) la cual aporta información estructural adicional de la interacción tridimensional del

material, pues es un reflejo de los bordes de láminas en ambos tipos de estructuras (nanotubos y grafenos). Con esta vibración es posible calcular el número de láminas, así como de las características electrónicas de las mismas.

La relación entre las intensidades de las bandas D y G (I_D/I_G) permite comparar el orden estructural entre diferentes muestras. Un grafito perfecto tendría una relación cercana a 0; un GO presenta una relación cercana a 1 ya que la oxidación genera defectos estructurales que hace que crezca la banda D; los nanotubos de carbono presentan también una relación cercana a 1 debido a la curvatura inherente.

Los espectros Raman fueron obtenidos en un microscopio confocal *Renishaw 2000* (*Rhenishaw Instruments*), empleando un ancho espectral desde 750 hasta 3500 cm^{-1}, usando como fuente de excitación un láser de argón de 514.5 nm, modelo *Specra-Physics 265*. La muestra se depositó sobre un portamuestras de vidrio empleando unas gotas de las suspensiones preparadas para el análisis microscópico.

3.4.3.3 Espectroscopia de fotoemisión de rayos X

La espectroscopia de fotoemisión de rayos X (XPS, del inglés *X-Ray Photoelectron Spectroscopy*) es una técnica de análisis superficial (3-5 nm) que proporciona información sobre los enlaces atómicos característicos de cada elemento. Con un haz de rayos X se excitan los niveles más internos de los átomos, esto provoca la emisión de foto-electrones que proporcionan información sobre la energía de cada nivel y, por tanto, sobre la naturaleza de cada átomo emisor. No obstante, es una técnica de análisis superficial, pues el poder de penetración de la radiación es de unos pocos nm de espesor, debido a la dispersión no coherente

causada por los átomos externos de los foto-electrones emitidos por los átomos internos.

Los espectros se obtuvieron usando un equipo *SPECS* operando por debajo de los 10^{-7} Pa de presión. Como fuente de rayos X se usó la línea Kα del magnesio a una potencia de 100 W. Los fotoelectrones emitidos por la muestra se detectaron mediante un analizador de electrones semiesférico.

La preparación de muestra se realizó siguiendo el mismo procedimiento que el descrito en el apartado 3.4.2.1. No obstante, para evitar cualquier influencia de la humedad, las muestras se secaron la noche anterior al análisis en una estufa precalentada a 100 ºC a una presión de 1 mBar.

El espectro general se utilizó para la obtención de la relación C/O, además de la cuantificación superficial de otras especies presentes en las muestras, como nitrógeno, cloro e iridio. Se integraron las intensidades relativas de los picos correspondientes al carbono C1s, al oxígeno O1s, al nitrógeno N1s, al cloro Cl2p y al iridio Ir4f teniendo en cuenta sus respectivos factores de sensibilidad.

El espectro de alta resolución C1s sirvió para el análisis de los grupos funcionales superficiales. Se llevó a cabo mediante la deconvolución, en 5 picos, de la región del espectro correspondiente al pico del carbono C1s por medio de mezclas de funciones Gaussianas y Lorentzianas.[70] Para llevar a cabo los ajustes, se fijó en todos los casos la energía de enlace de cada pico (eV) y su anchura a la semialtura, modificando el área del pico para ajustar los picos desconvolucionados a la curva correspondiente. En todos los casos el error cuadrático fue del orden de 10^{-5}. La tabla 3.1 muestra la identificación de los grupos funcionales y las energías aproximadas de los fotoelectrones emitidos.

Tabla 3.1 Caracterización de grupos funcionales oxigenados mediante XPS

Enlace	Energía (eV)
C-C sp^2	284,4
C-C sp^3	285,5
-C-OH	286,5
-C=O	287,7
-COOH	288,7

El espectro de alta resolución de nitrógeno N1s sirvió para la identificación de especies nitrogenadas, como grupos nitro (~406.0 eV) y los anillos de imidazolio (~402 eV). El espectro de alta resolución iridio Ir4f se empleó para la determinación del estado de oxidación del metal.

3.4.3.4 Espectroscopía de Absorción de rayos X

La espectroscopía de absorción de rayos X (XAS, del inglés *X-Ray Absorption Spectroscopy*) es una técnica ampliamente empleada para la determinación de la geometría local y/o estructura electrónica de la materia. Se basa en la excitación de electrones internos (por debajo de la capa de valencia) del átomo mediante irradiación con rayos X. La energía de estos electrones depende del propio átomo y de los entornos locales en los que este átomo se encuentre. Para que se produzca el fenómeno, se necesitan intensas, sintonizables y colimadas fuentes de radiación, con lo que se precisa el uso de fuentes sincrotrón.

Las medidas de absorción de rayos X, para la obtención de información de la esfera de coordinación del iridio en los complejos soportados, se realizaron en la línea de radiación Claess-BL22 del sincrotrón ALBA, España, así como en la línea BM23 del European Synchrotron Radiation Facility (ESRF, Francia). El anillo de

almacenamiento operaba con una energía de electrones de 3 GeV y una corriente media de 100 mA, en el modo de operación top-up. Las medidas se realizaron en modo de transmisión sobre pastillas de material a temperatura ambiente. El monocromador de radiación empleado fue un doble cristal fijo a la salida de Si (311), obteniendo un rechazo armónico menor de 10^{-5} a la salida del monocromador. Para la calibración, la resolución energética $\Delta E/E$ se estimó del orden de $8x10^{-5}$ en la línea L_3 del iridio midiendo simultáneamente una referencia de iridio metálico. Además, se midieron como referencias adicionales iridio metal, el complejo $IrClN_2OC_{15}H_{24}$ y la sal $IrCl_3$ para Ir^0, Ir^+ e Ir^{3+}, respectivamente. Los espectros de absorción de rayos X extendida de estructura fina (del inglés *Extended X-Ray Absorption Spectroscopy Fine Structure*) se extrajeron mediante el software Athena.[71] Las transformadas de Fourier de las señales EXAFS se calcularon usando un rango k típico de 3,0-13,3 $Å^{-1}$ en una ventana sinusoidal; el análisis estructural EXAFS se realizó usando fases teóricas y amplitudes calculadas en el código FEFF-6,[72] y los ajustes de los datos experimentales llevados a cabo en el espacio R se hicieron con el programa *ARTEMIS*.[72]

3.4.4 Análisis térmico

3.4.4.1 Análisis termogravimétrico

El análisis termogravimétrico (TGA, del inglés *Thermogravimetric Analysis*) permite realizar el estudio de la estabilidad térmica del material, conocer las temperaturas de deflagración, combustión o pirolisis, en función de la atmósfera aplicada, así como establecer las temperaturas a las que se desorben los grupos funcionales (propios o introducidos) como producto del aporte de energía en forma de calor.

El análisis termogravimétrico de las muestras se realizó en una termobalanza *TA Instruments SDT 2960*. Se obtuvieron tanto las curvas de pérdida de peso (TG) como las correspondientes a su derivada primera respecto del tiempo (DTG). A partir de ambas curvas se determinaron las temperaturas iniciales y finales de pérdida de peso, así como las temperaturas de máxima velocidad de pérdida de peso. Además, se determinó el grado de funcionalización de las muestras con los compuestos imidazólicos introducidos, en forma de porcentaje molar, por las pérdidas de peso a 400 ºC.[73]

$$mol\% = \frac{\%\ peso\ TG\ /\ MW\ Imid}{100/12} \qquad \text{[Ec. 3.1]}$$

Los ensayos se realizaron colocando 3-5 mg de muestra molida en un crisol adecuado (platino o cerámico en función del contenido metálico esperado de la muestra). El calentamiento se realizó a 10 ºC min^{-1} desde una temperatura inicial de 40 ºC hasta una temperatura final de 1000 ºC, bajo un flujo de nitrógeno de 100 mL min^{-1}, o bajo un flujo combinado de aire-nitrógeno de 200 mL min^{-1}.

3.4.4.2 Desorción a temperatura programada

Al igual que el análisis termogravimétrico, la desorción a temperatura programada (TPD, del inglés *Temperature Programmed Desorption*) permite conocer cómo se desorben los grupos funcionales superficiales y cuantificar su distribución en el material. Para ello, los materiales son sometidos a un calentamiento controlado y progresivo en atmósfera inerte, de manera que se desorberán gases característicos los cuales se pueden relacionar con los grupos superficiales.

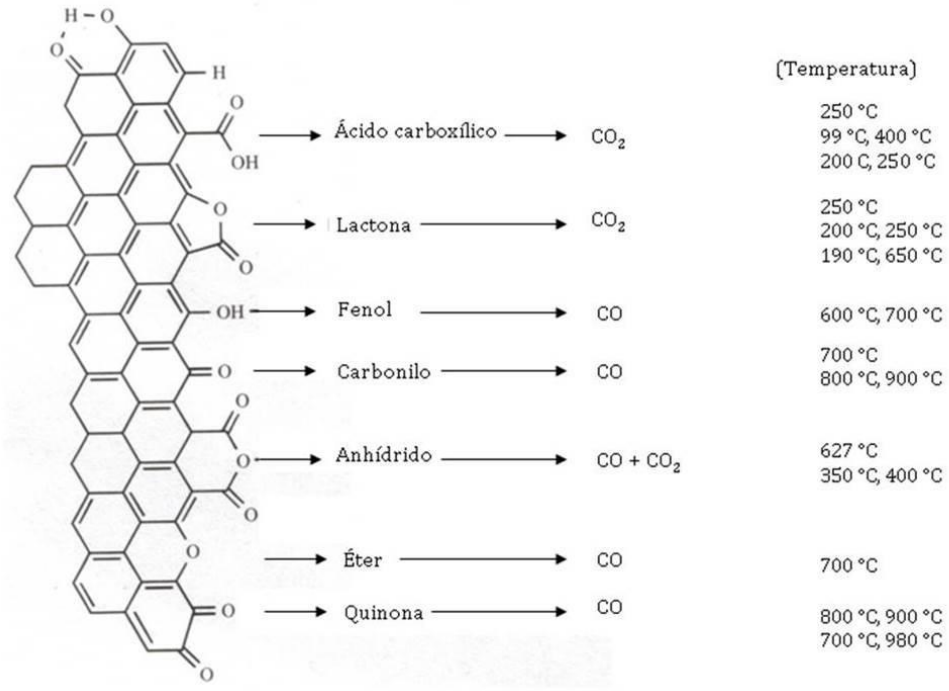

Figura 3.2. Desorción de grupos oxigenados con sus temperaturas de descomposición.[74]

Para los experimentos TPD se empleó un reactor de cuarzo en forma de U provisto de unos 50-100 mg de muestra, y se usó como gas de arrastre He con un flujo de 50 mL min^{-1}. La muestra se calentó hasta 1000 °C, con una velocidad de calentamiento de 5 °C min^{-1}, y se mantuvo a dicha temperatura durante 5 min. El análisis de los gases desorbidos, principalmente CO y CO_2, se llevó a cabo mediante un espectrómetro de masas *Omnistar* de *Pheiffer Vaccum* acoplado a la salida del reactor. El espectrómetro se encuentra conectado a un sistema informático de adquisición de datos que registró los fragmentos iónicos correspondientes a los gases desorbidos. Previamente al análisis cuantitativo se llevó a cabo una calibración de los gases a analizar utilizando mezclas patrón de concentración conocida.

La identificación de los grupos funcionales desorbidos en el análisis mediante TPD se realizó atendiendo a su temperatura de desorción. El análisis cuantitativo para la determinación de las cantidades de grupos funcionales presentes en la superficie del material se realizó por deconvolución del área bajo la curva siguiendo la metodología descrita por Figueiredo *y col*.[74]

3.4.5 Otras técnicas

3.4.5.1 Análisis elemental

La composición elemental de las muestras, en forma de carbono, hidrógeno, nitrógeno, oxígeno y azufre, es importante para el conocimiento del estado general de los grupos funcionales antes y después de los tratamientos aplicados, así como del estado de la estructura carbonosa de los nanomateriales de carbono.

Para el análisis elemental se utilizaron muestras molidas a < 200 μm de tamaño de partícula. El contenido en carbono, hidrógeno, nitrógeno y azufre de las muestras se determinó mediante combustión de 1 mg de muestra a 1050 ºC en un equipo *LECO-CHNS-932*. En estas condiciones, el carbono se transformó en CO_2, el hidrógeno en H_2O y el azufre en SO_2. Estos tres compuestos se detectaron y valoraron por su absorción mediante espectroscopia infrarroja. El nitrógeno formó NOx que se redujo con Cu a nitrógeno elemental, cuantificándose esta especie a partir de la señal obtenida con un detector de conductividad térmica (TCD, del inglés *Thermal Conductivity Detector*). El contenido en oxígeno se determinó en un horno de grafito *LEC VTF-900* acoplado al equipo anterior. La pirólisis de la muestra se realizó por calentamiento a 1350 ºC, bajo un flujo de He de 225 mL min^{-1}, utilizando CuO como oxidante. Las reacciones que tienen lugar son las siguientes:

$$C + O \rightarrow CO \qquad \text{[ec. 3.2]}$$

$$CO + CuO \rightarrow Cu + CO_2 \qquad \text{[ec. 3.3]}$$

El CO_2 resultante se valoró como en el caso anterior, obteniéndose de forma directa el contenido en oxígeno de la muestra.

3.4.5.2 Acoplamiento por plasma inducido – espectrometría de masas

El acoplamiento por plasma inducido (ICP-MS, del inglés *Inductively Coupling Plasma Mass Spectrometry*) es una variedad del método instrumental espectroscopía de absorción/emisión atómica, en donde la fuente de ionización y excitación de los átomos a analizar es un plasma generado por corrientes eléctricas producidas por inducción electromagnética. El plasma puede alcanzar una temperatura de 10000 K, lo que supone una energía tan alta que existen altas concentraciones de iones, generalmente Ar^+, y electrones libres, lo que permite ionizar gran cantidad de metales y no metales. El espectrómetro de masas separará estos iones completando el análisis, permitiendo detectar concentraciones muy bajas, del orden de una parte en 10^{15}.

El ICP se empleó para la determinación del contenido de iridio en las muestras, en un equipo *Agilent 7700x*. La preparación de las muestras incluyó un proceso de digestión siguiendo el método descrito por Elgrabi *y col*.[75] consistente en el tratamiento de 30 mg de muestra con 5 mL de una mezcla de ácidos nítrico y clorhídrico concentrados, en proporción 3:1 a 180 ºC durante 3 horas empleando irradiación microondas.

3.4.5.3 Análisis textural

Una de las características más relevantes de los nanomateriales de carbono es su elevada área superficial y su alta relación de aspecto superficie/volumen debido a las pequeñas dimensiones que presentan. Además, al ser sólidos carbonosos, presentan textura porosa, bien inherente, o bien por su agrupación tridimensional. El análisis de la textura porosa de los materiales permite conocer su superficie y el volumen de adsorbato que son capaces de adsorber, lo que permitirá conocer la distribución de sus poros, y por tanto su configuración espacial.

La caracterización textural de las muestras se llevó a cabo por medio de adsorción física de nitrógeno a 77 K en un sistema volumétrico *Micromeritics ASAP 2020*, al esperar poros comprendidos dentro de la categoría de mesoporos (2-50 nm de tamaño). En cada experimento se usaron 50-100 mg de muestra desgasificada a 40 ºC durante 50 h bajo un vacío de 10^{-3} Pa previo a cada análisis.

3.4.5.3.1 Área superficial

El área superficial se calculó por medio de la ecuación de Brunauer, Teller y Emmet (BET).[76] Para ello, se empleó la forma de linealización clásica (ecuación 3.4):

$$\frac{X}{n^a\ (1-X)} = \frac{1}{n_m^a} + \frac{C-1}{n_m^a}X \qquad \text{[Ec. 3.4]}$$

Donde X representa la presión relativa P/P^o, n^a es la cantidad de gas adsorbido a la presión P, n_m^a es la cantidad de gas requerido para formar una monocapa en la superficie adsorbente a la presión P, P^o es la presión de saturación de adsorbato a la

temperatura de adsorción y C es un parámetro relacionado con el calor de adsorción de la primera capa adsorbida, el cual viene determinado por:

$$C = \exp \frac{E_1 - E_L}{RT} \quad X \qquad \text{[Ec. 3.5]}$$

Donde E_1 es la entalpía de adsorción de la primera capa, E_L es la entalpía de licuefacción del adsorbato, R es la constante de los gases y T la temperatura.

El rango de linealidad de la ecuación BET abarca una zona limitada de la isoterma, pero de manera general se suele tomar un rango de presiones relativas comprendido entre 0.05 y 0.2. Esta linealización permite obtener la capacidad de la monocapa. Conocida esta y la superficie ocupada por una molécula de nitrógeno adsorbida, el área superficial puede ser determinada según:

$$S_{BET} = n_m^a \, \sigma \, N_A \qquad \text{[Ec. 3.6]}$$

Donde σ es el área que ocupa una molécula de adsorbato en la superficie de un sólido a la temperatura de adsorción (0.162 nm^2 para el nitrógeno a 77 K) y N_A es el número de Avogadro.

3.4.5.3.2 Volumen de microporos

El volumen de microporos se estimó mediante la aplicación de la linealización logarítmica (ecuación 3.7) de la ecuación de Dubinin – Radushkevich (DR)[77] a la isoterma de adsorción de nitrógeno:

$$\log W = \log W_0 - \ln 10 \, (RT/\beta E_0)^2 \log^2 (P^o/P) \qquad \text{[Ec. 3.7]}$$

Donde W es el volumen de adsorbato condensado en los microporos para un valor de temperatura T y presión relativa P/Pº. Como W se expresa como volumen de líquido, es necesario conocer la densidad de adsorbato en los microporos, que para la adsorción de nitrógeno se toma como 0.808 g cm^{-3}.[78] W_0 representa el volumen total de microporo accesible al adsorbato, E_0 es la energía característica (KJ mol^{-1}) y β es un factor de afinidad, que para el nitrógeno se toma de 0.34. Esta expresión resulta una línea recta en un rango de presiones comprendido entre 5 y 10 para valores de $\log^2$ (Pº/P) en la adsorción de nitrógeno.

3.4.5.3.3 Volumen de mesoporos

El volumen de mesoporos se calculó como la diferencia entre el volumen total y el volumen de microporos.

3.4.5.4 Ensayo de dispersión en disolventes

La capacidad de dispersión y estabilidad de las muestras generadas en diferentes disolventes, tanto agua como disolventes orgánicos, proporciona una valiosa información acerca de la selección del medio de reacción y presentación de las muestras a seleccionar para generar el sistema más homogéneo posible.

El ensayo de dispersión en distintos disolventes se realizó mediante la preparación, en viales de 10 mL, de suspensiones en varios disolventes de los nanomateriales de carbono de concentración 0,1 mg mL^{-1}. Los viales se introdujeron en un baño de ultrasonidos 30 min y se observó la estabilidad tras 24 h, una semana y dos meses. Los disolventes empleados fueron agua, dimetilformamida (DMF), acetona, etanol, THF y DCM.

3.4.5.5 Medidas de acidez y potencial electrocinético superficial

El pH de las muestras, así como su potencial electrocinético superficial (potencial zeta) son medidas importantes para el conocimiento de la carga global neta de la superficie de los materiales carbonosos.

Las medidas de pH se realizaron aplicando el siguiente procedimiento: En 20 mL de agua se añadieron 0,1 g de muestra, y la suspensión resultante se agitó magnéticamente hasta que se alcanzó el equilibrio, momento en el que se midió el pH utilizando un conductímetro – pH-metro *SevenEasy pH* de la casa Mettler Toledo. El potencial zeta, por su parte, se medió en un equipo *LaserZee-Meter 501*. Las movilidades electroforéticas se convirtieron en potenciales zeta según la ecuación de Smoluchowski. Para cada determinación, la muestra se acondicionó y equilibró antes de la medida mediante agitación de una mezcla con 0,05 g de muestra dispersada en 100 mL de agua y cloruro potásico 0,01 M durante las 18-24 h previas

3.5 EXPERIMENTOS DE ADSORCIÓN

Los experimentos de adsorción de benceno en agua se desarrollaron a temperatura ambiente en un reactor de vidrio de 50 mL provisto de agitación magnética y sin espacio en cabeza para evitar los problemas de liberación de aromáticos volátiles.[79]

En un experimento típico, se introdujeron 50 mL de una disolución acuosa de benceno de 200 ppm de concentración, y una cantidad variable de nanotubos de

carbono oxidados (10, 20 y 30 mg). A intervalos regulares se extrajo una alícuota de 2 mL de disolución filtrada a través de un tamiz de 0.2 µm de acetato de celulosa.

La concentración de benceno en las alícuotas se determinó mediante cromatografía liquida de alta eficiencia (HPLC) usando un equipo *Agilent 1100 series*. Se utilizó una columna cromatográfica tipo *Agilent Eclipse XDB-C8*, que se mantuvo a una temperatura constante de 27 ºC. De cada alícuota se inyectó un volumen de 20 µL. Se usó un detector UV-Vis trabajando a la longitud de onda de 252,16 nm. Como fase móvil se utilizó una mezcla de un 20% de agua y un 80% de acetonitrilo con un flujo de 1 mL min^{-1}.

La cantidad de benceno adsorbida, b_t, se puede estimar usando:

$$b_t = \frac{C_0 - C_t \ V}{w} \qquad \text{[ec 3.8]}$$

Donde C_0 es la concentración inicial de benceno en agua expresada en ppm, C_t es la concentración de benceno tras un cierto tiempo también expresada en ppm, V es el volumen de disolución expresado en litros y w es la masa de muestra expresada en gramos.

El equilibrio de adsorción se alcanzó en tiempos superiores a los 200 min. La cantidad de benceno adsorbida por los nanotubos de carbono en el equilibrio se definió como b_e. La determinación de la cantidad de benceno adsorbida se llevó a cabo utilizando una recta de calibrado externo. Las concentraciones de benceno en agua estuvieron comprendidas entre 22,5 y 225 ppm a intervalos regulares de las mismas.

3.6 EXPERIMENTOS CATALÍTICOS

La actividad catalítica de los complejos soportados NHC de iridio sobre nanomateriales de carbono se midió mediante ensayos de reducción de ciclohexanona a ciclohexanol por medio de procesos de transferencia de hidrógeno.

Las reacciones catalíticas se realizaron en un reactor de vidrio de 5 mL, equipado con un tapón sin grasa bajo atmósfera inerte. Las condiciones experimentales fueron optimizadas en trabajos anteriores.[80] El experimento típico consistió en la carga del reactor con 0,52 mL (5 mmol) de ciclohexanona, 4,5 mL de 2-propanol como el disolvente y el dador de hidrógeno, 0,07 mL (0,5 mmol) de 1,3,5-trimetilbenceno actuando de patrón interno, 0,1 mL (0,025 mmol) de una disolución básica 0.24 N de KOH en 2-propanol y 0,005 mmol (0,1 mol%) del catalizador. La cantidad a añadir de material con el complejo soportado depende de la cantidad de iridio determinada mediante medidas de acoplamiento por plasma inductivo (ICP), variando de un sistema a otro.

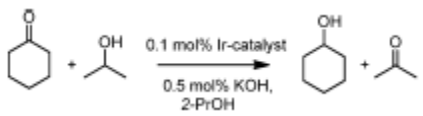

[Ec. 3.9]

Tras la adición de todos los componentes, el sistema se mantuvo bajo agitación magnética hasta completa disolución del complejo homogéneo o 10 min en caso del heterogéneo. A continuación, se fijó como temperatura de reacción 80 ºC mediante un baño termostatizado. Diferentes alícuotas de 1 μL fueron tomadas a intervalos regulares para monitorizar el progreso de la reacción mediante cromatografía de gases.

Se empleó el sistema *Agilent 4890 D* de inyección manual y detección por llama de ionización (FID, del inglés *Flame Ionization Detector*). Las condiciones del inyector se fijaron en 275 ºC de temperatura para asegurar la volatilización de los compuestos, trabajando en modo splitless bajo un flujo total de 289 mL min^{-1} a 12,3 psi de presión. El detector trabajó a 250 ºC, bajo un flujo de 35 mL min^{-1} de hidrógeno y 350 mL min^{-1} de aire en helio extrapuro. El cromatógrafo contiene con una columna capilar *HP-INNOWax*, de dimensiones 25 m x 0,2 mm x 0,4 μm (4594 platos teóricos), sometida a una presión de 12.3 psi y un flujo de 6 mL min^{-1}, lo que se traduce en una velocidad en su interior de 93 cm s^{-1}. El horno se mantuvo a una temperatura inicial de 50 ºC, la cual aumentó en cada experimento a 250 ºC a una velocidad de calentamiento de 25 ºC min^{-1}, con un tiempo de residencia de 30 s.

Tras la finalización de la reacción, el catalizador fue recuperado mediante dilución con 2-propanol fresco seguido de centrifugación (*Sigma 2-16KL*, 5000 rpm 2180 g) y lavado 3 veces con 10 mL de 2-propanol, descartando el sobrenadante y reservando el sólido, el cual se secó a vacío. Tras ello, se estudió la ciclabilidad del catalizador sometiéndolo a un nuevo experimento catalítico en las mismas condiciones que el primer ciclo pero sin añadir en ningún caso precursor de catalizador fresco. El último ciclo estudiado en todos los casos se realizó sin atmósfera protectora.

4. RESULTADOS

RESULTADOS

Como ya se ha comentado en el capítulo 1, los nanomateriales de carbono como los nanotubos y los materiales grafénicos son excelentes candidatos para ser utilizados en soportes de catalizadores. Comparten las propiedades de los materiales de carbono clásicos, y a la vez, su pequeña dimensión permite que los efectos cuánticos dominen sus características, lo que conlleva la aparación de nuevas y excelentes propiedades. Además, se han descrito los complejos organometálicos NHC de iridio como excelentes y robustos catalizadores homogéneos de procesos de reducción evitando las hidrogenaciones convencionales.

La sinergia entre las bondades de los carbenos N-heterocíclicos de iridio actuando como catalizadores en las transferencias de hidrógeno junto a las nuevas propiedades que ofrecen los nanomateriales de carbono permitirá la síntesis de nuevos sistemas híbridos capaces de mejorar los resultados existentes previamente documentados en la bibliografía, en términos de actividad catalítica, estabilidad y reciclabilidad.

A continuación, en esta sección de resultados se muestran los resúmenes de los cinco artículos que forman parte de esta memoria, seguidos de los originales de sus publicaciones. En cada uno de ellos se ha realizado una breve descripción de los resultados obtenidos más relevantes.

4.1 ARTÍCULO I

"Influencia del grado de alineamiento de nanotubos de carbono crecidos por el método CVD en su funcionalización y capacidad de adsorción"

Diamond and Related Materials **2013** *37*, 1-7

En este capítulo se estudia la oxidación selectiva de dos tipos de nanotubos de carbono, alineados o dispuestos aleatoriamente, con diferentes agentes oxidantes, aplicando tratamientos de severidad creciente.

Aunque ambos tipos de nanotubos se obtuvieron mediante el método CVD, los nanotubos alineados o tipo césped presentaron una mejor estructura aromática con menos defectos, con lo que es de esperar un diferente comportamiento frente a los agentes oxidantes. Por tanto, la aplicación de los diferentes tratamientos oxidativos podría controlar el desarrollo de grupos funcionales oxigenados.

En todos los tratamientos se produjo la eliminación del carbón amorfo que se genera durante el proceso de síntesis, así como de los metales responsables del crecimiento de los tubos. Además, se observó una progresiva reducción de diámetros y longitudes conforme aumenta la severidad del tratamiento.

Contrariamente a lo publicado anteriormente por otros autores, los nanotubos tipo césped mostraron el mayor número de funciones oxigenadas tras los tratamientos menos oxidantes, sobre todo en los grupos hidroxilo y carbonilo. Por su parte, las condiciones más oxidantes son las únicas capaces de generar una alta concentración de grupos carboxío, siendo esta superior de nuevo en los nanotubos tipo césped, posiblemente debido a la generación de defectos en su estructura junto al acortamiento de los nanotubos.

Para comprobar el efecto de los grupos funcionales en las propiedades de los nanotubos, se estudiaron sus propiedades de adsorción de contaminantes antes de soportar los catalizadores, siguiendo la línea abierta por el Grupo de Materiales Compuestos al desarrollar materiales con excepcionales características como adsorbentes de contaminantes en fase líquida. Estos sistemas utilizaban carbones activados preparados a partir de breas de mesofase de aceite de antraceno, un subproducto altamente aromático procedente de la destilación del alquitrán (30 % del alquitrán total), polimerizado mediante un tratamiento térmico asistido por oxígeno.

Aunque está comprobada la capacidad de adsorción de nanotubos de carbono "puros", el desarrollo de grupos funcionales oxigenados y de porosidad tuvieron un efecto positivo en la capacidad de retención de las especies presentes en el medio. En los ensayos de adsorción de benceno en disolución acuosa, los nanotubos alienados mostraron cinéticas más rápidas que sus correspondientes nanotubos alineados. La mejor capacidad de adsorción fue observada en los nanotubos más oxidados. Esto es posiblemente debido a la mayor presencia de grupos funcionales oxigenados, los cuales permiten una mejor capacidad de dispersión en el medio, así como la formación de uniones de tipo π con el adsorbato, factores que favorecen la adsorción. Ambos nanomateriales, no obstante, presentan mejores datos que otros adsorbentes publicados en la literatura, con excepción de los carbones activados derivados de aceite de antraceno.

Contents lists available at SciVerse ScienceDirect

Diamond & Related Materials

journal homepage: www.elsevier.com/locate/diamond

Influence of the alignment degree of CVD-grown carbon nanotubes on their functionalization and adsorption capacity

M. Blanco [a], P. Álvarez [a,*], C. Blanco [a], N. Campos [b], D. Gómez [b], R. Menéndez [a]

[1]Instituto Nacional del Carbón, CSIC., P.O. Box 73., 33080 Oviedo, Spain
[2] ITMA Materials Technology, C/Calafates 11, 33417 Avilés, Spain

ARTICLE INFO

Article history:
Received 8 October 2012
Received in revised form 9 April 2013 Accepted 15 April 2013
Available online 28 April 2013

Keywords:
Carbon nanotube, alignment, functionalization, benzene adsorption

ABSTRACT

Oxygen functionalized multiwalled carbon nanotubes (CNTs) were prepared from aligned and bundle-like CVD-grown CNTs by chemical treatment with different reagents of increased oxidation degree. As the severity in the oxidation degree increases elimination of the amorphous carbon is observed. However, contrary to what was previously reported, aligned CNTs treated in less severe oxidation conditions they exhibit an increased number of oxygen containing functional groups (COH/CO groups). Meanwhile, when treated in the more severe oxidation conditions, they have the highest number of COOH groups due to the appearance of defects and shortening of the tubes. In the benzene adsorption in water, aligned CNTs display faster kinetics in all cases. The best adsorption capacity is achieved with aligned CNTs treated in very severe conditions possibly due to their enhanced solubility in water, which favors electrostatic interactions and π–π interactions between the benzene rings and the CNT walls.

1. Introduction

Aromatic compounds such as benzene and toluene are organic pollutants commonly used as solvents in industrial operations [1], and they are frequently found in the groundwater of gasoline-contaminated sites [2]. Since they are carcinogenic, and/or mutagenic agents, their removal from the wastewaters is critical to ensure the safety of our water supplies. However, these recalcitrant pollutants usually elude conventional treatments and therefore undermine the efficiency of water treatment plants [3]. Conventional activated carbons have been widely used for this purpose [1], but investigation of new adsorbents

* Corresponding author. Tel.: +34 985119090; fax: +34 985297662. E-mail address: par@incar.csic.es (P. Álvarez).

0925-9635/$ – see front matter
http://dx.doi.org/10.1016/j.diamond.2013.04.006

with higher adsorption capacities and efficiencies is still required.

Carbon nanotubes (CNTs) have unique properties that have shown great potential on a commercial scale in conventional drinking water purification systems, mainly due to their capacity to remove a wide range of biological contaminants including viruses [4], bacteria [5] and also recalcitrant compounds [6–8]. The large adsorption capacity of CNTs is mainly attributed to their specific pore structure and surface properties, including defects and functional groups. Moreover, their surface characteristics and mesopore volume that are favorable for adsorption can be further enhanced by treating the nanotubes with acids [6], gaseous compounds [9], or just heating them [10]. To our knowledge, there are few studies that describe the effect of CNT morphology on the removal of contaminants. Furthermore, there is a lack of information about the relationship between surface modifications (in terms of functional groups introduced) in CNTs of different morphologies and the effect on their adsorption properties.

CNTs with different morphologies (i.e. bundle-like or aligned) can be easily prepared by CVD [11,12] by simply controlling the characteristics of the catalyst. One advantage of vertically aligned synthesis for adsorption application is that the final CNT product contains fewer impurities and a better Csp^2 carbon structure than those obtained through bulk synthesis. This would contribute to increasing the π-electron density in the graphene layer and thereby augment the intensity and magnitude of the dispersive interactions which, according to other authors, enhance the adsorption potential [13]. Also, vertically aligned CNTs offer additional technological advantages because they can be spun into fibers, cables or cloths, which is of special interest for the technological implementation of the nanotubes in the purification sector [12]. However, the poorer water solubility of aligned nanotubes could be considered a negative factor [14]. In order to exploit the technological potential of aligned nanotubes in the adsorption of benzene from water, further research into the effect of the modification of surface properties on the adsorption capacity of aligned carbon nanotubes is necessary.

In this work, we study the effect of CNT morphology (bundle-like or aligned) on the surface properties after oxygen modification and how this affects the capacity of CNTs to adsorb benzene. Four different treatments of increasing severity were tested. The CNTs obtained were characterized by Raman spectroscopy, TGA, XPS, BET

and solubility tests to determine the type and amount of functional groups introduced in each treatment as well as their effect on the adsorption properties of benzene in aqueous solutions.

2. Experimental methods

2.1. Adsorbents

Forest-like carbon nanotubes (A-NT) were vertically grown by means of thermal chemical vapor deposition (CVD) on top of silicon wafers using an alumina-supported iron-based catalyst. The CVD system used consists of a quartz tube at atmospheric pressure placed inside a furnace, into which the gases are introduced. Commercial CVD-grown carbon nanotubes (bundle like) were obtained from Sigma-Aldrich and used for comparative purposes (B-NT).

2.1.1. Preparation of the catalyst by CVD process

Silicon [100] wafers were used as a substrate. 500 nm of silicon oxide was grown on their surface by means of sputtering to serve as a passivation layer in the formation of carbides during the synthesis process. Next, a layer of 10 nm of alumina was also sputtered. Finally, a 5 nm film of iron was deposited by thermal evaporation. The catalysts were introduced into the quartz tube where they were subjected to a thermal process consisting in soaking the samples at 600 °C in a hydrogen atmosphere. As a result, the iron layer nucleated to form metal–catalyst nanoislands supported on the porous surface of the alumina. The nanoislands thus formed acted as a seed for the growth of carbon nanotubes.

Afterwards, the temperature was raised to 750 °C and a flow of ethylene was passed through the quartz tube as the carbon precursor gas for 0.5, 1 or 2 h. After a cooling process (to room temperature) in an argon atmosphere, vertically-aligned carbon nanotubes formed on the substrate. The carbon nanotubes were detached from the surface by gently scraping them off with the help of tweezers. The nanotubes were denoted **A-NT-X**, where X refers to 0.5, 1 and 2 h according to the ethylene flow time used.

2.2. Chemical treatment of the carbon nanotubes

The vertically-aligned (A-NT) and bundle-like (B-NT) carbon nanotubes were subjected to four different

treatments of increasing severity: (i) 0.3 g of both types of carbon nanotubes was dispersed in 70 mL of concentrated HCl. The mixture was magnetically stirred at 60 °C for 2 h. After the addition of 250 mL of water and centrifugation at 4700 rpm for 30 min, the supernatant was discarded and the process was repeated till neutral pH was reached. The solids collected were dried at 100 °C until constant weight. These were labeled **A-NT-HCl** and **B-NT-HCl**. (ii) 0.3 g of both types of carbon nanotubes was dispersed in 25 mL of a 1:1 mixture of ammonium hydroxide (28%) and hydrogen peroxide (30%). The mixture was magnetically stirred at 80 °C for 5 h, then diluted with 250 mL of water and centrifuged at 4700 rpm for 30 min. The supernatant was discarded and the process was repeated till neutral pH. The dried solids collected were labeled **A-NT-AP** and **B-NT-AP**. (iii) 0.3 g of CNTs was dispersed in 70 mL of a nitric acid 3 M solution. The mixture was magnetically stirred at 60 °C for 15 min, sonicated for 2 h and then diluted with 250 mL of water. After centrifugation at 4700 rpm for 30 min, the supernatant was discarded and the process was repeated till neutral pH. The collected solid was dispersed in 70 mL of hydrogen peroxide (30%) and the mixture was magnetically stirred at 60 °C for 15 min, and then sonicated for 2 h. The solid was collected by filtration and washed with water. The dried solids thus obtained were named **A-NT-NP** and **B-NT-NP**. (iv) 0.3 g of CNTs was dispersed in 40 mL of a 3:1 mixture of concentrated sulphuric and nitric acid. The mixture was sonicated for 10 min, magnetically stirred at 80 °C for 20 min and then sonicated for another 20 min. Finally, it was diluted with 250 mL of water. The supernatant was discarded by centrifugation at 4700 rpm for 30 min and the process was repeated until neutral pH. The dried solids obtained were named **A-NT-SN** and **B-NT-SN**.

2.3. Characterization of the carbon nanotubes

XPS was performed on a SPECS system operating at 10^{-7} Pa connected to a Mg Kα X-ray source (100 W). All of the spectra were energy-calibrated by assigning 284.4 eV to the C1s binding energy at the “graphitic” peak. Relative atomic concentrations were calculated by integrating the peak areas according to the Shirley background correction procedure and using atomic sensitivity factors [15]. To evaluate the functional groups of the samples, the XPS C1s peaks were curve-fitted using a Gaussian–

Lorentzian peak shape, assigning 284.4 eV for the graphitic band (Csp^2), 284.8 eV for the defects band (Csp^3), 285.8 eV for the single C-O bond (C-OH), 287.2 eV for the double C=O bond (C=O), 288.5 eV for the carboxylic acids band (COOH) and 289.9 eV for the carbonates band (OCOO) [16]. Raman spectra were recorded from 750 to 3500 cm^{-1} on a Renishaw 2000 Confocal Raman Microprobe (Rhenishaw Instruments, England) using a 514.5-nm argon ion laser. Thermogravimetric analyses were carried out in a TA SDT 2960 analyzer. 5 mgof each samplewas placed in a platinum crucible which was then introduced into the thermobalance. The temperature was increased to 1000 °C at a heating rate of 10 °C min^{-1} under a nitrogen flow of 100 mL min^{-1}, or under a combined flow of nitrogen and air at 200 mL min−1. TEM observations were performed on a JEOL 2000 EX-II instrument operating at 160 kV. SEM images were obtained using a field emission gun scanning electron microscope (Carl Zeiss SMT) operating at 3.0 kV. The textural characteristics of the samples were analyzed by means of N2 adsorption at 77 K, performed in an ASAP 2020Micromeritics apparatus using around 100 mg of sample in each experiment. Before the experiments, the sample was outgassed at 40 °C for 50 h under vacuum (pressure below 10^{-3} Pa). The N2 adsorption isotherm was used to calculate the BET surface area (SBET) in the relative pressure range of 0.05–0.20, the total pore volume at a relative pressure of 0.99; the total micropore volume (Vmicro) by means of the Dubinin–Radushkevich equation [17]; the volume of mesopores (Vmeso) by difference between the total and the microporous volume and the pore size distribution applying the density functional theory (DFT) [18]. FTIR spectra were recorded at room temperature using an attenuated total reflection (ATR) mode with a diamond plate of one bounce and a Fourier transform infrared spectrometer (FTIR, Nicolet 8700 FTIR, Thermo Scientific) fittedwith a DFT (deuterated triglycine sulfate) detector. The pH measurements were performed as follows: A sample of 0.1 g of nanotubes was added to 20 mL of water and the suspension was stirred until equilibrium was reached. Then the pH of solution was measured. Electrokinetic potentials (zeta potentials) of nanotubes were determined using a Laser Zee Meter 501. The electrophoretic mobilities were converted into zeta potentials according to Smoluchowski's equation. For each determination, 0.05

g of sample was dispersed in 100 mL of a 0.01 M KCl solution at neutral pH and the slurry magnetically stirred for at least 18–24 h before the measurements were carried out. AFM characterizations of the catalyst were performed using a Cervantes atomic force microscope from Nanotec Electronica™ operating under ambient conditions. Nanosensor™ PPP-NCH PointProbe Plus microcantilevers were used to image the sample via attractive regime amplitude-modulated mode imaging. Solubility measurements were performed by dissolving variable amounts of the CNTs in 10 mL of water. After being subjected to ultrasounds for 15 min, the suspension was left at room temperature and then examined for the presence of any precipitate.

2.4. Batch adsorption experiments

Analytical batch adsorption experiments were conducted in a 50 mL stoppered glass device with no head-space and equipped with a magnetic stirring device [19]. Analytical grade benzene was used to prepare the initial solutions. In a typical experiment, various amounts of CNTs (10, 20 and 30 mg) were added to 50 mL of a benzene solution of 200 ppm. Aliquots were extracted from the solution at regular intervals through a disposable filter. The filtrates were immediately measured by means of HPLC analysis (Agilent 1100 series). The column temperature was set at 27 °C and a UV detector was set to operate at 252.16 nm. Liquid flow rates of 1 mL min^{-1} were used in the HPLC column (Agilent Eclipse XDB-C8), the mobile phase being composed of 80% acetonitrile and 20% water. The amount of benzene adsorbed onto the carbon nanotubes at a given time, *q* (mg/g), was evaluated as:

$$q = (C_0 - C_t) \times V/m \quad (1)$$

where C_0 and C_t are the respective concentrations of adsorbate in solution at time zero and time *t*, and V/m represents the dosage of the adsorbent; V, the volume of the solution (L) and W the mass of adsorbent (g). No temporal variation in the concentrations of benzene was observed during the blank experiments performed in the absence of carbon nanotubes.

3. Results and Discussion

3.1. Oxidative treatment of aligned and forest-like CVD-growth CNTs

Two CVD-growth CNTs in the form of bundles (**B-NT**) or arrays (**A-NT**)

were selected to be treated under different conditions. While the bundle-like CNTs are commercial, the growth of the aligned ones had to be optimized (see supplementary information). Analysis of the TEM images of the parent CNTs indicates that **B-NT** have a very heterogeneous size distribution, with diameters varying from 5 to 30 nm, walls with a thickness of 2 to 10 nm and a length of several microns. In contrast to B-NT, **A-NT** exhibits a more homogeneous size distribution, with diameters varying from 7 to 14 nm, narrower walls (1–3 nm) and a longer length (325 μm). These nanotubes are arranged in a forest-like configuration. Both tubes show the presence of amorphous carbon (see supplementary information) and catalyst particles are observed also in both samples although in lower extent in **A-NT**, as quantified by thermogravimetric analysis (3 wt.% of metallic particles in **A-NT** and 5 wt.% in **B-NT**). The higher ID/IG ratio of A-NT as determined by Raman spectroscopy (1.05 for B-NT and 0.90 for A-NT) is in agreement with those results and confirms higher length and/or more perfect carbon structure of the aligned grown nanotubes.

The increment of the severity of the oxidation treatment (in increased severity order: **X-NT-HCl, X-NT-AP**, **X-NT-NP** and **X-NT-SN**) produces different modifications in their morphology. The elimination of the metal particles (CVD catalyst) was observed in all cases, which is accompanied by a partial opening of the tips. A possible mechanism for this process might be that the pentagon–heptagon rings present in the tip, which are a natural result of the CVD process, are attacked by an oxidizing agent, which generates a hole that allowing the metal nanoparticles to

Table 1. Analysis of the N_2 adsorption, pH and XPS C1s deconvolution results on treated bundle-like and forest-like CNTs.

Sample	Raman	XPS	XPS C1s (%)									
	ID/IG[a]	C/O[b]	Csp[2]	Csp[3]	COH	CO	COOH	OCOO	BET[c]	Vmicro[d]	Vmeso[e]	pH
A-NT	0.901	186	62.4	12.6	10.2	3.8	2.1	8.9	–	–	–	–
A-NT-HCl	0.868	48.5	62.8	12.0	10.5	3.7	1.9	9.1	93	0.09	1.30	5.98
A-NT-AP	0.882	19	60.0	12.0	11.4	5.3	1.8	9.5	100	0.05	1.20	5.17
A-NT-NP	0.948	8	54.6	15.9	14.1	3.2	3.2	9.0	97	0.06	1.25	4.51
A-NT-SN	0.983	4	36.8	21.8	19.7	3.1	11.7	6.9	90	0.02	0.52	2.97
B-NT	1.056	130	61.1	13.4	9.8	3.7	2.6	9.4	–	–	–	–
B-NT-HCl	0.986	49	60.7	12.2	10.2	4.8	3.4	8.7	212	0.09	1.35	6.93
B-NT-AP	1.047	32	62.6	10.8	9.7	5.7	3.0	8.2	240	0.09	1.95	5.81
B-NT-NP	1.077	24	60.6	13.3	11.7	3.6	3.5	7.3	274	0.11	1.91	3.93
B-NT-SN	1.091	3	35.0	21.2	18.1	6.0	10.7	9.0	54	–	0.32	3.13

[a]Raman Defective/Graphitic band ratio, [b]Carbon/Oxygen XPS Ratio, [c]BET surface area (m^2/g), [d]Microporous volume (cm^3/g), [e]Mesoporous Volume (cm^3/g)

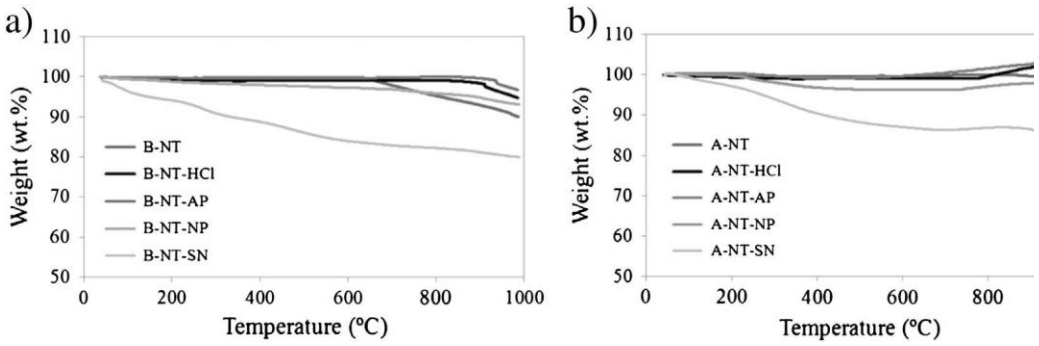

Fig. 1. TGA curves of treated (a) bundle-like carbon nanotubes and (b) forest-like carbon nanotubes.

dissolve [20,21].

A progressive decay of the amorphous carbon as the severity increases is also observed by TEM and confirmed by TGA in the form of a decrease in weight that is lost at temperatures above 600 °C in all the tubes compared to the untreated ones (see supplementary information). This also contributes to the progressive disaggregation of the CNTs, effect becoming appreciable also during the treatment with HCl. Interestingly it is observed that the bundles in **B-NT** disaggregate to a greater extent than the arrays in **A-NT** which is indicative of a more effective elimination of amorphous carbon.

The progressive increment in the severity of the treatment also has an effect in the length and diameter of the tubes. Thus, during the less severe oxidation conditions, (**X-NT-HCl**, X = A or B) the length and diameter of the CNTs seem to have been only slightly modified with respect to the original samples [22]. At more severe conditions (**X-NT-NP**) a reduction in their mean diameter (19 nm for **B-NT-NP** and 12 nm for **A-NT-NP**) and in their lengths from hundreds to tens of microns is observed. This reduction is even more noticeable in the samples from the most severe conditions, **X-NT-SN**, with variations in length range from hundreds of microns to hundreds of nanometers, whereas the reductions in their mean diameters range from 20 to 15 nm in **B-NT** and from 15 to 10 nm in **A-NT-SN**. Furthermore, in **A-NT-SN** there is a partial opening of the upper part of the nanotubes which is a consequence of the more intense oxidation of its surface.

The ID/IG ratio of the CNTs (Table 1) is higher in all cases in the aligned

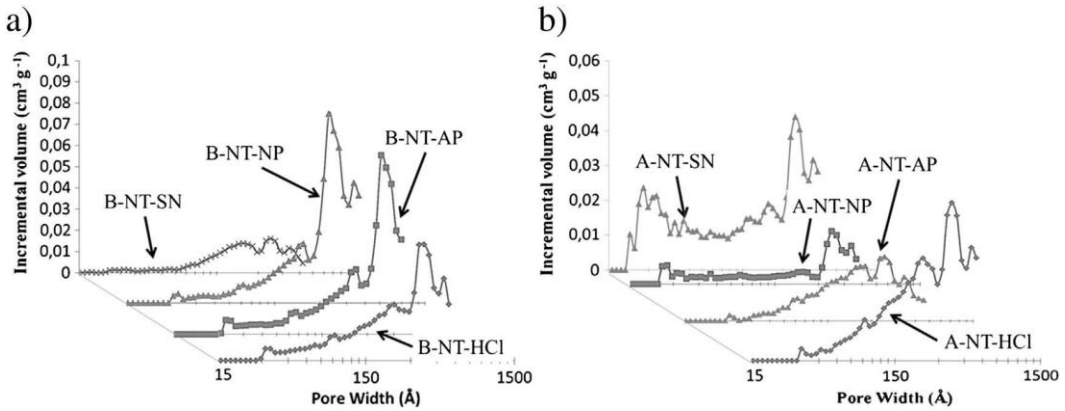

Fig. 2. Pore size distribution of a) **B-NT** and b) **A-NT** samples.

CNTs as a consequence of their more homogeneous morphology. Taking into account the previous analysis results, the decrease in this ratio after the HCl treatment (passing from 1.05 to 0.98 in bundle nanotubes compared to from 0.90 to 0.86 in the case of the aligned nanotubes) could be ascribed to the elimination of the amorphous carbon, while the progressive increment in this value with the severity of the oxidation treatment is explained by a progressive increase in structural defects after treatment.

3.2. Effect of the treatment on the surface chemistry of the CNTs

Of special importance for the application of CNTs for adsorption purposes is the type and amount of the functional groups that need to be introduced in the treatments. XPS analysis of the oxygen functionalities reveals interesting findings. In all cases the progressive decrease in the C/O ratio (Table 1) agrees with the gradual introduction of oxygen functional groups (although the elimination of amorphous carbon observed with HCl treatment cannot be ignored). What is of greater importance, however, is the lower C/O ratio observed in the treated aligned tubes in the AP and NP treatments compared to that of the corresponding bundle-like tubes. This contradicts the data previously reported in the literature, which indicated the preferential introduction of oxygen-containing functional groups into the bundle-like carbon nanotubes rather than into more oriented structures. The deconvolution of the high resolution XPS C1s spectra obtained for the nanotubes allowed determining the type and amount of functional groups present at their surface. The lower amount of Csp^2 bonds (60.0% and 54.6% in **A-NT-AP** and **A-NT-NP**

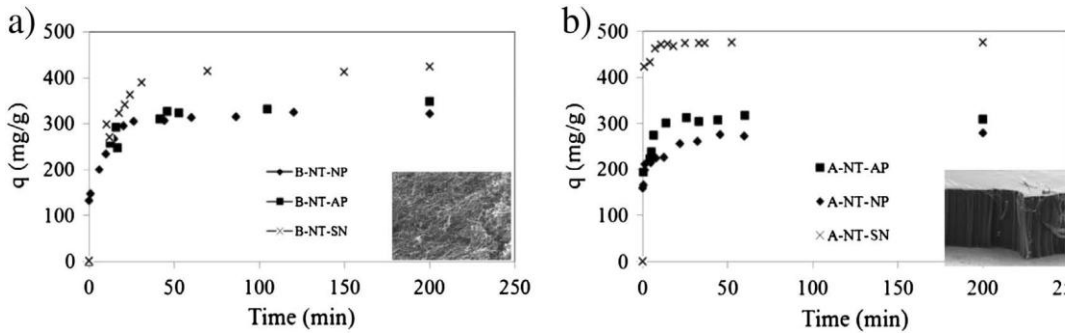

Fig. 3 Effect of the contact time on benzene adsorption for (a) B-NT-x and (b) A-NT-x. SEM images (insets) clarify each CNT structure, bundle-like or aligned.

versus 62.6 and 60.6% in **B-NT-AP** and **B-NT-NP**) suggests that this could be related to a functionalization of the basal surface of the aligned CNTs as a result of their longer length. Analysis of the oxygen containing functional groups indicates the preferential introduction of C\OH groups (11.4 and 14.1% for **A-NT-AP** and **A-NT-NP** versus 9.7 and 11.7% for **B-NT-AP** and **B-NT-NP**) which are probably located at the surface of the CNTs. TGA under nitrogen supports these findings, evidencing the progressive lower temperature of the initial weight loss (500 °C), attributed to the functionalization of the walls (Fig. 1). FTIR spectra are in accordance with these data (see supplementary information).

The opposite trend for the C/O ratio is observed with the more severe treatment, in which **B-NT-SN** exhibits a higher ratio. This confirms that the introduction of functional groups in the CNTs depends not only on the severity of the treatment but also on the morphology of the nanotubes. This is in agreement with the larger increase in Csp^3 bonds in the case of **A-NT-SN** (up to 21.8%) despite the substantial decrease in Csp^2 bonds observed for both samples, down to 36.8% in **A-NT-SN** and 35.0% in **B-NT-SN**. Carbonate groups are almost invariant in all the samples studies (≈9.0%). What is especially worth noting, however, is the greater content in acid groups found in the less oxidized samples, **A-NT-SN** (11.7% compared to 10.7% for **B-NT-SN**). This could be related to the partial opening of the tip of the aligned nanotubes, which would increase the number of edges where the acid groups are located.

Table 2. Results of linear regression of Lagergreen, pseudo-second order, Freunlich and Langmuir models

Sample	Lagergreen model		Pseudo-second order model			Freundilch model			Langmuir model		
	K_1 (min^{-1})	$r^{2\,a}$	K_s (min^{-1})	q_e(mg/g)	$r^{2\,a}$	K_f	n	$r^{2\,a}$	K_{lg}	1/n	$r^{2\,a}$
A-NT-AP	0.103	0.940	0.0060	277	0.999	3.70	1.21	0.997	0.539	0.0008	0.992
A-NT-NP	0.156	0.960	0.0030	312	0.999	2.44	0.74	0.990	0.639	0.0014	0.994
A-NT-SN	0.146	0.840	0.0110	476	0.999	4.22	0.95	0.994	0.208	0.0002	0.994
B-NT-AP	0.041	0.980	0.0016	322	0.999	0.02	0.52	0.997	1.048	0.0041	0.998
B-NT-NP	0.021	0.940	0.0007	333	0.995	0.06	0.53	0.995	0.799	0.0032	0.999
B-NT-SN	0.034	0.900	0.0005	434	0.999	0.31	0.66	0.997	0.499	0.0018	0.999

[a]Regresion coefficient

3.3. Effect of the treatment on the adsorption properties of the CNTs

Our previous results have revealed that the introduction of functional groups can be modulated by the type of nanotube and treatment. These changes have an effect on the adsorption properties of the nanotubes, which can be, in a first approach, determined from the analysis of the N_2 adsorption isotherms (Table 1). As can be seen, the BET surface area increases with the severity of the treatment with slight variations in the micropore volume that are due to the tip opening up and to the elimination of amorphous carbon during the treatment. However, this does not occur in the severest treatment, where there is a decrease in BET area with the only presence of mesopores. A similar decrease in BET surface area has been reported in the literature and attributed to the functionalization of the external and internal surface of the nanotubes, where the formation of surface functional groups is associated with the destruction of the nanotube walls [23–25].

It is observed that the type of nanotubes and the treatment applied has an influence on the pore size distribution of the samples obtained (Fig. 2). Two types of mesopores were identified in all samples. The broad multi-peaks observed above 230 Å can be ascribed to the interparticle pores due to strong aggregation among nanotubes [26], while the peaks located below 60 Å relates with the intraparticle pores. This later peak is distinctive of the typical cylinder-shape mesopores of each carbon nanotubes. In B-NT nanotubes, the maximum of this peak in centered at 34 Å (corresponding to the internal diameter of the nanotubes [27]). This value remains almost unaltered for all the treatments applied. This is not the case of the **A-NT** nanotubes, in which

Table 3. Comparison in benzene adsorption of various adsorbents

Adsorbent	mg/g benzene	Reference
Activated carbon (granular)	212	[7]
Activated carbon (powder)	40	[28]
Activated carbon (anthracene oil-based pitch)	815	[|9]
Esmectite	98	[32]
Carbon char	0.2	[33]
Clay	1	[34]
Zeolite	27	[28]
MWCNT(NaOCl)	248	[7]
SWCNT (NaOCl)	60	[35]
MWCNT (HNO_3)	130	[7]
MWCNT (H_2SO_4/HNO_3)	510	This study

a slightly decrease from 34 Å (internal diameter of **A-NT-HCl** and **A-NT-AP**) to 27 Å in **A-NT-NT** is observed. Furthermore, **A-NT-SP** exhibits the appearance of multi-peak at those regions, probably as a consequence of the partial opening of the upper part of the nanotubes previously observed by other techniques.

Of special relevance for the adsorption properties of the nanotubes is their tendency to be dispersed in an aqueous medium (water solubility). For both types of CNTs, bundle-like and forest-like, only the samples treated under the most oxidative conditions (**B-NT-SN** and **A-NT-SN**) were well dispersed in water (see supplementary information). This may have been due to the large amount of carboxylic acids on their surface, which would have increased their polarity. The other samples with lower concentration of acids are less polarized and have problems to disperse in this medium [28]. Additionally, the pH measured for each sample is in agreement with this acidity increase observed with the severity of the treatment applied. After one month, only **A-NT-SN** was observed to be stable in solution, in accordance with the higher surface functionalization of this sample. At this stage, the main purpose of surface modification should be to enhance their hydrophilicity and dispersibility in aqueous media.

3.4. Benzene adsorption isotherms

The benzene concentration ranges (200 ppm) and experimental conditions (room temperature and pH) in this study were selected according to the data facilitated by one of the

industries producing benzene contaminated water [19] and were considered therefore as ideal conditions to carry out these studies.

The effect of benzene adsorption with contact time with an initial concentration of 200 mg L^{-1} is illustrated in Fig. 3a for bundle-like CNTs and in Fig. 3b for forest-like CNTs. The results indicate a rapid increase in the amount of benzene adsorbed with contact time followed by a slow increase until it reaches equilibrium after approximately 50 min. Furthermore, in the case of forest-like carbon nanotubes, equilibrium is reached in a shorter time (20 min for **A-NT-X**) than bundle-like carbon nanotubes due to the faster kinetics.

These times are shorter than others previously reported for benzene adsorption at carbon nanotubes (i.e. 240 min as reported by Su et al. [7]) for an initial concentration of 200 mg L^{-1}. For a better comparison between samples, the kinetic data obtained for each sample were curve-fitted in two different kinetic models, the first order kinetic model, Lagergreen model, and the pseudo-second order model, both well established in the literature. The kinetic constant rates (K_l for Lagergreen model and K_s for the pseudo-second order model) and the correspondent square errors, obtained for each sample are summarized in Table 2. The results indicate that the pseudo-second order is a better model to describe the kinetics in both types of carbon nanotubes (better regression coefficient). Similar result was also observed for other types of carbon materials (activated carbons [19] and carbon nanotubes [29]). Comparing the performance of both types of carbon nanotubes the better performance of the aligned carbon nanotubes is emphasized, which seems to indicate that surface properties of these aligned nanotubes play a positive role in the kinetics of adsorption and point to a faster initial transfer of benzene at the near surface boundary layers [8]. The comparison of the pseudo-second order kinetic rate constant and the q_e value calculated from the model equation for the nanotubes prepared in this work (Table 2) with those extracted from previous works [19] highlights their good kinetic performance.

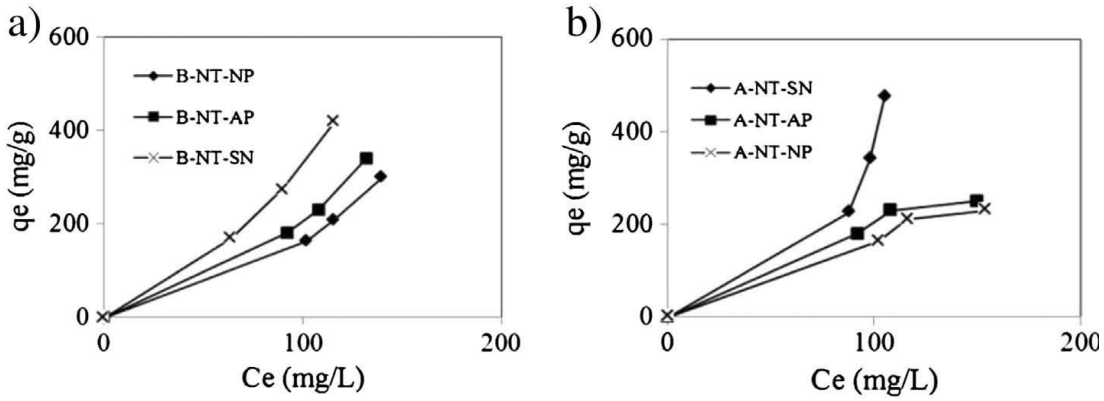

Fig 4. Adsorption isotherms of benzene adsorption on treated (a) bundle-like and (b) forest-like carbon nanotubes.

The equilibrium adsorption data for the different solutions were also calculated using the adsorption values recorded at the longest times in the kinetic experiments, once the different concentrations had stabilized. Fig. 4 shows the benzene adsorption isotherms derived from the kinetic data recorded at the longest adsorption times. The results indicate that in the **B-NT** nanotubes (Fig. 4a) benzene adsorption reached a maximum value somewhere inside the 300–400 mg/g range, whereas for **A-NT** nanotubes the range was wider, from 200 to 500 mg/g (Fig. 4b).

Those values are in the range of those calculated by means of the pseudo-second order kinetic model and corroborate the ability of the model to describe the process. Also, the data obtained were analyzed by using two types of isotherm models, the Langmuir model [30], which assumes a no uniform surface of the sorbent and the Freundlich model [31], which considers that the surface is uniform. The specific constant (K_f and K_{lg} respectively) and related parameters (n and 1/n) obtained are summarized in Table 2. According to the regression criteria, (r^2) the Langmuir isotherm is, in most cases, the most suitable model characterizing the adsorption of benzene onto the surface of the nanotube.

Comparing the results obtained with those reported by other authors (Table 3) we observe an enhancement in the benzene adsorption capacity of our samples with respect to that obtained by oxidized carbon nanotubes (single or multiwalled), zeolites, clays and most of the powder or granular

carbons (with the exception of the anthracene oil-based activated carbons). We can conclude that vertically aligned CNTs, if properly treated, will make good adsorbents for environmental protection purposes.

From the above results, it can be seen that the surface treatment of all the nanotubes, according the series AP<NP<SN (Fig. 4). However, in this regard several points should be considered. It was observed that for AP and NP the adsorption properties of bundle-like carbon nanotubes are higher than those of forest-like nanotubes. This is consistent with a higher BET surface area of the bundle-like CNTs and their lower degree of functionalization compared to that of their forest like counter parts. The results agree with the proposed adsorption mechanism via dispersive interactions in which the attraction between the π-orbitals on the SWCNT basal planes and the electronic density in the benzene aromatic rings are predominant (π–π electron-donor–acceptor interactions) [13,36], since these CNTs, in comparison with the aligned ones, B-NT have a better Csp^2 structure (60.0 and 54.6% in the aligned CNTs versus 62.6 and 60.6% in the bundle CNTs) and a smaller amount of acid groups (1.8 and 3.2% in the aligned CNTs versus 3.0 and 3.5% in the bundle CNTs). A possible explanation for the poor benzene adsorption of the aligned nanotubes could be related to their lower water solubility (supplementary information), possibly because of their longer length.

The opposite trend was observed in the case of the CNTs treated under the severest conditions. A higher adsorption performance was obtained for the aligned nanotubes, with values of ≈510 mg/g for **A-NT-SN** as against ≈420 mg/g for **B-NT-SN**. The increased water solubility of **A-NT-SN** may have been responsible for this better performance.

Although π–π electron-donor–acceptor interactions in which the carboxylic oxygen-atom is involved cannot be discarded [7], the small differences in the amount of this functional group among the samples could not explain the enhanced adsorption capacity of the aligned nanotubes (10.7% versus 11.7% in aligned CNTs). Furthermore, the pH calculated for both nanotubes is similar, and also the values of Z potential calculated at the pH conditions examined (−28.1 and −27.9 mV for **A-NT-SN** and **B-NT-SN** respectively). Considering that the main difference between these CNTs is their Csp^2 structure (35.0% for **B-**

NT-SN vs 36.8% for **A-NT-SN**), it is possible that this enhanced adsorption could be due instead to the greater accessibility of benzene to the CNT adsorption sites where dispersive interactions are also predominant.

4. Conclusions

The treatment of aligned and bundle-like carbon nanotubes using reagents with increased oxidation degree led to a proportional increment in the oxygen functional groups at the surface and at the tips of the nanotubes. Contrary to what was stated before, the treatment with the less oxidizing agents was more effective in aligned nanotubes possibly due to their more homogeneous surface properties and greater length, mainly in the form of COH/CO groups. Only the strongest oxidizing agent introduced more oxygen functional groups in bundle-like CNTs (lower C/O ratio) although with a lower amount of COOH groups. This was related to a partial opening of the aligned CNTs at those conditions. These facts modified the capacity of forming stable suspensions in water and the adsorption behavior of the CNTs. Thus, in the comparative study of benzene adsorption aligned CNTs exhibited faster kinetics. They also exhibit higher adsorption capacity only when they were exposed to the strongest oxidation conditions. The results obtained confirm that with the adequate treatment it is possible to prepare aligned carbon nanotubes with the potential to be competitive as adsorbents of benzene in industrial wastewater.

Prime novelty statement

This article includes original and fully interpreted advances in utilization of carbon nanotubes (CNTs) as water adsorbents. The article includes detailed characterization of the changes in morphology and functionalization during pre-treatment of two types of CNTs (bundle-like and aligned), with a view to determine the effect of the alignment in their adsorption capacities. Compared to previously published works, unexpected results were obtained when the effect of alignment was studied in detail and contributes to a more effective use of CNTs in adsorption applications. Therefore, authors consider the article fits the requirements for publishing in the journal.

Acknowledgments

The authors thank the Spanish Science and Innovation Ministry (CONSOLIDER INGENIO 2010, Ref. CSD2009-00050; MAT2010-16194; INNPACTO, Ref. IPT-2011-0951-390000 and Ramón y Cajal program) and FICYT (Ref. COF 11–34) for their financial support. Matías Blanco thanks the Spanish Education Ministry for his FPU grant (Ref. AP2010-0025).

Appendix A. Supplementary data

Supplementary data to this article can be found online at http://dx.doi.org/10.1016/j.diamond.2013.04.006

References

[1] H. Hindarso, S. Ismadji, F. Wicaksama, M. Mudjijati, N. Indraswati, J. Chem. Eng. Data 46 (2001) 788.

[2] W.W. Eckenfelder, Industrial Water Pollution Control, 2nd ed. McGraw Hill International Editions, Singapore, 1989.

[3] A.A.M. Daifullah, B.S. Girgis, Colloids Surf. A Physicochem. Eng. Asp. 214 (2003) 181.

[4] X. Ren, C. Chen, M. Nagatsu, X. Wang, Chem. Eng. J. 2–3 (2011) 16.

[5] V.K.K. Upadhyayula, S. Deng, M.C. Mitchell, G.B. Smith, Sci. Total Environ. 408 (2009) 1.

[6] C. Lu, F. Su, S. Hu, Appl. Surf. Sci. 254 (2008) 7035.

[7] F. Su, S. Hu, Colloids Surf. A Physicochem. Eng. Asp. 353 (2010) 83.

[8] F. Yu, M. Jie, Y. Wu, J. Hazard. Mater. 192 (2011) 1370.

[9] Y. Cheng, C. Liu, F. Li, H.M. Cheng, J. Porous Mater. 13 (2006) 141.

[10] C. Lu, F. Su, Sep. Purif. Technol. 58 (2007) 113.

[11] C. Zhang, S. Pisana, C.T. Wirth, A. Parvez, C. Ducati, S. Hoffman, S.J. Robertson, Diamond Relat. Mater. 17 (2008) 1447.

[12] Q. Liao, J. Sun, L. Gao, Carbon 46 (2008) 544.

[13] L.R. Radovic, J.F. Silva, J.L. Ume, J.A. Menéndez, L. Caly, A.W. Scaroni, Carbon 35 (1995) 1339.

[14] S.C. Ramos, G. Vasconcelos, E.F. Antunes, A.O. Lobo, V.J. Trava-Airoldi, E.J. Corat, Diamond Relat. Mater. 19 (2010) 752.

[15] P.M.A. Sherwood, in: D. Briggs, M.P. Seah (Eds.), Practical Surface Analysis, Auger and X-ray Photoelectron Spectroscopy, vol. 1, Wiley, New York, 1990, p. 574.

[16] Y. Geng, S.J. Wang, J. Kim, J. Colloid Interface Sci. 336 (2009) 592.

[17] M.M. Dubinin, Carbon 27 (1989) 457–467.

[18] N.A. Seaton, J.P.R.B. Walton, N. Quirke, Carbon 27 (1989) 853–861.

[19] N.G. Asenjo, P. Álvarez, M. Granda, C. Blanco, R. Santamaría, R. Menéndez, J. Hazard. Mater. 192 (2011) 1525.

[20] J. Zhang, H. Zou, Q. Qing, Y. Yang, Q. Li, Z. Liu, X. Guo, Z. Du, J. Phys. Chem. B 107 (2003) 3712.

[21] B.W. Clare, D.L. Kepert, Inorg. Chim. Acta 343 (2003) 1.

[22] V. Datsyuk, M. Kalyva, K. Papagelis, J. Parthenios, D. Tasis, A. Siokou, I. Kallitsis, C. Galiotis, Carbon 46 (2008) 833.

[23] S. Gotovac, C.M. Yang, Y. Hattori, K. Takahashi, H. Kanoh, K. Kaneko, J. Colloid Interface Sci. 314 (2007) 18.

[24] L. Li, B. Wu, B.Q. Xu, Carbon 44 (2006) 2973.

[25] T. Hemraj-Benny, T.J. Bandosz, S.S. Wong, J. Colloid Interface Sci. 317 (2008) 375.

[26] C.M. Chin, M. Shih, H. Tsai, Appl. Surf. Sci. 256 (2010) 6035.

[27] Q.F. Hou, X.C. Lu, X.D. Liu, B.X. Hu, J.Q. Cui, J. Shen, Surf. Coat. Technol. 190 (2005) 394–399.

[28] S.M. Koh, J.B. Dixon, Appl. Clay Sci. 18 (2001) 111–112.

[29] M. Wiśniewski, P.A. Gauden, A.P. Terzyk, P. Kowalczyk, A. Pacholczyk, S. Furmaniak, J. Colloid Interface Sci. 391 (2013) 74–85.

[30] T. Wigmans, Carbon 27 (1989) 13–22.

[31] L.E. Vijan, M. Neagu, Rev. Roum. Chim 57 (2012) 85–93.

[32] J.F. Lee, M.M. MOrtland, C.T. Chiou, D.E. Kyle, S.A. Boyd, Clays Clay Miner. 38 (1990) 113–120.

[33] I.H. Cho, Environ. Eng. Res. 2 (1997) 201–205.

[34] S. Sharmasarkar, W.F. Jaynes, G.F. Vances, Water Air Soil Pollut. 119 (2000) 257–273.

[35] W. Chen, L. Duan, D. Zhu, Environ. Sci. Technol. 41 (2007) 8295–8300.

[36] F. Avilés, J.V. Cauich-Rodríguez, L. Moo-Tah, A. May-Pat, R. Vargas-Coronado, Carbon 47 (2009) 2790.

SUPPLEMENTARY DATA

S1: Preparation of the CVD catalyst

S2: Optimization of the conditions for the CVD growing

S3: Raman analysis of CNTs

S4: TEM Characterization of the carbon nanotubes used in this work

S5: Solubility characteristics of the carbon nanotubes used in this work

S6: FTIR spectra of the adsorbents

S1: Preparation of the CVD catalyst

The catalyst employed to produce the vertically aligned carbon nanotubes (A-NT) included a 10 nm layer of Al_2O_3 deposited over silicon oxide that acts as a barrier layer to prevent Ostwald ripening and the diffusion of the catalyst (35 nm Fe nanoparticles) into the substrate. FIG. S1 (a, b and c) describes the morphology of the resulting catalyst in each successive step of preparation, as characterized by FESEM and the AFM analysis, showing the homogeneous dispersion of Fe nanoparticles over the Al_2O_3 surface (FIG. S1,d). This configuration gave rise to high-purity vertically-aligned multiwall carbon nanotubes, with the largest yield of CNTs per process and unit area of substrate.

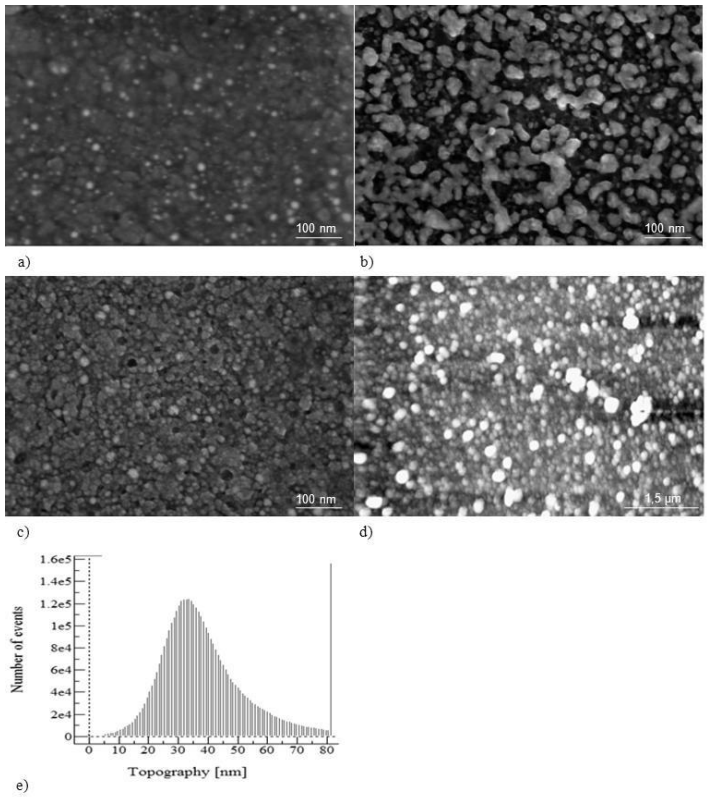

FIG. S1: FESEM images of (a) the Al_2O_3 surface, (b) Fe deposited over the Al_2O_3 surface, (c) the Fe catalyst after H_2 treatment, (d) AFM image of the Fe catalyst and (e) the correspondent topography diagram.

S2: Optimization of the conditions for the CVD growing

Three different duration of the injection of ethylene were tested, 0.5, 1 and 2 h (labelled respectively **A-NT-0.5**, **A-NT-1** and **A-NT-2**). The length of the CNTs obtained at each time was determined by means of SEM (FIG. S2), the metal impurities and presence of amorphous carbon by means of TGA analysis (FIG. S3) and confirmed by Raman analysis (FIG. S4).

The results revealed that an increment from 0.5 h to 1 h increased the length of the nanotubes from ~150 μm to ~325 μm while the metal impurities were reduced from ~ 5 wt. % to ~ 3 wt. %, as demonstrated by TGA in air, and the amorphous carbon (which was lost in air at 400ºC) was reduced from 4 to 0.5 wt. %. Interestingly, after 2 h, growth was observed to be slower (~375 μm length) and amorphous carbon appeared, as confirmed by TGA, in the form of 2 wt. % of amorphous carbon, as well as a low amount of metal catalyst residues (~1 wt. %) [1].

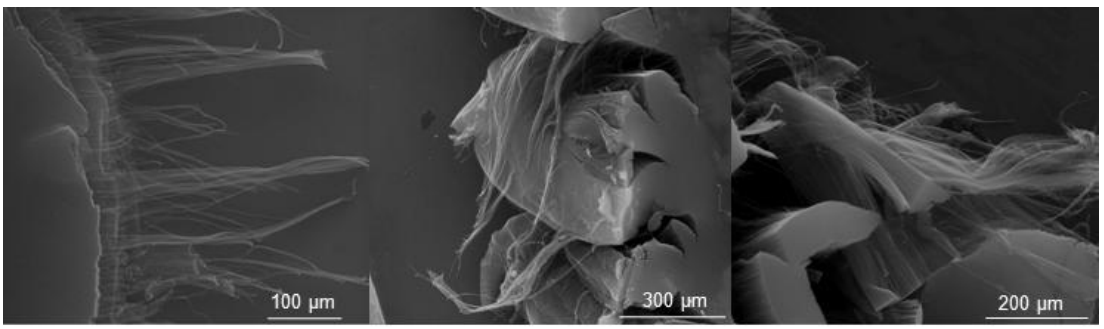

FIG. S2. SEM images of **A-NT** samples obtained at different duration of the injection of ethylene during the CVD process (a**) A-NT-0.5**; b) 1h: **A-NT-1** and c) **A-NT-2**)

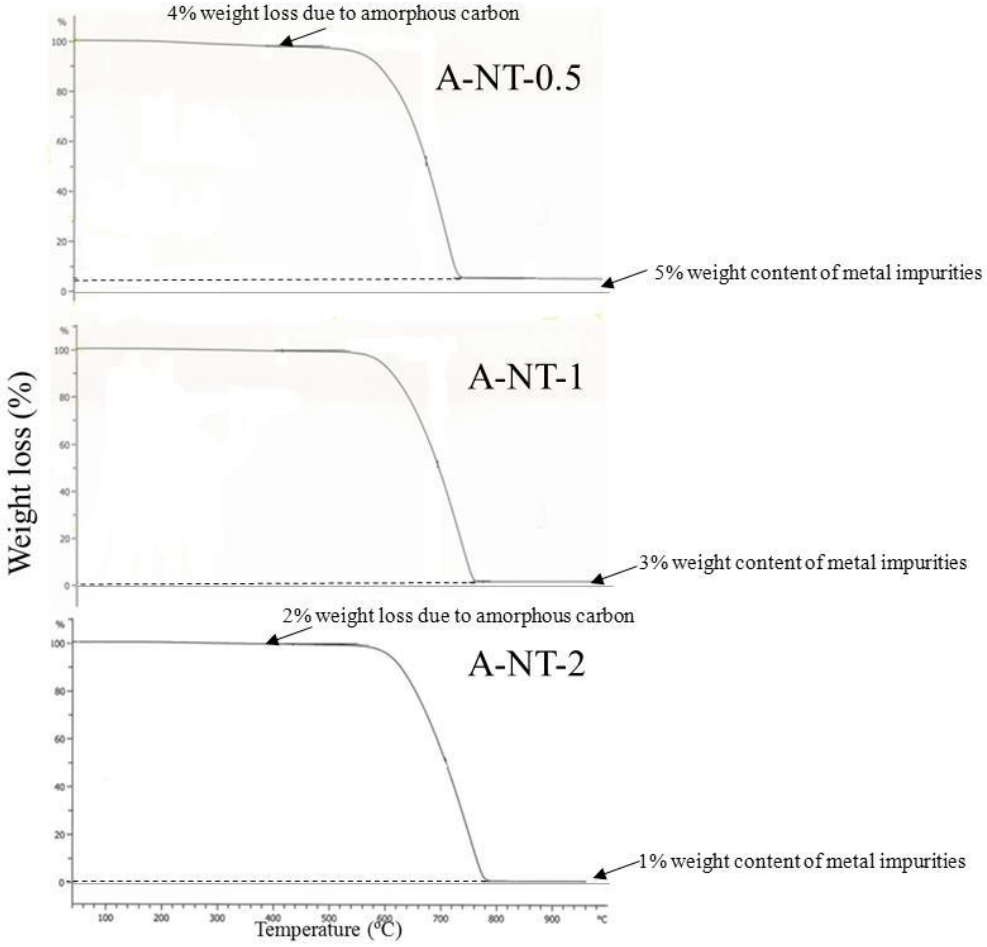

FIG. S3. TGA curves of **A-NT** samples obtained at different duration of the injection of ethylene during the CVD process.

S3: Raman analysis of CNTs

Raman measurements (FIG. S4) evidenced that the amount of impurities increased with the time of growth as the ratio between the intensity of the D and G peaks increased [2] for each sample.

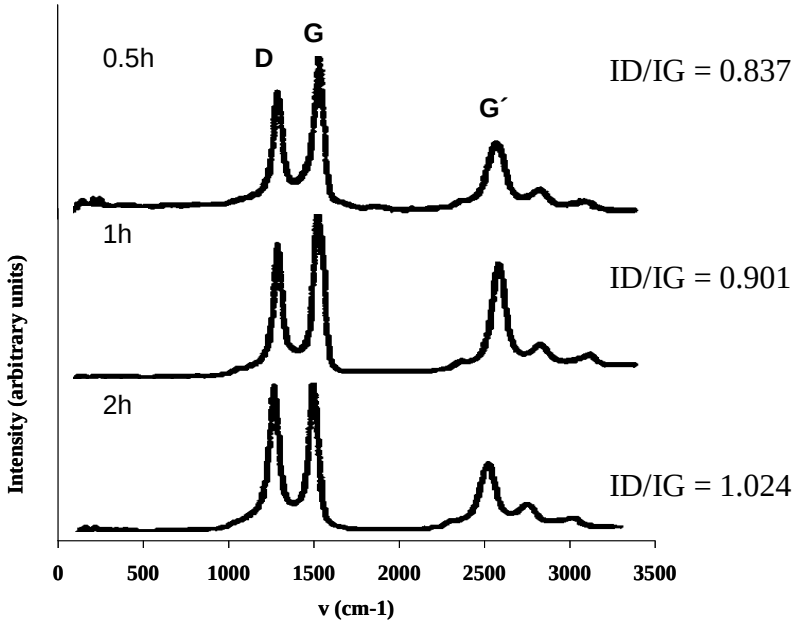

FIG. S4: Raman spectroscopy of the **A-NT** samples

In order to develop CNTs for water purification purposes, experimental conditions which would favour a high length and low presence of defects were selected. The time of injection of ethylene was fixed at 1 h (**A-NT-1**, labelled **A-NT** in the main text for clarity)

S4: TEM Characterization of the carbon nanotubes used in this work

TEM observations were performed on a JEOL 2000 EX-II instrument operating at 160 kV. SEM images were obtained using a field emission gun scanning electron microscope (Carl Zeiss SMT) operating at 30.0 kV.

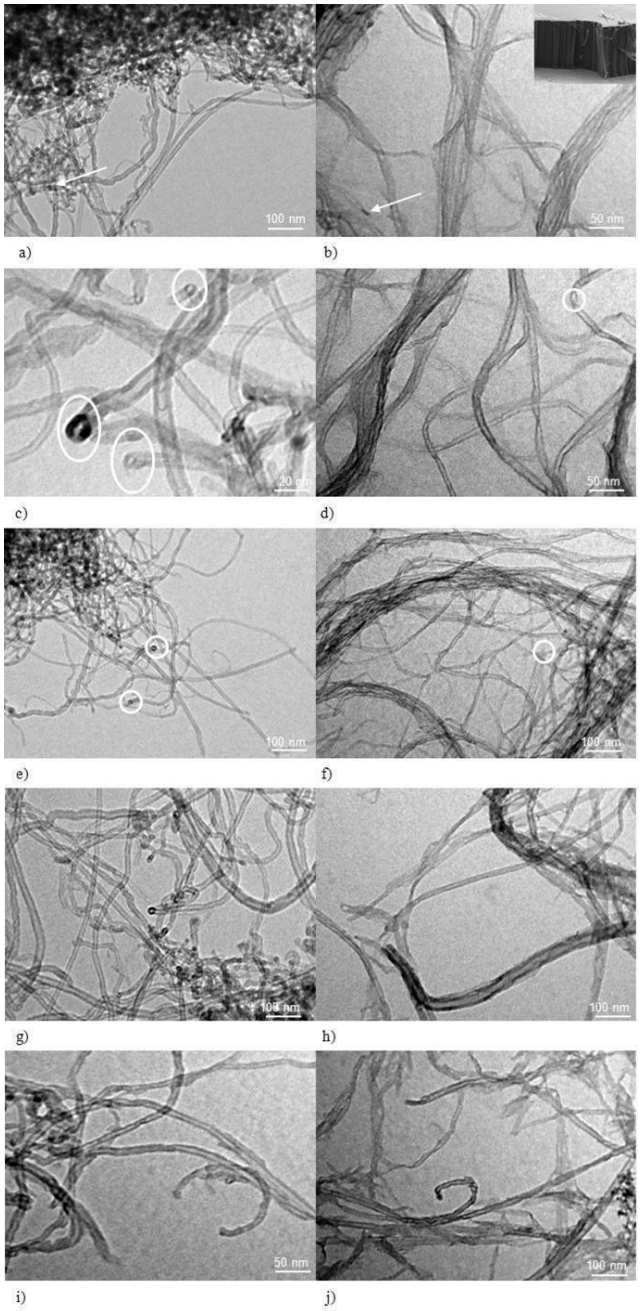

FIG S5. TEM images of carbon nanotubes (a) **B-NT**, (b) **A-NT** (inset: SEM image showing the forest-like structure) (c) **B-NT-HCl**, (d) **A-NT-HCl**, (e) **B-NT-AP** (f) **A-NT-AP**, (g) **B-NT-NP** (h) **A-NT-NP**, (i) **B-NT-SN** and (j) **A-NT-SN**

S5: Solubility characteristics of the carbon nanotubes used in this work

Solubility measurements were performed by dissolving variable amounts of the CNTs in 10 mL of water. After being subjected to ultrasounds for 15 min, the suspension was left at room temperature and then examined for the presence of any precipitate.

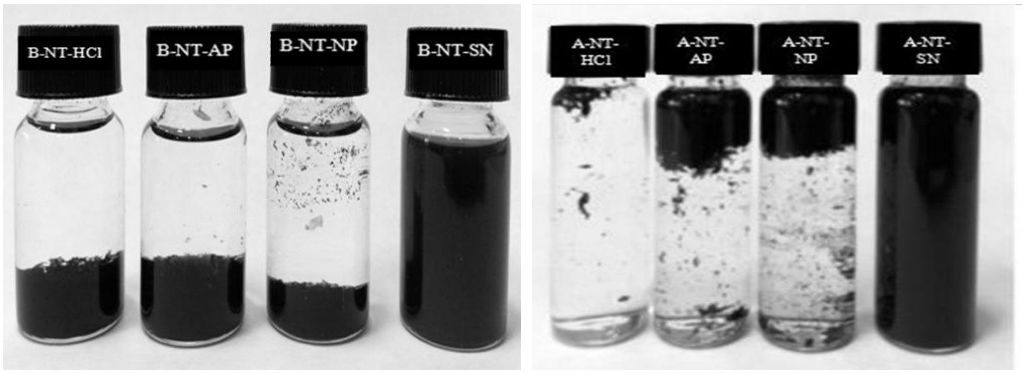

FIG. S6. Digital images of **B-NT-X** and **A-NT-X** in water.

S6: FTIR spectra of the adsorbents

FTIR spectra of the adsorbents were recorded at room temperature using an attenuated total reflection (ATR) mode with a diamond plate of a bounce and a Fourier transform infrared spectrometer (FTIR, Nicolet 8700 FTIR, Thermo Scientific) fitted with a DFT (deuterated triglycine sulphate) detector.

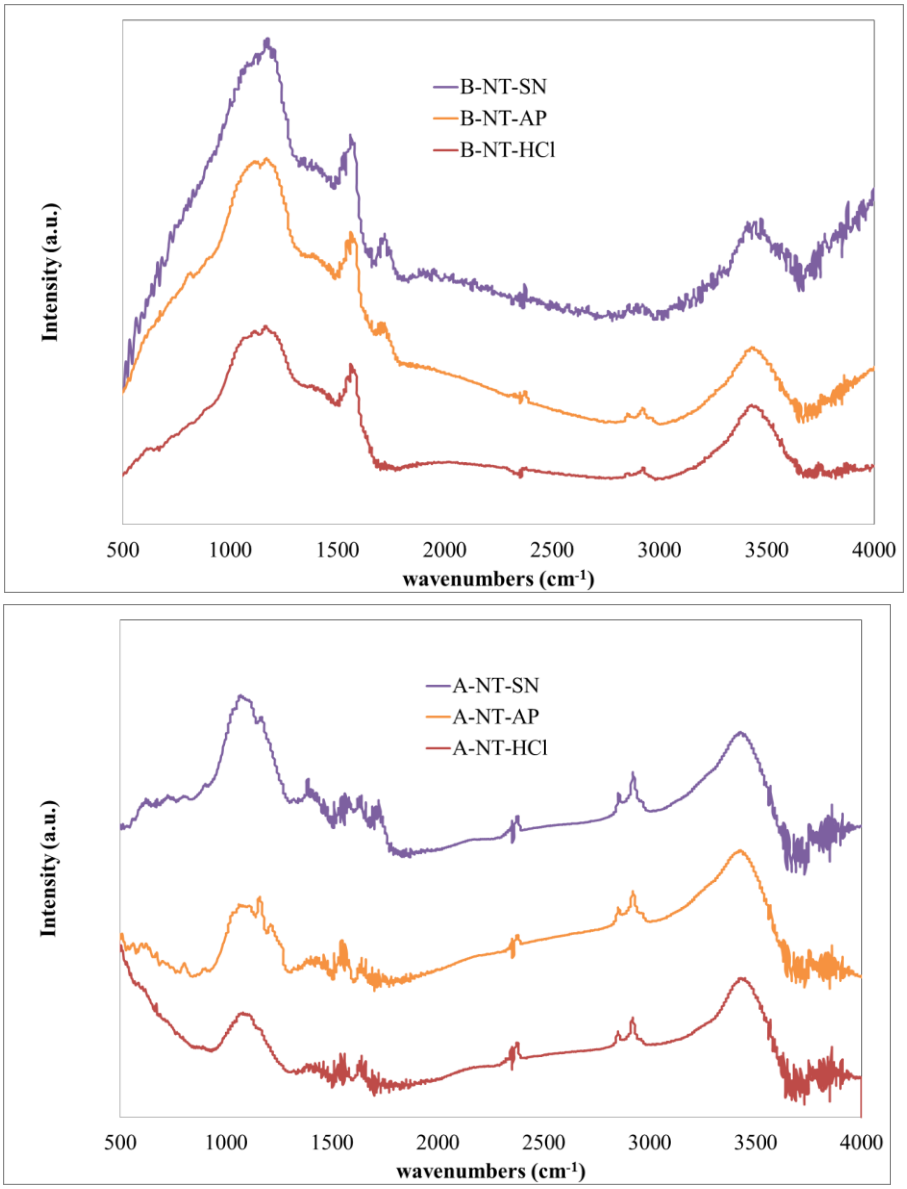

Figure S7: FTIR spectra of the adsorbents

References:

[1] V. Shanov, Y. Yeo-Heung, M.J. Schulz, Journal of the University Of Chemical Technology and Metallurgy, 41 (2006) 377.

[2] A. Jorio, E. Kauppinen, A. Hassanien, Carbon-Nanotube Metrology, Carbon Nanotubes, Topics in Applied Physics, 111 (2008) 63.

4.2 ARTÍCULO II

"Incremento de la actividad catalítica de carbenos N-heterocíclicos de iridio covalentemente enlazados a nanotubos de carbono"

ACS Catalysis **2013**, *3*, 1307-1317

El gran desarrollo de grupos funcionales oxigenados que presentaron los nanotubos de carbono sometidos al tratamiento de oxidación más severo, así como sus excelentes propiedades de adsorción, hacen de estos materiales candidatos idóneos para satisfacer los objetivos del Proyecto de preparación de complejos metálicos soportados sobre materiales de carbono. La gran cantidad de grupos oxigenados que presentan ambos tipos de nanotubos oxidados hace posible el desarrollo de rutas de funcionalización con todo tipo de catalizadores orgánicos e inorgánicos empleando reacciones de esterificación y/o amidación clásicas. Dentro de las opciones disponibles, se eligieron para este trabajo, en colaboración con el Grupo de Catálisis Homogenea por Compuestos Organometálicos de la Universidad de Zaragoza, complejos organometálicos de tipo carbeno N-heterocíclico (NHC) de iridio, conocidos en la literatura por ser catalizadores activos y estables de una gran cantidad de procesos, como hidroformilaciones e hidrosililaciones, y también reacciones de reducción por procesos de transferencia de hidrógeno. La presencia, además, de grupos funcionales dadores en la esfera de coordinación del metal parece generar un efecto positivo en la catálisis. Esos grupos están presentes en las estructuras oxidadas de los materiales de carbono, con lo que se debería esperar el mismo efecto positivo.

Aunque los nanotubos alineados presentaron mejores características así como mayor número de centros de funcionalización, el abastecimiento de los mismos era muy limitado, por lo que se optó por el empleo de nanotubos comerciales. En este

capítulo se trata, por lo tanto, la funcionalización de estos nanotubos oxidados **CNT-ST** con complejos N-heterocíclicos de iridio para el ensayo de su actividad catalítica.

El procedimiento de funcionalización se basó en el uso de los grupos carboxilo superficiales, fácilmente activables con cloruro de tionilo, para la introducción en un segundo paso de una sal de imidazolio, los compuestos [MeImH$(CH_2)_3$OH]Cl (**1**) y [MeImH(1-cyclohexyl-2-ol)]I (**2**). Los correspondientes complejos NHC de iridio fueron sintetizados en un tercer paso mediante reacción de los materiales funcionalizados con las sales de imidazolio, **CNT-ST-1** y **CNT-ST-2**, con el precursor de complejos NHC, [Ir(μ-OMe)(cod)]$_2$ (se omite el interfijo ST por claridad). A efectos comparativos, se prepararon los complejos homogéneos NHC de iridio análogos con funciones de tipo acetoxi terminales **5** y **6**, así como blancos de reacción empleando los nanotubos oxidados directamente con el complejo precursor de complejos NHC de iridio, **CNT-Ir**.

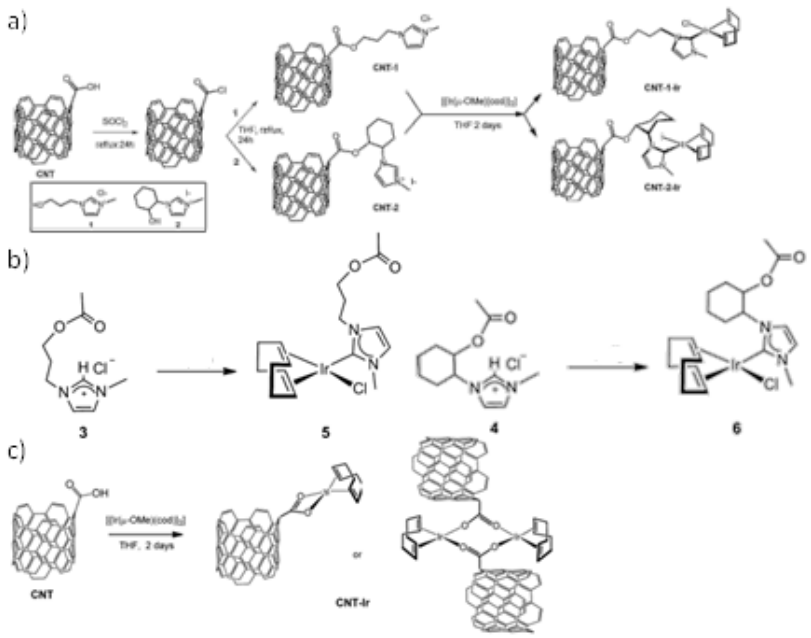

Figura 4.1. a) Esquema de funcionalización de los nanotubos de carbono oxidados con complejos NHC de iridio; b) síntesis de los complejos homogéneos; c) síntesis de los blancos de reacción

La caracterización de las muestras permitió confirmar tanto la presencia de las sales precursoras como de los complejos organometálicos covalentemente soportados sobre los nanotubos de carbono, obteniendo unas eficiencias en la síntesis de un 95 % para ambos complejos, basándose en la cantidad de sal de imidazolio anclada. Por su parte, la caracterización de los nuevos complejos homogéneos reveló la correcta síntesis de ambas unidades. Finalmente, el iridio detectado en los blancos de reacción generó partículas más grandes vistas al microscopio de transmisión, como consecuencia de la no formación de los complejos NHC. Dichas regiones tuvieron una mayor energía de enlace en sus espectros XPS, lo que no se puede adscribir a la presencia de Ir (I). Posiblemente se formen nanopartículas o clusters de iridio con los grupos funcionales oxigenados.

Todas las muestras homogéneas y heterogéneas fueron ensayadas como catalizadores en la reacción de reducción de ciclohexanona a ciclohexanol por procesos de transferencia de hidrógeno, usando 2-propanol/KOH como medio de reacción y como dador de hidrógeno, en unas condiciones optimizadas en trabajos anteriores.

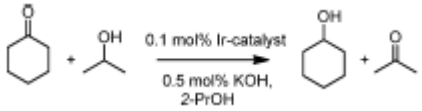

Ec. 3.9

Los sistemas híbridos nanotubo – complejos NHC de iridio resultaron activos en las condiciones estudiadas, así como sus correspondientes complejos homogéneos. Se registraron TOFs iniciales del orden de 5550 h^{-1} sin observarse períodos de inducción en ninguna muestra. Ambos tipos de catalizadores consiguieron conversiones completas, aunque los complejos soportados resultaron ser más activos que sus correspondientes catalizadores homogéneos. La especie más activa a cualquier tiempo siempre fue **CNT-1-Ir**. La mayor actividad de las especies

soportadas puede ser debida al confinamiento cuántico que la cavidad interior del nanotubo puede ejercer, actuando como un "nano-reactor".

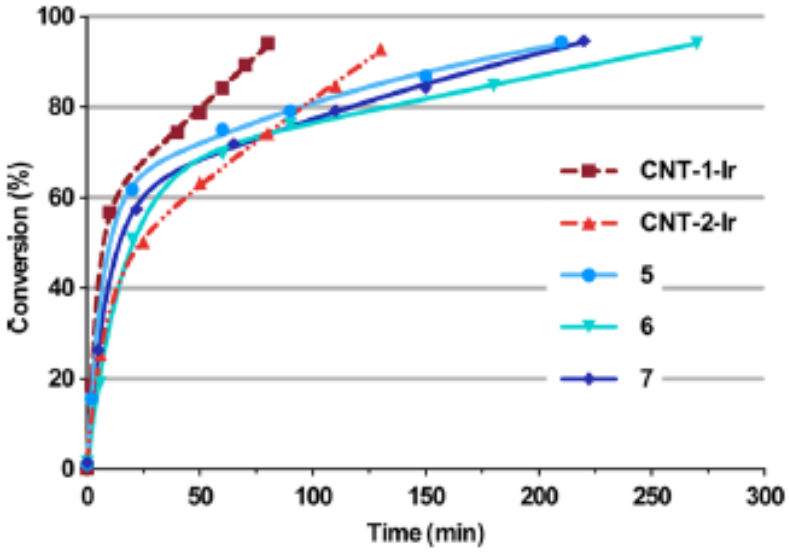

Figura 4.2 Actividad catalítica

Por otra parte, un posible efecto de superficie basado en la interacción de los grupos funcionales con las diferentes especies por las que el metal discurre durante su ciclo catalítico también podría explicar el incremento en la actividad. Si los grupos oxigenados presentes en las paredes de los nanotubos establecen enlaces estabilizantes del tipo puente de hidrógeno durante los pasos clave de transferencia de hidrógeno, como son la migración de hidruro y β-eliminación de hidrógeno propuestos en el mecanismo de la transferencia de hidrógeno, el efecto positivo demostrado anteriormente con grupos dadores se podría repetir empleando los grupos funcionales del soporte.

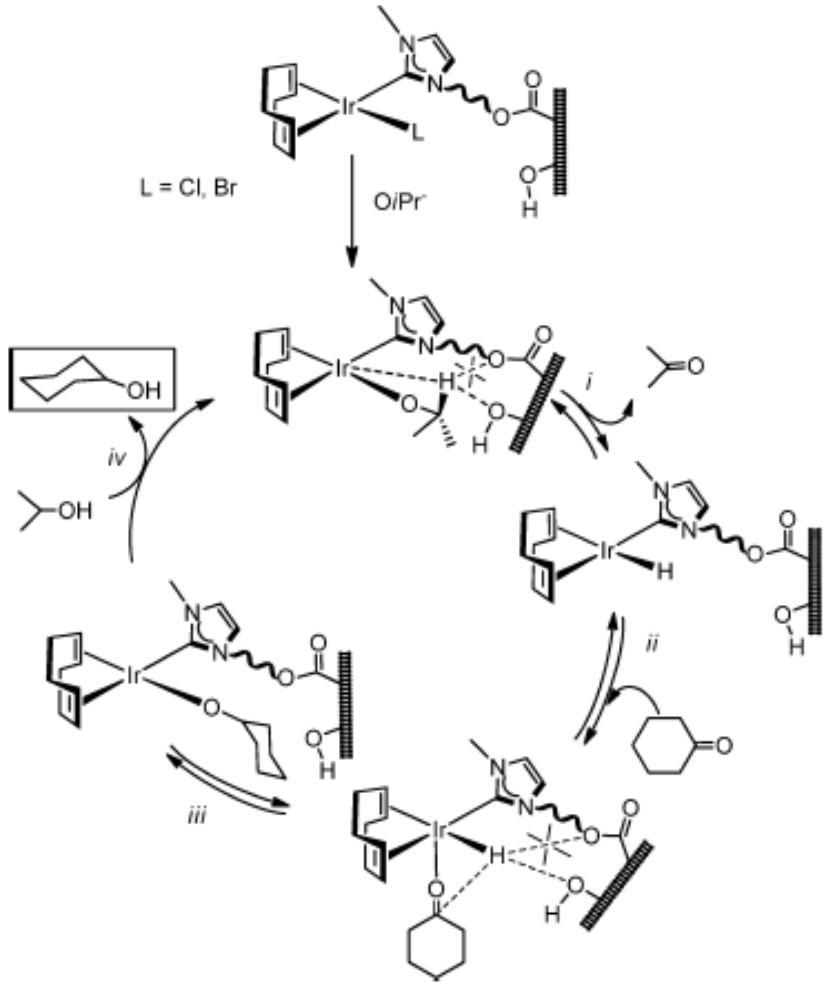

Figura 4.3 Propuesta de ciclo catalítico empleando soportes de carbono

Finalmente, en claro contraste con las muestras homogéneas, los catalizadores soportados fueron reciclados obteniendo conversiones similares en los mismos tiempos tras cinco ciclos catalíticos consecutivos sin añadir precursor de catalizador fresco. Además, se demostró su estabilidad al aire al realizar el quinto ciclo sin atmósfera protectora ya que no se detectó pérdida alguna de actividad.

ACS Catalysis
Research Article
pubs.acs.org/acscatalysis

Enhanced Hydrogen-Transfer Catalytic Activity of Iridium N-Heterocyclic Carbenes by Covalent Attachment on Carbon Nanotubes

Matías Blanco,[†] Patricia Álvarez,[†] Clara Blanco,[†] M. Victoria Jiménez,[‡] Javier Fernandez-Tornos,[‡] Jesús J. Pérez-Torrente,[‡] Luis A. Oro,[‡] Rosa Menéndez[†]

† Instituto Nacional del Carbón INCAR-CSIC. 33011, Oviedo, Spain
‡ Departamento de Química Inorgánica, Instituto de Síntesis Química y Catalisis Homogenea-ISQCH, Universidad de Zaragoza-C.S.I.C., 50009-Zaragoza, Spain

Supporting Information

ABSTRACT: Oxidized multiwall carbon nanotubes (CNT) were covalently modified with appropriate hydroxyl-ending imidazolium salts using their carboxylic acid groups. Characterization of the imidazolium-modified samples through typical solid characterization techniques, such as TGA or XPS, allows for the determination of 16 wt % in **CNT-1** and 31 wt % in **CNT-2** as the amount of the imidazolic fragments in the carbon nanotubes. The imidazolium-functionalized materials were used to prepare nanohybrid materials containing iridium N-heterocyclic carbene (NHC)-type organometallic complexes with efficiencies as high as 95%. The nanotube-supported iridium−NHC materials were active in the heterogeneous iridium-catalyzed hydrogen-transfer reduction of cyclohexanone to cyclohexanol with 2-propanol/KOH as hydrogen source. The iridium hybrid materials are more efficient than related homogeneous catalysts based on acetoxy-functionalized Ir−NHC complexes with initial TOFs up to 5550 h^{-1}. A good recyclability of the catalysts, without any loss of activity, and stability in air was observed.

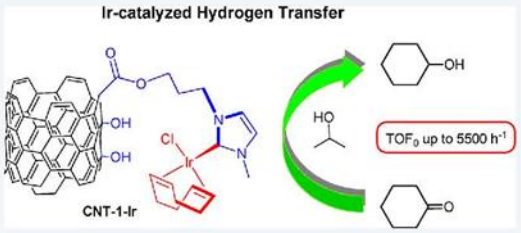

KEYWORDS: *carbon nanotubes, functionalization, iridium, transfer hydrogenation, confinement effect, heterogeneous catalysis*

INTRODUCTION

Carbon-based materials are one of the most versatile matrixes for developing heterogeneous catalysts with enhanced activity.[1] As a particular class within this type of carbon nanostructures, multiwall carbon nanotubes (CNTs) hold a number of inherent properties that make them attractive for catalytic applications. They have, for example, graphite-like walls and an adequate surface area, being more stable toward oxidation (about 650 °C) than activated carbon, and more reactive than graphite. Furthermore, they exhibit an excellent chemical stability (as they are inert in the majority of the reaction media) and also a controlled porosity. A wide range of functional

Received: January 30, 2013
Revised: March 26, 2013

dx.doi.org/10.1021/cs4000798 | ACS Catal. 2013, 3, 1307−1317

groups can be grafted onto these materials, and in addition, the presence of hollow channels gives rise to new physical properties (e.g., confinement effect).[2] Oxidation is undoubtedly the most common and simplest method to anchor molecular catalysts onto nanotubes and carbon fibers.[3] The oxidation of the nanotubes can be achieved through multiple oxidative agents (air, plasma, electrochemical methods, redox agents, etc.)[4] although it is the use of oxidizing acids, such as nitric and sulphuric acid,[5] which generates a large amount of oxygenated functional groups at the walls (mainly hydroxyl groups) and the tips (mainly carboxylic groups) of the nanotubes without seriously affecting their structure. Thus, by this way it is possible to support platinum, palladium, or gold nanoparticles[6,7] or organometallic complexes, such as the Wilkinson catalyst,[8] on carbon nanotubes. In spite of the successful chemistry of carbon nanotubes with covalent functionalization and the observed mild operating conditions of the catalytic systems based on molecular compounds, there are only a few examples described in the literature.[9]

N-Heterocyclic carbenes (NHC)[10] have recently attracted widespread attention in homogeneous catalysis since they can be used to generate active and stable organometallic complexes.[11] In addition, their tunable character allows for the control of the sterical and electronic properties at the metal center. Additionally, the catalytic activity of the organometallic compounds can be improved by using a carbonaceous support. A good strategy for anchoring NHC ligand precursors on the carbon materials consists of generating ester or amide bonds between the carbon material and the imidazolium ligand using the rich, oxygenated surface chemistry of oxidized carbon nanotubes.[12] In this context, it is worth mentioning that free carbenes have been used as anchor points at CNT side walls.[13]

The hydrogen transfer process is a good strategy for promoting the reduction of C=O and C=N bonds to generate alcohols or amines under mild conditions that avoids the use of hydrogen gas or other dangerous reducing agents.[14,15] Efficient rhodium and iridium hydrogen transfer catalysts are mainly based both on phosphine and N-donor ligands,[14] although NHC ligands have also been applied to the design of hydrogen

transfer catalysts. It has been found that, in contrast to phosphine-based catalysts, iridium−NHC complexes are more active in the reduction of a wide range of unsaturated compounds, such as aldehydes, ketones, or even imines, than their Rh−NHC analogues. Recently, a number of highly efficient iridium−NHC catalysts have been reported.[16] In particular, iridium(I) complexes with hemilabile O- and N-donor functionalized NHC ligands, with methoxy, dimethylamino, and pyridine as donor functions, are efficient catalyst precursors for the transfer hydrogenation of unsaturated compounds in 2-propanol/KOH.[17] However, to the best of our knowledge, there are no reports about the covalent immobilization of iridium complexes on solid supports, in particular, carbon nanotubes, and their application as heterogeneous catalysts in hydrogen transfer. The covalent attachment could improve the activity of the catalysts by permitting the easy recovery and subsequent recyclability of the catalysts.[18]

In this work, the covalent functionalization of oxidized carbon nanotubes with appropriate imidazolium salts is described. To this end, the carboxylic acids were used to form a covalent linkage with the ending OH functional group present in the imidazolium salt. In a second step, the nanotube pendant imidazolium functional groups were employed to generate the corresponding NHC-carbene complexes by reaction with the iridium organometallic compound. $[Ir(\mu\text{-}OMe)(cod)]_2$. The catalytic activity of the supported catalysts in the hydrogen transfer reduction of cyclohexanone to cyclohexanol was studied over five consecutive cycles, the last one in air atmosphere in order to determine the reusability and stability of the supported catalyst. Finally, a comparative study with related homogeneous catalysts is also reported.

RESULTS AND DISCUSSION

Characterization of Parent and Functionalized Supports. The carbon nanotubes used in this work were prepared by acid treatment of commercial CVD multiwalled nanotubes (Raw CNT), giving rise to the CNT sample. According to the TEM observations (Figure 1), the CNTs are 200−600 nm long and exhibit heterogeneous distributions of inner and outer diameters with average values of 6 and 12 nm, respectively. Due to the acid treatment to which the CNT samples were subjected, these

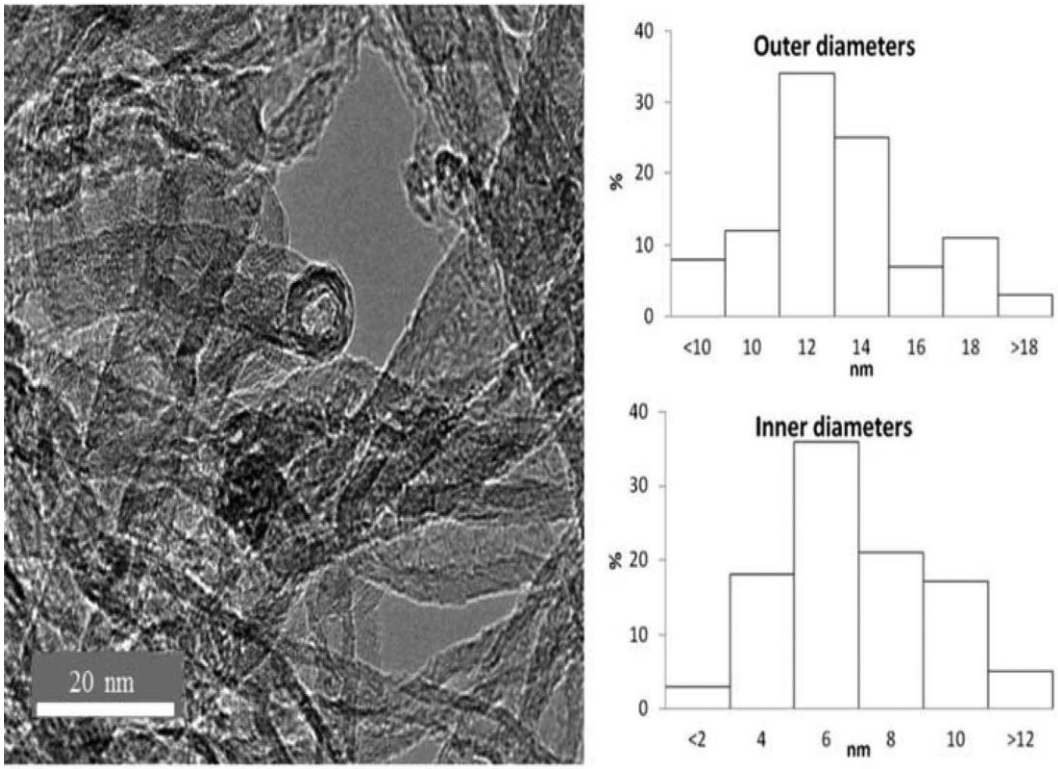

Figure 1. HRTEM image of the oxidized CNT with their (inner and outer) diameter distributions.

were free of amorphous carbon and catalyst particles which were confirmed by EDX spectroscopy and TG analysis (see Supporting Information).[19] Both ends of their tips are open, making the inner cavity of the tubes accessible. This was confirmed by the nitrogen adsorption isotherm (see Supporting Information) which evidenced a small hysteresis loop related to the presence of samples with both ends of the tubes open.[20] From these data a mesopore volume content of 0.32 cm^3 g^{-1} was calculated (V_p, Table 1) with no microporosity detected. The calculated surface BET area (S_{BET}) was 54 m^2 g^{-1}. These data are in accordance with the features expected for acid-treated nanotubes.[20]

The Raman spectra (see Supporting Information) showed an increment of the I_D/I_G ratio after the acid treatment, from 1.104 in raw CNT to 1.178 in **CNT**, which is consistent with the appearance of defects (i.e., C−O bond formation) during oxidation treatment.

Table 1. XPS, Elemental Analysis, Surface Area (S_{BET}), and Volume Pore (V_p) of the Functionalized CNT Samples

Sample	C/O[a]	N1s[b]	%N[c]	Csp[2] [d] 284.4[e]	Csp[3] [d] 285.5[e]	C-O[d] 285.5[e]	C=O[d] 286.5	COOH[d] 288.5[e]	OCOO[d] 290.0e	S_{BET}[f]	V_p[g]
Raw-CNT	130			72.8	10.5	8.2	3.9	2.5	1.5	210	2.29
CNT	3	0.4	0.1	64.4	17.1	7.0	3.2	5.4	2.8	54	0.32
CNT-1	6	1.1	1.4	60.3	16.7	9.6	4.5	3.7	5.2	57	0.62
CNT-2	5	1.9	2.1	58.3	16.1	11.9	4.8	2.3	6.9	86	0.69

[a]Carbon/oxygen atomic ratio. [b]Atomic percentage. [c]Determined by elemental analysis. [d]Deconvolution bands of the XPS C1s peak. [e]Data expressed in eV. [f]$m^2\ g^{-1}$. [g]$cm^3\ g^{-1}$.

The amount of the functional groups introduced at the walls of the tubes during the acid oxidation can be estimated by means of X-ray photoelectron spectroscopy (XPS). The XPS general spectrum of the CNT sample (Table 1) reveals the presence of oxygen at the external surface of the nanotubes in an atomic C/O ratio of 3, which agrees with the oxygen content of oxidized nanotubes reported in the literature.[21] Analysis of the high-resolution C1s peak[22] indicates that the oxygen is mainly in the form of C−O and C=O (7.0 and 3.2%, respectively), with a carboxylic acid group content of 5.4%. Due to steric hindrance, it is to be expected that the acid groups will be located at the edges of the tubes or in defects formed during the acid treatment.21 Additionally, temperature programmed desorption (TPD) experiments (see Supporting Information) corroborate the presence of oxygenated functional groups in the carbon nanomaterial in the form of 4.68 mmol g^{-1} of desorbed CO_2 and 4.21 mmol g^{-1} of desorbed CO. Deconvolution of the CO_2 and CO curves[23] allowed assignment of 3.81 mmol g^{-1} to carboxylic acid groups.

In order to achieve covalent linkage to organometallic compounds, carbon nanotubes were functionalized with specific imidazolium ligands containing OH-ending groups in the sequence depicted in Scheme 1. As can be seen, the carboxylic groups were initially converted into acid chlorides by reaction with thionyl chloride. These acid chloride groups were subsequently reacted with the

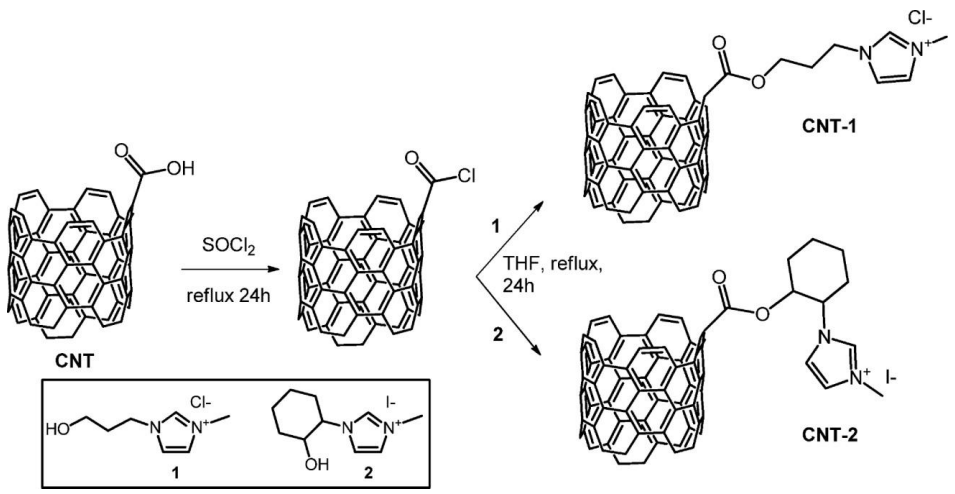

Scheme 1. Covalent Functionalization of the Parent Carbon Nanotubes with Imidazolium Salts

imidazolium ligands 1 and 2 through their OH functions. The imidazolium salt, 1-(3- hydroxypropyl)-3-methyl-1H-imidazol-3-ium chloride, [MeImH(CH2)3OH]Cl (**1**), was synthesized by treating methylimidazole with 3-chloropropan-1-ol as described recently by Doumèche.[24] 1-(2-Hydroxycyclohexyl)-3-methyl - 1H-imidazol-3-ium iodide, [MeImH(1-cyclohexyl-2-ol)]I (**2**), was synthesized by treating oxabicyclo[4.1.0]heptane with imidazole followed by reaction with methyl iodide in accordance with the procedure of Thiel.[25] Both imidazolium salts were isolated as off-white solids in good yields and fully characterized by NMR.

This two-step procedure gave rise to the functionalized carbon nanotubes **CNT-1** and **CNT-2**. The ^{1}H NMR in deuterated acetone, where both **CNT-1** and **CNT-2** are slightly soluble, confirmed the successful esterification with the imidazolium salts. The signals corresponding to the imidazolic OH groups were not detected in the spectra, but it was possible to recognize those corresponding to the imidazolium groups. Particularly, the upfield shifted signals of the characteristic H of imidazolium rings (H2), were observed at δ 8.66 and 8.65 ppm for **CNT-1** and **CNT-2**, respectively. The signals for the olefinic protons in the rings were also observed at δ 7.40 and

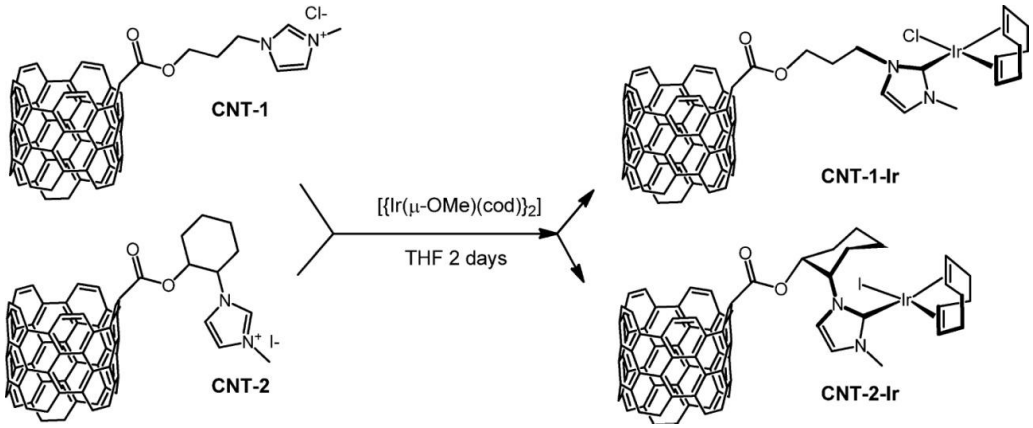

Scheme 2. Synthesis of NHC−Iridium Complexes Anchored on the Carbon Nanotubes

7.38 ppm, respectively, with the expected 2:1 ratio compared to imidazolium H (see Supporting Information for details). All these data clearly indicate the linkage of the imidazolium group to the CNT material, as was the case for the amide functionalized carbon nanotubes.[26]

Elemental analysis of the nanotubes indicated an increment in the nitrogen content from 0.1% for the parent CNT to 1.4% for **CNT-1** and 2.1% for **CNT-2**, which is consistent with the linkage of the imidazolium (N-containing) ligand. The higher value obtained in the case of **CNT-2** can be attributed to the presence of a secondary alcohol in 2 which is thermodynamically more reactive toward esterification than the primary alcohol function in 1. An alternative way of quantification for the amount of linked imidazolium salt is the determination by means of thermogravimetric analysis (TGA, Supporting Information). The weight loss at 400 °C (16 wt % for **CNT-1** and 31 wt % for **CNT-2**) corresponds to the whole imidazolium fragment.[26] An estimation of the molar percentage with respect to the carbon can also be calculated by taking into account the molecular weight of the imidazolium fragment.[27] Thus, the values obtained were 1.03 mole % for **CNT-1** and 1.27 mole % for **CNT-2**, which are also in accordance with the elemental analysis.

By means of XPS (Table 1), an increment in the atomic nitrogen percentage with respect to the parent CNT (from 0.4% in CNT up to 1.1%

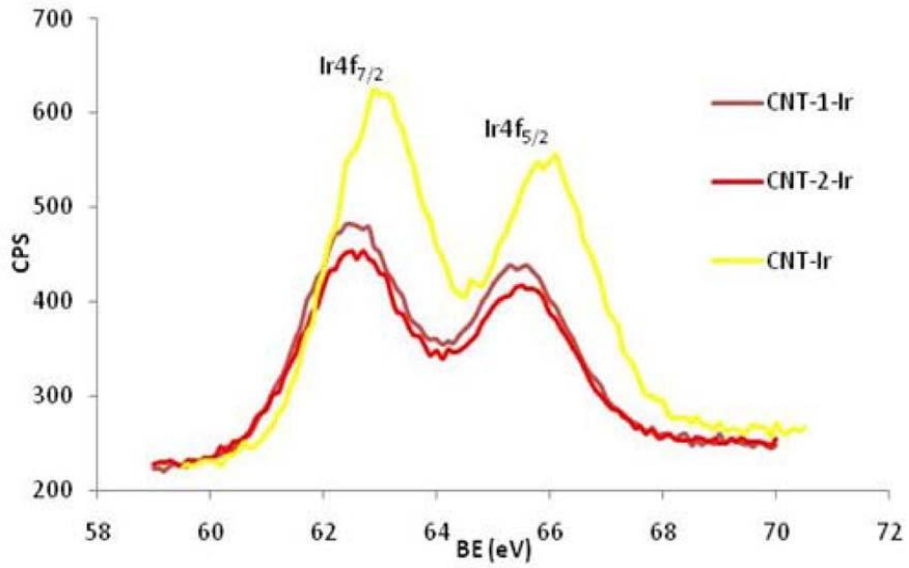

Figure 2. XPS spectra for the Ir4f core level of the hybrid catalysts

in **CNT-1** and 1.9% in **CNT-2**) was also observed and ascribed to the imidazolic fragments. These results suggest that imidazolium nitrogen atoms in the samples could be located on the external surface of the tubes. However, from a comparison with the elemental analysis data, which are representative of the total amount of nitrogen present in the sample, it is suggested that the increment in the nitrogen content detected by elemental analysis is indicative of the presence of anchored imidazolium salts in the inner cavity of the tubes. Deconvolution of the high-resolution C1s peak (Table 1) of the materials revealed the increase in the binding energy of the C−O band at 285.5 eV, which is attributed to the C−N moieties of the imidazolium ring overlapping this band. Also in support of this argument is the decrease in the COOH peak in favor of functional groups at higher binding energies, which is associated with transformation of the acids into ester moieties due to linkage with the imidazolium ligand.

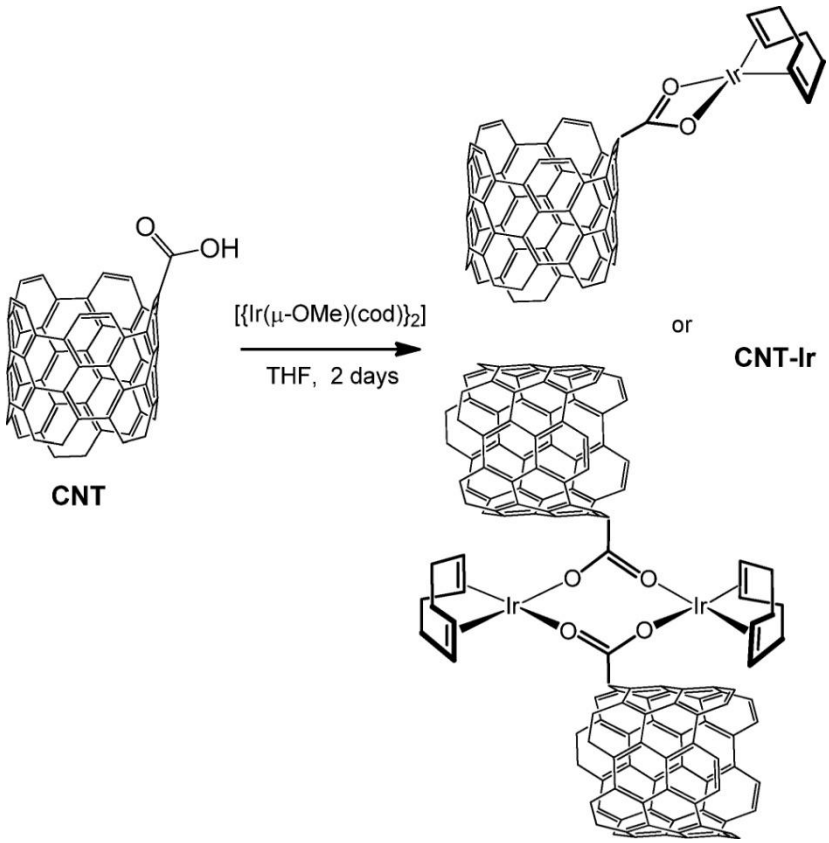

Scheme 3. Possible Anchoring Modes of Ir(I)-cod Fragment through the Carboxylic Groups in **CNT-Ir**

Finally, TEM observation of **CNT-1** and **CNT-2** samples confirms that the length and diameter of the nanotubes were not modified during the functionalization process (images in the Supporting Information).

Synthesis and Characterization of Iridium Hybrid Catalysts. The deprotonation of the 2-carbon in the imidazolium heterocycle is required for the synthesis of NHC-carbene complexes.[28] In this context, OH-functionalized imidazolium salts have proven to be useful precursors for the preparation of OH-functionalized metal−NHC complexes through well-established synthetic methodologies,[29] In this way, the imidazolium-functionalized nanotubes samples **CNT-1** and **CNT-2** were reacted with the iridium(I) dimer compound $[Ir(\mu\text{-}OMe)(cod)]_2$ (cod =1,5-cyclooctadiene) to produce the hybrid

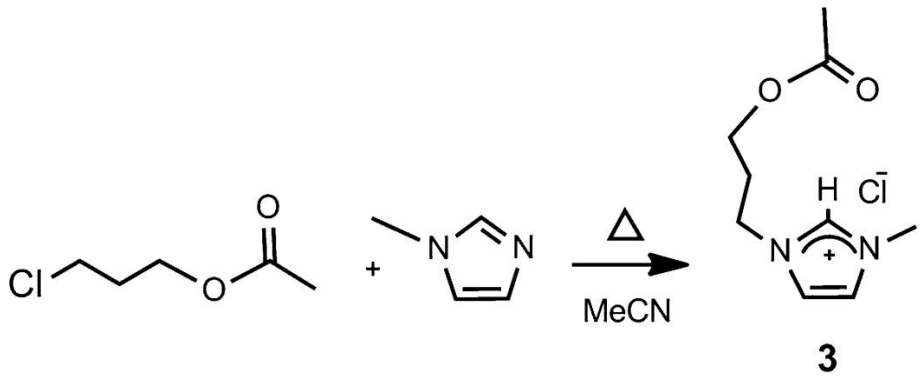

Scheme 4 Synthesis of the Imidazolium Salt [MeImH$(CH_2)_3OCOCH_3$]Cl (**3**)

catalysts **CNT-1-Ir** and **CNT-2-Ir** (Scheme 2). The deprotonation of the imidazolium salts linked to the CNTs by the methoxo ligands generated free carbene ligands that were trapped by the metal fragment "Ir(cod)" which completes the coordination sphere with the corresponding counterion (X = Cl, I). Insoluble materials were obtained in both cases, probably as a consequence of the increment in the molecular weight of the samples, which makes them completely insoluble in the reaction media. In fact, these materials were no longer soluble in polar media, which precludes NMR characterization. Although there is no direct evidence, it is thought that the coordination of the iridium complex to the functionalized nanomaterials was achieved through the carbene atom of the heterocycle moiety in a way similar to that of the Ir−NHC homogeneous catalysts. For comparative purposes, the reaction of parent CNT with $[Ir(\mu\text{- OMe})(cod)]_2$ was also studied, which led to the formation of the sample **CNT-Ir** (Scheme 3).

The amount of iridium in the hybrid catalyst was determined by means of ICP-MS measurements. The calculated values were 10.1 wt % for **CNT-1-Ir** and 12.2 wt % for **CNT-2-Ir**. The maximum amount of iridium that can be loaded can also be estimated on the basis of half of the amount of nitrogen introduced into each nanotube sample (two nitrogen atoms per NHC-carbene ring), which are 10.5 and 13.1 wt %, for **CNT-1-Ir** and **CNT-2-Ir**, respectively. From a comparison for the two sets of data it can be concluded that, in both cases, more than 95% of the imidazolium ligands are coordinated to iridium.

The sample without NHC-carbene imidazolium linkers, **CNT-Ir**, gave 21 wt% of iridium. Since the amount of nitrogen both before and after the treatment with the methoxo iridium complex is negligible, it is evident that the attachment of the iridium to the nanotube should be different to that found in samples **CNT-1-Ir** and **CNT-2-Ir**. This was corroborated by an analysis of the Ir4f XPS peak of the three samples (Figure 2). The spectra show two characteristic peaks, the $Ir4f_{7/2}$ peak centered at 62.4 eV and the $Ir4f_{5/2}$ peak centered at 65.6 eV for both **CNT-1-Ir** and **CNT-2-Ir** which are typical of Ir(I) compounds.[30] However, in the sample without NHC linkers, CNT-Ir, the maxima is shifted toward higher voltages at 63.0 and 66.1 eV for $Ir4f_{7/2}$ and $Ir4f_{5/2}$, respectively. This fact could be indicative of the presence of iridium in an upper oxidation state as some iridium oxide,[31] but the presence of very different iridium species, as for example iridium nanoparticles,[32] carboxylate-complexes[33] (Scheme 3), or even small di- or triorganometallic clusters,[34] cannot be ruled out. In this context, nickel and iron NPs have been revealed as efficient catalysts for the transfer hydrogenation of ketones.[35] However, to the best of our knowledge, there are no reports on the application of Ir-based NPs in catalytic hydrogen transfer reactions.

Figure 3 shows the HRTEM and HAADF-STEM images obtained for **CNT-1-Ir**. Similar results were obtained for **CNT-2-Ir** (not shown). A first analysis of the samples (and confirmed by EDX, see Supporting Information) reveals the presence of supported iridium catalyst homogeneously distributed at the surface of the nanotubes. Furthermore, some electron-dense regions were detected in the inner cavity of the tubes, which would indicate an inner attachment of the organometallic compound. Iridium species with diameters as low as 0.17−0.27 nm are observed which, according to other authors,[36] could be attributed to the presence of molecular iridium complexes anchored on the surface. The images also show the presence of greater electron-dense regions (1.2−1.4 nm) formed probably as a consequence of the beam damage, which caused migration of the Ir atoms (possibly facilitated by the flexible linkers), formation of iridium clusters, and even subsequent breakup of the resultant clusters into smaller iridium nanoparticles.[37] In fact, electron-dense regions with average sizes of 1.2 nm were also observed

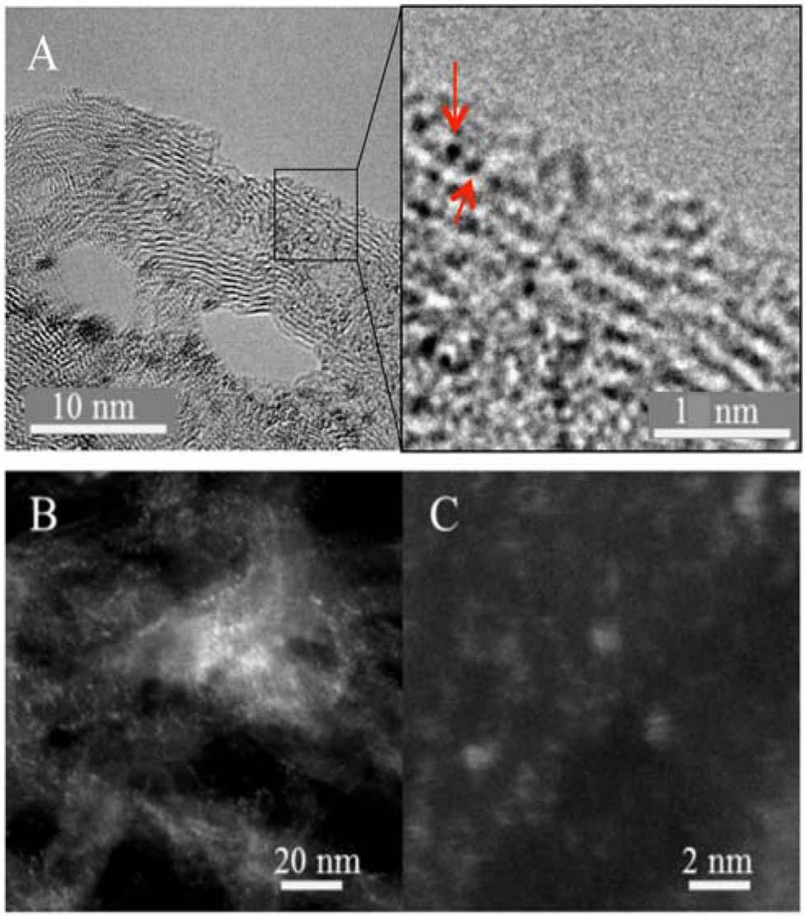

Figure 3. HRTEM (a) and HAADF-STEM (b and c) images of **CNT- 1-Ir**.

when dilute samples of the homogeneous iridium analogues, $[Ir(\mu\text{-}OMe)(cod)]_2$ and complex **5** (see below), are evaporated on a carbon grid and then imaged under the same conditions, due to similar electron beam damages (see Supporting Information). These data are in accordance with the XPS data previously described for those materials.

Synthesis and Characterization of Acetoxy-Functionalized Ir (I)−NHC Complexes. Homogeneous catalysts related to the iridium hybrid materials containing NHC ligands functionalized with an ester group were synthesized in order to contrast their catalytic activity. Following the general procedures for the preparation of imidazolium salts,

3-(3- acetoxypropyl)- 1-methyl-1H-imidazol-3-ium chloride, [MeImH$(CH_2)_3OCOCH_3$]Cl (**3**), was synthesized by reacting methyl imidazole with 3-chloropropylacetate in acetonitrile at 90 °C for 3 days (Scheme 4). The colorless oil obtained was characterized by high- resolution mass spectrometry (ESI-HRMS), ^{1}H and ^{13}C{^{1}H} NMR spectroscopy. The characteristic NC*H*N resonance of the imidazolium ring was observed at 9.03 ppm in the ^{1}H NMR. The acetoxy group was observed at 2.04 ppm in the ^{1}H and at 172.53 and 20.73 in the ^{13}C{^{1}H} NMR spectra.

The imidazolium salt 1-[trans-2-acetoxycyclohex-1-yl]-3-methyl-1H-imidazol-3-ium iodide, [MeImH-(cyclohexylacetate)]I (**4**), was prepared by ring-opening of epoxycyclohexane with imidazole together with acylation to isopropenylacetate followed by alkylation with CH_3I.[25,38]

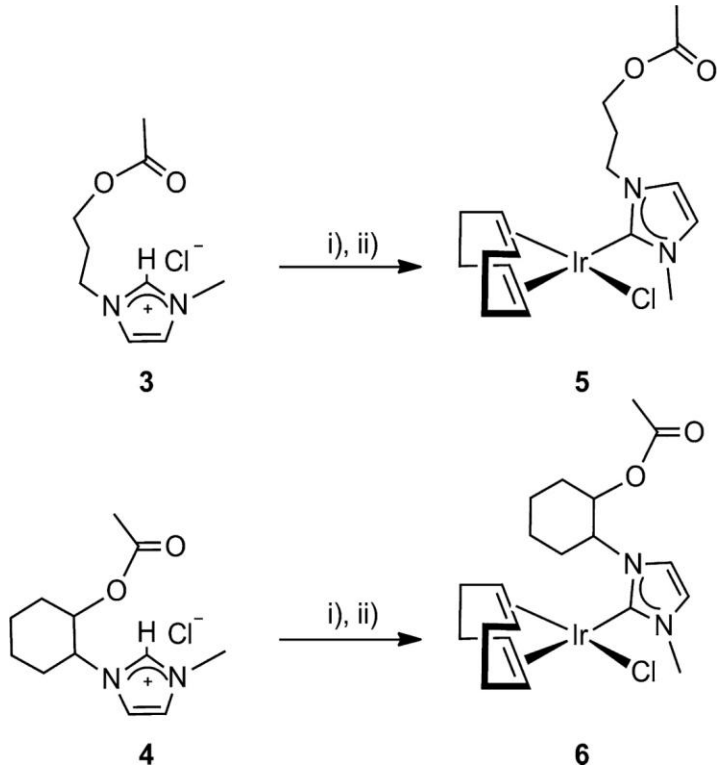

Reagents and conditions: i) Ag_2O, CH_2Cl_2, 48 h, 298 K; ii) ½ [{Ir(μ-Cl)cod)}$_2$] in acetone, 298 K.

Scheme 5 Synthesis of Complexes [IrCl(cod)(MeIm$(CH_2)_3OCOCH_3$] (**5**) and [IrCl(cod)(MeIm-(cyclohexyl-OCOCH$_3$)] (**6**)

Complexes [IrCl(cod)(MeIm$(CH_2)_3OCOCH_3$] (**5**) and [IrCl(cod)(MeIm(cyclohexyl-$OCOCH_3$)] (**6**) were prepared from **3** and **4**, respectively, following a two-step procedure. First, the corresponding imidazolium salt was treated with Ag_2O to give a solution of NHC−Ag complex. Then, the concentrated solutions obtained after elimination of the excess of silver oxide were reacted with 0.5 equiv of $[\{Ir(\mu\text{-}Cl)(cod)\}_2]$ dissolved in acetone at room temperature to give the new Ir(I)−NHC complexes which were isolated as yellow solids with good yields (Scheme 5).

Compounds **5** and **6** were characterized by elemental analysis, mass spectrometry (MALDI-TOF), and NMR spectroscopy. The ^{1}H NMR spectra showed no resonances attributable to the NCHN proton, which confirms the deprotonation of the imidazolium fragment. The coordination of the carbene to the iridium center becomes evident in the $^{13}C\{^1H\}$ NMR spectra which exhibit the characteristic upfield resonance for the carbenic carbon atom at 180.89 ppm (**5**) and 180.64 ppm (**6**). These chemical shifts lie in the usual range for related Ir(I)−NHC complexes.[39] In accordance with the proposed structure, the NMR spectra of the complexes showed four resonances for the =C*H* olefinic protons of the 1,5-cyclooctadiene ligand, both in the ^{1}H and in the $^{13}C\{^1H\}$ NMR spectra. This observation is in agreement with the existence of different ligands in *trans* positions and is indicative of the lack of an effective symmetry plane in the molecules probably as a result of the hindered rotation[40] around the carbene−iridium bond due to the effect of substituents in the NHC ligand. On the other hand, the complexes are neutral as was evidenced by the conductivity measurements in acetone which confirm the coordination of the chloro ligand in both complexes.

Table 2. Catalytic Hydrogen Transfer from 2-Propanol to Cyclohexanone with Iridium Acetoxy-Functionalized Iridium(I)−NHC Complexes and Iridium Hybrid Catalysts[a,b]

Entry	Catalyst	Time (min)	Conversion (%)	TON	TOF_0 (h^{-1})	TOF_{50} (h^{-1})
1	**5**	210	94	941	4680	2500
2	**6**	270	92	924	2292	1579
3	**7**	230	95	952	3020	2000
4	**CNT-1-Ir**	80	94	943	5550	3750
5	**CNT-2-Ir**	130	93	932	2540	1200
6	**CNT-Ir**	180	10	101	30	-
7	**CNT-2**	180	0	-	-	-

[a]Reaction conditions: catalyst/substrate/KOH ratio of 1/1000/5, $[catalyst]^0 = 1 \times 10^{-3}$ M in 2-propanol at 80 °C. [b]The reactions were monitored by GC using mesitylene as internal standard.

Catalytic Activity and Recycling. The iridium hybrid catalysts **CNT-1-Ir** and **CNT-2-Ir** and related homogeneous catalysts **5** and **6** were tested as catalyst precursors for the reduction of cyclohexanone to cyclohexanol using 2-propanol as hydrogen source (eq 1, catalytic reaction conditions for transfer hydrogenation of cyclohexanone with 2-propanol). The utilized reaction conditions were those previously optimized for hydrogen transfer processes involving several unsaturated substrates, including cyclohexanone, catalyzed by [IrBr(cod)-(MeIm(2-methoxybenzyl))].[17] Also, 2-propanol was used as hydrogen source because of its nontoxic nature with a moderate boiling point, being at the same time the reaction solvent. Standard catalyst loads of 0.1 mol %, with 0.5 mol % of KOH as cocatalyst, and at 80 °C were routinely employed.

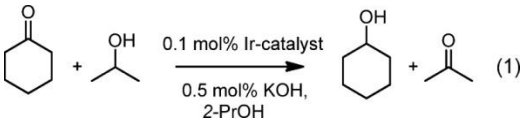

(1)

The reaction times required to reach conversions over 90% (as determined by GC using mesitylene as internal standard) and the average turnover frequencies (TOF), calculated at the

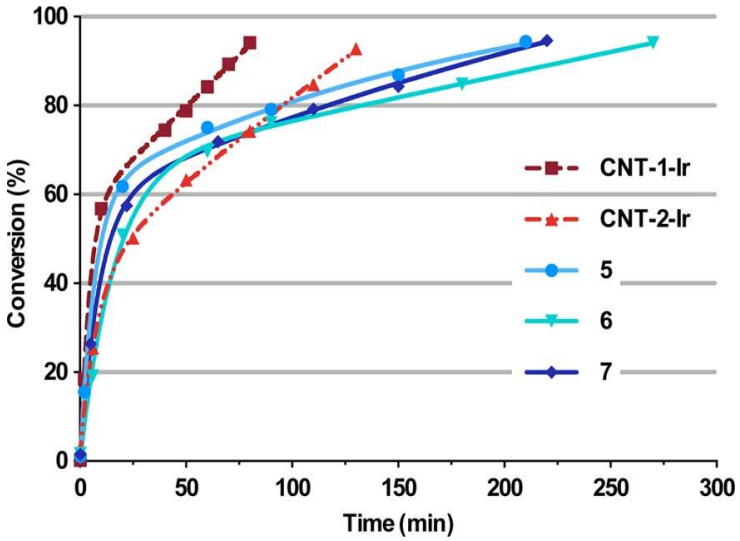

Figure 4. Reaction profiles for transfer hydrogenation of cyclohexanone by homogeneous and heterogeneous catalysts.

initial time and at 50% conversion, for all the examined catalysts are shown in Table 2. The results of the tests were compared with those obtained from two blank experiments. As the first blank, we used **CNT-Ir** as catalyst which contains no NHC carbene linker between the carbon material and iridium. As can be observed in Table 2 (entry 6) only 10% conversion was achieved after 3 h of reaction. Thus, catalysts without an Ir− NHC core have a poor balance. The second blank tested was the carbon material **CNT-2**, i.e. CNT functionalized with the imidazolium salt 2 but without iridium. The reaction under these conditions led to 0% conversion after 3 h (Table 2, entry 7). These results illustrate the activity of iridium complexes in hydrogen transfer reactions[14] and, in particular, the outstanding efficiency of the NHC-based iridium catalysts. In addition, the influence of the acetoxy group on the functionalized NHC carbene iridium complexes **5** and **6** was analyzed by contrasting their catalytic activity to that exhibited by the known complex [Ir(cod)(Me_2Im)I] (**7**) (Me_2Im = 1,3-dimethyl-imidazol-2- ylidene) with an unfunctionalized NHC ligand,[41] synthesized following the Herrmann method.[42]

Both the homogeneous and the supported iridium catalytic systems were found to be active in the transfer hydrogenation of cyclohexanone to cyclohexanol. In general, as can be observed in Table 2 (entries 1−2, and 4−5) heterogeneous catalysts **CNT-1-Ir** and **CNT-2-Ir** were more active than the corresponding homogeneous catalysts **5** and **6** which become evident from the required time to reach conversions over 90%. Interestingly, a 94% conversion in only 1.3 h was obtained using CNT-1-Ir as catalyst with an average TOF at 50% conversion of 3750 h^{-1}. In both series, the catalysts containing was detected, as cyclohexanone reduction was observed immediately after thermal equilibration of the reactant

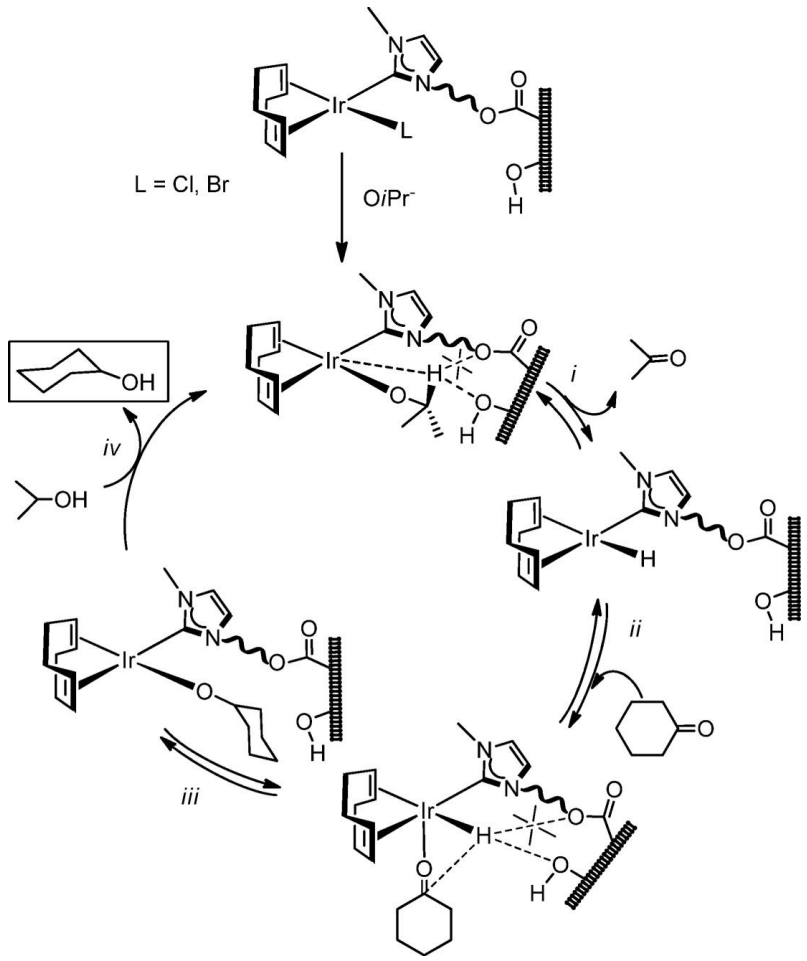

Scheme 6. Proposed Mechanism for the Catalytic Transfer Hydrogenation of Cyclohexanone by the Nanotube- Supported Iridium−NHC Catalysts

Table 3. Catalysts recyclability and stability study

Sample	**CNT-1-Ir**					**CNT-2-Ir**				
run	1	2	3	4	5[a]	1	2	3	4	5[a]
Time (min)	80	80	80	80	90	130	130	130	130	130
Conversión (%)	96	95	96	94	95	95	94	93	94	96

[a] Cycle performed in air

mixture. In general, the kinetic profiles are very similar for all the homogeneous and heterogeneous catalysts. However, the hybrid catalyst **CNT-1-Ir** is the most active species at any time, and even catalyst **CNT-2-Ir** is more active than the homogeneous systems for conversions over 70%. The lower catalytic activity exhibited by **CNT-2-Ir** could be related to steric hindrance caused by the rigid cyclohexylacetate linker to the nanotube walls, making more difficult the access of the cyclohexanone to the active center and also the release of cyclohexanol after reduction.

From the similarities observed between the catalytic reaction profiles, it can be inferred that the reaction mechanism does not change dramatically when the catalyst is supported. Thus, an inner-sphere transfer hydrogenation mechanism with a monohydride complex as active catalytic species can be expected, similar to that proposed for the transfer hydrogenation of unsaturated compounds in 2-propanol/KOH catalyzed by iridium(I) complexes having hemilabile O- and N-donor functionalized NHC ligands.[17] On the basis of this mechanism in homogeneous phase, the closely related mechanism depicted in Scheme 6 is proposed for the hybrid catalysts. The first step is the β-H elimination from the alkoxo complex [Ir(O^iPr)(cod)(NHC-OCO-CNT)] to generate the hydride intermediate [IrH(cod)(NHC-OCO-CNT)] with the concomitant formation of acetone (step i). The coordination of the cyclohexanone substrate to the unsaturated hydride complex (step ii) and the migratory insertion into the Ir−H bond (step iii) result in the formation of a new supported alkoxo complex. Finally, the protonation of the alkoxo ligand by 2-propanol (solvent) results in the formation of cyclohexanol regenerating the starting alkoxo supported complex in an alkoxide exchange reaction (step iv).

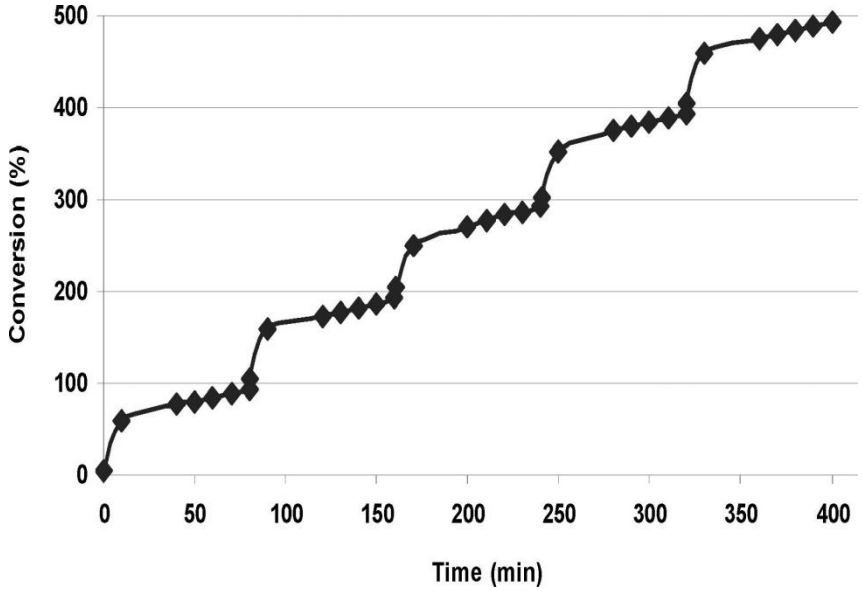

Figure 5. Time dependence of the transfer hydrogenation of cyclohexanone catalyzed by **CNT-1-Ir** in five consecutive runs. The fifth cycle was performed in air.

We have shown that the presence of a methoxy group on the functionalized NHC ligand in the homogeneous catalyst [Ir($NCCH_3$)(cod)(O-NHC)] (O-NHC = MeIm(2-methoxybenzyl) has an impact on catalytic activity which was associated, through experimental tests combined with DFT calculations, to weak interactions in the forward and backward hydrogen transfer from the hydride intermediate [IrH(cod)(O-NHC)] (hydride migration and β-H transfer).[17] The calculations showed an interaction between the β-H on the alkoxo ligand and the oxygen atom of the methoxy fragment of the NHC ligand, which resulted in a net destabilization of the alkoxo intermediate that facilitates the β-H elimination step in route to the key hydrido intermediate species.

The catalytic performance of catalysts **5** and **6** (having acetoxy-functionalized NHC ligands) that is comparable to that of **7** (with an unfunctionalized NHC ligand) is evidence that the acetoxy linker is not responsible for the superior catalytic activity of the supported catalysts. Thus, the enhanced catalytic activity observed for nanotube-supported iridium−NHC catalysts could be related to the influence of additional functionalities on the support. In this case, the −OH groups remaining on the nanotube walls could play the role of the methoxy function in the homogeneous systems, assisting for

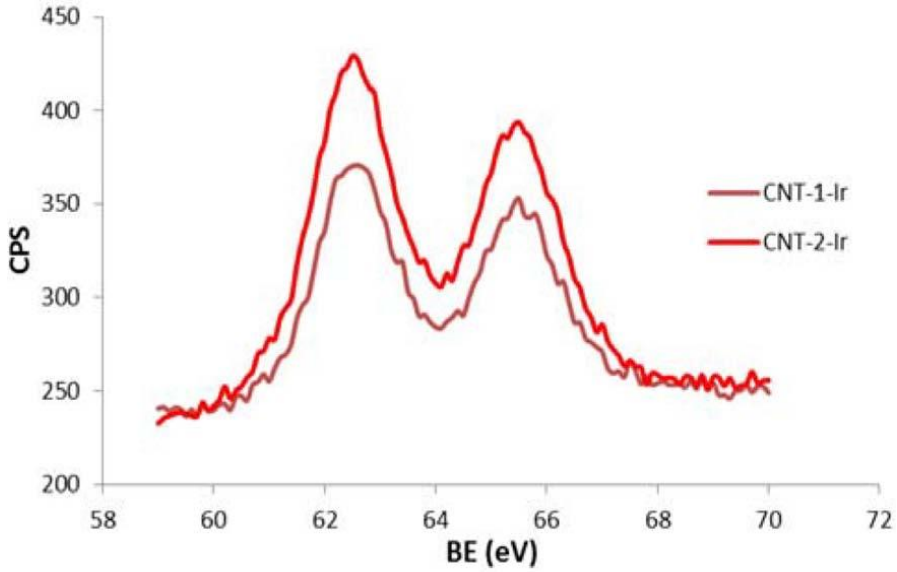

Figure 6. XPS Ir4f region of **CNT-1-Ir** and **CNT-2-Ir** after the catalytic cycles.

the key H-transfer involved both in the hydride migration and β-H transfer steps (Scheme 6). In this context, the flexibility of the linker should have an important effect, which is in agreement with the superior catalytic performance of **CNT-1-Ir**.

Recycling studies were carried out with both nanotube supported iridium−NHC catalysts. The black solids obtained after the catalysis were simply filtered and washed with fresh 2- propanol (4 × 5 mL) and then subjected to another catalytic cycle by addition of further cyclohexanone / KOH / i-PrOH. Interestingly, both supported catalysts exhibited catalytic activity the same as that of the fresh catalysts after four consecutive cycles under an argon atmosphere (Table 3, with comparable conversions after similar times and identical reaction profiles (Figure 5). Furthermore, in sharp contrast with the air-sensitivity of the iridium−NHC-based catalyst, these nanotube-supported catalysts were air stable. As it is shown in Table 3, quantitative conversion of cyclohexanone was also achieved when the catalytic reactions were conducted under an air atmosphere in an additional final fifth cycle. The reproducibility of the results and the recycling performance of the catalyst are illustrated in Figure 5 where the same profile feature was observed for every step, even in the catalytic run performed in air.

At the end of the catalysis runs, the physical state of our catalysts was examined. The XPS measurements of the postcatalysis samples (Figure 6) gave the same binding energy values on the $Ir4f_{7/2}$ and $Ir4f_{5/2}$ peaks than before the catalytic cycles. The results clearly suggest that the iridium complexes supported on the carbon nanotubes have not been modified in the hydrogen transfer process. Additionally, HRTEM images of samples **CNT-1-Ir** and **CNT-2-Ir** after the hydrogen transfer cycles (see Supporting Information) exhibit electron dense regions similar to those before the hydrogen transfer cycles.

CONCLUSIONS

We have demonstrated that the ester covalent functionalization of oxidized multiwalled carbon nanotubes with imidazolium salts can be achieved by using the surface carboxylic functional groups generated in the oxidizing acid treatment. The imidazolium-functionalized materials were used to prepare a nanohybrid catalyst containing iridium−NHC-carbene type organometallic complexes with very high efficiencies. The nanotube-supported iridium−NHC materials are efficient heterogeneous hydrogen transfer catalysts for the reduction of cyclohexanone to cyclohexanol using 2-propanol as hydrogen source. Interestingly, the iridium hybrid materials exhibit a more superior performance than related homogeneous catalysts based on acetoxy-functionalized NHC ligands giving almost complete conversions in shorter reaction times. Nevertheless, both types of catalysts present very similar reaction profiles that suggest a similar operating mechanism.

In addition, the heterogeneous catalysts remained stable through successive catalytic runs. This fact confirms that the supported catalyst can be reused in consecutive cycles without any loss of activity, even under an air atmosphere. The confinement effect, due to the porosity of the material, or a surface effect based on the potential cooperation of hydroxyl functional groups on the nanotube walls might explain the notable improvement observed in the catalytic activity.

EXPERIMENTAL SECTION

Scientific Equipment. Characterization of Supports and Hybrid Catalysts. NMR spectra were recorded on a Bruker

Advance 300 or a Bruker Advance 400 spectrometer: ^{1}H (300.1276 MHz, 400.1625 MHz) and ^{13}C (75.4792 MHz, 100.6127 MHz). NMR chemical shifts are reported in ppm relative to tetramethylsilane and referenced to partially deuterated solvent resonances. Coupling constants (*J*) are given in hertz. Spectral assignments were achieved by a combination of $^{1}H–^{1}H$ COSY, ^{13}C APT, and $^{1}H–^{13}C$ HSQC experiments. MALDI-TOF mass spectra were obtained on a Bruker MICROFLEX spectrometer using DCTB (trans-2-[3- (4-tert-butylphenyl)-2-methyl-2propenylidene]malononitrile) or DIT (Ditranol) as matrixes.[44] Electrospray mass spectra (ESI-MS) were recorded on a Bruker MicroTOF-Q using sodium formate as reference. Conductivities were measured in $\sim 5 \times 10^{-4}$ M acetone solutions of the complexes using a Philips PW 9501/01 conductimeter. The catalytic reactions were analyzed on an Agilent 4890 D system equipped with an HP-INNOWax capillary column (0.4 μm, 25 m × 0.2 mm i.d.) using mesitylene as internal standard.

Thermogravimetric analyses (TGA) of the materials were performed in a TA SDT 2960 analyzer thermobalance. The procedure was as follow: 5 mg of sample was heated in the thermobalance at 10 °C min^{-1} to 1000 °C using a nitrogen/air flow (1:1) of 200 mL min^{-1}. The molar percentage of imidazole introduced into the carbon nanomaterials can be estimated by quantifying, from the TGA profiles, the weight loss percentage in the range below 400 °C, according to the method described in the literature.[27] Transmission electron microscopy (TEM) was carried out on a JEOL 2000 EX-II instrument operating at 160 kV. High-resolution images of transmission electron microscopy HRTEM and high-angle annular dark-field HAADF-STEM images of the samples were obtained using a JEOL JEM-2100F transmission electron microscope, equipped with a field-emission-gun (FEG) operating at 200 kV. Energy dispersive X-ray spectroscopy (EDX) was used to verify the atomic composition of the catalyst. The samples were prepared by casting a few drops of 1 mg mL^{-1} ethanol suspensions of the samples over the carbon grids. To minimize exposure of the samples to the air, these were transferred to the lacey carbon grid into a glovebox filled with ultrahigh-purity argon and from the glovebox to the TEM holder to minimize the time required to introduce it into the microscope. The textural characteristics of the samples were

analyzed using N2 adsorption at 77 K. These analyses were performed on ASAP 2020 Micrometrics equipment using around 100 mg of sample in each experiment. Before the experiments, the samples were outgassed at 40 °C for 50 h under vacuum (pressure below 10^{-3} Pa) in order to avoid the desorption of functional groups or damaging the imidazolium salts or the complexes. The apparent surface area (S_{BET}) was determined from the N_2-adsorption isotherm using the BET equation in the range of P/P° between 0.05 and 0.245. The micropore volume was calculated by applying the Dubinin−Radushkevich equation to the N_2 adsorption isotherms,[46] and the total pore volume was obtained from N_2 adsorption when P/P° = 0.99. The volume of mesopores was calculated by subtracting the micropore volume from the total pore volume. Elemental analyses were performed on a LECO CHNS-932 microanalyzer and a LECO-VTF-900 furnace coupled to the microanalyzer. Temperature-programmed desorption (TPD) experiments were performed in a U-shaped quartz cell coupled to a mass spectrometer in order to determine the amount and type of oxygenated functionalities. A sample consisting of 50 mg was heated up to 1000 °C, at a heating rate of 5 °C min^{-1}, under a helium flow rate of 50 mL min^{-1}. The total amount of CO and CO_2 evolved was evaluated in a mass spectrometry analyzer. The X-ray photoemission spectroscopy (XPS) was performed in a SPECS system operating under a pressure of 10^{-7} Pa with a Mg Kα X-ray source. The type of functional groups in the carbon nanotubes was quantified by deconvolution of the high-resolution C1s XPS peak in Gaussian and Lorentzian functions.[47] The amount of iridium present in the samples was determined by means of inductively coupled plasma mass spectrometry (ICP-MS) in an Agilent 7700x instrument; the samples were digested following the method described by Elgrabi *et al.*;[48] briefly, 30 mg of sample was treated with 5 mL of a mixture of concentrated nitric and hydrochloric acids (3:1 ratio) at 180 °C for 3 h under microwave irradiation.

Raw Materials. The solvents were distilled immediately prior to use from the appropriate drying agents or obtained from a Solvent Purification System (Innovative Technologies). D_2O, $CDCl_3$, and acetone-d_6 were purchased from Euriso-top and used as received. All chemicals, including multiwall carbon nanotubes (MWCNT) were purchased from Aldrich, and reagent grade or better

quality was employed in all the experimental work. MeImH (N-methyl-imidazole) and cyclohexanone were distilled prior to use. Raw CVD-grown multiwall carbon nanotubes were oxidized by means of a mixture of sulphuric acid (97%) and nitric acid (60%) in a 3:1 ratio at 80 °C for 20 min, followed by 20 min of ultrasonication. The reaction was quenched with water, and then the mixture was centrifuged for 30 min at 4700 rpm. The supernatant was discarded, and the remaining solid was washed again with water and centrifuged. The process was repeated until neutral pH to give the parent oxidized carbon nanotubes (CNT).

The imidazolium salts, [MeImH(CH_2)$_3$OH]Cl (**1**)[24] and [MeImH(1-cyclohexyl-2-ol)]I (**2**),[25] and the starting organometallic compounds [{Ir(μ-OMe)(cod)}$_2$][49] were prepared according to the literature procedures.

Preparation of 3- (3-Acetoxypropyl) - 1 - methyl-1H-imidazol- 3-ium Chloride (3). 3-Chloropropylacetate (1.54 mL, 12.5 mmol) was added to a solution of N-methylimidazole (1.00 mL, 12.5 mmol) in acetonitrile (15 mL), and the mixture refluxed for 72 h. The colorless oil formed was separated by decantation, washed with n-hexane, and dried in vacuum. Yield: 83%. Anal. Calcd. for $C_9H_{15}ClN_2O_2$: C, 49.93; H, 6.91; N, 12.81. Found: C, 50.14; H 6.85; N, 12.90. ESI-HRMS (CH_3CN) m/z = 183.11 $[M]^+$. ^{1}H NMR (298 K, $CDCl_3$): δ = 9.03 (s, 1H, NC*H*N), 7.69 (d, *J* = 2.0, 1H, CH Im), 7.61 (d, *J* = 2.0, 1H, CH Im), 4.35 (t, *J* = 7.1, 2H, NCH_2), 4.14 (t, *J* = 5.9, 2H, OCH_2), 3.95 (s, 3H, NCH_3), 2.25 (m, 2H, CH_2), 2.04 (s, 3H, $OCCH_3$). ^{13}C{^{1}H} NMR (298 K, CDCl3): δ 172.53 (C=O), 136.87 (NC*H*N), 125.03 (CH Im), 123.76 (CH Im), 61.96 (OCH_2), 47.96 (NCH_2), 36.52 (NCH_3), 30.25 (CH_2), 20.70 (OCH_3).

Preparation of trans-2-(1H-imidazol-1-yl)cyclohexyl acetate. Synthesized from reaction of isopropenylacetate (6.0 mL, 54 mmol), trans-2-(1-imidazolyl)cyclohexanol (1.5 g, 9.0 mmol), and immobilized lipase B from Candida Antarctica (150 mg, Sigma-Aldrich) in 10 mL of $CHCl_3$. Yield: 56%. ^{1}H-NMR (298 K, CD_3Cl): δ = 7.50 (br, 1H, NCHN), 7.03 (t, *J* = 1.2, 1H, CH Im), 6.93 (t, *J* = 1.2, 1H, CH Im), 4.88 (m, 1H, NCH), 3.94 (m, 1H, OCH), 2.13 (m, 2H, CH_2), 1.87 (s, 3H, CH_3), 1.84 (m, 2H, CH_2), 1.50−1.35 (m, 4H, CH_2).

Preparation of 1-(2-Acetoxycyclohex-1-yl) - 3 - methyl- 1H-imidazol-3-ium Iodide (4). The compound was prepared following a procedure similar to that described by Thiel.[25] Thus, CH_3I (0.307 g, 2.16 mmol) was added to a solution of trans-2-(1H-imidazol-1-yl) cyclohexyl acetate (0.410 g, 1.97 mmol) in 15 mL of CH_3CN and refluxed overnight. After removing the solvent, the resulting white solid was recrystallized from 2-propanol at 0 °C. Yield: 85%. ^{1}H-NMR (298 K, CD_3Cl): δ 10.24 (s, 1H, NC*H*N), 7.38 (t, *J* = 1.8, 1H, CH Im), 7.33 (t, *J* = 1.8, 1H, CH Im), 4.95 (m, 1H, NCH), 4.52 (m, 1H, OCH), 4.15 (s, 3H, NCH_3), 2.40 (m, 1H, CH_2), 2.18 (m, 1H, CH_2), 1.98 (s, 3H, CH_3), 1.89 (m, 2H, CH_2), 1.62−1.40 (m, 4H, CH_2).

General Procedure for the Preparation of [IrCl(cod)-(MeImROCOCH3)] (R = -$(CH_2)_3$- (5); R = -C_6H_{10}- (6)). The iridium complexes containing acetoxy-functionalized NHC ligands were synthesized through the following two-step procedure. Step 1: A mixture of the imidazolium salts (0.611 mmol) and Ag_2O (0.116 g, 0.5 mmol) were refluxed in dichloromethane (20 mL) for 48 h. The excess of Ag_2O was removed by filtration to give a colorless solution of the NHC− silver complexes. Step 2: Suspensions of $[\{Ir(\mu\text{-}Cl)(cod)\}_2]$ (0.205 g, 0.305 mmol) in acetone (15 mL) were added to concentrated solutions of the previously obtained NHC−silver complexes in CH_2Cl_2 (1 mL). The mixtures were stirred for 24 h at room temperature to give brownish suspensions. The AgX formed was removed by filtration, and the resulting orange solutions obtained were evaporated to dryness under vacuum. The residue was treated with hexane several times to afford the compounds as brownish-yellow solids, which were separated by decantation and dried in vacuum.

[IrCl(cod)(MeIm(CH_2)$_3$OCOCH$_3$)] (5): Yield: 61 %. Anal. Calcd. $C_{17}H_{26}ClN_2O_2Ir$: C, 39.41; H, 5.06; N, 5.41. Found: C, 39.50; H, 5.11; N, 5,53. ^{1}H NMR (298 K, $CDCl_3$): δ 6.85 (d, *J* = 2.0, 1H, CH Im), 6.82 (d, *J* = 2.0, 1H, CH Im), 4.59 (m, 2H CH_2N, 1H CH cod), 4.32 (m, 1H, CH cod), 4.16 (m, 2H, CH_2O), 3.95 (s, 3H, CH_3 Im) 2.98, 2.84 (m, 1H, CH cod), 2.33 (m, 2H, CH_2 cod), 2.21 (m, 2H CH_2, 2H CH_2 cod), 2.10 (s, 3H, OCH_3) 1.81-1.56 (m, 4H, CH_2 cod). $^{13}C\{^1H\}$ NMR (298 K, $CDCl_3$): δ = 180.89 (NCN), 171.12 (OCO), 121.94, 120.37 (CH Im), 84.89, 84.60 (CH cod), 61.73 (CH_2N), 51.89, 51.30 (CH cod),

47.55 (CH_2O), 37.48 (CH_3 Im), 34.01, 33.44 (CH_2 cod), 30.38 (CH_2), 30.03, 29.31 (CH_2 cod), 21.10 (OCH_3). MS (MALDI-ToF, DIT matrix, CH_2Cl_2) *m/z* = 519.4 [M + H], 483.2 [M – Cl].

IrCl(cod)(MeIm(ciclohexil)OCOCH$_3$)] (6): Yield: 55 %. Anal. calcd. $C_{20}H_{30}ClIrN_2O_2$: C, 43.04; H, 5.42; N, 5.02. Found: C, 44.01; H, 5.98; N, 4.89. ^{1}H NMR (298 K, $CDCl_3$): δ 6.89 (d, *J* = 2.0, 1H, CH Im), 6.82 (d, *J* = 2.0, 1H, CH Im), 5.32 (m, 1H, CHO), 5.13 (m, 1H, CHN), 4.61 (br, 2H, CH cod), 3.96 (s, 3H, NCH_3), 3.34 (m, 1H, CH cod), 3.01 (m, 1H, CH cod), 2.25 (m, 4H CH_2, 4H cod), 1.90 (s, 3H, OCH_3), 1.81–1.42 (m, 4H CH_2, 4H cod). $^{13}C\{^1H\}$ NMR (298 K, $CDCl_3$): 180.64 (NCN), 170.22 (OCO), 122.17, 119.75 (CH Im), 84.28, 84.00 (CH cod), 73.11 (CHO), 62.77 (CHN), 51.61, 51.67 (CH cod), 37.61 (NCH_3), 33.86, 33.72, 33.56, 32.01 (CH_2), 29.88, 29.66, 24.90, 24.24 (CH_2 cod), 21.07 (OCH_3). MS (MALDI-ToF, DIT matrix, CH_2Cl_2) m/z = 558.3 [M], 523.3 [M – Cl].

Preparation of the Functionalized Nanotubes CNT-1 and CNT-2. The oxidized carbon nanotubes were functionalized with the imidazolium salts following a two-step procedure. First, 0.1 g of oxidized carbon nanotubes (CNT) was refluxed in 40 mL of thionyl chloride for 24 h under a nitrogen atmosphere. The resultant product was washed three times with 20 mL of anhydrous tetrahydrofuran (THF) and dried for 2 h under vacuum. Then, the solid was dispersed in 15 mL of anhydrous THF, and 70 mg of imidazolium salt, **1** or **2**, was added under a nitrogen atmosphere. The mixture was refluxed for 24 h. The solid was filtered, and washed with THF (3 × 20 mL), dichloromethane (3 × 20 mL), and ethanol (3 × 20 mL). The solids collected were dried at 100 °C in a preheated furnace. The samples obtained were labeled as **CNT- 1** for the imidazolium salt **1** and **CNT-2** for the imidazolium salt **2**.

Preparation of Hybrid Catalysts CNT-1-Ir and CNT-2- Ir. Functionalized carbon nanotubes (with 0.2 mmol of imidazolium salt estimated from the TGA analyses) were mixed with $[Ir(\mu\text{-}OMe)(cod)]_2$ (69.6 mg, 0.105 mmol) in 10 mL of THF under an argon atmosphere. The mixture was refluxed for 2 days and then immersed into an ultrasonic bath for 30 min. The resultant solid was recovered by centrifugation, washed with THF (5 × 10 mL) and diethyl ether (2 × 5 mL) and dried under vacuum.

General Procedure for Transfer Hydrogenation Catalysis. The catalytic transfer hydrogenation reactions were carried out under an argon atmosphere in thick glass reaction tubes fitted with a greaseless high-vacuum stopcock. In a typical experiment, the reactor was charged with a solution of cyclohexanone (0.52 mL, 5.0 mmol) in 2-propanol (4.5 mL), internal standard (mesitylene, 70 μL, 0.5 mmol), base (0.1 mL, 0.025 mmol of a KOH solution 0.24 N in 2-propanol) and the catalyst (0.005 mmol, 0.1 mol %). The weight of the supported catalysts used in each catalysis experiment was calculated according to the ICP measurements, assuming that all the iridium in the sample corresponds to active catalyst sites. In that way, 9.51 mg of **CNT-1-Ir** (10.1 wt % of iridium) and 7.88 mg of **CNT-2-Ir** (12.2 wt % of iridium) were added. The resulting mixture was stirred at room temperature until complete solution of the catalyst in the case of homogeneous catalyst or 10 min in the case of heterogeneous catalyst and then placed in a thermostatic oil bath at the required temperature, typically 80 °C. Conversions were determined by gas chromatography analysis under the following conditions: column temperature 35 °C (2 min) to 220 °C at 10 °C/min at flow rate of 1 mL/min using ultra pure He as carrier gas.

The material was recovered by centrifugation, once the reaction was completed, and washed with an additional amount of 2-propanol. Several catalytic cycles were performed with this material without adding any fresh catalyst precursor, and in the supported catalysts, at least the last one was carried out without inert atmosphere.

ASSOCIATED CONTENT

Supporting Information

Nitrogen adsorption isotherms, Apparent surface area and porevolume, Raman spectra, area ratio for the D and G bands, TPD profiles, TGA curves, TEM and HRTEM images, and ^{1}H NMR data. This material is available free of charge via the Internet at http://pubs.acs.org.

AUTHOR INFORMATION

Corresponding Author

*E-mail: par@incar.csic.es (P.Á.), vjimenez@unizar.es (M.V.J.).

Notes

The authors declare no competing financial interest.

ACKNOWLEDGMENTS

The authors thank MICINN (Projects Consolider Ingenio 2010 CSD2009-00050 and CTQ 2010-15221) and the Diputación General de Aragón (E07) for their financial support. P.Á. thanks MICINN for her Ramón y Cajal contract. J.F.-T. and M.B. acknowledge their fellowships from MICINN and MECD.

REFERENCES

(1) Schaetz, A.; Zeltner, M.; Stark, W. J. ACS Catal. 2012, 2, 1267−1284.

(2) Pan, X.; Bao, X. Acc. Chem. Res. 2011, 44, 553−562.

(3) Wildgoose, G. G.; Abiman, P.; Compton, R. G. J. Mater. Chem. 2009, 19, 4875−4886.

(4) Aqel, A.; Abou El-Nour, K. M. M.; Ammar, R. A. A.; Al-Warthan, A. Arab. J. Chem. 2012, 5, 1−23.

(5) Osorio, A. G.; Silveira, I. C. L.; Bueno, V. L.; Bergmann, C. P. Appl. Surf. Sci. 2008, 255, 2485−2489.

(6) Serp, P.; Castillejos, E. ChemCatChem 2010, 2, 41−47.

(7) Wang, Z.; Zhang, Q.; Kuehnera, D.; Xua, X.; Ivaska, A.; Niu, L. Carbon 2008, 46, 1687−1692.

(8) (a) Pérez-Cadenas, M.; Lemus-Yegres, L. J.; Román-Martínez, M. C.; Salinas-Martínez de Lecea, C. Appl. Catal. A 2011, 402, 132−138. (b) Lemus-Yegres, L. J.; Román-Martínez, M. C.; Such-Basáñez, I.; Salinas-Martínez de Lecea, C. Microporous Mesoporous Mater. 2008, 109, 305−316.

(9) Karousis, N.; Tagmatarchis, N.; Tasis, D. Chem. Rev. 2010, 110, 5366−5397.

(10) (a) Arduengo, A. J., III; Rasika Dias, H. V.; Harlow, R. L.; Kline, M. J. Am. Chem. Soc. 1992, 114, 5530−5534. (b) Herrmann, W. A. Angew. Chem., Int. Ed. 2002, 41, 1290−1309. (c) Bourissou, D.; Guerret, O.; Gabbaï, F. P.; Bertrand, G. Chem. Rev. 2000, 100, 39−91.

(11) (a) Hahn, F. E.; Jahnke, M. C. Angew. Chem., Int. Ed. 2008, 47, 3122−3172. (b) Crudden, C. M.; Allen, D. P. Coord. Chem. Rev. 2004, 248, 2247−2273. (c) Benhamou, L.;

Chardon, E.; Lavigne, G.; Bellemin-Laponnaz, S.; César, V. Chem. Rev. 2011, 111, 2705−2733. (d) Peris, E. Top. Organomet. Chem. 2007, 21, 83−116.

(12) (a) He, P.; Urban, M. W. Biomacromolecules 2005, 6, 2455−2457. (b) Wu, Z.; Feng, W.; Feng, Y.; Liu, Q.; Xu, X.; Sekino, T.; Fujii, A.; Ozaki, M. Carbon 2007, 45, 1212−1218. (c) Deng, X.; Jia, G.; Wang, H.; Sun, H.; Wang, X.; Yang, S.; Wang, T.; Liu, Y. Carbon 2007, 45, 1419−1424. (d) Malarkey, E. B.; Reyes, R. C.; Zhao, B.; Haddon, R. C.; Parpura, V. Nano Lett. 2008, 8, 3538−3542. (e) Fagnoni, M.; Profumo, A.; Merli, D.; Dondi, D.; Mustarelli, P.; Quartarone, E. Adv. Mater. 2009, 21, 1761−1765. (f) Andersson, C.-H.; Grennberg, H. Eur. J. Org. Chem. 2009, 4418−4421.

(13) Lawrence, E. J.; Wildgoose, G. G.; Aldous, L.; Wu, Y. A.; Warner, J. H.; Compton, R. G.; McNaughter, P. D. Chem. Mater. 2011, 23, 3740−3751.

(14) (a) Gladiali, S.; Alberico, E. Chem. Soc. Rev. 2006, 35, 226−236. (b) Gladiali, S.; Mestroni, G. Transferhydrogenations. In Transition

Metals for Organic Synthesis: Building Blocks and Fine Chemicals; Beller, M., Bolm, C., Eds.; Wiley-VCH: Weinheim, Germany, 1998, Vol. 2; pp 97−119.

(15) (a) Guijarro, D.; Oscar, P.; Yus, M. Tetrahedron Lett. 2011, 52, 789−791. (b) Haraguchi, N.; Tsuru, K.; Arakawa, Y.; Itsuno, S. Org. Biomol. Chem. 2009, 7, 69−75. (c) Canivet, J.; Süss-Fink, G. Green Chem. 2007, 9, 391−397. (d) Ikariya, T.; Blacker, A. J. Acc. Chem. Res. 2007, 40, 1300−1308.

(16) (a) Azua, A.; Mata, J. A.; Peris, E.; Lamaty, F.; Martínez, J.; Colacino, E. Organometallics 2012, 31, 3911−3919. (b) Gonell, S.; Poyatos, M.; Mata, J. A.; Peris, E. Organometallics 2012, 31, 5606−5614. (c) Gierz, V.; Urbanaite, A.; Seyboldt, A.; Kunz, D. Organometallics 2012, 31, 7532−7538. (d) Chiyojima, H.; Sakaguchi, S. Tetrahedron Lett. 2011, 52, 6788−6791. (e) Newman, P. D.; Cavell, K. J.; Hallett, A. J.; Kariuki, B. M. Dalton Trans. 2011, 40, 8807−8813. (f) Diez, C.; Nagel, U. App. Organomet. Chem. 2010, 24, 509−516. (g) Pontes da Costa, A.; Viciano, M.; Sanaú, M.; Merino, S.; Tejeda, J.; Peris, E.; Royo, B. Organometallics 2008, 27, 1305−1309. (h) Kownacki, I.; Kubicki, M.; Szubert, K.; Marciniec, B. J. Organomet. Chem. 2008, 693, 321−328. (i) Hahn, F. E.; Holtgrewe,

C.; Pape, T.; Martin, M.; Sola, E.; Oro, L. A. Organometallics 2005, 24, 2203−2209. (j) Mas- Marzá, E.; Poyatos, M.; Sanaú, M.; Peris, E. Organometallics 2004, 23, 323−325. (k) Albrecht, M.; Crabtree, R. H.; Mata, J. A.; Peris, E. Chem. Commun. 2002, 32−33. (l) Hillier, A. C.; Lee, H. M.; Stevens, E. D.; Nolan, S. P. Organometallics 2001, 20, 4246−4252.

(17) Jiménez, M. V.; Fernández-Tornos, J.; Pérez-Torrente, J. J.; Modrego, F. J.; Winterle, S.; Cunchillos, C.; Lahoz, F. J.; Oro, L. A. Organometallics 2011, 30, 5493−5508.

(18) Shaterian, H. R.; Yarahmadi, H.; Ghashang, M. Tetrahedron 2008, 64, 1263−1269.

(19) Avilés, F.; Cauich-Rodríguez, J. V.; Moo-Tah, L.; May-Pat, A.; Vargas-Coronado, R. Carbon 2009, 47, 2970−2975.

(20) Lu, C.; Su, F.; Hu, S. Appl. Surf. Sci. 2008, 254, 7035−7041.

(21) Datsyuk, V.; Kalyva, M.; Papagelis, K.; Parthenios, J.; Tasis, D.; Siokou, A.; Kallitsis, I.; Galiotis, C. Carbon 2008, 46, 833−840.

(22) Chiang, Y. C.; Lin, W. H.; Chang, Y. C. Appl. Surf. Sci. 2011, 257, 2401−2410.

(23) Figueiredo, J. L; Pereira, M. F. R.; Freitas, M. M. A.; Órfão, J. M. M. Ind. Eng. Chem. Res. 2007, 46, 4110−4115.

(24) Bekhouche, M.; Blum, L. J.; Doumèche, B. ChemCatChem 2011, 3, 875−882.

(25) Glas, H.; Herdtweck, E.; Spiegler, M.; Pleier, A. K.; Thiel, W. R. J. Organomet. Chem. 2001, 626, 100−105.

(26) Park, M. J.; Lee, J. K.; Lee, B. S.; Lee, Y. W.; Choi, I. S.; Lee, S. Chem. Mater. 2006, 18, 1546−1551.

(27) Baskaran, D.; Mays, J. W.; Bratcher, M. S. Angew. Chem., Int. Ed. 2004, 43, 2138−2142.

(28) Herrmann, W. A. Angew. Chem. 2002, 114, 1342−1363; Angew. Chem., Int. Ed. 2002, 41, 1290−1309.

(29) (a) Zarka, M. T.; Bortenschlager, M.; Wurst, K.; Nuyken, O.; Weberskirch, R. Organometallics 2004, 23, 4817−4820. (b) Edworthy, I. S.; Arnold, P. L. Chem. Soc. Rev. 2007, 36, 1732−1744. (c) Kühl, O. In Functionalised N-Heterocyclic Carbene Complexes; John Wiley & Sons: Chichester. UK. 2010; Chapter 4. (d) Eguillor, B.; Esteruelas, M. A.; García-Raboso, J.; Oliván, M.; Oñate, E.; Pastor, I. M.; Peñafiel, I.; Yus, M. Organometallics 2011, 30,

1658−1667. (e) Kong, Y.; Wen, L.; Song, H.; Xu, S.; Yang, M.; Liu, B.; Wang, B. Organometallics 2011, 30, 153−159. (f) Benitez, M.; Mas-Marza, E.; Mata, J. A.; Peris, E. Chem. Eur. J. 2011, 17, 10453−10461.

(30) Crotti, C.; Farnetti, E.; Filipuzzi, S.; Stener, M.; Zangrando, E.; Moras, P. Dalton Trans. 2007, 133−142.

(31) Lee, W. H.; Kim, H. Catal. Commun. 2011, 12, 408−411.

(32) Zahmakiran, M. Dalton Trans. 2012, 41, 12690−12696.

(33) (a) Díaz-Auñón, J. A.; Román-Martínez, M. C.; Salinas-Martínez de Lecea, C. J. Mol. Cat. A: Chem. 2001, 170, 81−93. (b) Giordano, R.; Serp, P.; Kalck, P.; Kihn, Y.; Schreiber, J.; Marhic, C.; Duvail, J.-L. Eur. J. Inorg. Chem. 2003, 610−617.

(34) Fritsch, A.; Légaré, P. Surf. Sci. 1984, 145, L517−L523.

(35) (a) Gawande, M. B.; Guo, H.; Rathi, A. K.; Branco, P. S.; Chen, Y.; Varmad, R. S.; Peng, D.-L. RSC Adv. 2013, 3, 1050−1054. (b) Sonnenberg, J. F.; Coombs, N.; Dube, P. A.; Morris, R. H. J. Am. Chem. Soc. 2012, 134, 5893−5899. (c) Alonso, F.; Riente, P.; Yus, M. Acc. Chem. Res. 2011, 44, 379−391.

(36) Lu, J.; Serna, P.; Aydin, C.; Browning, N. D.; Gates, B. C. J. Am. Chem. Soc. 2011, 133, 16186−16195.

(37) Uzun, A.; Ortalan, V.; Browning, N. D.; Gates, B. C. J. Catal. 2010, 269, 318−328.

(38) Barz, M.; Glas, H.; Thiel, W. R. Synthesis 1998, 1269−1273.

(39) (a) Vicent, C.; Viciano, M.; Mas-Marza, E.; Sanaú, M.; Peris, E. Organometallics 2006, 25, 3713−3720. (b) Mas-Marza, E.; Sanaú, M.; Peris, E. Organometallics 2006, 25, 3063−3069. (c) Poyatos, M.; Maisse-François, A.; Bellermin-Laponnaz, S.; Gade, L. H. Organometallics 2006, 25, 2634−2641. (d) Poyatos, M.; Mas-Marza, E.; Mata, J. A.; Sanaú, M.; Peris, E. Eur. J. Inorg. Chem. 2006, 158−162. (e) Field, L. D.; Messerle, B. A.; Vuong, K. Q.; Turner, P. Organometallics 2005, 24, 4241−4250. (f) Zeng, J. Y.; Hsieh, M. H.; Lee, H. M. J. Organomet. Chem. 2005, 690, 5662−5671. (g) Mas-Marza, E.; Sanaú, M.; Peris, E. Inorg. Chem. 2005, 44, 9961−9967. (h) Poyatos, M.; Mas-Marza, E.; Mata, J. A.; Sanaú, M.; Peris, E. Eur. J. Inorg. Chem. 2003, 1215−1221.

(40) Enders, D.; Gielen, H. J. Organomet. Chem. 2001, 617−618, 70−80.

(41) Vázquez-Serrano, L. D.; Owens, B. T.; Buriak, J. M. Chem. Commun. 2002, 2518−2519.

(42) Köcher, C.; Herrmann, W. A. J. Organomet. Chem. 1997, 532, 261−265.

(43) Malek Abbaslou, R. M.; Soltan, J.; Dalai, A. K. Appl. Catal., A 2010, 379, 129−134.

(44) Ulmer, L.; Mattay, J.; Torres-García, H. G.; Luftmann, H. Eur. J. Mass Spectrom. 2000, 6, 49−52.

(45) Brunauer, S.; Emmett, P. H.; Teller, E. J. J. Am. Chem. Soc. 1938,60, 309−319.

(46) Dubinin, M. M. Progress in Surface and Membrane Science; Academic Press: London, 1975; Vol. 9.

(47) Sherwood, P. M. A. In Practical Surface Analysis in Auger and Xray Photoelectron Spectroscopy, Briggs, D., Seah, M. P., Eds.; Wiley: New York, 1990; Vol. 1, p 574.

(48) Elgrabli, D.; Floriani, M.; Abella-Gallar, S.; Meunier, L.; Gamez, C.; Delalain, P.; Rogerieux, F.; Boczkowski, J.; Lacroix, G. Part. Fibre Toxicol. 2008, 5, 20−33.

(49) Usón, R.; Oro, L. A.; Cabeza, J. A. Inorg. Synth. 1985, 23, 126−127.

SUPPORTING INFORMATION

Figure S1. Nitrogen adsorption isotherm of **Raw-CNT** at 77 K.

Figure S2. Nitrogen adsorption isotherm of **CNT** at 77 K

Figure S3. Superposition of nitrogen adsorption isotherms of **Raw-CNT/CNT/CNT-1/CNT-1-Ir** at 77 K**.**

Table S1. Apparent surface area and pore volume from N_2-physisorption/desorption studies.

Figure S4. Raman spectra of **Raw-CNT**, **CNT**, **CNT-1**, **CNT-2**, **CNT-1-Ir**, **CNT-2-Ir.**

Table S2. Area ratio for the D and G bands of **Raw-CNT**, **CNT**, **CNT-1**, **CNT-2**, **CNT-1-Ir**, **CNT-2-Ir**.

Figure S5. TPD profiles of CO and CO_2 release during the heating of **CNT**

Figure S6. Deconvolution of the TPD profiles for **CNT**.

Figure S7. TGA curves of **CNT-1** and **CNT-2**.

Figure S8. TEM images of **CNT-1** and **CNT-2**.

^{1}H NMR data for CNT-1 and CNT-2.

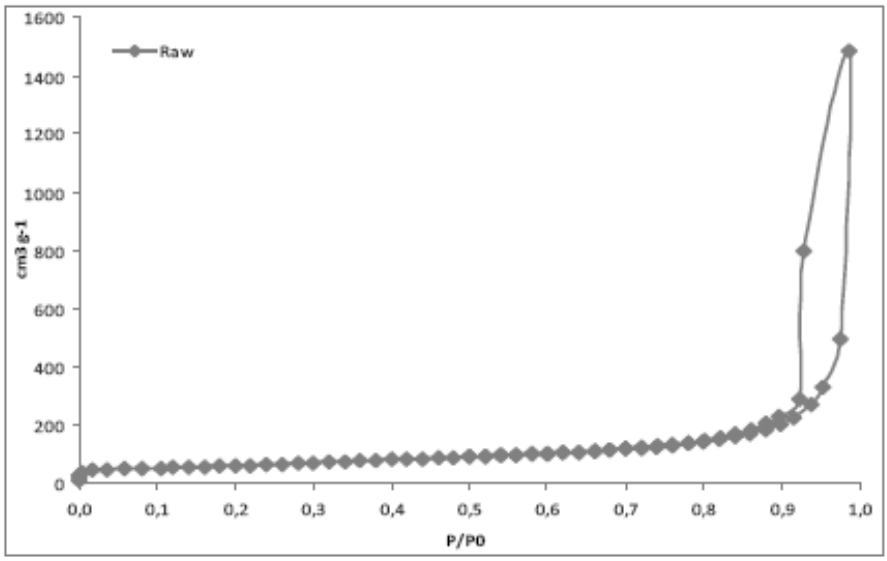

Figure S1. Nitrogen adsorption isotherm of **Raw-CNT** at 77 K

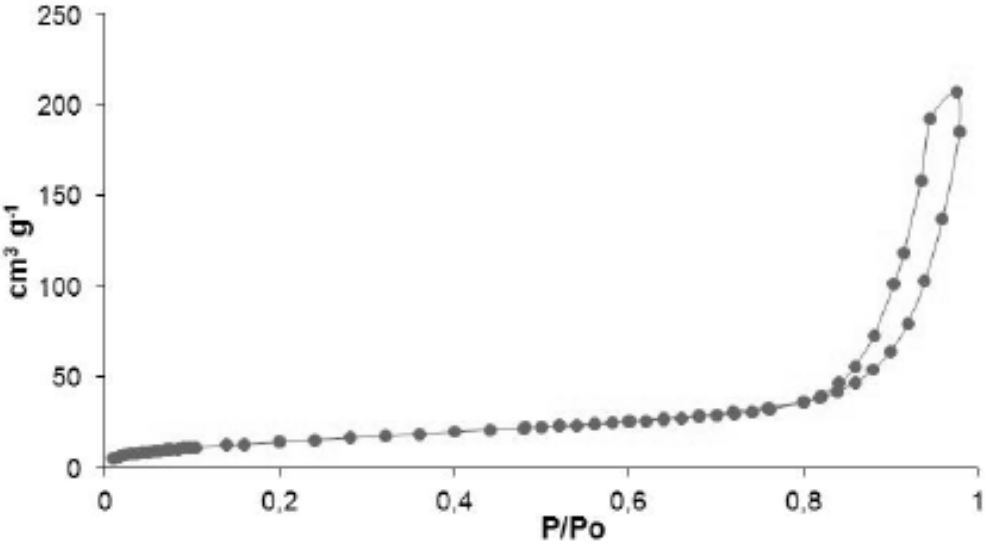

Figure S2. Nitrogen adsorption isotherm of **CNT** at 77 K

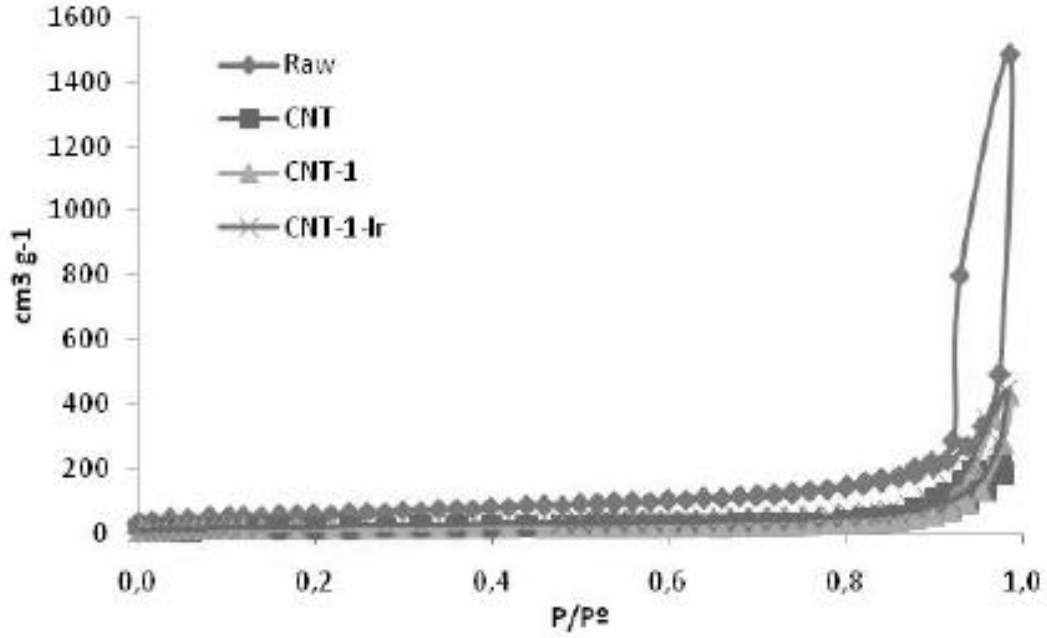

Figure S3. Superposition of nitrogen adsorption isotherms of **Raw-CNT/CNT/CNT-1/CNT-1-Ir** at 77 K**.**

Table S1 Apparent surface area and pore volume from N_2-physisorption/desorption studies.

Entry	Sample	S_{BET} [$m^2 g^{-1}$][a]	V_p [$cm^3 g^{-1}$][b]
1	**Raw CNT**	210	2.29
2	**CNT**	54	0.32
3	**CNT-1**	57	0.62
4	**CNT-1-Ir**	86	0.69

[a] Aparent surface area. [b] Pore volume.

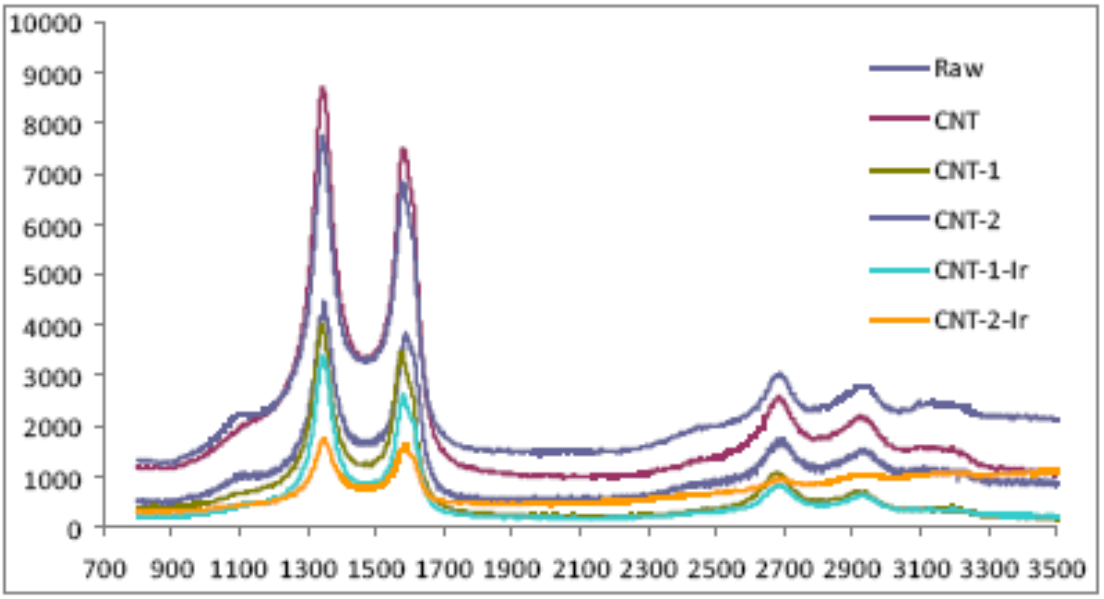

Figure S4. Raman spectra of **Raw-CNT**, **CNT**, **CNT-1**, **CNT-2**, **CNT-1-Ir**, **CNT-2-Ir.**

Table S2. Area ratio for the D and G bands of **Raw-CNT**, **CNT**, **CNT-1**, **CNT-2**, **CNT-1-Ir**, **CNT-2-Ir**.

Sample	I_D/I_G
Raw-CNT	1.104
CNT	1.178
CNT-1	1.156
CNT-2	1.137
CNT-1-Ir	1.304
CNT-2-Ir	1.203

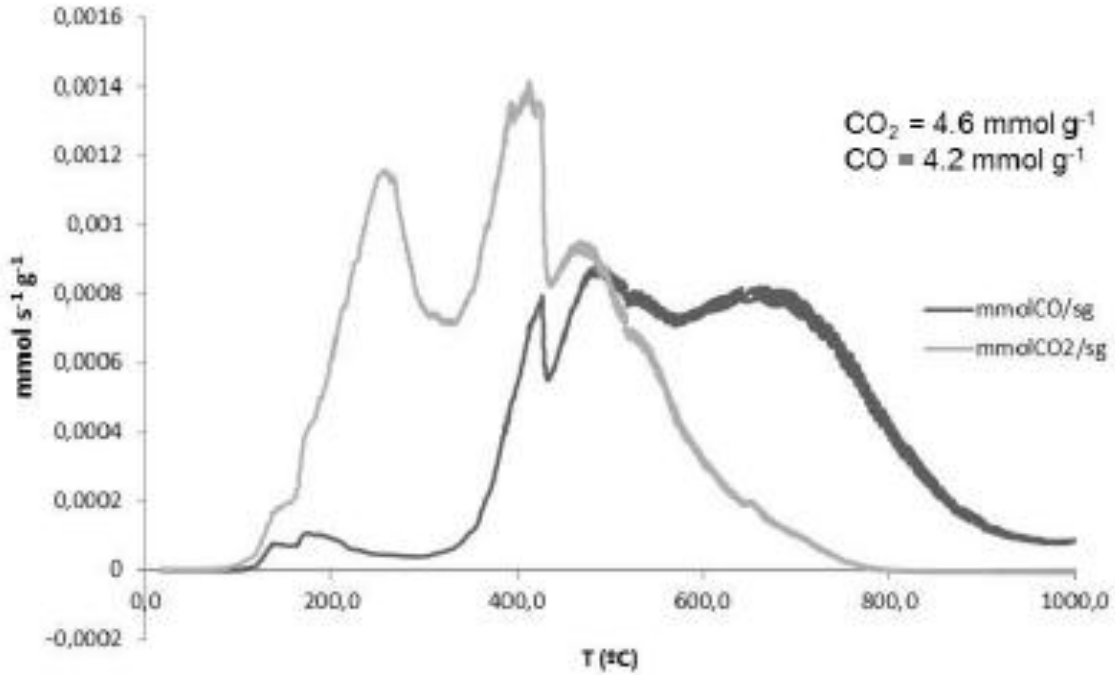

Figure S5. TPD profiles of CO and CO_2 release during the heating of **CNT**

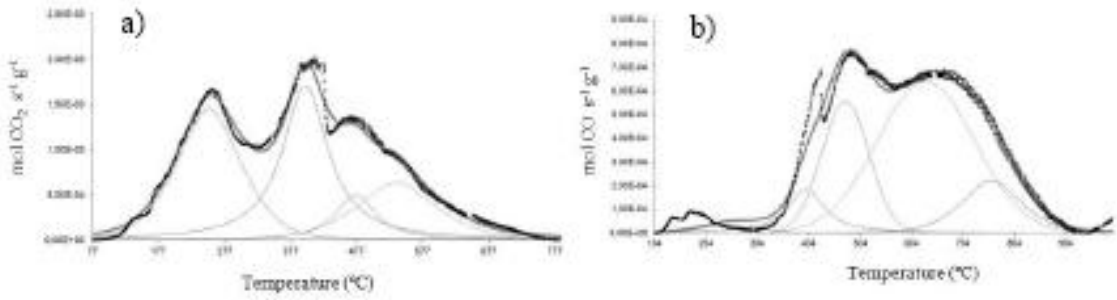

Figure S6. Deconvolution of the TPD profiles for **CNT**.

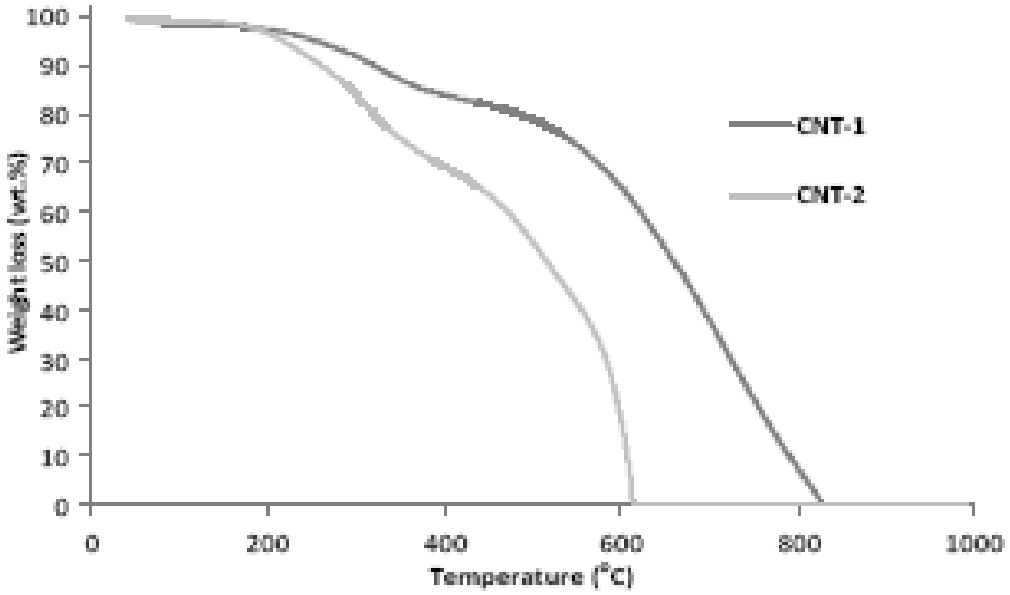

Figure S7. TGA curves of **CNT-1** and **CNT-2**.

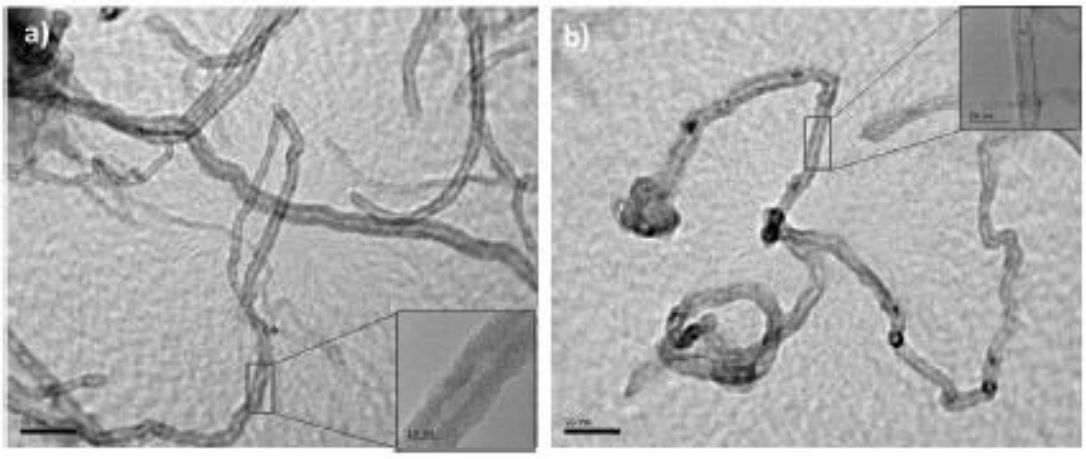

Figure S8. TEM images of **CNT-1** and **CNT-2**.

NMR data:

^{1}H-NMR resonances for CNT-1 (298K, acetone-d_6): δ 8.66 (s, 1H, CH), 7.42 (s, 1H, CH), 7.38 (s, 1H, CH), 4.45 (t, J = 5.9, 2H, CH_2), 3.76 (s 3H CH_3), 3.54 (t, J = 5.9, 2H CH_2), 2.13 (m, 2H, CH_2). OH signal is not detected.

^{1}H-NMR resonances for CNT-2 (298K, acetone-d_6): δ 8.65 (s, 1H, CH), 7.43 (s, 1H, CH), 7.41 (s, 1H, CH), 4.07 (m, 1H, CH), 3.72 (s, 3H, CH_3), 3.38 (s, 1H, CH), 1.60 (m, 4H, CH_2), 1.37 (m, 4H, CH_2). OH signal is not detected.

4.3 ARTÍCULO III

“Inmovilización covalente de catalizadores NHC-iridio en nanotubos de carbono con distinto grado de oxidación”

Enviado a Catalysis, Science and Technology

Los métodos de purificación y oxidación de nanotubos de carbono descritos en la sección 4.1 producen el suficiente número de grupos funcionales oxigenados como para ser empleados en la preparación de complejos organometálicos que actuarán como catalizadores. Además, el diferente grado oxidación de la estructura carbonosa genera una química superficial con distinto comportamiento catalítico. En este capítulo se discute la modificación covalente de cuatro de estos materiales con distinto grado de oxidación, con complejos NHC de iridio.

La modificación covalente se realizó activando los grupos carboxilo de todos los materiales iniciales con $SOCl_2$, siguiendo el mismo procedimiento descrito en el capítulo anterior. No obstante, el ligando introducido en este caso fue N-metilimidazol (MI), generando las muestras **CNT-X-MI**, donde **X** es el grado de oxidación del nanotubo. El último paso consistió en el anclaje del complejo de iridio empleando los materiales anteriormente modificados, como se describe en la figura 4.4, para obtener los materiales híbridos **CNT-X-MI-Ir.**

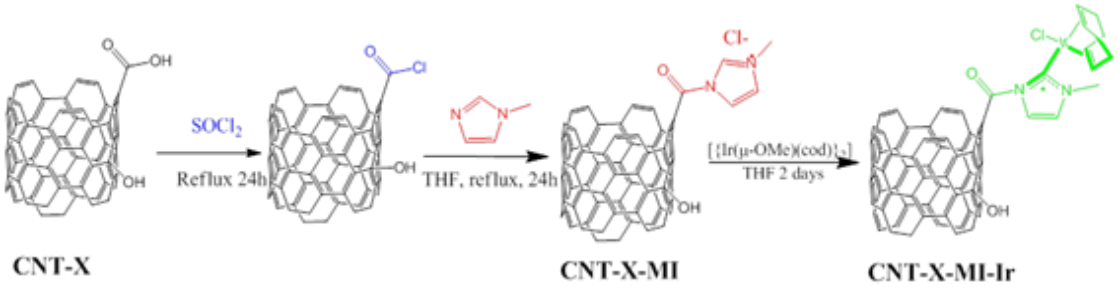

Figura 4.4 Funcionalización covalente de los nanotubos con diferente grado de oxidación

La caracterización de las muestras demostró la presencia de las unidades imidazólicas al observar un progresivo aumento en los contenidos de nitrógeno en los materiales tratados, una mayor relación ID/IG en los espectros Raman y mayores desorciones en los perfiles termogravimétricos. La cantidad de ligando detectada se relaciona directamente con el grado de oxidación al que fue sometido. Además, regiones electrón-densas del tamaño adecuado (0.15-0.25 nm) se observaron en el microscopio de transmisión, correspoendites a Ir (I) según sus espectros de XPS.

Los cuatro materiales híbridos se ensayaron como catalizadores en la reducción de ciclohexanona por transferencia de hidrógeno. Todas las muestras resultaron ser catalizadores activos y estables, presentando una buena ciclabilidad y estabilidad al aire al no observarse pérdida de actividad tras cinco ciclos sucesivos, incluidos los realizados al aire. El comportamiento catalítico también se puede correlacionar con el grado de oxidación del material inicial (figura 4.5), al obtener mejores resultados conforme aumenta la oxidación del materal, siendo la especie más activa la muestra **CNT-ST-MI-Ir**, con una actividad muy comparable al material **CNT-ST-1-Ir** descrito en el capitulo anterior.

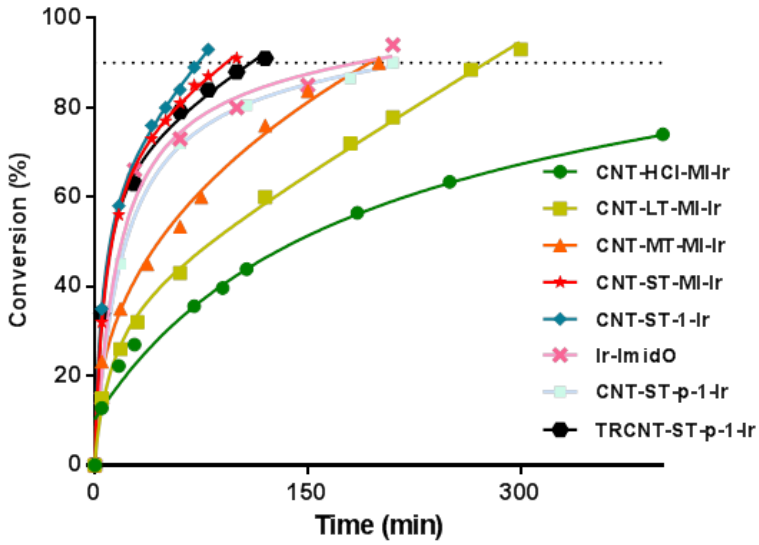

Figura 4.5 Actividad catalítica

Los resultados de los ensayos catalíticos pueden ser explicados en función de la diferente química superficial estudiada. Así, las superficies de los materiales empleados controlan la actividad catalítica, de manera que las oxidaciones suaves generan estructuras sp^2 con un alto grado de perfección y pocos grupos funcionales oxigenados, desarrollan poca porosidad y apenas abren las puntas. La dispersión en el medio de reacción de estos materiales es muy pobre, y la difusión de reactivos y productos es más complicada, lo que hace que descienda la actividad.

Sin embargo, en los nanotubos más oxidados sucede el fenómeno contrario al estar más funcionalizados y presentar más defectos, con lo que la difusión y dispersión aumenta la velocidad en la muestra **CNT-ST-MI-Ir**. Además, la estructura defectuosa permite el acceso de los reactivos a la cavidad interior de los nanotubos, con lo que también pueden suceder efectos de confinamiento

Catalysis Science & Technology

ARTICLE

Covalent immobilization of NHC-iridium catalysts on carbon nanotubes with increasing oxidation degree

Received 00th January 20xx,
Accepted 00th January 20xx

DOI: 10.1039/x0xx00000x

www.rsc.org/catalysis

Matías Blanco,[a] Patricia Álvarez,[a] Clara Blanco,[a] M. Victoria Jiménez*[b], Javier Fernández-Tornos,[b] Jesús J. Pérez-Torrente,[b] Luis A. Oro[b] and Rosa Menéndez*[a]

CVD-grown multiwalled carbon nanotubes were purified applying four treatments with increasing oxidation severity in order to eliminate the impurities which develops an inherent progressive oxygen functionalization. Iridium N-heterocyclic carbenes complexes were covalently anchored to those oxydated surfaces through their surface carboxylic acids. The immobilized iridium catalyst developed are active in the reduction of cyclohexanone by hydrogen transfer processes but they have different surface chemistry. The catalytic activity is therefore determined by the type and amount of surface chemical groups being the most active catalyst the one supported is the most oxydized support.

1. Introduction

N-heterocyclic carbene (NHC) iridium complexes are active precursors in the reduction of C=O and C=N bonds to generate alcohols or amines under mild conditions under transfer hydrogenation processes conditions. [1,2] In one part, the tunable character of NHC-metal transition homogeneous catalysts allows for the control of the sterical and electronic properties at the metal centre.[3] In the other part, the catalytic activity of the organometallic compounds can be improved anchoring them in carbonaceous support permitting, addittionally, the easily recovery and subsequent recyclability of the catalysts.[4,5]

Carbon nanotubes (CNT),[6] among other carbon materials, present excellent electronic, thermal, chemical and mechanical properties[7-9] which made them stable to support molecular metal transition complexes. All the synthetic methods used in their production, *i.e.* arc discharge, laser vaporization or CVD,[10] produces impurities that join every produced CNT batch, mainly based on amorphous carbon particles and traces of the metals used for the growth of the nanotubes.[11] Purification methods could involve thermal annealing, electrochemical or magnetic treatments, but the most applied procedures are based on different acid/oxidant treatments in order to dissolve the metals and eliminate the carbon impurities.[12] It is known that these treatments affect the carbon walls of the CNTs too. The oxidation surface chemistry of CNTs is reasonably well-established,),[13] and after those oxidation processes surface

[a] *Instituto Nacional del Carbón INCAR-CSIC, P.O. Box 73, 33080, Oviedo, Spain. rosmenen@incar.csic.es*
[b] *Department of Inorganic Chemistry, Instituto de Síntesis Química y Catálisis Homogénea (ISQCH-CSIC). University of Zaragoza, 50009, Zaragoza Spain. vijimenez@unizar.es*
Electronic Supplementary Information (ESI) available: [Raman spectra, TGA curves, elemental analyses, XPS measurements, additional TEM images, EDX spectra, GC experiments and catalytic recycling data]. See DOI: 10.1039/x0xx00000x

oxygen groups are deployed after the purification, mainly carboxylic acids on the edges, tips and defects, and hydroxylic and epoxy groups on the basal planes.[14] depending on the grade of oxidation.[15-17] Several proposals about the mechanism involving the oxidation of the walls are reported in the literature, but all of them agree with the severity of the treatments directly relates with the degree of oxidation.

The covalent immobilization of the iridium-NHC complexes on the CNTs could be achieved taking advantage of their oxygenated surface chemistry but their development as hybrid catalysts is under expansion in comparison with other suitable supports, and of course, detailed catalytic studies based on proper models of supported catalysts with gradable oxidation parameters of their surfaces are scarce.

Keeping in mind recent advances of transition metal complexes covalently attached to carbon surfaces, some of active transfer hydrogenation Ir-NHC supported complexes of our group,[4,5] this paper proposes the covalently anchoring of methylimidazolylyde iridium NHC complexes using the carboxylic acids of different oxidized CNTs supports with an increasing severity treatments. The catalytic activity, stability and cyclability of the resultant hybrid materials in transfer hydrogenation reactions are studied as a function of the surface chemistry of their corresponding support.

2. Experimental

Materials

All the chemicals, including starting multiwalled carbon nanotubes, were purchased from Aldrich. Reagent or HPLC grade were employed in all the experiments. Solvents were distilled immediately prior to use from the appropriate drying agents or obtained from a Solvent Purification System (Innovative Technologies). The starting organometallic compound $[Ir(\mu\text{-}OMe)(cod)]_2$ (cod = cyclooctadiene) was prepared according to standard literature procedure.[18]

Oxidation of the nanotubes

Carbon nanotubes were subjected to four different purification treatments of increasing severity: (a) 0.3 g of raw carbon nanotubes was dispersed in 70 mL of concentrated HCl. The mixture was magnetically stirred at 60 °C for 2 h. The suspensions were washed by addition of several portions of 250 mL of water, centrifugation, and elimination of the supernatant till neutral pH was reached. The solids collected were dried at 100 °C until constant weight, and labelled as **CNT-HCl**. (b) 0.3 g of raw carbon nanotubes was dispersed in 25 mL of a 1:1 mixture of ammonium hydroxide (28%) and hydrogen peroxide (30%). The mixture was magnetically stirred at 80 °C for 5 h, then a repeated procedure of washing till neutral pH as in the precedent preparation. These solids were dried and labelled as **CNT-LT**. (c) 0.3 g of raw CNT was dispersed in 70 mL of a solution of nitric acid 3 M. The mixture was magnetically stirred at 60 °C for 15 min, sonicated for 2 h and then diluted with 250 mL of water. After

centrifugation, the washing procedure with water was repeated till neutral pH as in the precedent preparations. The collected solids were dispersed in 70 mL of hydrogen peroxide (30%) and the mixture was magnetically stirred at 60 °C for 15 min, and then sonicated for 2 h. The solid was collected by filtration, washed with water and dried over 100 °C until constant weight. The dried solids obtained were named as **CNT-MT**. (d) 0.3 g of raw CNT was dispersed in 40 mL of a 3:1 mixture of concentrated sulphuric and nitric acid. The mixture was sonicated for 10 min, magnetically stirred at 80 °C for 20 min and then sonicated for another 20 min. Finally, it was diluted with 250 mL of water, and after centrifugation, the washing procedure with water was repeated till neutral pH as in the precedent preparations. The solids were dried over 100 °C until constant weight, and named as **CNT-ST**.

Covalent functionalization of the nanotubes

The cationic iridium complexes bearing methyl imidazol-2-ylidene ligands were anchored to the oxidized carbon nanotubes through ester functions applying a three-step procedure. 100 mg of **CNT-X** was refluxed in 40 mL of thionyl chloride for 24 h in argon atmosphere. Excess of $SOCl_2$ was removed under vacuum, and the resultant product was washed three times with 20 mL of tetrahydrofuran (THF) and dried for 2 h under vacuum. Then, the solid was dispersed in 15 mL of THF, and N-methylimidazole (2 mL, 25.1 mmol) was added. The mixture was refluxed for 24 h. The solid was filtered, and washed with THF (3 × 20 mL), dichloromethane (3 × 20 mL), and ether (2 × 20 mL). The solids collected were dried at 100 °C in a preheated furnace for 2 h and the dried samples were labeled as **CNT-X-MI**. The resulting imidazolium functionalized carbon nanotubes (100 mg) were reacted with $[Ir(\mu\text{-}OMe)(cod)]_2$ (100 mg, 0.150 mmol) in THF (20 mL) under argon atmosphere. The mixtures were refluxed for 2 days and then immersed in an ultrasonic bath for 30 min at room temperature. The resultant solids were recovered by centrifugation, washed with THF (5 x 10 mL) and diethyl ether (2 x 5 mL), and dried under vacuum. The hybrid materials were labelled as **CNT-X-MI-Ir**, where X relates with the degree of oxidation of the nanotube (HCl, LT, MT and ST).

General procedure for the transfer hydrogenation catalysis

The catalytic transfer hydrogenation reactions were carried out under argon atmosphere in thick glass reaction tubes fitted with a greaseless high-vacuum stopcock. In a typical experiment, the reactor was charged with a solution of cyclohexanone (0.52 mL, 5.0 mmol) in 2-propanol (4.5 mL), internal standard (mesitylene, 70 μL, 0.5 mmol), base (0.1 mL, 0.025 mmol of a KOH solution 0.24 M in 2-propanol) and the catalyst (0.005 mmol, 0.1 mol %). The resulting mixture was stirred at room temperature for 10 min, and then placed in a thermostatic oil bath at the required temperature, typically 80 ºC. Conversions were determined by gas

chromatography analysis under the following conditions: column temperature of 35 ºC (2 min) up to 220 ºC at 10 ºC min^{-1}, a flow rate of 1 mL min^{-1} using ultrapure He as carrier gas. Once the reaction was completed, the hybrid iridium-NHC catalysts were recovered by centrifugation and washed with additional amounts of 2-propanol (3 x 10 mL). Several catalytic cycles were performed with these materials, under the same experimental conditions, in argon atmosphere, and without adding any fresh catalyst precursor. The last cycle was carried out in air.

Characterization methods

The catalytic reactions were analyzed on an Agilent 4890 D system equipped with an HP-INNOWax capillary column (0.4 μm, 25 m x 0.2 mm i.d.) using mesitylene as internal standard. Thermogravimetric analyses (TGA) of the materials were performed in a TA SDT 2960 analyzer thermobalance. The procedure used was as follows: 3 mg of sample was heated in the thermobalance at 10 ºC min^{-1} to 1000 ºC using a nitrogen flow of 200 mL min^{-1}. Raman spectra of the parent oxidized nanotubes and the imidazolium-modified materials were recorded from 750 to 3500 cm^{-1} on a Renishaw 2000 Confocal Raman Microprobe (Rhenishaw Instruments, England) using a 514.5 nm argon ion laser. Images of high-resolution transmission electron microscopy (HRTEM) were recorded using a JEOL JEM-2100F transmission electron microscope, equipped with a field-emission-gun (FEG) operating at 200 kV, equipped with an Oxford Instruments microprobe to perform Energy-dispersive X-ray spectroscopy (EDX), in order to verify the atomic composition of the catalyst. The samples were prepared by casting a few drops of 1 mg mL^{-1} ethanol suspensions of the materials over the carbon grids. Elemental analyses were performed on a LECO-CHNS-932 micro-analyser equipped with a LECO-VTF-900 furnace coupled to the micro-analyzer. The X-ray photoemission spectroscopy (XPS) spectra were recorded using a SPECS system operating under a pressure of 10^{-7} Pa with a Mg Kα X-ray source. Functional groups in the parent materials were quantified by deconvolution of the high resolution C1s XPS peak employing Gaussian and Lorentzian functions.[19] The binding energy profiles were deconvoluted as follows: undamaged structures of sp^2-hybridized carbon (284.5 eV), damaged structures or sp^3-hybridized carbons, (285.5 eV), C-O groups (286.5 eV), C=O functional groups (287.7 eV) and COO groups (288.7 eV). A Shirley background-function was used to adjust the background of the spectra. The amount of iridium present in the samples was determined by means of Inductively Coupled Plasma Mass Spectrometry (ICP-MS) in an Agilent 7700x instrument. The samples were digested following a method described elsewhere.[20] Briefly, 30 mg of sample was treated with 5 mL of a mixture of concentrated nitric and hydrochloric acid (3:1 ratio) at 180 ºC for 3 h under microwave irradiation.

3. Results and Discussion

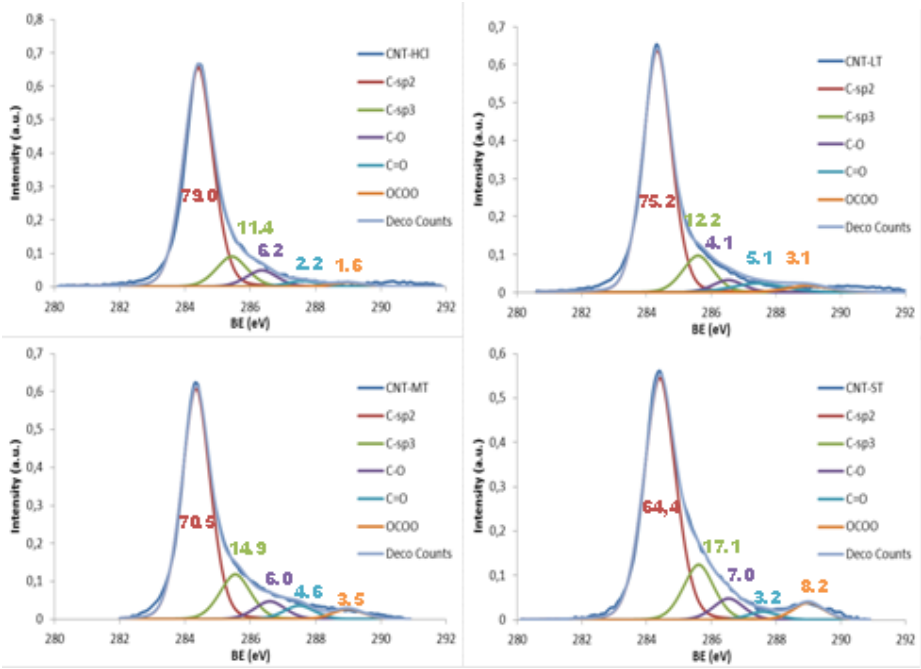

Fig 1. XPS C1s fitting of the parent material a) **CNT-HCl**, b) **CNT-LT**, c) **CNT-MT** and d) **CNT-ST**

Commercial CVD-grown multiwalled carbon nanotubes were chemically purified applying reagents with increasing oxidation strength, i.e., hydrochloric acid, a mixture of hydrogen peroxide and ammonium hydroxide, diluted nitric acid and hydrogen peroxide and a mixture of warm concentrated sulphuric and nitric acids.[21] As a result of those treatments, an increment in the D band of the Raman spectra, related to the defects on the carbon nanotubes walls of those oxidized samples is observed directly proportional to the severity of the oxidation.. Furthermore, the C/O ratio (calculated by elemental analysis) also decreases gradually. It is noticeable that the ongoing oxidation processes on the materials generates oxygen functional groups at edges, defects and basal planes of the nanotubes. Those surface groups were analyzed by deconvolution of the C1s band in the XPS spectra (Fig. 1), what also confirm the progressive introduction of oxygen groups as the severity of the oxidation increases.. Additionally, the diminution in the C sp^2 band and the intensification in the C sp^3 are both consequences of those oxidation processes. Interestingly, the largest amount of carboxylic acids with also the highest amount of hydroxylic groups, are generated in the most aggressive oxidation, corresponding to the **CNT-ST** sample.

The treatment of the parent oxidized nanotubes (**CNT-X**) with thyonil chloride followed by reaction with N-methylimidazole allow the functionalization of those nanotube materials with methylimidazolium salts by alkylation of the heterocycle with the more reactive pendant acyl choride groups. The basic methoxo ligand in the precursor complex $[Ir(\mu\text{-}OMe)(cod)]_2$ (cod = cyclooctadiene)

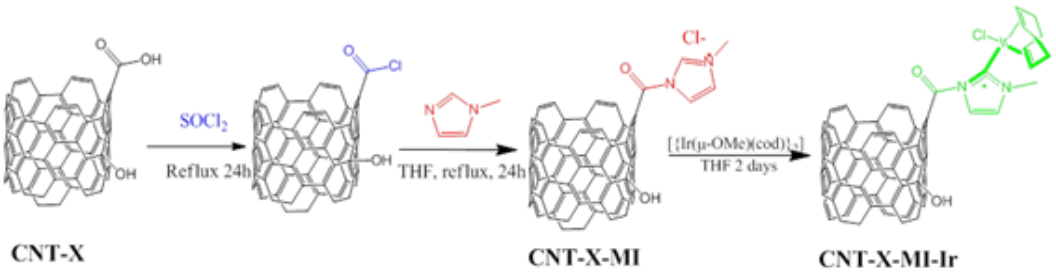

Scheme 1

reacts with the acid proton of the C2 of the supported imidazolium to generate anchored iridium NHC complexes (Scheme 1). A higher ID/IG Raman ratio was obtained in every sample comparing the parent-oxidized with imidazole-treated materials, which indicated a positive functionalization (ESI).[22] In addition, the elemental analysis (ESI) shows a steady increase in the amount of nitrogen, which corresponds to the functionalization of the carbon materials with the imidazolium groups. The more functionalized support is that which was subjected to the more oxidizing treatment, **CNT-ST-MI**. In addition, the imidazolium group weight losses determined in the TGA curves in range with the previous data, and more pronounced desorptions were detected compared to the starting materials, attributed to the imidazole unit introduced in the materials (ESI).[23] However, that functionalization prevents the accurate high-resolution XPS C1s peaks quantification of the oxygen groups in the treated materials due to the overlapping of the C-N band (286.0 eV) with the C-O band (286.5 eV). Nevertheless, high-resolution XPS N1s band of the functionalized samples reveal a unique band at 401.5 eV. From those XPS spectra the proper atomic ratio N:Cl of ca. 2:1 was obtained in every case studied which is agreement with the presence of the imidazole ring (ESI).

The totally insoluble aspect of the material, together with the detection of methanol by gas chromatography of the filtered mother liquids in the reaction with $[Ir(\mu\text{-}OMe)(cod)]_2$ (ESI), suggest the progress in the supporting of the iridium-NHC complex in the carbon nanomaterials. This is substantiated by the high-resolution transmission electron microscopy images of the four types of gradually oxidized carbon nanotube hybrid materials (**CNT-X-MI-Ir**) showed in Fig. 2. Homogeneous distributions of electron-dense regions were detected with diameters ranging 0.15-0.3 nm all throughout outer and inner walls (white circles). The metallic spots correspond to iridium particles as was confirmed by EDX (ESI). Although larger iridium particles are also detected, the Ir4f region of the XPS spectra show for all samples two maxima centered at 62.4 and 66.5 eV, which correspond to Ir(I) species.[24] Those larger spots, more marked on the unprotected outer walls, could be clusters or nanoparticles possibly formed for beam irradiation inside the microscope chamber.[25] Similar size distributions were observed for other supported molecular iridium catalysts or even for graphene-based hybrid catalyst.[4,5]

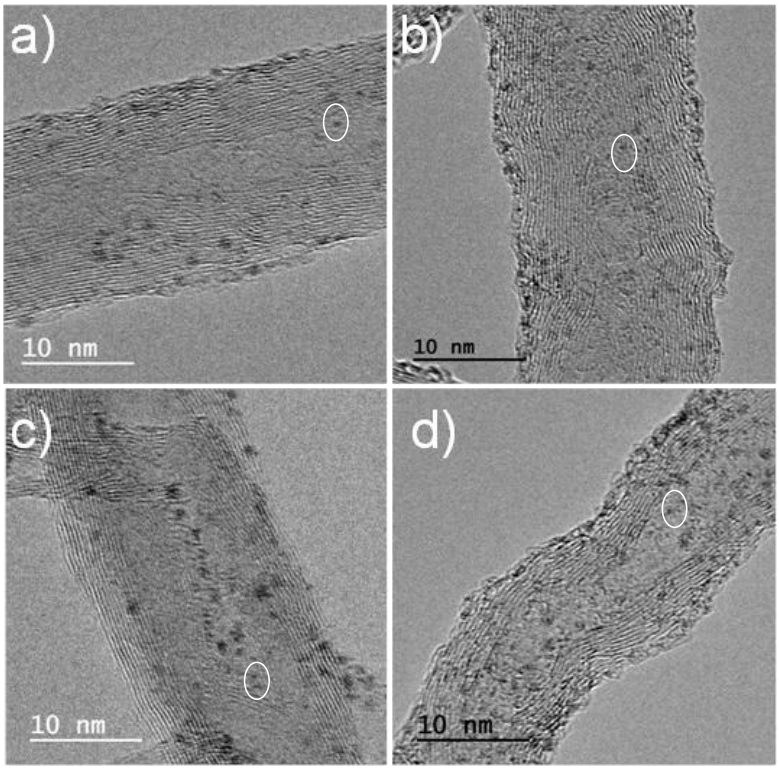

Fig 2. HRTEM images of a) **CNT-HCl-MI-Ir,** b) **CNT-LT-MI-Ir,** c) **CNT-MT-MI-Ir** and d) **CNT-ST-MI-Ir**

All the materials exhibited the same appearance in terms of number of layers and interlayer distances compared to their parent nanotubes (ESI), which indicates that functionalization has not caused any damage to the nanotube layers. The amount of the iridium in the nanotubes, determined by means of ICP-MS (Table 1), varies progressively from 3.1 % for the less oxidized material, **CNT-HCl-MI-Ir**, until 12.3 % for the most oxidized material, **CNT-ST-MI-Ir**, The ratio of these iridium amounts in the **CNT-X-MI-Ir** materials with the maximum of iridium expected calculated from the nitrogen elemental analysis of their precedent **CNT-X-MI** nanotubes displayed in Table 1 gives us the degree of NHC-Ir formation in the different materials. That ratio varies from moderate conversions *ca.* 53 % and 66 % for the less oxidized material **CNT-X-MI-Ir,** (X = HCl and LT respectively,) to almost quantitative conversions *ca.* 94 % and 98 % for **CNT-X-MI-Ir** (X = MT and ST, respectively). The low conversion results for the former materials gives an idea of the poor dispersion capacity in a polar reaction media of the less oxidized samples in the reaction medium together with less accessibility of the reactive acyl chloride groups.[26]

Once the anchoring of iridium NHC organometallic complexes on the inner and outer surfaces of the nanotubes was confirmed, the hybrid materials were tested as catalysts in

Table 1 Catalytic Hydrogen transfer results[a,b]

Catalyst	%Ir[c]	Time (min)	Conv (%)	TON	TOF_0 (h^{-1})	TOF_{50} (h^{-1})
CNT-HCl-MI-Ir	3.1	900	91	912	10988	304
CNT-LT-MI-Ir	6.1	300	93	934	11253	722
CNT-MT-MI-Ir	10.0	200	90	903	10880	934
CNT-ST-MI-Ir	12.3	100	91	911	10976	5246
CNT-ST-1-Ir		80	94	943	11361	3750
Ir-ImidO	-	200	94	941	11124	2823

[a]Reaction conditions: catalyst/substrate/KOH ratio of 1/1000/5, $[catalyst]_0 = 1 \times 10^{-3}$ M in 2-propanol at 80 °C. [b]The reactions were monitored by GC using mesitylene as internal standard. [c]Determined by means of ICP-MS

the reduction of cyclohexanone to cyclohexanol by hydrogen transfer processes, employing 2-propanol both as hydrogen source and as a non-toxic solvent with a moderate boiling point. The reaction conditions were improved with related O-functionalized NHC iridium(I) homogeneous compounds as [IrBr(cod)(MeIm(2-methoxybenzyl))] in previous works.[3] Standard catalyst loads of 0.1 mol %, with 0.5 mol % of KOH as co-catalyst, and 80 ºC were routinely employed (Scheme 2).

Iridium supported catalysts prepared without imidazolium ligand, the related molecular acetoxy-functionalized NHC complex [IrCl(cod)(MeIm$(CH_2)_3OCOCH_3$] (**Ir-ImidO**),[4] and analogous supported Ir-NHC complexes on oxidized carbon nanotubes bonded through the surface carboxylic acids[4] and the surface hydroxylic groups in severe oxidized and thermally reduced nanotubes were also evaluated for comparative purposes. It is noteworthy that none of the iridium free carbon nanotube-based materials showed any catalytic activity (ESI). Reaction times required for reaching higher conversions than 90 %, and the catalytic parameters (turnover numbers TON and initial TOF_0 and 50 % turnover frequencies TOF_{50}) are depicted in Table 1, while the conversion vs time profiles are plotted on Fig 3.

The keto-methyl imidazol-2-ylidene based NHC-iridium catalyst supported on carbon nanotubes (**CNT-X-MI-Ir**) were active in the transfer hydrogenation conditions tested with no induction periods observed. In general, all the studied hybrid materials show similar kinetic profiles, but appreciable differences in the activity are perceived. The hybrid material **CNT-ST-MI-Ir** is the most active catalyst at any time comparing with the samples produced with the different oxidation procedures **CNT-X-MI-Ir**. The conversion achieved for **CNT-ST-MI-Ir** was above 90 % in 1.6 h and initial TOF of 10976 h^{-1}, while **CNT-HCl-MI-Ir**, **CNT-LT-MI-Ir** and **CNT-MT-MI-Ir** required 15 h, 5 h and 3.3 h, respectively, to attain the same conversion. In addition, that hybrid catalyst, **CNT-ST-MI-Ir,** reaches complete conversion in shorter times than the reaction time required for related acetoxy homogeneous catalyst, [IrCl(cod)(MeIm$(CH_2)_3OCOCH_3$], **Ir-ImidO** (3.3 h). Furthermore, its catalytic activity is very close to that corresponding to the supported acetoxy-based Ir-NHC oxidized carbon nanotube hybrid catalysts obtained from 3-(3-hydroxypropyl)-

methyl-imidazol-2-ylidene, **CNT-ST-1-Ir**;[4] in fact, conversions below 70 % are quite similar.

Those materials **CNT-ST-MI-Ir** and **CNT-ST-1-Ir** have a similar degree of oxygen group functionalization but they differ from the flexible carbon chain which bonds the NHC carbene ligand what seems an optional element in the catalysis activity (Scheme 3). In spite of that similarity in the reaction profiles (Fig. 3), a surface effect due to the support structure is supposed to be the responsible of the variations in the activity between the **CNT-X-MI-Ir** catalysts. The carbon structure of those supports treated with purification procedures resulting in weaker oxidized supports (HCl, LT and MT treatments) that exhibit, according to the characterization techniques, an extended sp^2 structure with higher C/O ratios and low intrinsic porosity with tips scarcely opened. This reduction of hydrophilic functional groups also implies a lower dispersion capacity in the polar catalytic reaction medium which difficult the access of the reactants to the active sites, and in particular, to those settled in the inner cavity of the nanotube. On the other hand, the more severe oxidation treatment (ST treatment) results in a defective structure, plenty of holes, oxygen moieties, structural defects and opened tips.[27,28]

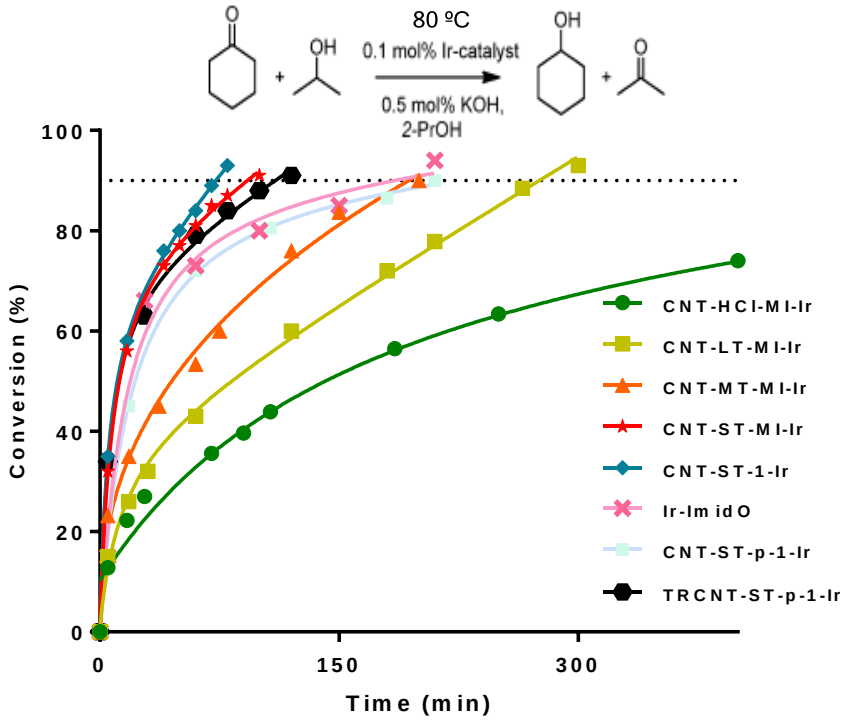

Fig 3. Representation of the reduction of cyclohexanone (%) versus time (min) for the transfer hydrogenation of cyclohexanone with 2-propanol using the indicated heterogeneous catalysts (0.1%) at 80 ºC. Continuous lines represent a mathematical fit with the experimental data points

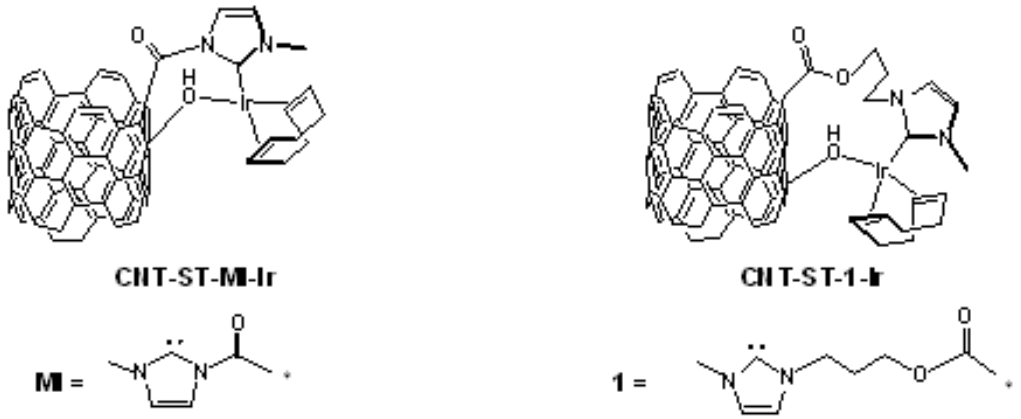

Scheme 3

Thus, the defective structures contain suitable exposed active centers situated in the holes and open channels where reactants can arrive to inner-bonded iridium complexes more easily in the diffusional stages of the heterogeneous catalytic process. In those circumstances, the nanotube acts as a "nano-reactor" offering a confinement effect established by the close-place of the inner cavity of the nanotube and enhancing the catalysis activity.

That surface effect is not the only aspect to be considered in that carbon nanotube hybrid catalysts. In fact, the argument is contradictory for the case of the -OH functionalized catalysts **CNT-ST-p-1-Ir** and **TRCNT-ST-p-1-Ir** where the reduced material, **TRCNT-ST-p-1-Ir,** is substantially more active than the obtained from the starting oxidized material **CNT-ST-p-1-Ir** (Fig 3). The catalysts based on reduced materials display an increase in the amount of Csp^2 bonds and a decrease in the functional groups, but they are more active, which means the iridium centers become more accessible comparing with their oxidized parent materials. In spite of their different catalytic behavior, they own similar first-neighbors coordination shells as is deduced from their EXAFS measurements, but the differences, however, should be related with the different localization of the iridium centers in the hybrid catalysts. These –OH functionalized systems own the active centers located at the basal plane of the nanotubes, rather different than the –COOH functionalized materials, where the Ir-NHC complexes are at the holes and defects for. Therefore, the thermal reduction provides a cleaner surface in which the accessibility of the reactants becomes easier compared to the weak oxidized supports. That observations could be of a great importance because gives a clear idea of how should be the functionalization in order to get more active catalysts

Finally, recycling studies were carried out with the four samples studied (ESI). The black solids obtained after the catalysis were recovered, washed and subjected to another catalytic cycle. Any loss of activity was detected as similar conversion in related times was obtained for every sample after 5 consecutive cycles. In addition, the kinetic profiles are very close to those

plotted on Fig. 3, even performing the final one under air atmosphere, in sharp contrast with other homogeneous iridium-NHC complexes developed before.[4]

4. Conclusions

The covalent functionalization of progressively oxidized carbon nanotubes with an iridium N-heterocycle carbene complex through the surface carboxylic acids has been performed. The load of the imidazolium ligand and the iridium itself on the supports depends on the grade of oxidation of the parent nanotube employed.

The catalytic activity of the supported iridium NHC complexes on the transfer hydrogenation of cyclohexanone is also dependent on the surface chemistry and the degree of oxidation of the nanotubes in which they are supported. As the more oxidized support is the one which develops the more active catalysts, the correct amount and type of oxygen groups and structural defects must be present in the surface of the material in order to allow the dispersion of the materials in the reaction media and the diffusion of the reactants into the active centres, combined with an adequate stabilization of the metal in order to obtain good catalytic performances.

Acknowledgements

The authors thank the Spanish Ministry of Economy and Competitiveness (MINECO/FEDER) (Projects Consolider Ingenio 2010 CSD2009-00050 and CTQ2013-42532-P), and the Diputación General de Aragón (E07) for their financial support. Dr. P. A. thanks MINECO for a Ramón y Cajal contract. M. B. acknowledges his fellowship from MECD (AP2010-0025).

Notes and references

1 M. N. Hopkinson, C. Richter, M. Schedler. F. Glorius. *Nature* 2014, **510**, 485-495
2 A. C. Hillier, H. M. Lee, E. D. Stevens, S. P. Nolan. *Organometallics* 2001, **20**, 4246-4252.
3 M. V. Jiménez, J. Fernández-Tornos, J. J. Pérez-Torrente, F. J. Modrego, S. Winterle, C. Cunchillos, F. J. Lahoz, L. A. Oro. *Organometallics* 2011, **30**, 5493−5508.
4 M Blanco. P. Álvarez, C. Blanco, M. V. Jiménez, J. Fernández-Tornos, J. J. Pérez-Torrente, L. A. Oro, R. Menéndez. *ACS Catal.* 2013, **3**, 1307-1317.
5 M. Blanco, P. Álvarez, C. Blanco, M. V. Jiménez, J. Fernández-Tornos, J. J. Pérez-Tornos, L. A. Oro, R. Menéndez. *Carbon* 2015, **83**, 21-31
6 S. Iijima, *Nature*, 1991, **354**, 56-58.
7 C. T. White, T. N. Todorov. *Nature* 1998. **393**, 240-242.
8 J. P. Lu. *Physical Review Letters* 1997, **79**, 1297.
9 J. Zhao, R.H. Xie, *Journal of Nanoscience and Nanotechnology*, 2003, **3**, 459-462
10 M. Wilson, K. Kannagaram G. Smith, B. Raguse, Nanotechnology. Basic Science and Emerging Technologies. CRC Press, London. 2002
11 S. Porro, S. Musso, M. Vinante, L. Vanzetti, M. Anderle, F. Trotta, A. Tagliaferro. *Physica E* 2007, **37,** 58–61

12 A. Aqel, K. M. M. Abou El-Nour, R. A. A. Ammar, A. Al-Warthan, *Arab. J. Chem* 2012, **5**, 1-23.
13 Gregory G. Wildgoose, Poobalasingam Abiman and Richard G. Compton, J. Mater. Chem., 2009, 19, 4875 – 4886
14 V. Datsyuk, M.K.K. Papagelis, J. Parthenios, D. Tasis, A. Siokou, I. Kallitsis, C. Galiotis. Carbon 2008, 46, 833-840.
15 J. Zhang, H. Zou, Q. Qing, Y. Yang, Q. Li, Z. Liu, X. Guo, Z. Du. J. Phys. Chem. B 2003, 107, 3712-3718.
16 F. Avilés, J. V. Cauich-Rodríguez, L. Moo-Tah, A. May-Pat, R. Vargas-Coronado, Carbon 2009, 47, 2970-2976
17 A. G. Osorio, I. C. L. Silveira, V. L. Bueno, C. P. Bergmann. Applied Surface Science 2008, 255, 2485–2489.
18 R. Usón, L. A. Oro J. A. Cabeza. *Inorg. Synth*. 1985, **23**, 126–127.
19 P. M. A. Sherwood in Practical Surface Analysis in Auger and X-ray Photoelectron Spectroscopy; D. Briggs, S. M. P. Eds.; Wiley: New York, 1990, Vol. 1, pp. 574.
20 D. Elgrabli, M. Floriani, S. Abella-Gallar, L. Meunier, C. Gamez, P. Delalain, F. Rogerieux, J. Boczkowski, G. Lacroix, *Part. Fibre Toxicol*. 2008, **5**, 20–33.
21 M. Blanco, P. Álvarez, C. Blanco, N. Campos, D. Gómez, R. Menéndez. Diam. Rel Mater. 2013, 37, 1-7.
22 M. S. Dresselhaus, G. Dresselhaus, R. Saito, A. Jorio. Physics Reports 2005, 409, 47–99
23 M. J. Park, J. K. Lee, B. S. Lee, Y. W. Lee, I. S. Choi, S. Lee. Chem. Mater. 2006, 18, 1546−1551.
24 C. Crotti, E. Farnetti, S. Filipuzzi, M. Stener, E. Zangrando, P. Moras. Dalton Trans. 2007, 133−142.
25 J. Lu, P. Serna, C. Aydin, N. D. Browning, B. C. Gates. J Am Chem Soc. 2011, 133, 16186–16195.
26 D. G. Reesa, P. J. Halling. Enzyme and Microbial Technology 2000, 27, 549–559.
27 F. Su, C. Lu, S. Hu. Colloids and Surfaces A, 2010, 353, 83-91.
28 F. Su, C. Lu, S. Hu. Applied Surface Science, 2008, 254, 7035-7041

ELECTRONIC SUPPORTING INFORMATION

Summary

Extended Characterization

- Raman Measurements
- TGA
- Elemental analyses
- Additional TEM images
- XPS measurements
- Gas chromatography data

Catalytic activity

EXTENDED CHARACTERIZATION

Raman measurements

Raman spectra of parent oxidized and treated carbon nanotubes are shown in Figure S.1. The characteristic D band (~1340 cm^{-1}), associated to the defects present in the structure, and the graphitic G band (~1580 cm^{-1}) appeared with the typical nanotube pattern. Interestingly, in every case the D band is increased comparing the functionalized sample with its corresponding parent nanotube material. This effect is commonly reported on the literature as a consequence of the positive functionalization. Table S.1 gathers the ID/IG ratios of parent and functionalized nanotubes

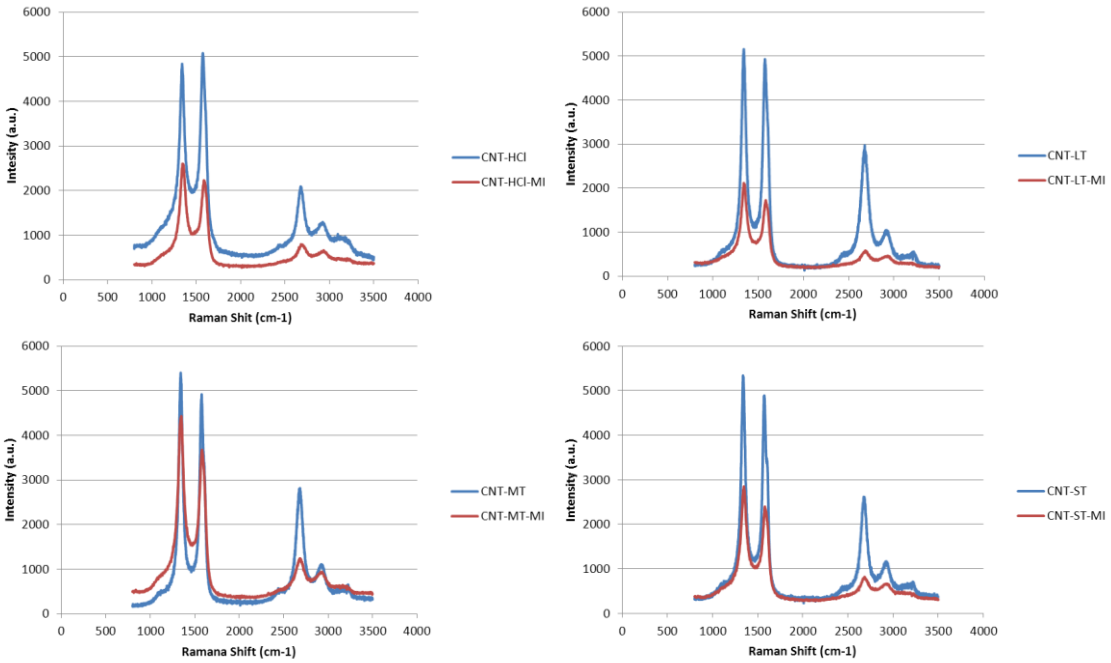

Figure S.1 Raman spectra

Table S.1 Raman ID/IG ratios

Sample	ID/IG
CNT-HCl	0.968
CNT-HCl-MI	1.123
CNT-LT	1.047
CNT-LT-MI	1.224
CNT-MT	1.077
CNT-MT-MI	1.213
CNT-ST	1.091
CNT-ST-MI	1.105

Thermogravimetric Analyses

Figure S.2 shows the TGA curves of the oxidized and the modified samples with N-methylimidazole, in which the modification is clear as the weight loss at 300 ºC – 400 ºC of the modified samples is different from their corresponding parent materials. This behavior is caused by the decoration of the carboxylic acids with the imidazole ring.

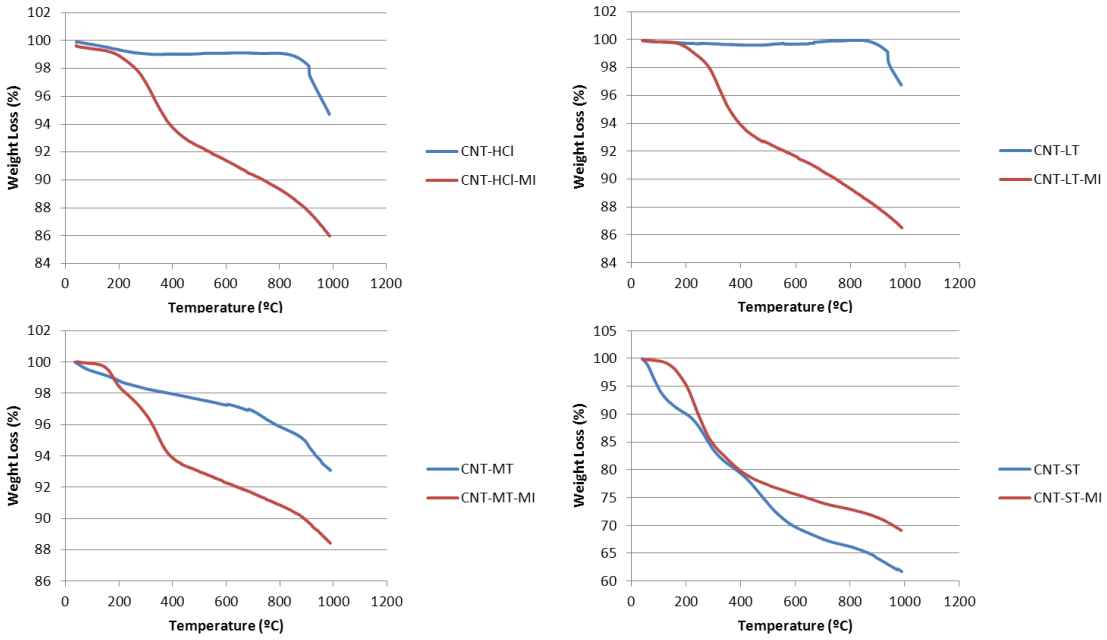

Figure S.2 TGA plots of the oxidized and treated samples

Elemental analysis

In Table S.2 are depicted the results from the elemental analyses of oxidized and imidazolium-modifies materials

Table S.2 Elemental analyses of the parent and treated carbon nanotubes

Sample	%C	%H	%N	%O	%S
CNT-HCl	97,47	0,19	0,40	1,72	0,22
CNT-HCl-MI	94,92	0,76	1,01	2,48	0,83
CNT-LT	96,08	0,24	0,57	2,31	0,49
CNT-LT-MI	93,89	0,76	1,56	2,76	0,68
CNT-MT	97,37	0,23	0,47	1,69	0,24

CNT-MT-MI	92,80	0,72	1,85	3,75	0,69
CNT-ST	78,02	0,90	0,10	20,94	0,04
CNT-ST-MI	72,93	2,04	2,33	21,56	1,53

It is noteworthy that the nitrogen content is incremented in all the functionalized samples regarding the corresponding parent material, which is in agreement with the introduction of the N-containing imidazole ring.

Additional TEM images

Any additional modifications or residues were found on the materials as a result of the functionalization treatment with the imidazolic compound or the organometallic complex (images on the main text) by comparison with the parent nanotubes.

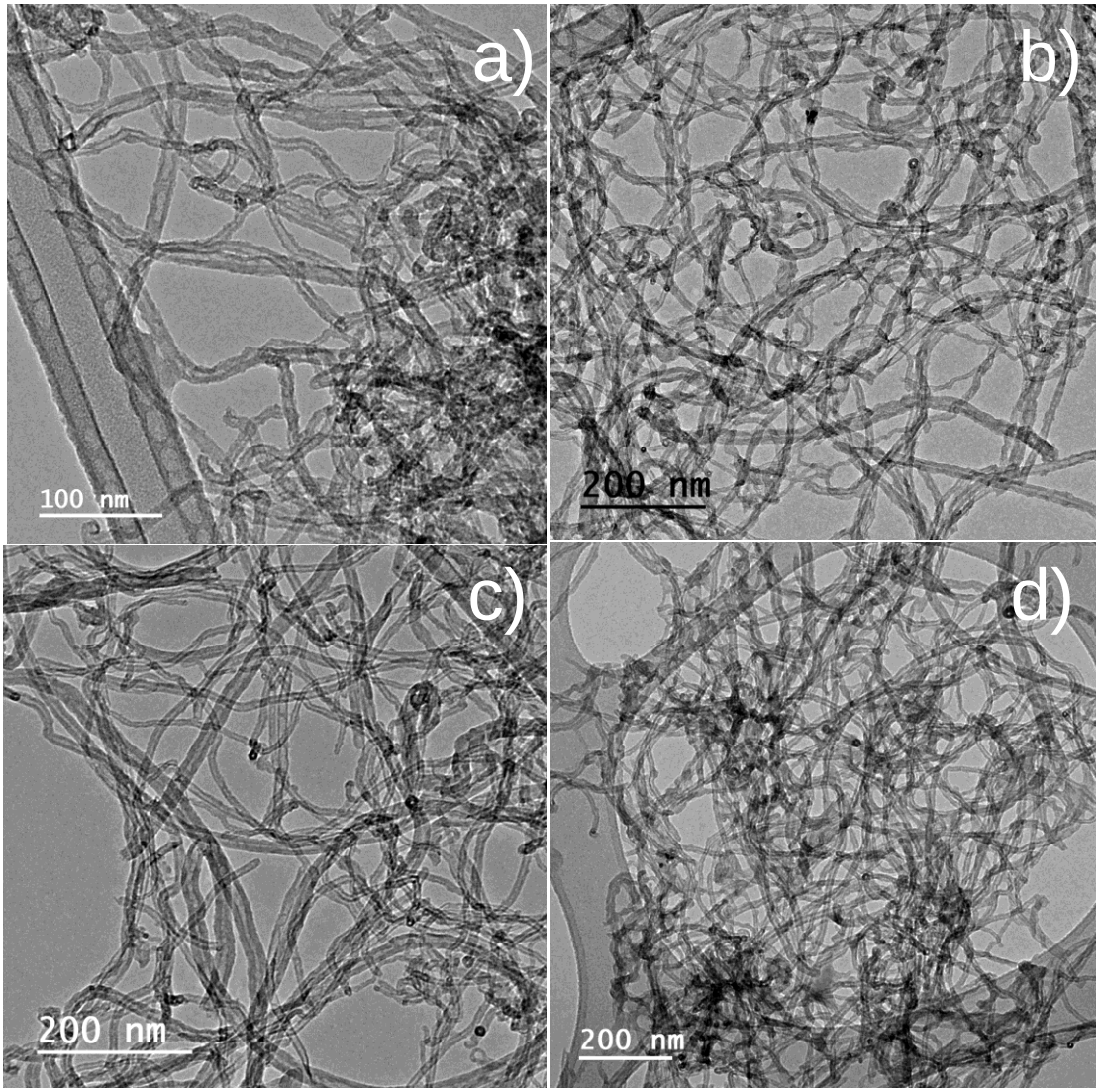

Figure S.3 TEM images of a) **CNT-HCl**, b) **CNT-LT**, c) **CNT-MT** and d) **CNT-ST**

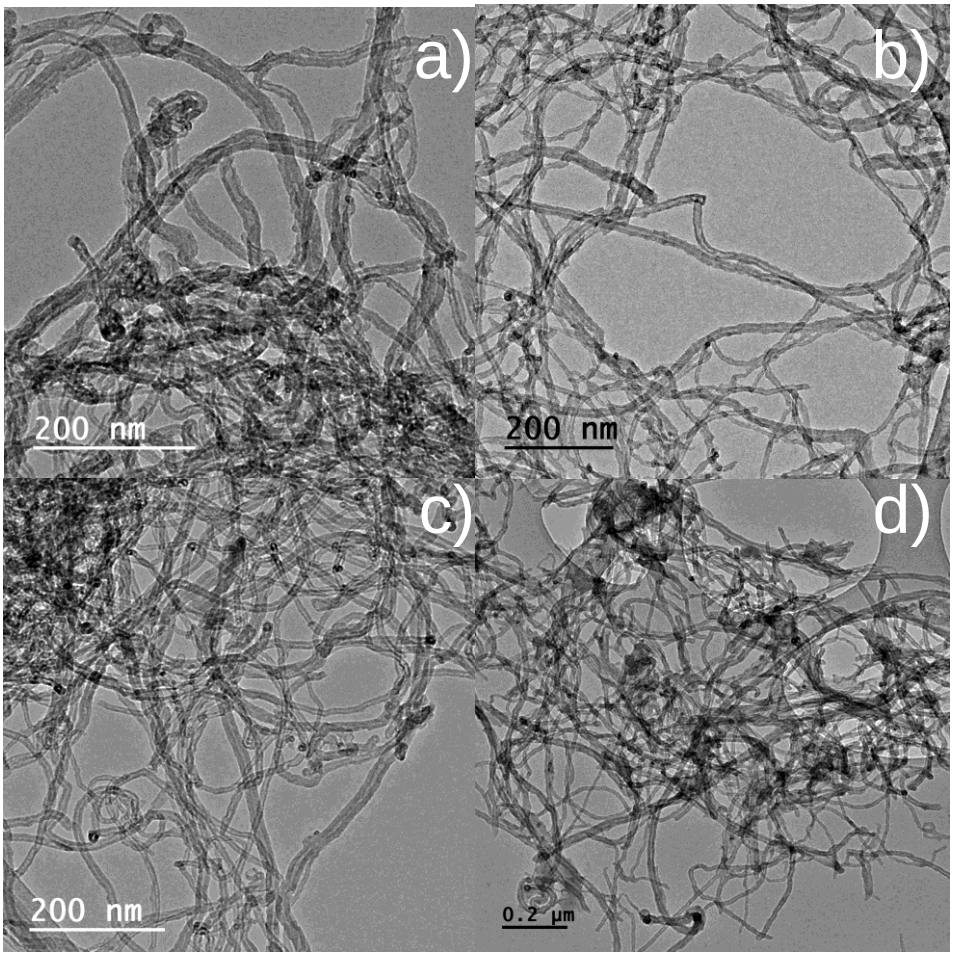

Figure S.4 TEM images of a) **CNT-HCl-MI**, b) **CNT-LT-MI**, c) **CNT-MT-MI** and d) **CNT-ST-MI**

EDX spectra of the iridium complexes supported on the nanotubes are shown in Figure S.5. The iridium atom is clearly detected.

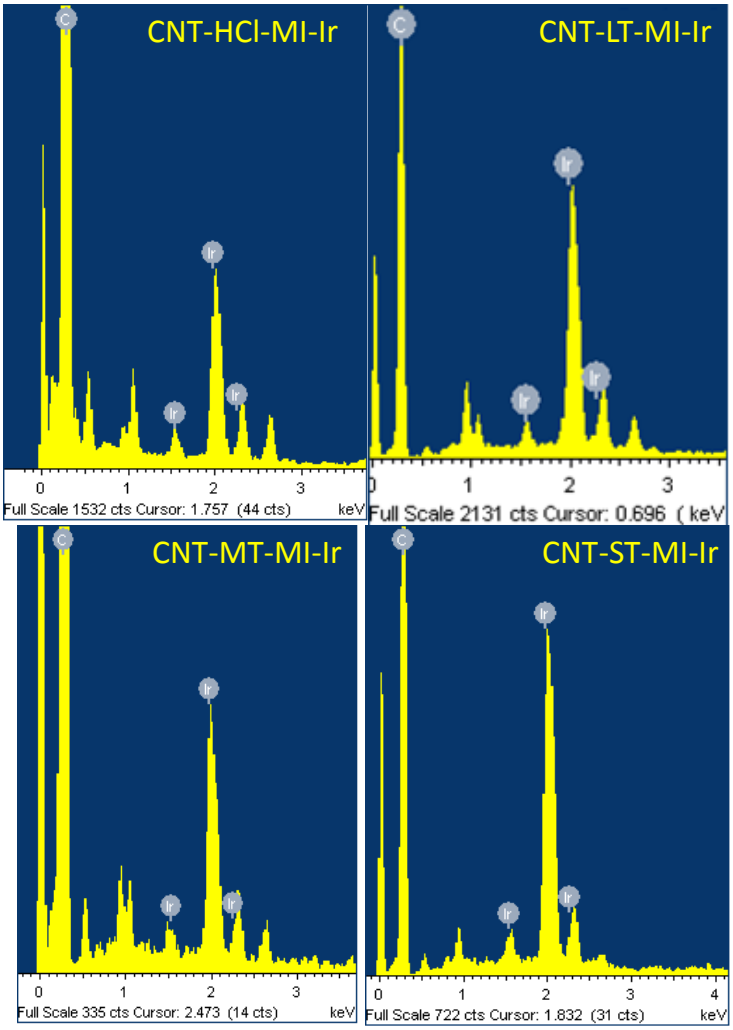

Figure S.5 EDX Spectra of iridium NHC functionalized samples.

XPS measurements

In table S.3 are shown the atomic percentages of N1s and Cl2p found on the XPS analysis of the imidazolium modified samples:

Table S.3 Atomic distribution of nitrogen and chlorine in the imidazolium modified samples

Sample	N1s (%)	Cl2p (%)
CNT-HCl-MI	0.9	0.5
CNT-LT-MI	1.4	0.6
CNT-MT-MI	1.7	0.8
CNT-ST-MI	2.2	1.3

Nitrogen and chlorine lies in the proper 2:1 ratio in all treated samples.

The XPS Ir4f region of the spectra of the iridium NHC supported on the different-oxidation-grade carbon nanotubes are depicted in Figure S.6. Maxima were found at 62.4 eV and 65.6 eV respectively, which totally correspond to iridium (I) species. These results are similar to those reported before with different Ir(I) NHC complexes supported on carbon nanomaterials by our group.

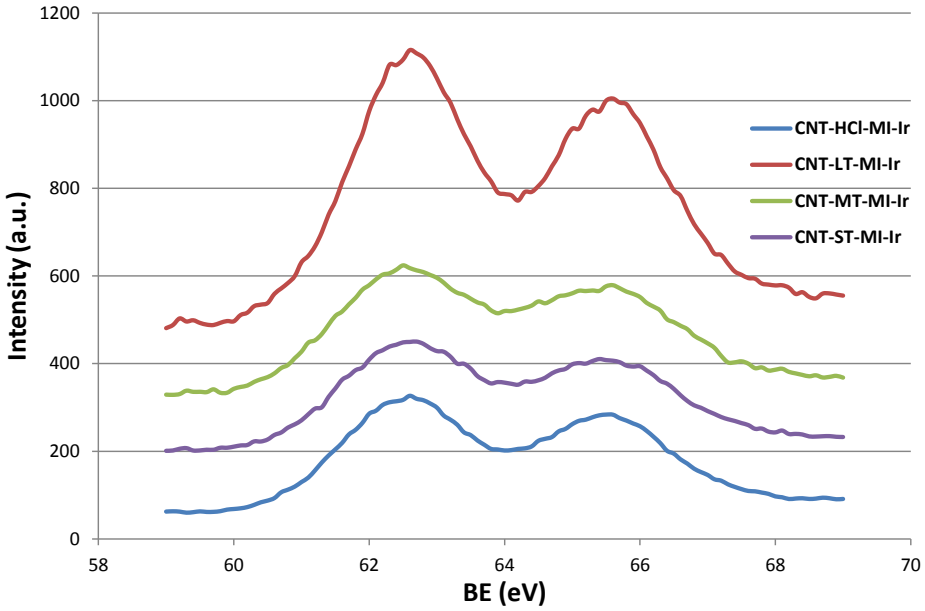

Figure S.6 XPS Ir4f region of the functionalized samples

Gas Chromatography data

The mother liquids of the reaction of the CNT-X-MI with $[Ir(\mu\text{-}OMe)(cod)]_2$ was analyzed by GC, detecting the presence of methanol after the deprotonation of the C2 carbon in the imidazole ring which led to the formation of the carbene. Figure S.7 depicts the chromatographic curves with the control experiment in order to identify the solvent peaks.

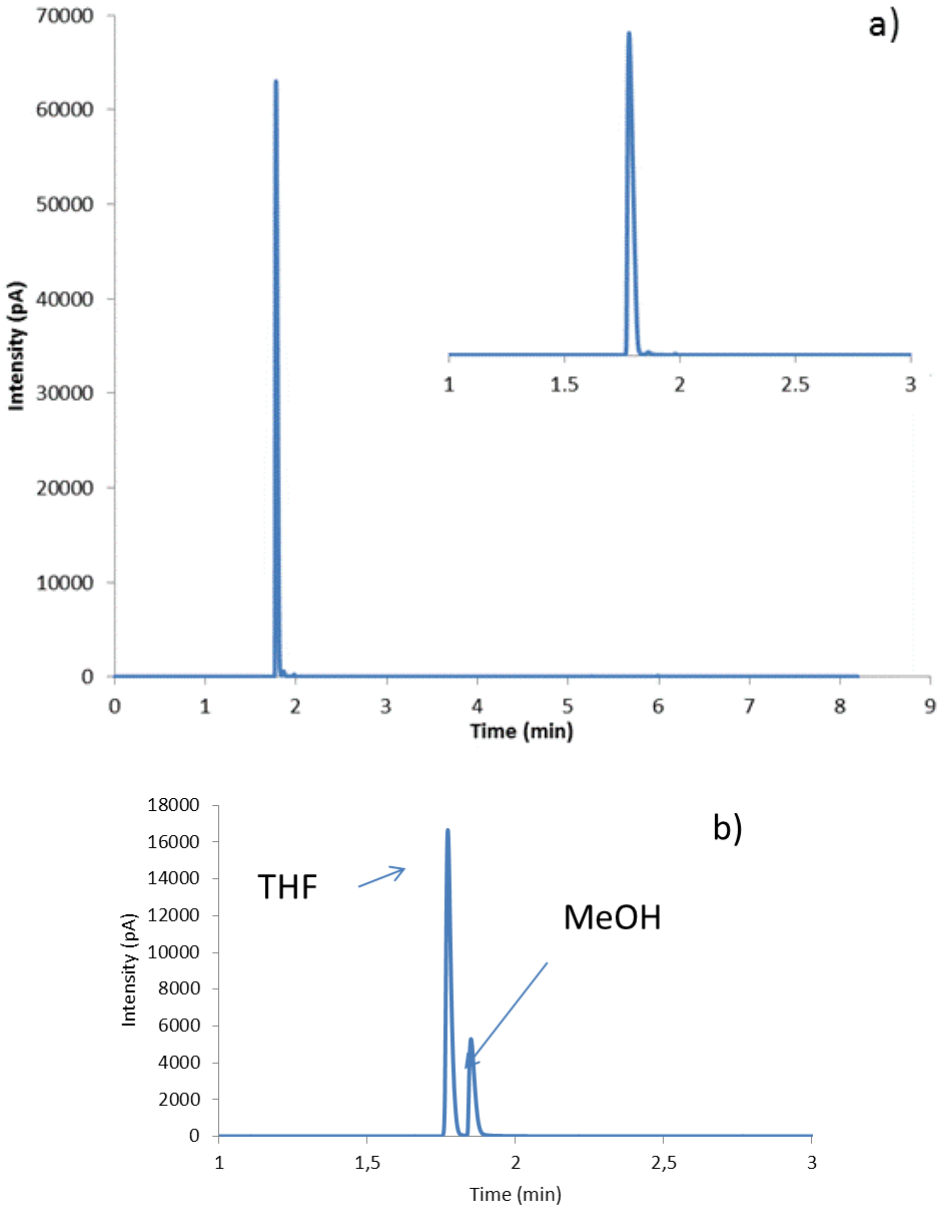

Figure S.7 Chromatographic plots of a) filtered mother liquid (inset: magnification) and b) control experiment.

CATALYTIC ACTIVITY

The hybrid materials catalytic performance in the transfer hydrogenation of cyclohexanone to cyclohexanol was evaluated using 2-propanol both as hydrogen source and as a non-toxic solvent. The catalytic conditions had been previously tested and optimized for a set of O-functionalized NHC iridium (I) related complexes, such as [IrBr(cod)(MeIm(2-methoxybenzyl))]. Standard catalyst loads of 0.1 mol%, with 0.5 mol% of KOH as co-catalyst, and 80 °C were routinely employed (Eq. (1)).

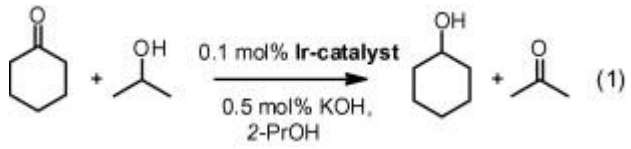

All the catalysts evaluated presented excellent cyclability performance (Figure S.8), obtaining similar conversions in related times. In addition, stability in air was evaluated carrying the last cycle out in air atmosphere. Any loss of activity was detected.

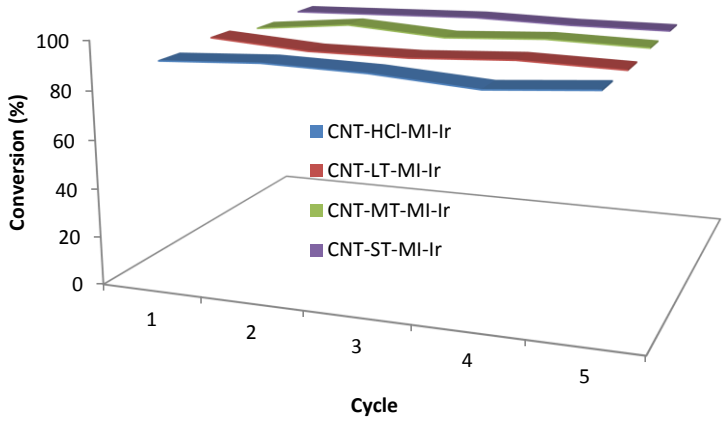

Figure S.8 Recycling studies.

4.4 ARTÍCULO IV

"Catalizadores híbridos grafeno-NHC-iridio construidos a través de un enlace covalente –OH"

Carbon **2015,** *83*, 21-31

Tras la funcionalización covalente de nanotubos de carbono a través de los grupos carboxilo, discutida en capítulos anteriores, el siguiente paso fue explorar la química de otros grupos funcionales oxigenados presentes en el esqueleto de los materiales oxidados. Tradicionalmente, muchos autores funcionalizaron materiales cerámicos, poliméricos y carbonosos aprovechando la gran afinidad que presentan los compuestos orgánicos de silicio con los grupos OH superficiales. Sin embargo, su gran toxicidad así como su complicado manejo supusieron su descarte a la hora de seleccionar esta estrategia.

Otros autores utilizaron reacciones orgánicas para la formación de un carbonato lábil que pudiese ser desplazado por un nucleófilo para la funcionalización de polímeros en sus grupos hidroxilo. Hasta donde nuestro conocimiento alcanzó, esta estrategia no se había empleado nunca con nanomateriales de carbono, ni siquiera con materiales de carbono en general. Por ello, se planteó la funcionalización selectiva de óxido de grafeno con complejos NHC de iridio empleando este nuevo procedimiento de decoración de grupos OH, y este es el tema sobre el que versa el contenido de este capítulo. Se emplearon también los correspondientes materiales grafénico obtenido por reducción térmica a 400 ºC, donde los ácidos carboxílicos fueron eliminados, pero aún persisten funciones oxigenadas que se pueden emplear en los tratamientos de funcionalización. Basándose en la experiencia adquirida con los nanotubos de carbono, se empleó como nucleófilo la sal de imidazolio **1** en todas

las muestras estudiadas al demostrar el correspondiente complejo NHC de iridio mayor actividad catalítica.

En primer lugar se caracterizaron los materiales de partida, observando como el método de síntesis de **GO-C** (se omite el sufijo C por claridad) genera un gran abanico de funciones oxigenadas, principalmente en forma de grupos OH y COOH. Al reducir el material térmicamente a 400 ºC para obtener **TRGO**, además de la eliminación de grupos oxigenados, se produce la reconstrucción parcial de la red aromática, aumentando el contenido de Csp^2 y disminuyendo el oxígeno. A pesar de la pérdida de hidrofilidad, la muestra reducida presenta un alto contenido de grupos OH con un contenido prácticamente despreciable de carboxilos.

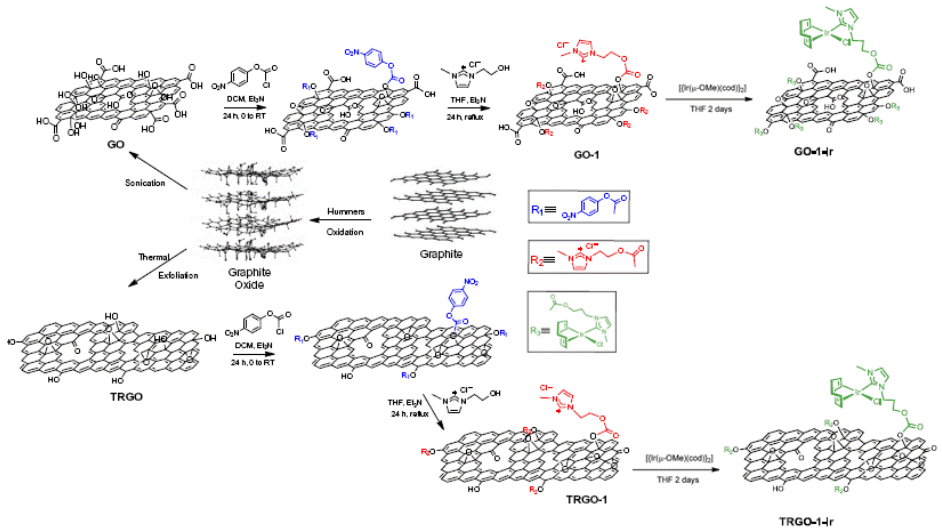

Figura 4.6 Ruta de funcionalización empleando los grupos OH

Tras el tratamiento de funcionalización, se comprobó que la sal de imidazolio **1** estaba covalentemente anclada a los nanomateriales, tanto en el oxidado **GO-1** como en el reducido **TRGO-1**, al no detectarse la señal del OH en los espectros de ^{1}H-RMN y observarse un aumento en el contenido de nitrógeno en los espectros XPS y

en las determinaciones de análisis elemental. Además, no se detectó señal alguna sobre la presencia del intermedio de reacción en ninguna de las muestras estudiadas, tanto el patrón de aromaticidad característico en ^{1}H-RMN ni la señal del grupo nitro en los espectros XPS y FTIR. Al introducir sobre los materiales modificados el complejo NHC de iridio (**GO-1-Ir** y **TRGO-1-Ir**), se detectó la presencia de spots de tamaño adecuado (0,15-0,3 nm) mediante observación de las muestras al microscopio de transmisión, que se correspondían con iridio (I) en sus espectros XPS. Tras estos resultados, quedaba demostrada la eficacia del nuevo método de funcionalización de nanomateriales de carbono. Muestras de control con los propios soportes (oxidado y reducido) tratados con el complejo precursor de iridio (**GO-Ir** y **TRGO-Ir**) presentaron partículas más grandes con el iridio más oxidado, como resultado de una posible reacción con los grupos funcionales libres.

Los materiales híbridos grafeno-NHC-iridio, así como las muestras de control, se utilizaron como catalizadores en la reacción de reducción de ciclohexanona a ciclohexanol. La figura 4.7 muestra la actividad catalítica de las muestras, donde se aprecia la baja conversión en los casos donde no se forma el complejo NHC. En cuanto a los materiales híbridos, ambos sistemas consiguen alcanzar conversiones completas, presentando además una excelente ciclabilidad y estabilidad al aire como en el caso de los nanotubos tratados en el capítulo anterior. No obstante, existe una gran diferencia de comportamiento entre el catalizador oxidado y el reducido, atribuible al mayor contenido de Csp^2 que presenta el último, junto con la presencia de grupos carboxilos libres en el primero, los cuales pueden capturar iridio disminuyendo la eficacia del sistema. Finalmente, el catalizador soportado sobre el material grafénico reducido presentó una mejor actividad que el complejo homogéneo **5** (identificado como **Ir-ImidO**), justificable por las interacciones positivas que el soporte puede ejercer sobre el metal, las cuales no se pueden dar en el caso homogéneo.

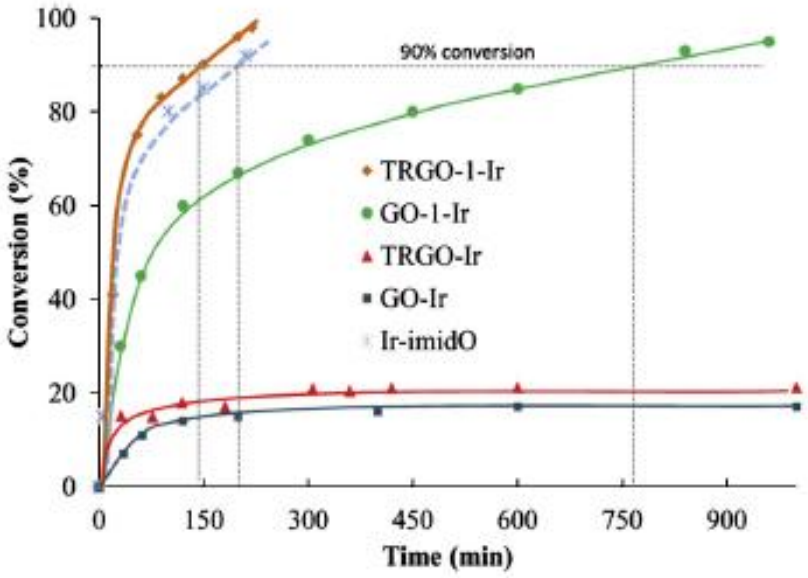

Figura 4.7 Actividad catalítica de los híbridos grafeno-NHC-iridio, muestras de control y complejo homogéneo **Ir-imidO**.

Available at www.sciencedirect.com
ScienceDirect
journal homepage: www.elsevier.com/locate/carbon

Graphene–NHC–iridium hybrid catalysts built through –OH covalent linkage

Matías Blanco[a], *Patricia Álvarez*[a], *Clara Blanco*[a], *M. Victoria Jiménez*[b,*], *Javier Fernández-Tornos*[b], *Jesús J. Pérez-Torrente*[b], *Luis A. Oro*[b], *Rosa Menéndez*[a,*]

ARTICLE INFO

Article history:

Received 18 August 2014 Accepted 7 November 2014 Available online 17 November 2014

Dedicated to the lasting Memory of Prof. Dr. María Pilar García for her valuable talent as human, teacher and chemist

* Corresponding authors.

E-mail addresses: vjimenez@unizar.es (M.V. Jiménez), rosmenen@incar.csic.es (R. Menéndez).

http://dx.doi.org/10.1016/j.carbon.2014.11.016 0008-6223

0008-6223

ABSTRACT

Graphene oxide (GO) and thermally reduced graphene oxide (TRGO) were covalently modified with imidazolium salts through their hydroxyl surface groups. The selective reaction of the –OH groups with *p*-nitrophenylchloroformate produced labile intermediate organic carbonate functions which were used for the covalent anchoring of a 197hloride-functionalized imidazolium salt. Nanohybrid materials containing iridium N-heterocyclic carbene (NHC)-type organometallic complexes were prepared by causing the imidazoliumfunctionalized materials to react with $[Ir(\mu\text{-}OMe)(cod)]_2$. The iridium content of the graphene-based hybrid catalysts, as determined by XPS and ICP-MS was the order of aprox. 5 and 10 wt.%, for the TRGO and GO-based materials, respectively. The graphene-supported iridium hybrid materials were active in the heterogeneous hydrogen-transfer reduction of cyclohexanone to cyclohexanol with 2-propanol/KOH as the hydrogen source. The thermally reduced graphene–NHC–iridium hybrid catalyst showed the best catalytic performance with an initial TOF of 11.500 h^{-1}, slightly better than the related acetoxyfunctionalized NHC iridium homogeneous catalyst. A good catalyst recyclability and stability were achieved.

1. Introduction

Graphenes are nowadays used in many research areas due to their unique properties, such as their excellent electronic behavior, their highly aromatic lattice which confers an exceptional mechanical strength and their extraordinary chemical stability in most reaction media [1–3]. These properties make them outstanding

supports for developing versatile matrixes for heterogeneous catalysts with an enhanced activity [4–6]. Graphene oxide (GO) is usually obtained by the chemical oxidation of graphite, a method which is also considered nowadays as one of the most promising for producing graphene materials on a large scale [7,8]. Structurally, GO can be considered as a graphene sheet decorated with oxygen functional groups at the basal planes (i.e. epoxy and hydroxyl groups) and edges (carboxylic acids), and with variable amounts of sp^3 hybridized carbon atoms disrupting the typical sp^2 carbon structure of graphene [9–11]. This distinctive structure of GO can easily be chemically functionalized to expand their field of application.

Functionalized graphene oxide has been extensively applied to a large number of different fields such as composite materials, catalysis, optoelectronics, supercapacitors, memory devices and drug delivery [12–14]. Furthermore, the presence of oxygen functional groups on the aromatic scaffold of GO allows these sheets to mediate ionic and nonionic interactions with a wide range of molecules. Interestingly, GO by itself or in combination with other materials, shows remarkable catalytic properties [15–18]. It is known that the presence of epoxy and hydroxyl functional groups on either side of the GO sheet imparts bifunctional properties that allow it to act as a structural node within metal–organic frameworks (MOFs), resulting in an enhancement of the catalytic activity due to synergistic effects between the framework and the catalytically active center [19]. In contrast, very few examples of supported molecular organometallic compounds on functionalized graphene oxides are reported to show catalytic activity [20–25]. In these cases, a covalent linkage between the carbonaceous surface and the organometallic compound is highly desirable in order to reduce leaching. The common strategies described in the literature to achieve covalent functionalization make use of the carboxylic groups that decorate the edges of the GO sheets. An example of this is the esterification with nucleophiles (such as alcohols, amines or amino acids), directly in basic medium, [26,27] or in the presence of $SOCl_2$, [28] oxalyl chloride, [29] or DCC (dicyclohexyl carbodiimide) [30,31]. Other oxygen-containing groups, different from carboxylic acids, are thermally more stable than the acid groups [32] and are therefore accessible within reduced graphene oxides (TRGO) in which the sp^2 carbon structure has been partially restored. For example, epoxy groups at the basal planes of the sheets have been used for functionalization via the amine groups of ionic liquids [33]. On the other hand, hydroxyl groups have been scarcely explored for the functionalization of graphene derivatives [34]. Most of the reported methods make use of difficult-

handling and toxic siloxane derivatives [35] and, as far as the authors are awared, none of them has been used to prepare hybrid catalyst by anchoring of organometallic species.

A number of highly efficient iridium-NHC (NHC = N-heterocyclic carbene) hydrogen transfer catalysts have been reported [36–46]. In particular, iridium (I) complexes with hemilabile O- and N-donor functionalized NHC ligands, with methoxy, dimethylamino, and pyridine as donor functions, are efficient catalyst precursors for transferring the hydrogenation of unsaturated compounds using 2-propanol/KOH as hydrogen source [47,48]. Interestingly, we have recently observed that iridium-NHC catalysts supported on carbon nanotubes via carboxylic acids exhibit an enhanced hydrogen- transfer catalytic activity compared to other related homogeneous systems [49].

The aim of this work is to prepare graphene-based hybrid catalysts by the covalent functionalization of GO and TRGO through their surface –OH groups. The grafting of the GO/TRGO surface with NHC ligand precursors was achieved by causing hydroxo-functionalized imidazolium salts to react with intermediate carbonate species. The imidazolium-functionalized graphene materials were used to prepare hybrid materials containing iridium–NHC type organometallic complexes which were evaluated as heterogeneous catalysts for the hydrogen transfer reduction of cyclohexanone over several cycles in order to determine the recyclability and stability of the supported catalysts. In addition, the catalytic activity of a related homogeneous acetoxy-functionalized NHC iridium catalyst is described for comparative purposes.

2. Experimental

2.1. Materials

All the chemicals, including powder graphite, were purchased from Aldrich. Reagent or HPLC grade qualities were employed in all the experiments. Solvents were distilled immediately prior to use from the appropriate drying agents or obtained from a Solvent Purification System (Innovative Technologies). The GO utilized in this work was prepared by applying a modified Hummers method to the commercial graphite as described previously [50]. TRGO was obtained from the corresponding graphite oxide by thermal treatment at 400 ºC in a horizontal furnace, under a nitrogen flow of 50 mL min^{-1}. The residence time at the final temperature was 60 min [50]. The imidazolium salt [MeImH$(CH_2)_3$OH]Cl (**1**), [51] the starting organometallic compound [Ir(μ-Ome)(cod)]$_2$ [52] and the acetoxy- NHC carbene complex [IrCl(cod)(MeIm$(CH_2)_3$OCOCH$_3$] (**Ir-**

ImidO) [49] were prepared according to standard literature procedures.

2.2 Characterization of graphene materials and hybrid catalysts

NMR spectra were recorded on a Bruker Advance 400 spectrometer operating at 400.16 MHz (^{1}H). NMR chemical shifts are reported in ppm relative to tetramethylsilane and referenced to partially deuterated solvent resonances. The catalytic reactions were analyzed on an Agilent 4890 D system equipped with an HP-INNOWax capillary column (0.4 μm, 25m x 0.2 mm i.d.) using mesitylene as internal standard. Thermogravimetric analyses (TGA) of the materials were performed in a TA SDT 2960 analyzer thermobalance. The procedure used was as follows: 3 mg of sample was heated in the thermobalance at 10 ºC min^{-1} to 1000 ºC using a nitrogen flow of 100 mL min^{-1}. Transmission electron microscopy (TEM) spectra were obtained on a JEOL 2000 EX-II instrument operating at 160 kV. High-resolution images of transmission electron microscopy HRTEM were recorded using a JEOL JEM-2100F transmission electron microscope, equipped with a field-emission-gun (FEG) operating at 200 kV. Energy-dispersive X-ray spectroscopy (EDX) was used to verify the atomic composition of the catalyst. The samples were prepared by casting a few drops of 1 mg mL^{-1} ethanol suspensions of the materials over the carbon grids. To minimize exposure of the samples to the air, these were transferred to the lacey carbon grid in a glovebox filled with ultrahigh-purity argon and then to the TEM holder in order to minimize the time required to introduce them into the microscope. Elemental analyses were performed on a LECO-CHNS-932 micro-analyser equipped with a LECO-VTF-900 furnace coupled to the micro-analyzer. The X-ray photoemission spectroscopy (XPS) spectra were recorded using a SPECS system operating under a pressure of 10^{-7} Pa with a Mg Ka X-ray source. Functional groups in the graphene materials were quantified by deconvolution of the high resolution C1s XPS peak employing Gaussian and Lorentzian functions [53]. The binding energy profiles were deconvoluted into the following: undamaged structures of sp^2-hybridized carbon (284.5 eV), damaged structures or sp^3-hybridized carbons (285.5 eV), C–O groups (286.5 eV), C=O functional groups (287.7 eV) and COO groups at 288.7 eV. The amount of iridium present in the samples was determined by means of Inductively Coupled Plasma Mass Spectrometry (ICP-MS) in an Agilent 7700x instrument. The samples were digested following a method described elsewhere [54]. Briefly, 30mg of sample was treated with 5 mL of a mixture of concentrated nitric and hydrochloric acid (3:1 ratio) at 180 ºC for 3 h under microwave irradiation.

2.3. Functionalization of graphene materials with 1-(3-hydroxypropyl)-3-methyl-1H-imidazol-3-ium chloride (1)

Both types of graphene materials (GO and TRGO) were functionalized with the imidazolium salt, 1-(3-hydroxypropyl)-3- methyl-1H-imidazol-3-ium chloride, [MeImH$(CH_2)_3$OH]Cl (**1**), following a two-step procedure. GO or TRGO (100 mg) was dispersed in 20 mL of dichloromethane (DCM). The resulting dispersion was cooled to 0 ºC in an ice bath and then, *p*-nitrophenylchloroformate (3.0 g, 15 mmol) and trimethylamine (2.1 mL, 15 mmol) were added under an inert atmosphere. The mixture was stirred for 24 h and allowed to reach room temperature slowly. The resulting solids were filtered and washed three times with DCM (20 mL) and then dried under vacuum for 2 h. In a second step, the imidazolium salt **1** (100 mg, 0.560 mmol) and a catalytic amount of trimethylamine (0.2 mL) were added, under an inert atmosphere, to the dispersions of graphene solids obtained in step 1 in tetrahydrofuran (THF) (15 mL), and refluxed for 24 h. The products were obtained by centrifugation/filtration, washed with THF (3 x 20 mL), DCM (3 x 20 mL), and ethanol (3 x 20 mL) and then, vacuum dried at 100 ºC in a preheated furnace until constant weight. The graphene samples obtained were labeled as **GO-1** and **TRGO-1** depending on the parent material used in each case, GO or TRGO, respectively.

In another experiment, a dispersion of GO (100 mg) in THF (15 mL) was refluxed for 24 h. Centrifugation/ filtration, washing with THF, DCM and ethanol, and vacuum drying at 100 ºC yielded the material **GO-Blank**.

2.4. Preparation of hybrid catalysts GO-1-Ir and TRGO-1- Ir

Imidazolium functionalized graphene materials, **GO-1** or **TRGO-1** (100 mg), were reacted with [Ir(μ-Ome)(cod)]$_2$ (100 mg, 0.150 mmol) in THF (10 mL) under an argon atmosphere. The mixtures were refluxed for 2 days and then immersed in an ultrasonic bath for 30 min at room temperature. The resultant solids were recovered by centrifugation, washed with THF (5 x 10 mL) and diethyl ether (2 x 5 mL), and dried under vacuum to produce **GO-1-Ir** and **TRGO-1-Ir**.

2.5. General procedure for transfer hydrogenation catalysis

The catalytic transfer hydrogenation reactions were carried out under an argon atmosphere in thick glass reaction tubes fitted with a greaseless high-vacuum stopcock. In a typical experiment, the reactor was charged with a solution of cyclohexanone (0.52 mL, 5.0 mmol) in 2-propanol (4.5 mL), internal standard

(mesitylene, 70 lL, 0.5 mmol), base (0.1 mL, 0.025 mmol of a KOH solution 0.24 M in 2-propanol) and the catalyst (0.005 mmol, 0.1 mol%). The weight of the supported catalysts used in each experiment was calculated according to ICP measurements, assuming that all the iridium in the sample corresponded to active catalyst sites, 9.34 mg of **GO-1-Ir** (10.2 %wt. of iridium) and 20.44 mg of **TRGO-1-Ir** (4.7 %wt. of iridium). The resulting mixture was stirred at room temperature until complete dissolution of the homogeneous catalyst, [IrCl(cod)(MeIm(CH_2)$_3$ $OCOCH_3$] (Ir-ImidO), [50] or for 10 min in the case of the heterogeneous catalyst, and then placed in a thermostatic oil bath at the required temperature, typically 80 ºC. Conversions were determined by gas chromatography analysis under the following conditions: a column temperature of 35 ºC (2 min) up to 220 ºC at 10 ºC/min, a flow rate of 1 mL/min using ultrapure He as carrier gas.

Once the reaction was completed, the hybrid catalysts were recovered by centrifugation and washed with additional amounts of 2-propanol (3 x 10 mL). Several catalytic cycles were performed with these materials, under the same experimental conditions, without adding any fresh catalyst precursor. The last cycle was carried out without an inert atmosphere.

3. Results and discussion

3.1 Functionalization of the –OH groups in graphene oxide (GO) and partially reduced graphene oxides (TRGO)

GO was synthesized from commercial graphite by means of the Hummers method. Following this procedure and, after sonication, water or dichloromethane homogeneous dispersions of monolayers of sp^2 carbon atoms decorated with different oxygen-containing functional groups were obtained (see Supporting information for details). As can be seen from the XPS images (Fig. 1a), the functional groups include carboxylic acids (7.9%), C=O (17.8%) and C–O (29.6%) groups. The presence of these functionalities at the basal planes of the sheet (alcohol or epoxy groups) or at the edges/holes (carboxylic acids, C=O groups) provides anchorage sites for the covalent linkage of different ligands allowing the formation of hybrid materials. However, the amount of carbon atoms in the sp^2 hybridization (36.2%) is quite modest compared to that of graphene. [55,56] Nevertheless, thermal treatment of graphite oxide at 400 ºC (**TRGO**, Fig. 1b) has led to the partial reconstruction of the sp^2 carbon structure (up to 71.4%), due to the elimination of the thermally unstable oxygen functional groups at this temperature (thermal reduction). Despite the inherent loss of

hydrophilicity, the thermally stable functional groups that are still remaining in **TRGO** allow to form stable water and dichloromethane suspensions. The most abundant oxygen-containing functions are the C–O groups (11.5%), while the COO content (including acid groups, that are the less thermally stable) [32,57] has decreased to 2.4%. In view of the decrease in the content of acid groups in this reduced material, the OH groups of both **TRGO** and the parent **GO**, were functionalized. This functionalization was achieved by means of the two-step procedure depicted in Fig. 2. In a first step, **GO** and **TRGO** materials were made to react with *p*-nitrophenyl chloroformate. This reagent selectively reacts with ‘‘isolated’’ hydroxyl groups with the subsequent formation of the corresponding *p*-nitrophenyl carbonate esters [58,59,34]. In a second step, the carbonates were treated with the imidazolium salt [MeImH$(CH_2)_3$OH]Cl (**1**), which contains a nucleophilic OH-ending group, in refluxing tetrahydrofuran for 24 h, resulting in the formation of new carbonate graphene derivatives, **GO-1** and **TRGO-1**, after *p*-nitrophenol displacement by the nucleophile OH-ending group of **1**.

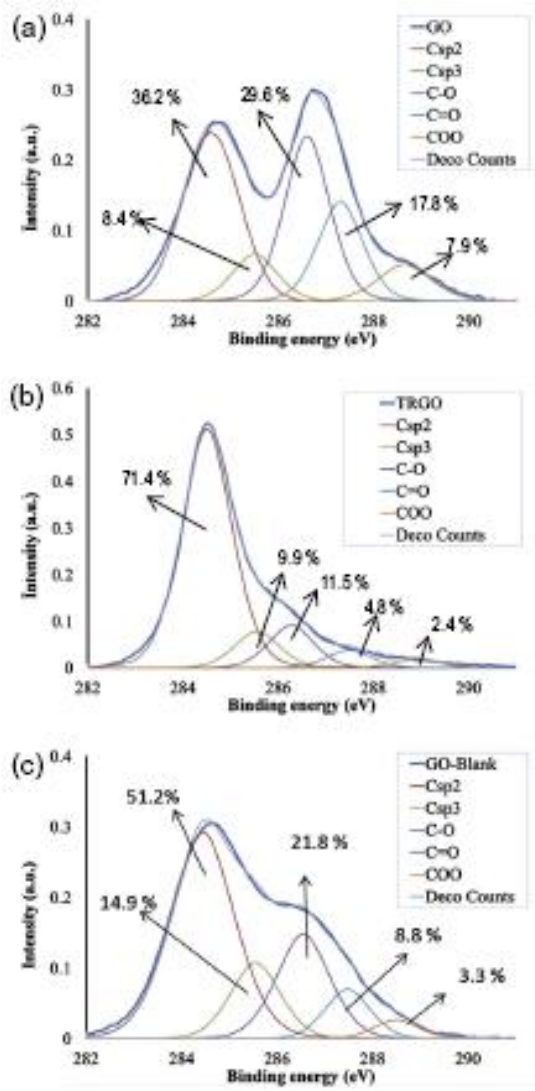

Fig. 1 XPS C1s spectra and deconvoluted curves of: (a) **GO**, (b) **TRGO**, and (c) **GO-Blank**.

GO-1 and **TRGO-1** form relative stable suspensions in acetone (see Supporting information), which allows them to be characterized by NMR spectroscopy. The ^{1}H NMR (acetone-d_6) spectra exhibit the typical set of signals for the imidazolium groups, at 7.41/7.35 ppm (H4 and H5) and 8.64 ppm (H2). Neither the corresponding signals of the nitrophenyl fragment nor the imidazolic –OH group can be observed in the spectra, which is in agreement with a covalent linkage of **1** to the graphene materials. The relatively few protons present in the graphene-based layered material are not noticeable in the ^{1}H NMR due to

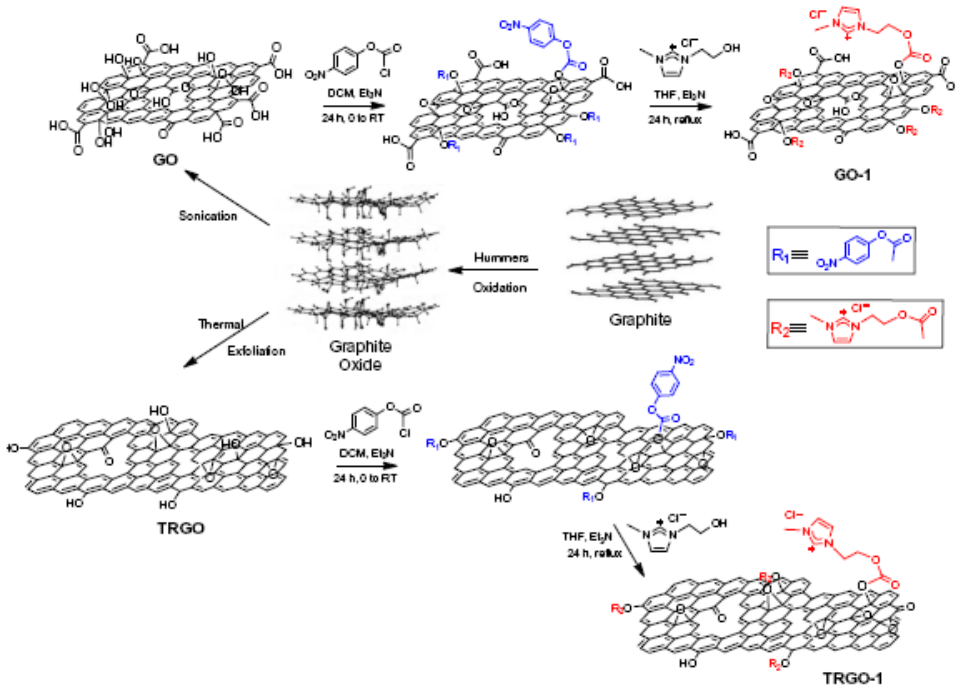

Fig 2. Covalent functionalization of the parent graphene materials, GO and TRGO, with the imidazolium salt [MeImH$(CH_2)_3$OH]Cl (**1**).

their poor relaxation, as is the case of the related CNT-based materials [49]. This precludes the characterization of the samples by solid-state ^{13}C-CP MAS NMR spectroscopy (see Supporting information).

It is well known that certain oxygen-containing functional groups of GO readily decompose at relatively low temperatures because of their low thermal stability [50]. Therefore, for comparative analytical purposes, a GO-Blank sample was prepared by refluxing suspensions of **GO** in boiling THF for 24 h. **TRGO** is obtained at much higher temperature making the relative material **TRGO-Blank** irrelevant. Comparison of the TGA curves of **GO** and **GO-Blank** obtained under nitrogen

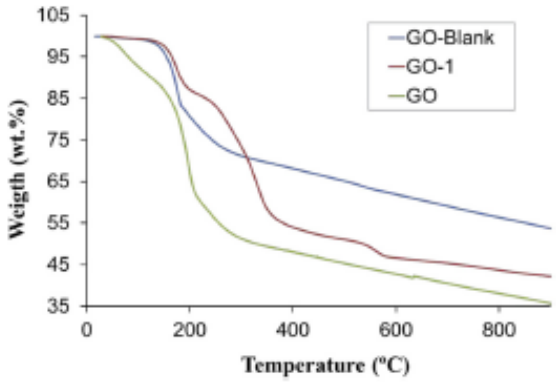

Fig. 3 Thermogravimetric analysis profiles of **GO**, **GO-1** and **GO-Blank**.

(Fig. 3) confirm the significant lower weight loss of **GO-Blank** at temperatures below 110 ºC, which is related with the elimination of carboxylic acids and/or, to a lesser extent, hydroxyl or epoxy groups located in the interior of the aromatic domains under the processing conditions established [60]. This result was corroborated by XPS analysis of the **GO-Blank** which shows a diminished amount of all types of C–O functional groups with the decrease in acid groups down to 3.3% (Fig. 1c). It can be therefore conclude that a large amount of the carboxylic acids in **GO** were lost due to the reaction conditions applied for the preparation of **GO-1**, and not due to reaction with the confirming the highly selective anchoring of the imidazolium to the –OH functionalities on the graphene material surface.

The imidazolium functionalization of **GO-1** and **TRGO-1** was further confirmed by elemental analysis (Table 1). The increase in the nitrogen content with respect to the parent GO and TRGO, from 0.1 wt.% in the parent samples up to 6.9 and 1.4 wt.% for **GO-1** and **TRGO-1**, respectively is consistent with the attachment of the imidazolium ligand to the

Table 1. Elemental analysis and XPS data of parent graphene materials (GO and TRGO) and imidazolium functionalized graphene-based materials (**GO-1** and **TRGO-1**).

Sample	Elemental analysis (wt. %)				XPS (%)	
	C	H	N	O	N	Cl
GO	49.1	2.4	0.1	48.4	0.0	0.0
TRGO	74.1	0.6	0.0	25.3	0.0	0.0
GO-1	51.8	3.4	6.9	37.9	5.6	2.5
TRGO-1	76.8	1.4	1.4	20.3	1.4	0.6

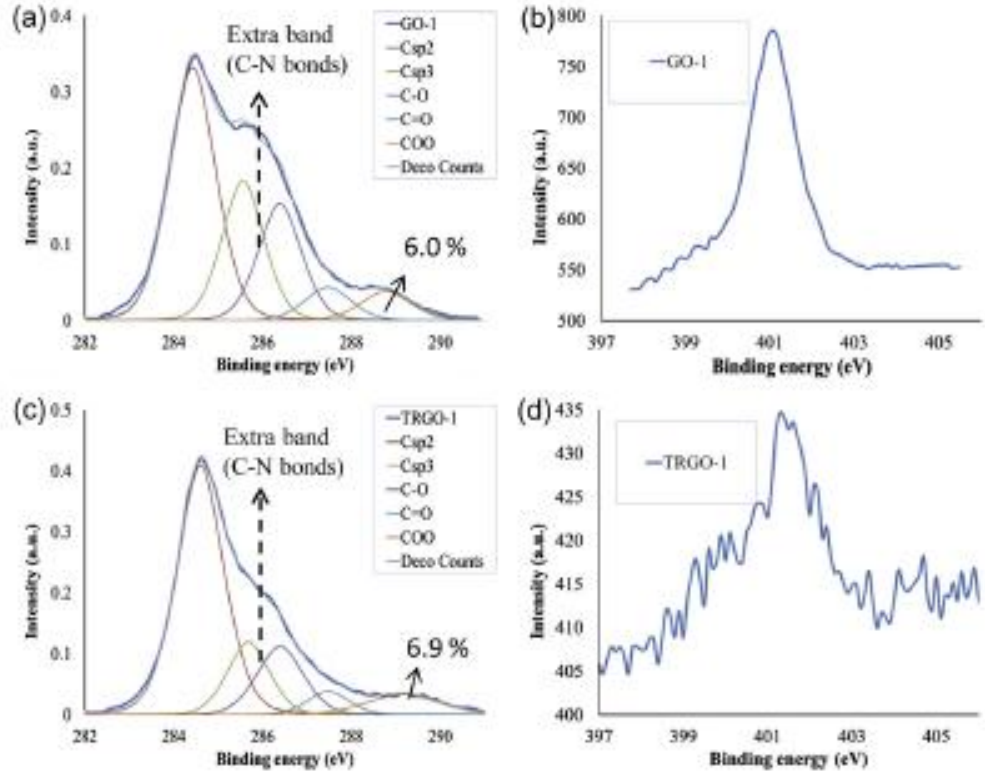

Fig 4. XPS C1s (a, c) and N1s (b, d) spectra and deconvoluted curves of the imidazolium functionalized graphene materials: (a, b) **GO-1**, and (c, d) **TRGO-1**.

graphene sheets. The smaller amount of nitrogen content in **TRGO-1** compared to that of **GO-1** is obviously related with the small number of C–O groups in the parent thermally reduced sample, which restricts its capacity to bond imidazolium salt. The increase in the atomic nitrogen content in these samples as calculated by XPS (Table 1) is also in agreement with the above conclusions. Furthermore, chlorine atoms were detected by XPS in a ratio 2:1 with the nitrogen content.

A detailed analysis of the high-resolution XPS C1s peaks of **GO-1** and **TRGO-1** (Fig. 4a and b, respectively) show a band typical for the C–N which is not present either in the parent materials or in the GO-Blank. Unfortunately, this band lies in between the Csp^3 and C–O bands, preventing its quantification. The increment in the intensity of the COO band in **TRGO-1** and **GO-1** with respect the parent **TRGO** and the thermally treated **GO-Blank** (to discriminate between the effect of temperature on the elimination of functional groups) is mainly ascribed to new carbonate groups that have been formed in the functionalization process. The XPS N1s spectra of the samples only show bonds typical of

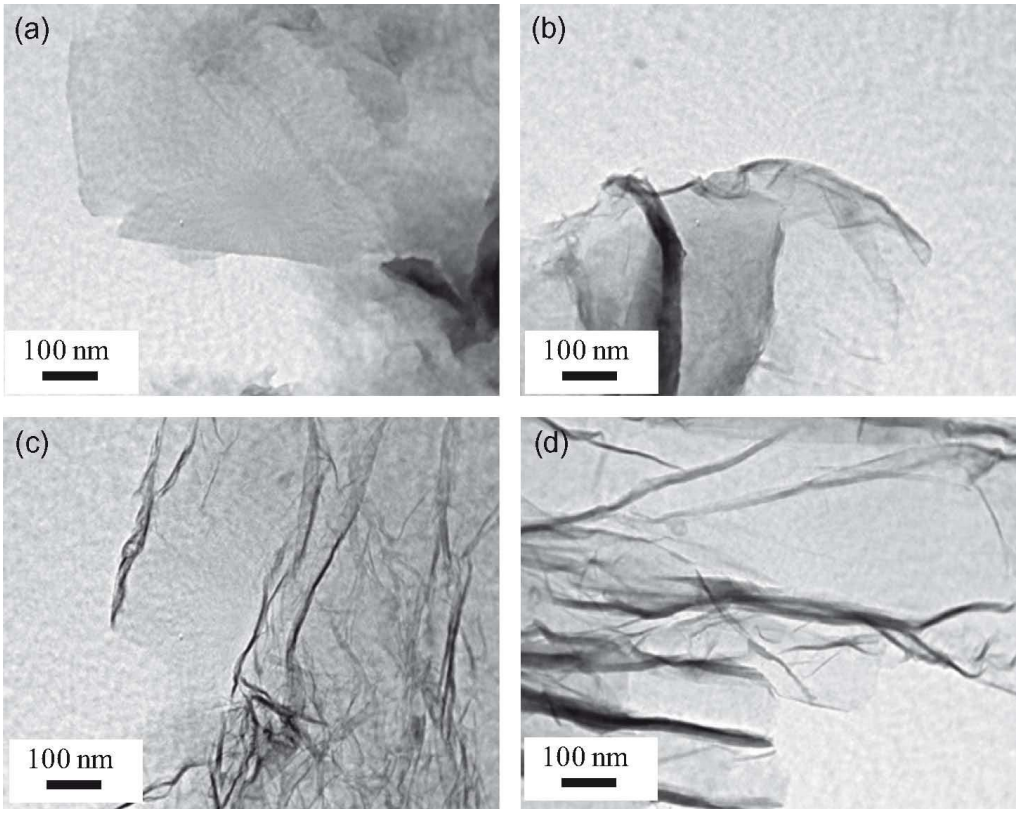

Fig 5. TEM images of (a) **GO**, (b) **TRGO**, (c) **GO-1**, and (d) **TRGO-1**.

imidazolium functional groups, while there is no evidence of NO_2 bonding (at 405 eV). This result is coherent with the displacement of the *p*-nitrophenol fragment what has been also corroborated by the FTIR spectra of intermediates and products, since the typical bands ascribed to the nitrophenyl group disappear after reaction with the imidazolium salt **1** (see S.I.).

The TEM images of **GO-1** and **TRGO-1** (Fig. 5c and d) are similar to those of the corresponding precursors, **GO** and **TRGO** (Fig. 5a and b). The thermally reduced samples also show the expected wrinkled appearance which indicates that functionalization has not caused any damage to the graphene layers.

3.2 Synthesis and characterization of hybrid graphene based- iridium catalysts

Hybrid catalysts containing supported iridium N-heterocyclic carbene (NHC) complexes, **GO-1-Ir** and **TRGO-1-Ir**, were prepared by reaction of the methoxo iridium(I) dimer compound $[Ir(\mu\text{-}Ome)(cod)]_2$ (cod = 1,5-cyclooctadiene) with the imidazolium

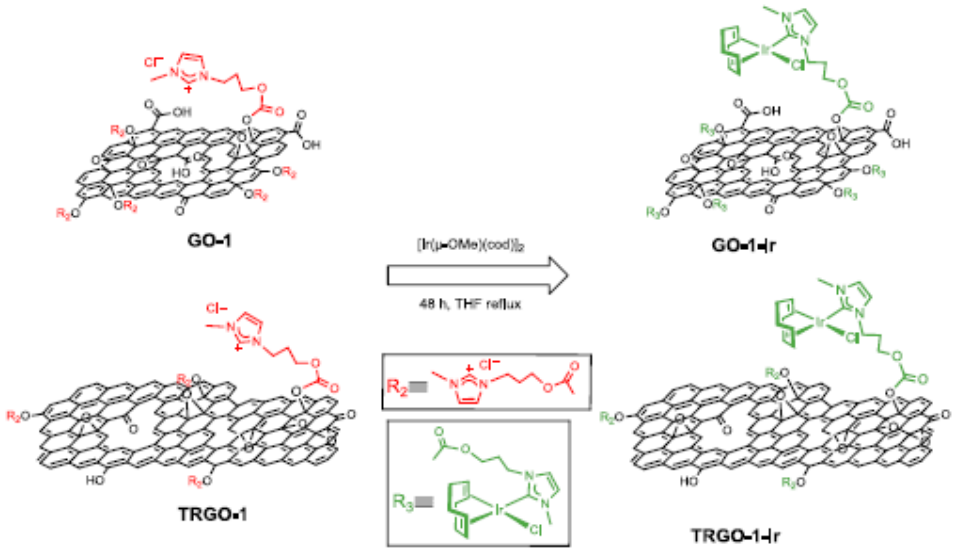

Fig 6. Synthesis of hybrid graphene-based-Ir-NHC materials.

functionalized graphene materials, **GO-1** and **TRGO-1**, as depicted in Fig. 6. Insoluble materials were obtained in both cases, probably as a consequence of the increment in the molecular weight, which prevents their characterization in solution by NMR. Evidence for the successful anchoring of the NHC–iridium complexes on the graphene oxide sheets was obtained by XPS spectroscopy. The materials **GO-Ir** and **TRGO-Ir** were prepared for comparative purposes by reaction of the unfunctionalized **GO** and **TRGO** (lacking the supported imidazolium ligand) with $[Ir(\mu\text{-Ome})(cod)]_2$.

The high-resolution Ir4f XPS band obtained for the hybrid graphene-based-iridium catalysts (Fig. 7) shows the two peaks characteristic of the iridium ($Ir4f_{7/2}$ and $Ir4f_{5/2}$). Both peaks are centered at 62.4 and 65.6 eV for the functionalized materials containing the NHC linkers, **GO-1-Ir** and **TRGO-1- Ir**. These values compare well with those of related iridium(I) compounds, [61] or nanotube-supported iridium–NHC hybrid materials recently reported by us [49]. However, in reference materials **GO-Ir** and **TRGO-Ir** which lack NHC linkers, the maxima have shifted towards higher binding energies, 63.0 and 66.1 eV, respectively. This suggests that in the absence of the imidazolium ligand **1** the iridium centers might be present in a higher oxidation state (i.e. iridium oxide) [62] or alternatively, taking part in very different iridium species, as for example, iridium nanoparticles, [63] carboxylate-complexes, [64,65] or clusters, [66,67].

The amount of iridium in the hybrid catalysts, as determined by means of ICP- MS measurements, was 10.2 wt.% for **GO-1-Ir** and 4.7 wt.% for

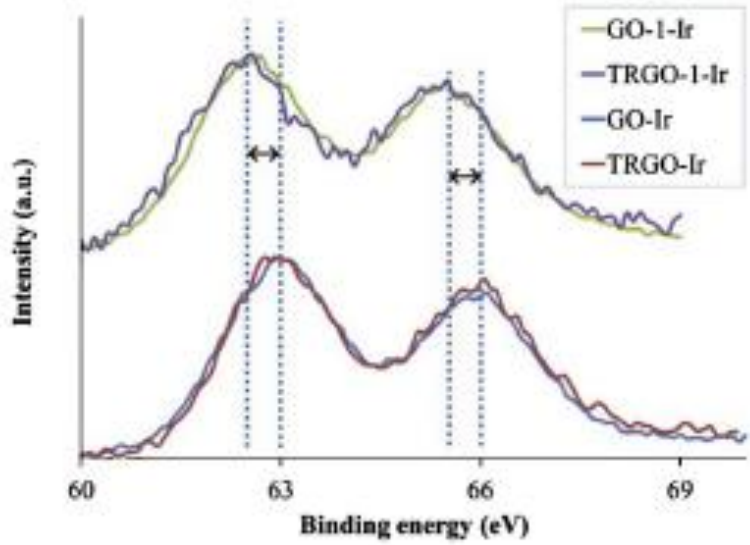

Fig 7. XPS spectra for the Ir4f core level of the graphene based iridium hybrid catalysts

TRGO-1-Ir. In agreement with these results, the atomic ratio C/Ir calculated by means of XPS was 25 for **GO-1-Ir** and 155 for **TRGO-1-Ir**. The iridium percentage in the **TRGO-1-Ir** material lies in the expected range according to the imidazolium salt linked to the material. However, for **GO-1-Ir** the iridium content is below the estimated value, which could be attributed to steric hindrance derived of the high density of functional groups. [55] For the samples lacking imidazolium functionality, **GO-Ir** and **TRGO-Ir**, the amount of iridium loaded was higher, 19.9 and 6.0 wt.%, respectively, most probably as a result of the different mode of attachment of the iridium to the oxygen functional groups of the graphene-based materials.

HRTEM images obtained for **GO-1-Ir** (Fig. 8) show the presence of supported iridium species homogeneously distributed on the surface of the graphene sheets, which is also confirmed by EDX spectroscopy (see Supporting information). Iridium species with diameters as low as 0.17–0.27 nm and as great as 1.2–1.4 nm and even larger were observed. According to other authors, these findings could be attributed to the presence of molecular iridium complexes anchored on the surface (lower diameters) together with iridium clusters or nanoparticles possibly formed by beam damage in an attempt to measure and determine the cause of iridium migration. These electron-dense regions have also been observed in the characterization of related molecular iridium analogues [49].

Although there is no direct evidence of the covalent coordination of the

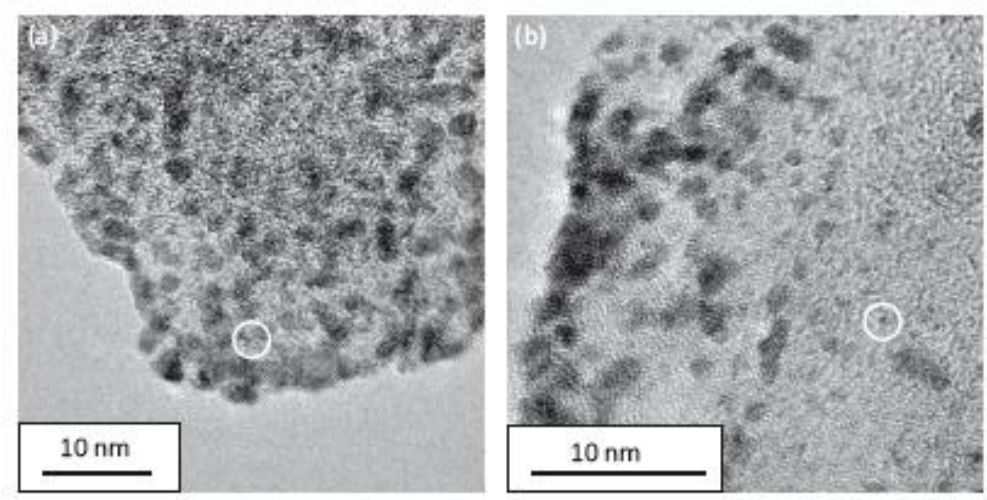

Fig 8. XPS spectra for the Ir4f core level of the graphene based iridium hybrid catalysts

IrCl(cod) metal fragments to the NHC functionalities decorating the graphene-based materials, the above results suggest that functionalization of the nanomaterials is achieved via the carbene atom of the heterocycle moiety in a similar way to that of the Ir-NHC homogeneous catalysts.

3.3 Hydrogen-transfer catalytic activity

GO-1-Ir and **TRGO-1-Ir** graphene-based materials having supported iridium NHC species were tested as catalysts for the hydrogen transfer reduction of cyclohexanone to cyclohexanol (Fig. 9) using 2-propanol both as hydrogen source and as a non-toxic solvent with a moderate boiling point. The catalytic transfer hydrogenation of several unsaturated substrates, including cyclohexanone, under homogeneous conditions had been previously tested and optimized for a set of O-functionalized NHC iridium(I) related complexes i.e. [IrBr(cod)(MeIm(2-methoxybenzyl))] [47]. Standard catalyst loads of 0.1 mol%, with 0.5 mol% of KOH as co-catalyst, and 80 ºC were routinely employed (Eq. (1)). The iridium supported catalysts prepared without

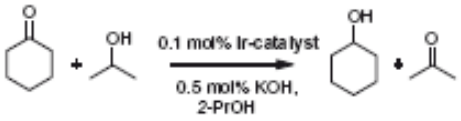

Fig 9. Equation of the hydrogen transfer reduction of cyclohexanone to cyclohexanol

imidazolium ligand, **GO-Ir** and **TRGO-Ir**, and the related molecular acetoxy-functionalized NHC complex [IrCl(cod)(MeIm$(CH_2)_3OCOCH_3$] (**Ir-ImidO**) [49] were also evaluated for comparative purposes. It is noteworthy that none of the iridium free graphene-based materials showed any catalytic activity.

Reaction profiles obtained of the heterogeneous and homogeneous

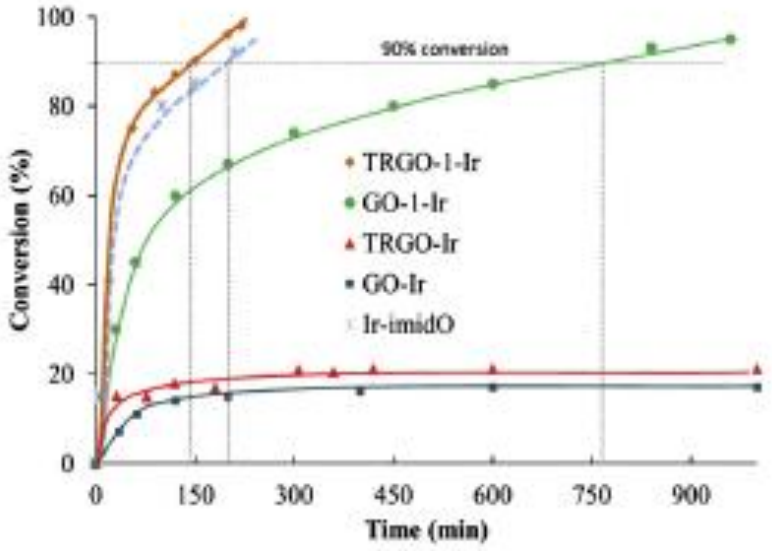

Fig 10. XPS spectra for the Ir4f core level of the graphene based iridium hybrid catalysts

catalysts are shown in Fig. 10. The relevant reaction parameters, including the reaction times required to reach 90% conversion and the turnover frequencies (TOF), for all the examined catalysts are summarized in Table 2. As can be seen in the conversion vs time reaction profiles (Fig. 10), no induction period was detected, as cyclohexanone reduction was observed immediately after the thermal equilibration of the reactant mixture. The reaction profiles illustrate the outstanding catalytic activity of the graphene supported iridium–NHC hybrid materials, **GO-1-Ir** and **TRGO-1-Ir**, compared to those materials when there is no a NHC linker between the carbon material and iridium, **GO-Ir** and **TRGO-Ir**. In fact, these materials became deactivated after 3 h and achieved less than 20% conversion. **TRGO-1-Ir** had best catalytic performance, performing even better than the homogeneous acetoxy-functionalized NHC catalyst [IrCl(cod)(MeIm$(CH_2)_3$OCOCH$_3$] (**Ir-ImidO**).

The reaction time required by **TRGO-1-Ir** to reach 90% conversion (as determined by GC using mesitylene as internal standard) was 150 min, a much shorter time than that observed for the homogeneous catalyst [IrCl(cod)(MeIm$(CH_2)_3$OCOCH$_3$] (**Ir-ImidO**) which was 200 min, and much better than the 760 min required by the **GO-1-Ir** material. These results point out to the influence of the graphene support in the enhancement of catalytic activity when compare with the homogeneous system. On the other hand, the superior catalytic

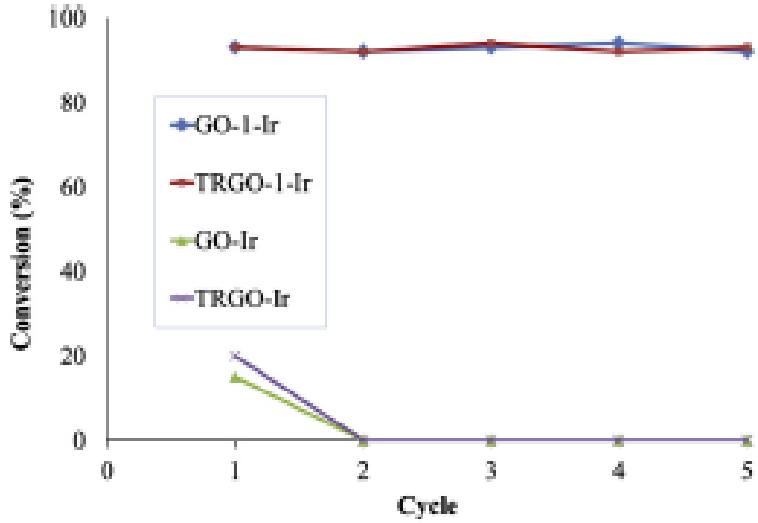

Fig 11. Reaction profiles showing the transfer hydrogenation of cyclohexanone by homogeneous and heterogeneous catalysts

activity of **TRGO-1-Ir** may be a consequence of the structural features of the reduced graphene material. The larger structural carbon sp^2 area of **TRGO** compared with the parent **GO** sample will also the poor catalytic performance of **GO- 1-Ir** could be related with the large variety of oxygen functional groups in this sample. These other groups (e.g. carboxylic acids) could also be reacting with the iridium precursor in a competitive way leading to the formation of iridium carboxylate or alkoxide complexes that have a much lower catalytic activity than the supported iridium NHC species.

Successful recycling studies were carried out on both graphene-supported iridium–NHC hybrid catalysts **GO-1-Ir** and **TRGO-1-Ir**. The catalyst without NHC linkers, **GO-Ir** and **TRGO-Ir**, showed no catalytic activity at all after the first cycle probably due to leaching of the iridium compounds after washing (Fig. 11). The recycling procedure simply requires filtration, washing of the catalysts with fresh 2-propanol (4 x 5 mL), and addition of further cyclohexanone/KOH/i-PrOH. This process was repeated four times in a protected atmosphere, and in the fifth run, the catalytic reactions were conducted in air. The results of cyclohexanone conversion after each catalytic run, with reaction times of 2.5 h for **TRGO-1-Ir** and 12.5 h for **GO-1-Ir**, are depicted in Fig. 10. Both graphene-supported iridium–NHC hybrid catalysts exhibited comparable conversions (Fig. 11) and with similar reaction profiles (see S.I.) in the successive experiments, even for the fifth cycle under no protected

Table 2. Catalytic hydrogen transfer from 2-propanol to cyclohexanone using graphene–Ir–NHC and graphene–Ir hybrid catalysts, and the related acetoxy-functionalized NHC-Ir homogeneous catalyst (**Ir-ImidO**).[a,b]

Catalyst	Time (min)[c]	TON	TOF_0 (h^{-1})[d]	TOF_{90} (h^{-1})
GO	760	947	11364	75
TRGO	150	964	11568	385
GO-1	-	147	441	-
TRGO-1	-	203	609	-
Ir-ImidO	200	941	11124	282

[a]Reaction conditions: a catalyst/substrate/KOH ratio of 1/1000/5, 0.1 mol% of catalyst in 5mL 2-propanol (5 mL) at 80 ºC. [b]The reactions were monitored by GC using mesitylene as internal standard. [c]Reaction time at 90% of conversion. [d]TOF, turnover frequency [(mol product/mol catalyst)/time (h)] were calculated at initial time of the reaction TOF_0, or at 90% of conversion TOF_{90}, respectively.

atmosphere. In contrast, the acetoxy-functionalized iridium–NHC homogeneous catalysts (**Ir-ImidO**) could not be recycled due to the difficulty of catalyst/products separation in addition to its air-sensitivity.

4. Conclusions

We have demonstrated that graphene oxides and partially reduced graphene oxides can be successfully functionalized through the hydroxyl surface groups. Covalent anchoring of A 214hloride-functionalized imidazolium salt was achieved through labile intermediate organic carbonate functions prepared by selective reaction of the –OH surface groups with pnitrophenylchloroformate. The imidazolium functionalized graphene materials were used to prepare hybrid materials containing supported iridium N-heterocyclic carbene (NHC) complexes covalently bonded through carbonate functions.

The hybrid graphene–iridium–NHC materials were successfully applied as catalysts in the hydrogen transfer reduction of cyclohexanone to cyclohexanol using 2-propanol as hydrogen source. Both heterogeneous catalysts showed similar reaction profiles thus suggesting a similar operating mechanism. Interestingly, a superior catalytic performance was achieved with the partially reduced graphene-based material. This catalytic activity was also slightly superior to that of the related acetoxy-functionalized NHC iridium homogeneous catalyst. This is probably due to the positive effect of the restored sp^2 carbon structure in partially reduced graphenes.

In contrast, the presence of remaining oxygen functional groups as competitive sites for the support of poorly active iridium complexes seems to be the reason for the low catalytic performance of hybrid catalyst based on graphene oxide lacking NHC-linkers.

It has also been demonstrated that the graphene-based heterogeneous hybrid catalysts remained stable through successive catalytic runs. The supported catalyst can be reused in five consecutive cycles without any loss of activity, even under an air atmosphere.

Acknowledgments

The authors thank the Spanish Ministry of Economy and Competitiveness (MINECO/FEDER) (Projects Consolider Ingenio 2010 CSD2009-00050 and CTQ 2013-42532-P), and the Diputación General de Aragón (E07) for their financial support. Dr. P. A. thanks MICINN for a Ramón y Cajal contract. J. F-T. and M. B. acknowledge their fellowships from MINECO and MECD (AP2010-0025). We thank Dr. Jose Maria Fraile (ISQCH, Universidad de Zaragoza-CSIC) for helpful discussion on ^{13}C-CPMAS.

Appendix A. Supplementary data

Supplementary data associated with this article can be found, in the online version, at http://dx.doi.org/10.1016/j.carbon.2014.11.016.

References

[1] Mao HY, Laurent S, Chen W, Akhavan O, Imani M, Ashkarran AA, *et al.* Graphene: promises, facts, opportunities, and challenges in nanomedicine. Chem Rev 2013;113:3407–24.

[2] Haddon RC. Graphene – the mother of two-dimensional (2-D) materials. Acc Chem Res 2013;46:1–3.

[3] Park S, Ruoff RS. Chemical methods for the production of graphenes. Nat Nanotechnol 2009;4:217–24.

[4] Dai L. Functionalization of graphene for efficient energy conversion and storage. Acc Chem Res 2013;46:31–42.

[5] Park J, Yan M. Covalent functionalization of graphene with reactive intermediates. Acc Chem Res 2013;46:181–9.

[6] Schaetz A, Zeltner M, Stark WJ. Carbon modifications and surfaces for Catalytic Organic Transformations. ACS Catal 2012;2:1267–84.

[7] Marcano DC, Kosynkin DV, Berlin JM, Sinitskii A, Sun Z, Slesarev A, *et al.* Improved synthesis of graphene oxide. ACS Nano 2010;4:4806–14.

[8] Zhao J, Pei S, Ren W, Gao L, Cheng H. Efficient preparation of large-area graphene oxide sheets for transparent conductive films. ACS Nano 2010;4:5245–52.
[9] Lerf A, He H, Forster M, Klinowski JJ. Structure of graphite oxide revisited. Phys Chem B 1998;102:4477–82.
[10] Szabo T, Berkesi O, Forgo P, Josepovits K, Sanakis Y, Petridis D, *et al.* Evolution of surface functional groups in a series of progressively oxidized graphite oxides. Chem Mater 2006;18:2740–9.
[11] Dreyer DR, Park S, Bielawski CW, Ruoff RS. The chemistry of graphene oxide. Chem Soc Rev 2010;39:228–40.
[12] Ramanathan T, Abdala AA, Stankovich S, Dikin DA, Herrera-Alonso M, Piner RD, *et al.* Functionalized graphene sheets for polymer nanocomposites. Nat Nanotechnol 2008;3:327–31.
[13] González Z, Botas C, Álvarez P, Roldán S, Blanco C, Santamaría R, *et al.* Thermally reduced graphite and graphene oxides in VRFBs. Carbon 2012;50:828–34.
[14] Krishnamoorthy K, Mohan R, Kim S. Graphene oxide as a photocatalytic material. J Appl Phys Lett 2011;98:244101.
[15] Navalo S, Dhakshinamoorthy A, Alvaro M, Garcia H. Carbocatalysis by graphene-based materials. Chem Rev 2014;114:6179–212.
[16] Shi P, Dai X, Zheng H, Li D, Yao D, Yao W, *et al.* Synergistic catalysis of Co_3O_4 and graphene oxide on Co_3O_4/GO catalysts for degradation of Orange II in water by advanced oxidation technology based on sulfate radicals. Chem Eng J 2014;240:264–70.
[17] Su C, Loh KP. Carbocatalysts: graphene oxide and its derivatives. Acc Chem Res 2013;46:2275–85.
[18] Pyun J. Graphene oxide as catalyst: application of carbon materials beyond nanotechnology. Angew Chem Int Ed 2011;50:46–8.
[19] Jahan M, Bao QL, Loh KP. Electrocatalytically active graphene porphyrin MOF composite for oxygen reduction reaction. J Am Chem Soc 2012;134:6707–13.
[20] Sabater S, Mata JA, Peris E. Catalyst enhancement and recyclability by immobilization of metal complexes onto graphene surface by noncovalent interactions. ACS Catal 2014;4:2038–47.
[21] Zhao Q, Li Y, Liu R, Chen A, Zhang G, Zhang F, *et al.* Enhanced hydrogenation of olefins and ketones with a ruthenium complex covalently anchored on graphene oxide. J Mater Chem A 2013;1:15039–45.
[22] Stankovich S, Piner RD, Chen X, Wu N, Nguyen ST, Ruoff RS. Synthesis of graphene-based nanosheets via chemical reduction of exfoliated graphite oxide. J Mater Chem 2006;16:155–8.
[23] Stankovich S, Piner RD, Nguyen ST, Ruoff RS. Synthesis and exfoliation of isocyanate-treated graphene oxide nanoplatelets. Carbon 2006;44:3342–7.
[24] Stankovich S, Dikin DA, Dommett GHB, Kohlhaas KM, Zimney EJ. Graphene-based

composite materials. Nature 2006;442:282–6.
[25] Viculis LM, Mack JJ, Mayer OM, Hahn HT, Kaner RB. Intercalation and exfoliation routes to graphite nanoplatelets. J Mater Chem 2005;15:974–8.
[26] Kakran M, Sahoo GN, Bao H, Pan Y, Li L. Functionalized graphene oxide as nanocarrier for loading and delivery of ellagic acid. Curr Med Chem 2011;18:4503–12.
[27] Mallakpour S, Abdolmaleki A, Borandeh S. Covalently functionalized graphene sheets with biocompatible natural amino acids. Appl Surf Sci 2014;307:533–42.
[28] Xu C, Wang X, Wang J, Hu H, Wan L. Modification of the electronic structures of graphene by viologen. Chem Phys Lett 2010;498:162–7.
[29] Karousis N, Economopoulos SP, Sarantopoulou E, Tagmatarchis N. Porphyrin counter anion in imidazolium modified graphene-oxide. Carbon 2010;48:854–60.
[30] Liu Y, Yu D, Zeng C, Miao Z, Dai L. Biocompatible graphene oxide-based glucose biosensors. Langmuir 2010;26:6158–60.
[31] Shen J, Shi M, Yan B, Ma H, Li N, Hu Y, *et al.* Covalent attaching protein to graphene oxide via diimide-activated
amidation. Colloid Surf B: Biointerfaces 2010;81:434438.
[32] Figueiredo JL. Modification of the surface chemistry of activated carbons. Carbon 1999;37:1379–89.
[33] Yang H, Shan C, Li F, Han D, Zhang Q, Niu L. Covalent functionalization of polydisperse chemically-converted graphene sheets with amine-terminated ionic liquid. Chem Commun 2009:3880–2.
[34] Shi J, Wang L, Zhang J, Ma R, Gao J, Liu Y, *et al.* A tumor targeting near-infrared laser-triggered drug delivery system based on GO@Ag nanoparticles for chemo-photothermal therapy and X-ray imaging. Biomaterials 2014;35:5847–61.
[35] Chen L, Chai S, Liu K, Ning N, Gao J, Liu Q, *et al.* Enhanced epoxy/silica composites mechanical properties by introducing graphene oxide to the interface. ACS Appl Mater
Interfaces 2012;4:4398–404.
[36] Modugno G, Monney A, Bonchio M, Albrecht M, Carraro M. Transfer hydrogenation catalysis by a N-heterocyclic carbene iridium complex on a polyoxometalate platform. Eur J Inorg Chem 2014:2356–60.
[37] Gülcemal S, Gökçe AG, C¸ etinkaya B. N-benzyl substituted N-heterocyclic carbene complexes of iridium(I): assessment in transfer hydrogenation catalyst. Inorg Chem 2013;52:10601–9.
[38] Azua A, Mata JA, Peris E, Lamaty F, Martínez J, Colacino E. Alternative energy input for transfer hydrogenation using iridium NHC based catalysts in glycerol as hydrogen donor and solvent. Organometallics 2012;31:3911–9.
[39] Gierz V, Urbanaite A, Seyboldt A, Kunz D. Rhodium complexes bearing 1,10-phenanthrolin analogue Bis-NHC ligands are active catalysts for transfer hydrogenation of ketones. Organometallics 2012;31:7532–8.

[40] Newman PD, Cavell KJ, Hallett AJ, Kariuki BM. Rhodium and iridium complexes of an asymmetric bicyclic NHC bearing secondary pyridyl donors. Dalton Trans 2011;40:8807–13.
[41] Diez C, Nagel U. Chiral iridium(I) bis(NHC) complexes as catalysts for asymmetric transfer hydrogenation. App
Organomet Chem 2010;24:509–16.
[42] Pontes da Costa A, Viciano M, Sanaú M, Merino S, Tejeda J, Peris E, *et al.* First Cp*-functionalized N-heterocyclic carbene and its coordination to iridium. Study of the catalytic properties. Organometallics 2008;27:1305–9.
[43] Hahn FE, Holtgrewe C, Pape T, Martin M, Sola E, Oro LA. Iridium complexes with N-allyl-substituted benzimidazol-2-ylidene ligands and their application in catalytic transfer hydrogenation. Organometallics 2005;24:2203–9.
[44] Mas-Marzá E, Poyatos M, Sanaú M, Peris E. A new rhodium(III) complex with a tripodal bis(imidazolylidene) ligand. Synthesis and catalytic properties. Organometallics 2004;23:323–5.
[45] Albrecht M, Crabtree RH, Mata JA, Peris E. Chelating biscarbene rhodium(III) complexes in transfer hydrogenation of ketones and imines. Chem Commun 2002:32–3.
[46] Hillier AC, Lee HM, Stevens ED, Nolan SP. Cationic iridium complexes bearing 218hloride218-2-ylidene ligands as transfer hydrogenation catalysts. Organometallics 2001;20:4246–52.
[47] Jiménez MV, Fernández-Tornos J, Pérez-Torrente JJ, Modrego FJ, Winterle S, Cunchillos C, *et al.* Iridium(I) complexes with hemilabile N-heterocyclic carbenes: efficient and versatile transfer hydrogenation catalysts. Organometallics 2011;30:5493–508.
[48] Türkmen H, Pape T, Hahn FE, C¸ etinkaya B. Efficient transfer hydrogenation using iridium and rhodium complexes of benzannulated N-heterocyclic carbenes. Eur J Inorg Chem 2008:5418–23.
[49] Blanco M, Álvarez P, Blanco C, Jiménez MV, Fernández-Tornos J, Pérez-Torrente JJ, *et al.* Enhanced hydrogen-transfer catalytic activity of iridium N-heterocyclic carbenes by covalent attachment on carbon nanotubes. ACS Catal 2013;3:1307–17.
[50] Botas C, Álvarez P, Blanco C, Santamaría R, Granda M, Gutiérrez MD, *et al.* Critical temperatures in the synthesis of graphene-like materials by thermal exfoliation–reduction of graphite oxide. Carbon 2013;52:476–85.
[51] Bekhouche M, Blum LJ, Doumèche B. Ionic liquid-inspired cations covalently bound to FDH improve its stability and activity in IL. ChemCatChem 2011;3:875–82.
[52] Usón R, Oro LA, Cabeza JA. Dinuclear methoxy, cyclooctadiene, and barrelene complexes of rhodium(I) and iridium(I). Inorg Synth 1985;23:126–7.
[53] Sherwood PMA. In: Briggs D, Seah MP, editors. Practical Surface Analysis in Auger and X-ray

Photoelectron Spectroscopy, vol. 1. New York: Wiley; 1990. P. 574.
[54] Elgrabli D, Floriani M, Abella-Gallar S, Meunier L, Gamez C, Delalain P, *et al.* Biodistribution and clearance of instilled carbon nanotubes in rat lung. Part Fibre Toxicol 2008;5:20–33.
[55] Botas C, Álvarez P, Blanco P, Granda M, Blanco C, Santamaría R, *et al.* Graphene materials with different structures prepared from the same graphite by the Hummers and Brodie methods. Carbon 2013;65:156–64.
[56] Botas C, Álvarez P, Blanco C, Santamaría R, Granda M, Ares P, *et al.* The effect of the parent graphite on the structure of graphene oxide. Carbon 2012;50:275–82.
[57] Chen D, Feng H, Li J. Graphene oxide: preparation, functionalization, and electrochemical applications. Chem Rev 2012;112:6027–53.
[58] Letsinger RL, Ogilvie KK. Use of p-nitrophenyl chloroformate in blocking hydroxyl groups in nucleosides. J Org Chem 1967;32:296–300.
[59] Oh JK, Drumright R, Siegwart DJ, Matyjaszewski K. The development of microgels/nanogels for drug delivery applications. Prog Polym Sci 2008;33:448–77.
[60] Gao X, Jang J, Nagase SJ. Hydrazine and thermal reduction of graphene oxide: reaction mechanisms, product structures, and reaction design. Phys Chem C 2010;114:832–42.
[61] Crotti C, Farnetti E, Filipuzzi S, Stener M, Zangrando E, Moras P. Evaluation of the donor ability of phenanthrolines in iridium complexes by means of synchrotron radiation photoemission spectroscopy and DFT calculations. Dalton Trans 2007:133–42.
[62] Lee WH, Kim H. Oxidized iridium nanodendrites as catalysts for oxygen evolution reactions. Catal Commun 2011;12:408–11.
[63] Zahmakiran M. Iridium nanoparticles stabilized by metal organic frameworks (IrNPs@ZIF-8): synthesis, structural properties and catalytic performance. Dalton Trans 2012;41:12690–6.
[64] Giordano R, Serp P, Kalck P, Kihn Y, Schreiber J, Marhic C, *et al.* Preparation of rhodium catalysts supported on carbon nanotubes by a surface mediated organometallic reaction. Eur J Inorg Chem 2003:610–7.
[65] Díaz-Auñón JA, Román-Martínez MC, Salinas-Martínez de Lecea C. $[Rh(\mu\text{-}Cl)(COD)]_2$ supported on activated carbons for the hydroformylation of 1-octene: effects of support surface chemistry and solvent. J Mol Cat A: Chem 2001;170:81–93.
[66] Mungse HP, Verma S, Kumar N, Sain B, Khatri OP. Grafting of oxo-vanadium Schiff base on graphene nanosheets and its catalytic activity for the oxidation of alcohols. J Mater Chem 2012;22:5427–33.
[67] Fritsch A, Légaré P. XPS study of small iridium clusters; comparison with the $Ir_4(CO)_{12}$ molecule. Surf Sci 1984;145:517–23.

SUPPLEMENTARY DATA

S1. Solvent stability

S2. AFM analysis of **GO**

S3. Raman spectrum of **GO-1**

S4. ^{1}H NMR spectra of **GO-1** and **TRGO-1**

S5. ^{13}C-CPMAS solid NMR spectrum of **GO-1-Ir**

S6. EDX (HRTEM) images of **GO-1-Ir** and **TRGO-1-Ir**

S7. FTIR spectra of parent, intermediate and functionalized materials

S8: Reaction profiles for transfer hydrogenation of cyclohexanone by **TRGO-1-Ir** for 5 consecutive cycles of recycling (last under air)

S.1 Solvent stability of Gos and TRGOs

GO, and **TRGO** form stable suspensions in water, DMF and acetone for a period of time superior to 2 months (Figure S1, a-d). The introduction of the imidazolium ligand also led to stable suspensions but for shorter periods of time (Figure S1, e-f). **GO-1-Ir** and **TRGO-1-Ir** do not form stable suspensions in those solvents (Figure S1, g-h).

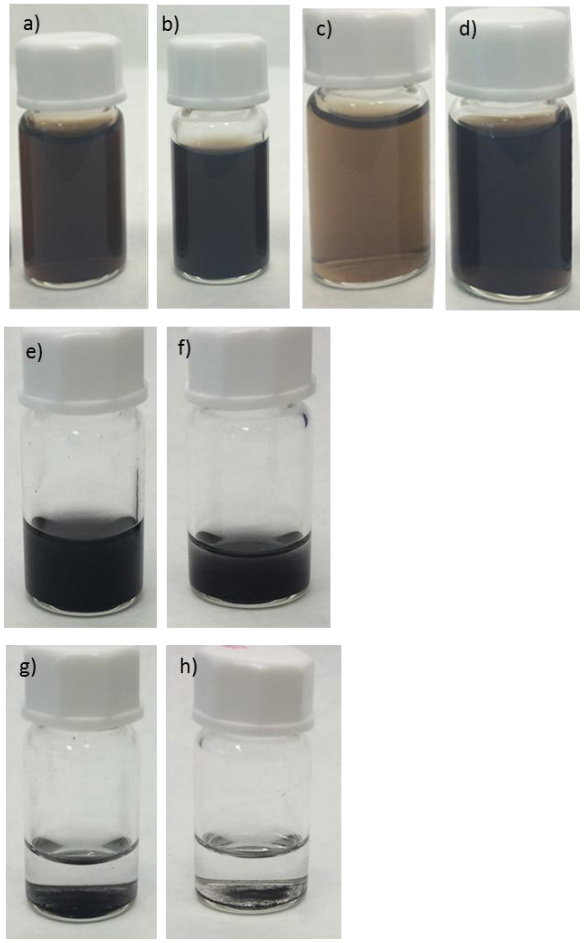

Figure S1. Images of **GO** in DMF (a), **GO** in acetone (b), **TRGO** in DMF (c), **TRGO** in acetone (d), **GO-1** in acetone (e), **TRGO-1** in acetone (f), **GO-1-Ir** in acetone (g) and **TRGO-1-Ir** in acetone (h).

S.2 AFM analysis of GO

Analysis of the Atomic Force Microscopy (AFM) images obtained from **GO** suspensions (Figure S2) indicates that is mainly composed by monolayers with an average height of ≈1.2 nm.

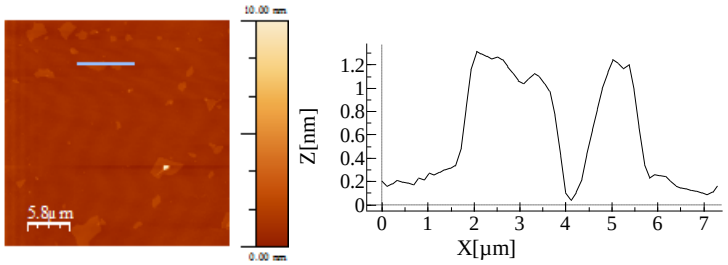

Figure S2. AFM images of **GO** sheets. The horizontal line indicates the sections corresponding to the traces shown on the right.

S.3 Raman spectrum of GO-1

As a representative example of the Raman spectra of the materials prepared in this work, Figure S3 shows the Raman spectrum of **GO-1**.

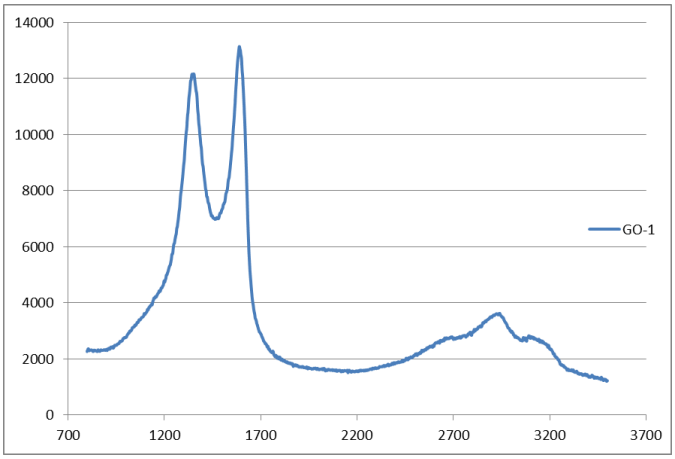

Figure S3. Raman spectrum of **GO-1**

S.4 NMR spectra of GO-1 and TRGO-1

GO-1 and **TRGO-1** form relatively stable suspensions in acetone-d_6 which has allowed their characterization by ^{1}H NMR. The spectra are depicted in Figure S4.

a)

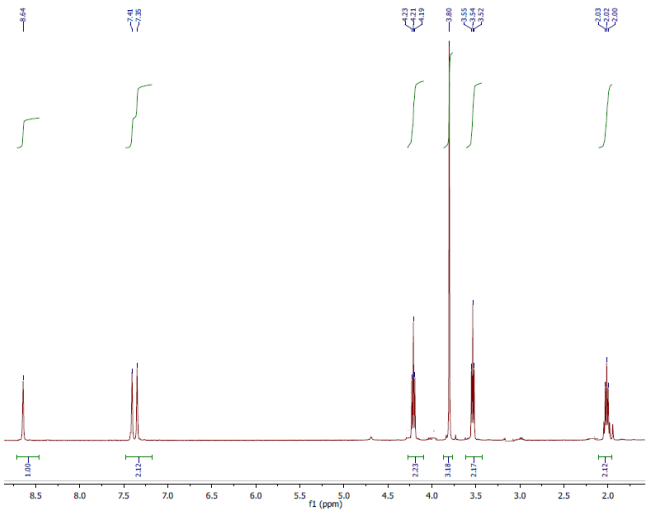

b)

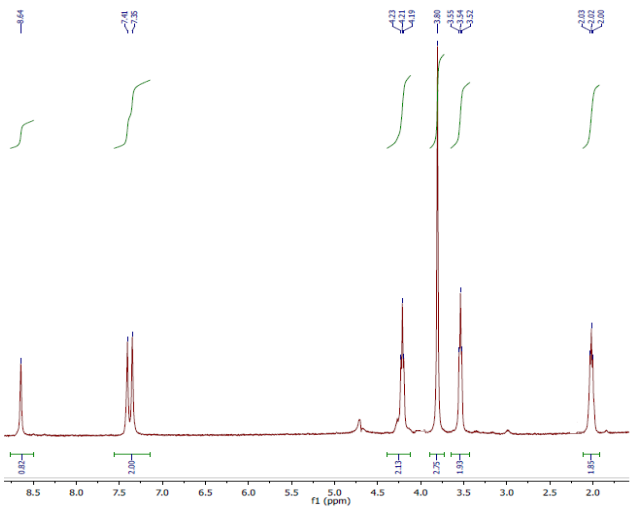

Figure S4. ^{1}H NMR (300K, acetone-d_6) spectra of **GO-1** (a) and **TRGO-1** (b)

S.5 ^{13}C CPMAS solid NMR spectrum of GO-1-Ir

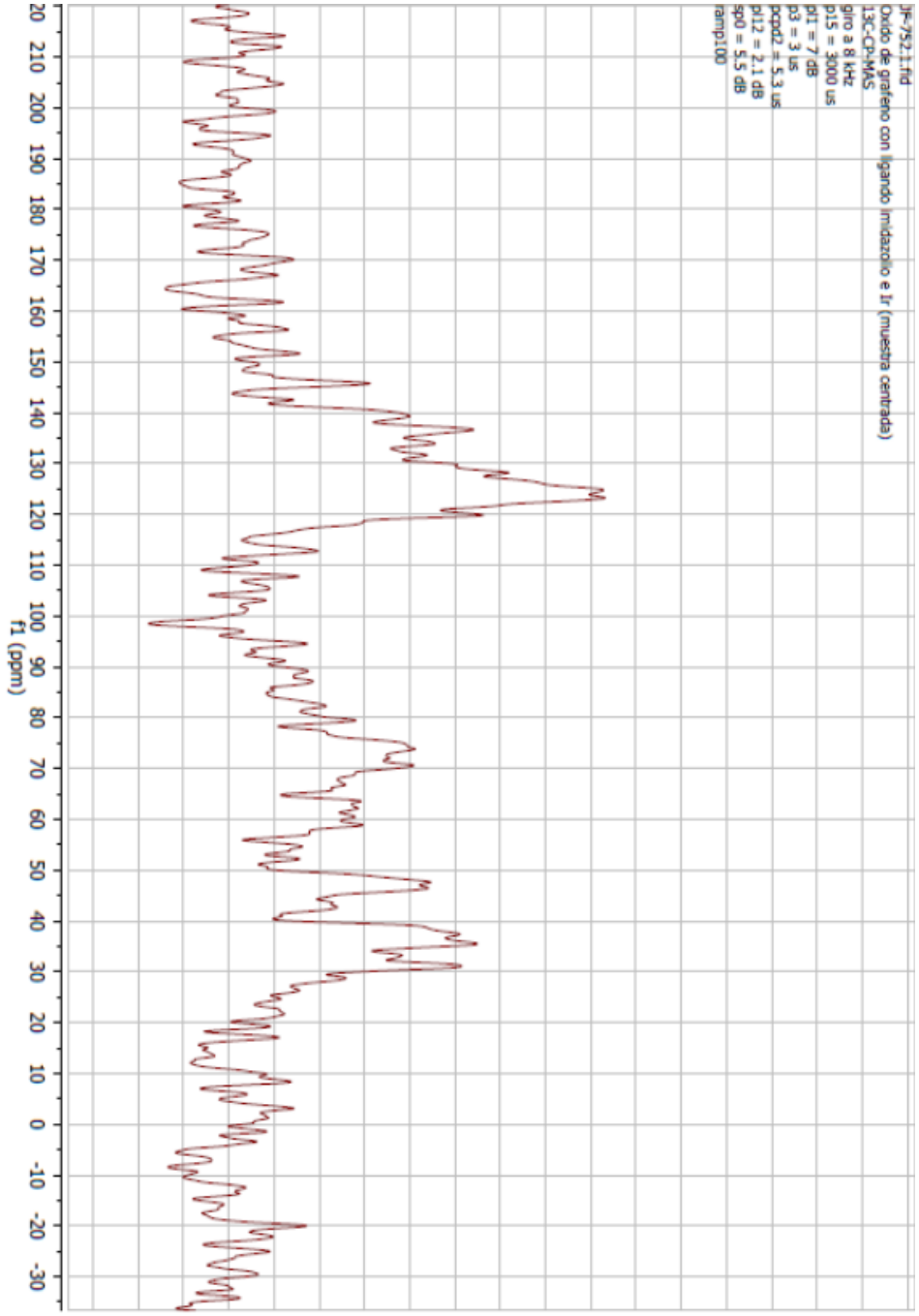

Figure S5. ^{13}C-CPMAS solid NMR spectrum of **GO-1-Ir**

S.6 EDX spectra of GO-1 and TRGO-1

The Energy- dispersive X-ray spectroscopy (EDX) spectra obtained from HRTEM measurements of **GO-1-Ir** and **TRGO-1-Ir** are depicted in Figure S6.

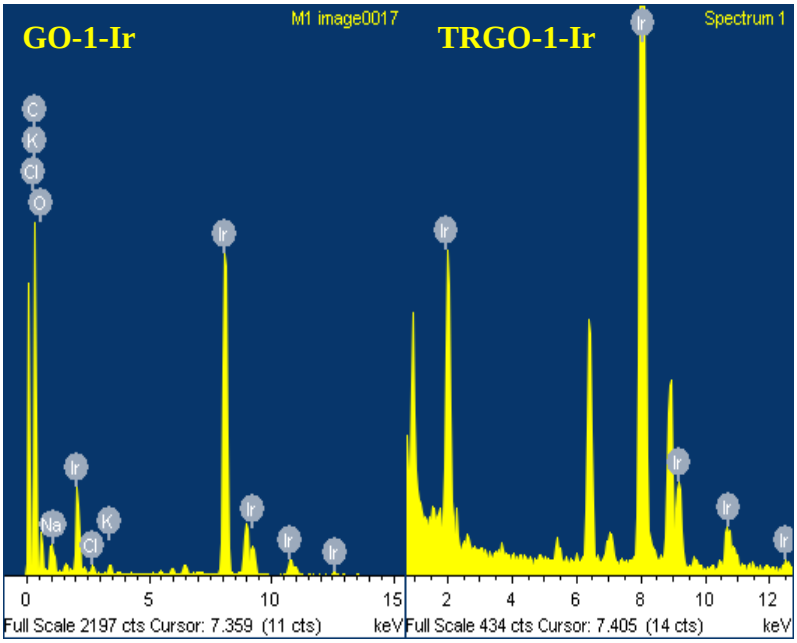

Figure S6. EDX spectra of **GO-1-Ir** and **TRGO-1-Ir**.

S.7 FTIR spectra

Fourier Transformed infrared (FTIR) spectra were recorded at room temperature, performing KBr pellets (KBr sample ratio 300:1), using a transmission mode in a Fourier transform infrared spectrometer (FTIR, Nicolet 8700 FTIR, Thermo Scientific) fitted with a DFT (deuterated triglycine sulfate) detector.

The FTIR spectra of the samples previous to the iridium introduction are depicted in Figure S7.

Green bands correspond to graphene signals and their variations correspond with that expected from the XPS and elemental analysis data. The *nitro* group of the intermediate samples (**GO-p** and **TRGO-p**) exhibits the characteristic N-O_2 and C-N bands (more pronounced in the non-thermally treated sample due to a higher abundance) which disappear after the reaction with ligand **1** to form **GO-1** and **TRGO-1**.

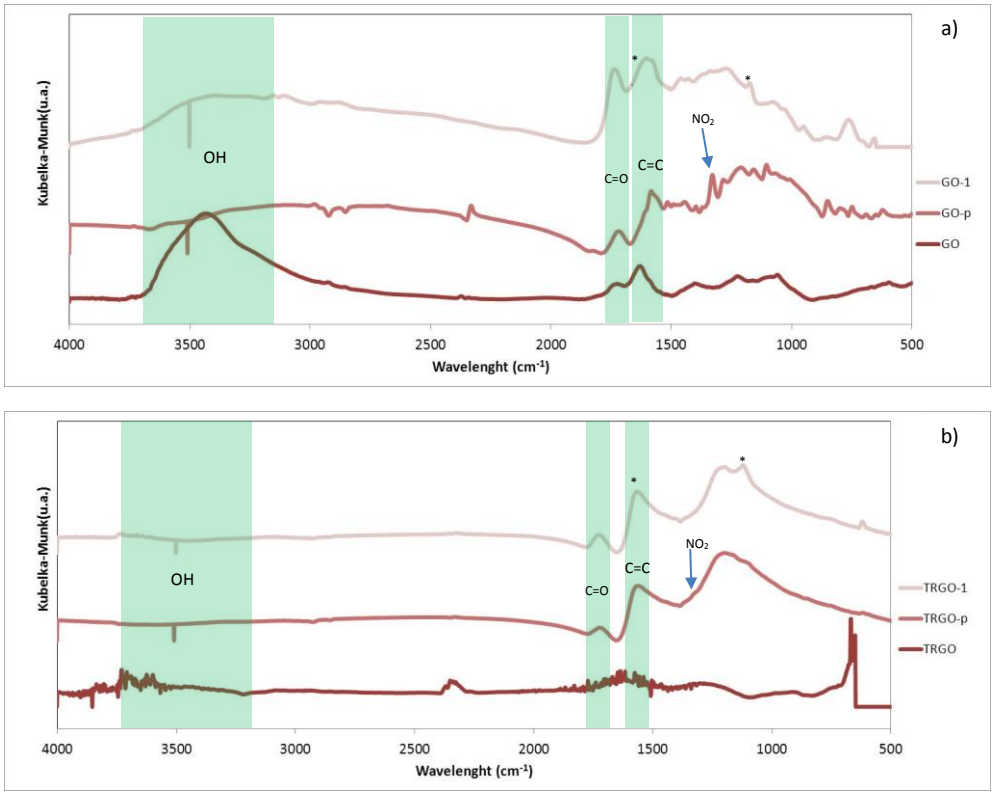

Figure S7. FTIR spectra of parent, intermediate and functionalized materials: a) oxidized support; b) thermally reduced.

S.8 Reaction profiles for transfer hydrogenation of cyclohexanone by TRGO-1-Ir for 5 consecutive cycles of recycling (last under air)

The catalysts used in this work were recycled in 5 consecutive cycles, the last being performed under air. For all samples, the reaction profiles in all cycles were found to be similar, with any loos of activity. As an example, the reaction profiles for TRGO-1-Ir as examples are depicted in Figure S8.

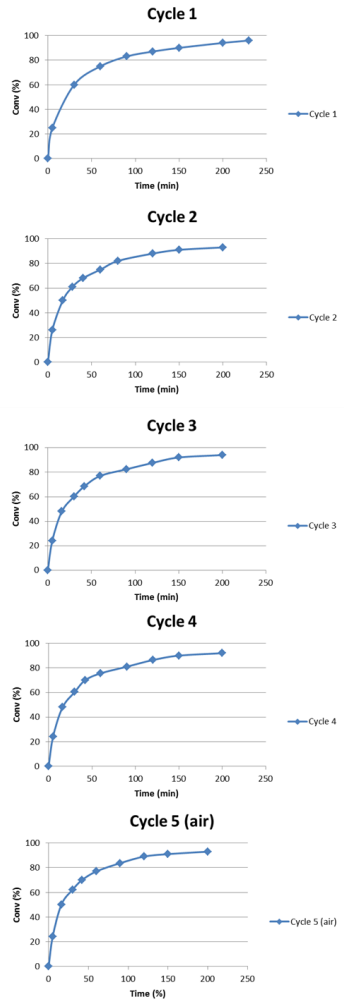

Figure S8: Reaction profiles for transfer hydrogenation of cyclohexanone by TRGO-1-Ir for 5 consecutive cycles of recycling (last under air).

4.5 ARTÍCULO V

"Efecto de las diferencias estructurales de nanotubos de carbono y grafeno NHC-iridio en el proceso de transferencia de hidrógeno catalítico" Carbon **2015,** en prensa

Tras la funcionalización covalente de óxido de grafeno a través de sus grupos hidroxilo, en este capítulo se discute la funcionalización de nanotubos de carbono oxidados **CNT-ST** (se omite el sufijo ST por claridad) y parcialmente reducidos **TRCNT** con el complejo NHC de iridio empleando la sal de imidazolio **1**, se siguió la misma estrategia que en el capítulo anterior. La figura 4.8 describe la ruta de funcionalización de nanotubos empleada.

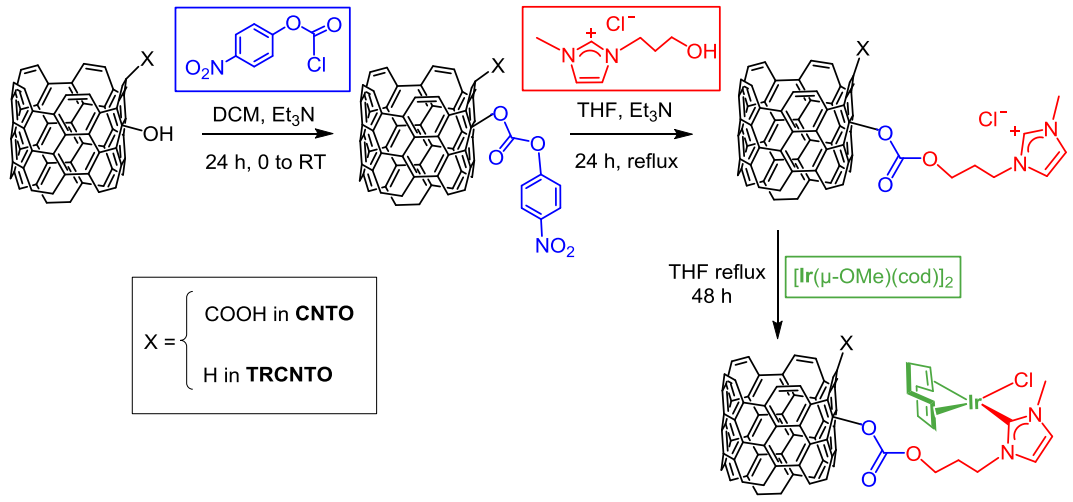

Figura 4.8 Ruta de funcionalización

Al igual que en los materiales grafénicos, los nanotubos de carbono oxidados y reducidos se funcionalizaron de forma efectiva a través de sus grupos hidroxilo como demuestran los incrementos de los contenidos de nitrógeno en análisis elemental y XPS, sin detectarse señales del compuesto intermedio en los espectros

de ^{1}H-RMN o FTIR. Se observaron por HRTEM regiones electrón-densas del tamaño adecuado, correspondientes a los complejos organometálicos. Las muestras presentaron un comportamiento muy similar a los materiales grafénicos anteriormente discutidos.

Los complejos organometálicos soportados sobre nanotubos de carbono tanto oxidados como reducidos presentaron actividad catalítica en la reducción de ciclohexanona a ciclohexanol por transferencia de hidrógeno. La actividad fue superior al complejo homogéneo **5** (identificado como **Ir-imidO**), presentando además excelente ciclabilidad y estabilidad al aire.

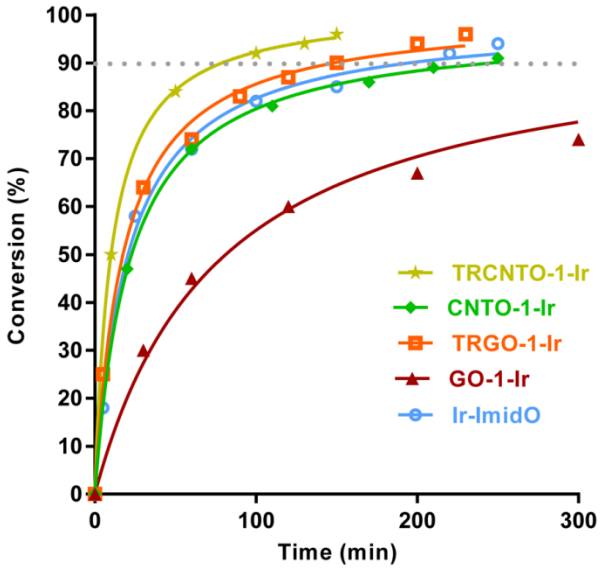

Figura 4.9 Actividad catalítica

No obstante, al comparar la actividad catalítica de los sistemas soportados sobre nanotubos o materiales grafénicos existe una diferencia entre ambos tipos de sistemas, ya que la actividad de los sistemas basados en nanotubos de carbono, tanto

oxidados o reducidos, es superior. Para explicar estos hallazgos, se realizó una profunda caracterización de ambos tipos de soportes.

Al igual que en los casos anteriores, se confirmó la presencia de iridio (I) covalentemente enlazado a los materiales tanto por XPS (región Ir4f con picos correspondientes a Ir(I) en 62.5 eV y 66.5 eV) como por XAS, al obtener el máximo de las curvas de absorción con una energía intermedia entre las referencias iridio metal e $IrCl_3$. No obstante, al analizar el entorno local del iridio mediante EXAFS, se detectó un gran desorden estructural en la muestra **GO-1-Ir** que podría ser el responsable de su baja actividad catalítica. Este desorden no se observa en las otras tres muestras estudiadas. Acudiendo a la estructura carbonosa de los soportes, se detectó una gran concentración de grupos funcionales oxigenados en las muestras oxidadas junto con una red aromática muy defectuosa, mientras que la reducción y reconstrucción parcial de la estructura del material en los soportes reducidos podría ser la causa de incremento de actividad, ya que la muestra con menos oxígeno y menos defectos, **TRCNT-1-Ir**, es la más activa. Por tanto, cuando los materiales han sido funcionalizados a través de sus grupos hidroxilo, la correcta cantidad y tipo de grupos funcionales es crítica y controla la actividad del sistema catalítico. Además, la reconstrucción de la aromaticidad del material causada por la reducción térmica también modifica el comportamiento catalítico del sistema final.

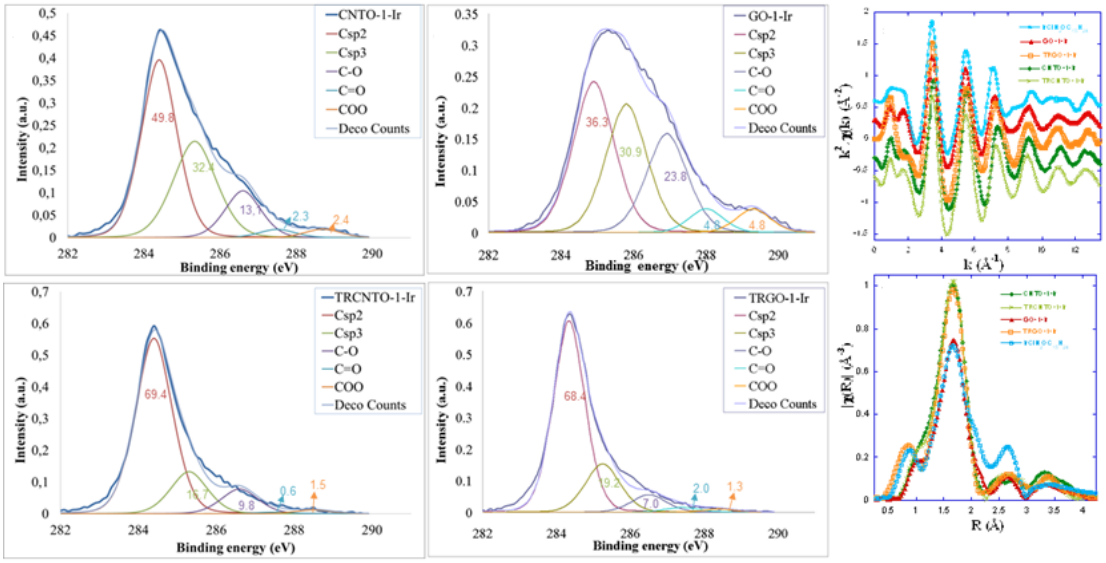

Figura 4.10. Caracterización de los sistemas híbridos basados en nanotubos de carbono y materiales grafénicos iridio-NHC

Finalmente, a partir de los datos de las señales EXAFS y del modelo estructural descrito en la base de datos cristalográficos, se pudo plantear un modelo de coordinación que descarta el ligando cloruro de la primera capa de ligandos del iridio. El metal está unido a 6 elementos ligeros, basados en 3 pares de distancias. Los dos primeros pares corresponden a los enlaces del metal con los atomos de carbono de la diolefina. Las otras dos distancias se asignan al enlace Ir-C del carbeno, asumiendo la misma para un enlace Ir-O, correspondiente a un grupo funcional oxigenado del soporte. A pesar de la simpleza del modelo, se obtiene un muy buen ajuste a los datos experimentales.

Available at www.sciencedirect.com
ScienceDirect
journal homepage: www.elsevier.com/locate/carbon

Effect of structural differences of carbon nanotubes and graphene based iridium-NHC materials on the hydrogen transfer catalytic activity

Matías Blanco[a], *Patricia Álvarez*[a], *Clara Blanco*[a], *M. Victoria Jiménez*[b,*], *Javier Fernández-Tornos*[b], *Jesús J. Pérez-Torrente*[b], *Javier Blasco*[c], *Gloria Subías*[c], *Vera Cuartero*[d], *Luis A. Oro*[b], *Rosa Menéndez*[a,*]

[a] Instituto Nacional del Carbón, INCAR-CSIC, Apdo., 73, 33080 Oviedo, Spain
[b] Departamento de Química Inorgánica, Instituto de Síntesis Química y Catálisis Homogénea-ISQCH, Universidad de Zaragoza-C.S.I.C., 50009 Zaragoza, Spain
[c] Instituto de Ciencia de Materiales de Aragón-ICMA, Departamento de Física de la Materia Condensada, CSIC-Universidad de Zaragoza, 50009-Zaragoza, Spain.
[d] ESRF-The European Synchrotron, 71, Avenue des Martyrs, Grenoble, France

ARTICLE INFO

Article history:
Received 11 June 2015 Accepted 7 November 2014 Available online 17 November 2014

* Corresponding authors.
E-mail addresses:
vjimenez@unizar.es (M.V. Jiménez),
rosmenen@incar.csic.es (R. Menéndez).

http://dx.doi.org/10.1016/j.carbon.2014.11.016 0008-6223
0008-6223

ABSTRACT

A proper design of heterogeneous molecular catalysts supported on carbon materials requires a systematic study of "metal−carbon support interactions" and their influence on catalytic activity. In this study, hybrid materials containing covalently anchored iridium N-heterocyclic carbene (NHC) organometallic complexes have been successfully prepared from oxidized and partially reduced carbon nanotubes (CNTs). The preparation method for these supported materials relies on the selective functionalization of the superficial hydroxylic groups using the imidazolium salt, 1-(3-hydroxypropyl)-3-methyl-1*H*-imidazol-3-ium chloride. The hydrogen transfer catalysis activity of these nanotube-based hybrid catalysts was tested by the reduction of cyclohexanone to cyclohexanol with 2-propanol, and the results of the tests were compared with those obtained using similar hybrid graphene-based catalysts. While EXAFS analysis revealed a common first coordination shell of the iridium atom for all the hybrid materials examined, independently of whether they were either supported on carbon nanotubes or graphene materials, catalytic activity in all the reduced materials was significantly superior. Moreover, catalytic systems based on reduced CNTs exhibited a better performance than those based on reduced graphene materials. Both these facts suggest there is a positive correlation between hydrogen transfer activity, reconstruction of the aromatic carbon structure and the smaller amount of oxygen functional groups.

1. Introduction

Technological development has provided us with available new one, two and three –dimensional carbon materials with a specific spatial and geometrical structure [1,2]. These highly versatile carbon materials are being currently used not only in electronic devices [3-6] but also as catalyst supports since their graphitic structure makes them inert in many chemical media [7]. For these reasons, in addition to their use as carbocatalysts, where oxidized functionalization is generally required [8-10], they have been profusely used as supports for hybrid materials having metal oxides, nanoparticles or molecular catalysts as the active sites. [7, 11-14]. These supports were initially evaluated as "innocent" materials due to their uniform hybridization, ordered structure and chemical inertness but it is known that the metal-support interactions are strongly dependent not only on the nature of the metal, but also on the type of carbon material chosen because their electronic [15,16], thermal [17] or mechanical properties [18,19] depend on their preparation method, origin and further modifications involving different surface treatments [20,21].

Carbon nanotubes (CNT) [22] and graphene [2] are the mono- and bi-dimensional long-range ordered versions, respectively, of these carbon materials. The synthetic methods used for carbon oxygen functionalization are well-established procedures. Graphene oxide (GO) is obtained from a severe oxidation process commonly employed for the chemical synthesis of graphene from graphite [23,24]. The sp^2 lattice of the graphene is disrupted upon oxidation by the introduction of oxygen functional groups, predominantly OH and epoxy in the interior of the basal plane while carboxylic acids are formed at the edges, and also where there are morphological defects (carbon atom vacancies) [25]. On the other hand, the oxidation processes, what introduce oxygen functionalization in the nanotubes (namely CNTO), are currently used as a purification step after synthesis [26]. Both oxidized carbon nanomaterials, GO and CNTO, have been utilized previously as catalysts themselves or as catalyst supports by making use of the surface groups in order to immobilize the active species [27-30]. Thus, not only metallic nanoparticles, but also enzymes or organometallic complexes have been anchored to these oxidized carbon nanomaterials using esterification/amidation reactions with oxygen groups. The activation of carboxylic acids with $SOCl_2$ [31] or carbodiimides [32], and the reactivity of hydroxylic groups towards silanes [33] are routinely employed in order to functionalize CNTO and GO with the catalyst precursors. In general, the catalytic studies conducted on nanohybrid catalyst based on CNT or graphene systems have shown

promising results in terms of activity, selectivity, stability and/or cyclability compared to the homogeneous or heterogeneous traditional systems [34].

Recently, our group found a protocol to immobilize iridium N-heterocyclic carbene (NHC) complexes on GO and thermally reduced GO materials by taking advantage of the carbon-based organic chemistry of the surface hydroxylic groups instead of using traditional siloxane chemistry [29]. The hybrid graphene–iridium–NHC materials were found to be efficient hydrogen-transfer catalysts exhibiting good recyclability. The effectiveness of the Ir(I)-NHC complexes as homogeneous catalysts in transfer hydrogenation of unsaturated compounds [36-41], in particular, those with hemilabile O- and N- donor functions in the NHC carbene ligand [42,43], is well known in the literature. In addition, an increase in the transfer hydrogenation catalytic activity of Ir-NHC complexes based on hemilabile O- and N- donor functions supported on CNT has been observed. [44] However, to date no systematic comparison of the catalytic activities and selectivities of different carbon-material based catalytic systems has been carried out and, to the best of our knowledge, the present study is unique in trying to establish the possible influence of the structure, surface chemistry and the reconstruction of the aromatic network on the catalytic activity of a hybrid organometallic complex–CNTO/GO carbon nanomaterial system. Despite the similar structure and properties of both materials, the geometrical and spatial differences could give rise to different local environments thereby influencing the catalytic activity.

This work has to tackle two critical points. Firstly, the covalent functionalization of oxidized and thermally reduced carbon nanotubes through surface OH groups to produce iridium-supported NHC-CNTO complexes comparable to hybrid iridium NHC-GO catalysts has to be performed. Secondly, study the catalytic activity in the transfer hydrogenation of cyclohexanone with 2-propanol to compare with that of hybrid GO catalysts materials. Specific features of the structure and the surface chemistry of the hybrid catalysts have been used in this work to explain the differences in the catalytic performance.

2. Experimental

2.1. Materials

All the chemicals, including the graphite powder and multiwalled carbon nanotubes, were purchased from Aldrich. Reagent or HPLC grade was employed in all the experiments. Solvents were distilled immediately prior to use with appropriate drying agents or obtained from a Solvent

Purification System (Innovative Technologies).

The oxidized CNTs (**CNTO**) utilized in this work were prepared by acid treatment of commercial bundle-type CNTs, as described previously [45]. The **GO** utilized in this work was prepared by applying a modified Hummers method to the commercial graphite, as reported in detail elsewhere [46]. **TRGO** and **TRCNTO** were obtained from **GO** and **CNTO** respectively by thermal treatment at 400ºC in a horizontal furnace, under a nitrogen flow of 50 mL min^{-1}. The residence time at the final temperature was 60 min [46].

The imidazolium salt [MeImH$(CH_2)_3$OH]Cl (**1**) [47] and the compound [Ir(μ-Ome)(cod)]$_2$ [48] were prepared according to standard literature procedures.

2.2 Characterization of Nanotube and Graphene materials and hybrid catalysts

Nuclear magnetic resonance (NMR) spectra were recorded on a Bruker Advance 400 spectrometer operating at 400.16 MHz (^{1}H). NMR chemical shifts are reported in ppm relative to tetramethylsilane and referenced to partially deuterated solvent resonances. The catalytic reactions were analyzed on an Agilent 4890 D system equipped with an HP-INNOWax capillary column (0.4 μm, 25 m x 0.2 mm i.d.) using mesitylene as internal standard. Transmission electron microscopy (TEM) spectra were obtained on a JEOL 2000 EX-II instrument operating at 160 kV. Images of high-resolution transmission electron microscopy (HRTEM) were recorded using a JEOL JEM-2100F transmission electron microscope, equipped with a field-emission-gun (FEG) operating at 200 kV, and fitted with an Oxford Instruments microprobe to perform Energy-dispersive X-ray spectroscopy (EDX), in order to verify the atomic composition of the catalyst. The samples were prepared by casting a few drops of 1 mg mL^{-1} ethanol suspensions of the materials over the carbon grids. To minimize exposure of the samples to the air, the suspensions were transferred to a lacey carbon grid using a glovebox filled with ultrahigh-purity argon and then to the TEM holder in order to minimize the time required to introduce them into the microscope. Elemental analyses were performed on a LECO-CHNS-932 micro-analyser equipped with a LECO-VTF-900 furnace coupled to a micro-analyzer. The X-ray photoemission spectroscopy (XPS) spectra were recorded using a SPECS system operating under a pressure of 10^{-7} Pa and equipped with a Mg Kα X-ray source. The functional groups in the graphene materials were quantified by deconvolution of the high resolution C1s XPS peak employing Gaussian and Lorentzian functions [49]. The binding energy profiles were deconvoluted as follows: undamaged structures of sp^2-hybridized carbon

(284.5 eV), damaged structures or sp^3-hybridized carbons (and C-N groups, 285.5 eV), C-O (and C-N groups, 286.5 eV), C=O functional groups (287.7 eV) and COO groups at 288.7 eV. The amount of iridium present in the samples was determined by means of Inductively Coupled Plasma Mass Spectrometry (ICP-MS) in an Agilent 7700x instrument. The samples were digested following a method described elsewhere [50]. Briefly, 30 mg of sample was treated with 5 mL of a mixture of concentrated nitric and hydrochloric acid (3:1 ratio) at 180 ºC for 3 h under microwave irradiation.

X-ray absorption spectroscopy (XAS) measurements were recorded at the BL22-Claess beamline from ALBA synchrotron (Spain) and at the BM23 beamline from the European Synchrotron Radiation Facility (ESRF, France). The measurements were carried out in transmission mode on pellets with an optimized thickness at room temperature. The beam was monochromatized by a fixed-exit-offset Si (311) double crystal in ALBA and a Si (111) one in ESRF. A harmonic rejection better than 10^{-5} was achieved by using a Si mirror coating on a dual toroid focusing mirror installed after the monochromator in both cases. The energy resolution $\Delta E/E$ was estimated to be about 8×10^{-5} at the Ir L_3-edge. A reference of metallic iridium was simultaneously measured for the calibration of the energy. XAS spectra of metal Ir, the complex [IrCl(cod)(MeImH$(CH_2)_3$OH)] and the salt $IrCl_3$ were also recorded as references for Ir(0), Ir(I) and Ir(III) respectively. The measurements obtained from both synchrotrons are comparable. Extended X-ray absorption fine structure (EXAFS) spectra were extracted using Athena software (part of the Demeter package) [51] The Fourier transforms (FTs) of the EXAFS signals were calculated over a k-range of 3.0–13.3 $Å^{-1}$ using a sine window. The EXAFS structural analysis was performed using theoretical phases and amplitudes calculated by means of the FEFF-6 code [52] and fits to the experimental data were carried out in R-space with the help of ARTEMIS program (also part of Demeter package) [51].

2.3. Functionalization of nanotube materials with 1-(3-hydroxypropyl)-3-methyl-1H-imidazol-3-ium chloride (1)

Using a similar procedure to that recently reported for graphene materials [35], **CNTO** and **TRCNTO** were functionalized with the imidazolium salt, 1-(3-hydroxypropyl)-3-methyl-1*H*-imidazol-3-ium chloride, [MeImH$(CH_2)_3$OH]Cl (**1**), following a two-step procedure. Briefly, **CNTO** or **TRCNTO** (100 mg) was dispersed in 20 mL of dichloromethane (DCM). The resulting dispersion was cooled to 0 ºC in an ice bath and then, *p*-nitrophenylchloroformate (3.0 g, 15 mmol) and 239hloride239239mine (2.1 mL, 15 mmol) were added under

an inert atmosphere. The mixture was stirred for 24 h and allowed to reach room temperature slowly. The resulting solids were filtered and washed three times with DCM (20 mL) and then dried under vacuum for 2 h. In a second step, the imidazolium salt **1** (100 mg, 0.560 mmol) and a catalytic amount of 240hloride240240mine (0.2 mL) were added, under an inert atmosphere, to the dispersions of nanotube solids obtained in step 1 in tetrahydrofuran (THF) (15 mL), and refluxed for 24 h. The products were obtained by centrifugation/filtration, washed with THF (3 x 20 mL), DCM (3 x 20 mL), and ethanol (3 x 20 mL) and then, vacuum dried at 100 ºC in a preheated furnace until constant weight. The nanotube samples obtained were labeled as **CNTO-1** and **TRCNTO-1** depending on the parent material used in each case, **CNT** or **TRCNTO**, respectively.

2.4. Preparation of hybrid catalysts CNTO-1-Ir and TRCNTO-1- Ir

CNTO-1 or **TRCNTO-1** (100 mg) were made to react with [Ir(μ-Ome)(cod)]$_2$ (100 mg, 0.150 mmol) (cod = 1,5-cyclooctadiene) in THF (10 mL) under an argon atmosphere. The mixtures were refluxed for 2 days and then immersed in an ultrasonic bath for 30 min at room temperature. The resultant solids were recovered by centrifugation, washed with THF (5 x 10 mL) and diethyl ether (2 x 5 mL), and dried under vacuum to produce **CNTO-1-Ir** and **TRCNTO-1-Ir**.

2.5. General procedure for transfer hydrogenation catalysis

The catalytic transfer hydrogenation reactions were carried out under an argon atmosphere in thick glass reaction tubes fitted with a greaseless high-vacuum stopcock. In a typical experiment, the reactor was charged with a solution of cyclohexanone (0.52 mL, 5.0 mmol) in 2-propanol (4.5 mL), internal standard (mesitylene, 70 μL, 0.5 mmol), base (0.1 mL, 0.025 mmol of a KOH solution 0.24 M in 2-propanol) and catalyst (0.005 mmol, 0.1 mol%). The weight of the supported catalysts used in each experiment was calculated according to ICP measurements, assuming that all the iridium in the sample corresponded to active catalyst sites, 9.34 mg of **GO-1-Ir** (10.2 %wt. of iridium) and 20.44 mg of **TRGO-1-Ir** (4.7 %wt of iridium) were used for the Gos, and 7.7 mg of **CNTO-1-Ir** (12.5 %wt. of iridium) and 9.5 mg of **TRCNTO-1-Ir** (10.1 %wt. of iridium) were employed for the CNTs. The resulting mixture was stirred at room temperature until complete dissolution of the homogeneous catalyst, [IrCl(cod)(MeIm$(CH_2)_3$ $OCOCH_3$] (**Ir-ImidO**) [35**¡Error! Marcador no definido.**], or for 10 min in the case of the heterogeneous catalyst, and then placed in a thermostatic oil bath at the required temperature, typically 80 ºC. Conversions were determined by gas

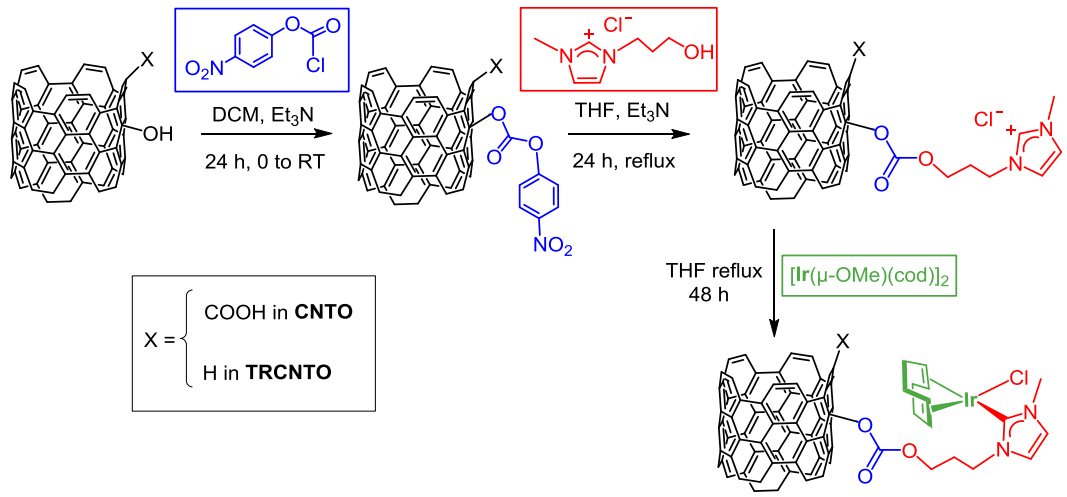

Fig 1. Synthesis of hybrid nanotube-based-Ir-NHC materials **CNTO-1-Ir** and **TRCNTO-1-Ir** through the covalent functionalization of the parent nanotube materials, **CNTO** and **TRCNTO**, with the imidazolium salt [MeImH$(CH_2)_3$OH]Cl (**1**).

chromatography analysis (HP-INNOWax capillary column -0.4 μm, 25 m x 0.2 mm i.d.-) under the following conditions: a column temperature of 35 ºC (2 min) up to 220 ºC at 10 ºC min^{-1} and a flow rate of 1 cm^3 min^{-1} using ultrapure He as carrier gas.

Once the reaction was completed, the hybrid catalysts were recovered by centrifugation and washed with additional amounts of 2-propanol (3x10 mL). Several catalytic cycles were performed with these materials, under the same experimental conditions, without adding any fresh catalyst precursor. The last cycle was carried out without an inert atmosphere.

3. Results and discussion

3.1 Preparation and catalytic activity of Nanotube-based Hybrid Catalysts

The nanotube-based hybrid catalysts were prepared following the reaction path depicted in Fig. 1 [35]. The "isolated" hydroxyl groups in the nanotubes react with *p*-nitrophenylchloroformate, with the subsequent formation of the corresponding *p*-nitrophenyl carbonate esters [53,54]. Thereafter, the nucleophilic OH-ending group of the imidazolium salt [MeImH$(CH_2)_3$OH]Cl (**1**) easily displaces the *p*-nitrophenol group, resulting in the formation of the carbonate intermediates, **CNTO-1** and **TRCNTO-1**. Reaction of the imidazolium groups of these materials

Table 1 – Elemental analysis and XPS characterization of imidazolium-functionalized carbon materials

Sample	Elemental Analysis		XPS (atom. %)						
	C/O	*N(wt.%)*	*N*	*Cl*	*Csp^2*	*Csp^3*	*C-O*	*C=O*	*COO*
CNTO	3.8	0.0	0.0	0.0	64.4	17.1	7.0	3.2	8.2
TRCNTO	11.8	0.0	0.0	0.0	70.6	13.9	9.3	2.3	3.9
GO	1.0	0.1	0.0	0.0	36.2	8.4	29.6	17.8	7.9
TRGO	2.9	0.0	0.0	0.0	71.4	9.9	11.5	4.8	2.4
CNTO-1	1.7	5.6	4.7	2.0	53.7	20.9*	18.8*	4.7	1.8
TRCNTO-1	6.7	2.5	1.4	0.6	57.1	17.8*	16.4*	7.2	2.0
GO-1	1.4	6.9	5.6	2.5	42.7	24.0*	21.1*	6.2	6.0
TRGO-1	3.8	1.4	1.4	0.6	58.2	15.6*	14.4*	6.1	6.9

* Includes the C-N bonds

with the methoxo iridium(I) dimer compound $[Ir(\mu\text{-}Ome)(cod)]_2$ (cod = 1,5-cyclooctadiene) gave the nanotube-based hybrid materials **CNTO-1-Ir** and **TRCNTO-1-Ir**.

The covalent linkage of the imidazolium ligand to the nanotube was confirmed by the characterization of the intermediate species **CNTO-1** and **TRCNTO-1.** These materials still form stable suspensions in acetone (see Supporting Information) and their ^1H NMR (acetone-d_6) spectra show a set of signals typical of imidazolium groups, i.e., 7.41/7.35 ppm (H4 and H5) and 8.64 ppm (H2) (see Supporting Information). Neither the signals corresponding to the nitrophenyl fragment nor those corresponding to the imidazolic –OH group can be observed in the spectra. The presence of nitrogen and chlorine in their XPS spectra at a N:Cl ratio of 2 also confirms these results (Table 1). From these analyses it is estimated that almost four times more imidazolium ligand is introduced in **CNTO-1** than in **TRCNTO-1**, what could be justified considering a larger amount of OH groups (at basal planes) in the **CNTO** parent material compared to those of **TRCNTO** as confirmed by FTIR analysis, together a better dispersion capacity of the material in the polar reaction medium (see Supporting Information). Additionally, the larger percentage of the C-O band on the C1s XPS curve, Table 1, observed for **TRCNTO** is attributed to an increase in unreactive epoxy or ether groups [55]. Similar

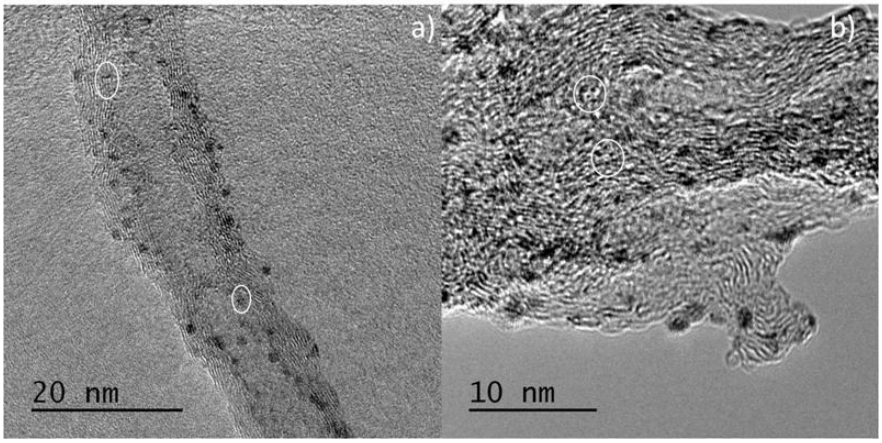

Fig. 2 HRTEM images of a) **CNTO-1-Ir** and b) **TRCNTO-1-Ir.**

tendencies were observed in the functionalization of graphene oxides and thermally reduced graphene oxides under the same experimental conditions [35].

The HRTEM images in Figure 2 of the hybrid materials with the N-heterocyclic carbene (NHC) iridium complexes show homogeneous distribution of electron-dense regions associated with the supported iridium species. In spite of the presence of these anchored iridium species in **CNTO** and **TRCNTO**, they exhibit the same appearance in terms of number of layers and interlayer distances as their parents (see Supporting Information) which indicates that functionalization has not caused any damage to the nanotube layers. The iridium spots observed (also confirmed by EDX, see Supporting Information) exhibit diameters from 0.17-0.27 nm (highlighted with white circles), which are in the range of the molecular complexes, to 1.2-1.4 nm and even larger, which are the case of clusters or nanoparticles possibly formed during beam irradiation inside the microscope chamber. Similar size distributions were observed for the graphene-based hybrid catalyst [35] or even for other supported molecular iridium catalysts [56,44].

The amount of iridium in the samples, calculated by means of ICP-MS, was 12.5 and 10.1 wt.% for **CNTO-1-Ir** and **TRCNTO-1-Ir**, respectively. The percentage of iridium in the **TRCNTO-1-Ir** material lies within the expected range, as is confirmed by the amount of imidazolium salt linked to the material (98%). However, the metal content in **CNTO-1-Ir** is below the estimated value (52%), which might be explained by the reduced amount of imidazolium ligands available due to steric hindrance resulting from the high density of functional groups [32].

Table 2 – Catalytic Hydrogen Transfer from 2-Propanol to Cyclohexanone using carbon nanotube and graphene based iridium-NHC hybrid catalysts, and the related acetoxy-functionalized NHC-Ir homogeneous catalyst [IrCl(cod)(MeIm$(CH_2)_3OCOCH_3$)] **(Ir-ImidO).**[a,b]

					Recyclability	
Catalyst	**Time (min)[c]**	**Conversion (%)**	**TOF_0 (h^{-1})[d]**	**TOF_{50} (h^{-1})[e]**	**Mean Conversion 4 cycles-Argon (%)**	**Conversion 5th cycle on Air (%)**
CNTO-1-Ir	210	89	3000	1304	93	92
TRCNTO-1-Ir	120	92	6000	3000	93	93
GO-1-Ir	760	93	1020	375	92	94
TRGO-1-Ir	150	90	3600	1685	93	92
Ir-ImidO	200	92	3000	1485	-	-

[a] Reaction conditions: catalyst/substrate/KOH ratio of 1/1000/5, 0.1 mol% of catalyst in 2-propanol (5 mL) at 80 °C. [b] The reactions were monitored by GC using mesitylene as internal standard. [c] Reaction time at 90% of conversion. [d, e] TOF, turnover frequency [(mol product/mol catalyst)/time (h)] were calculated at initial time (60s) or at 50% of conversion, TOF0, and TOF50, respectively.

The hydrogen-transfer catalytic activity of the samples was studied in the reduction of cyclohexanone to cyclohexanol using 2-propanol both as hydrogen source and as a non-toxic solvent. The catalytic conditions used were catalyst loads of 0.1 mol %, with 0.5 mol % of KOH as co-catalyst and 80 ºC, i.e., identical conditions to those recently reported for the same catalyst supported on graphene materials [35]. For comparative purposes, these results are also depicted in Fig. 3 and summarized in Table 2, together with those of the molecular acetoxy-functionalized NHC complex [IrCl(cod)(MeIm$(CH_2)_3OCOCH_3$)] (**Ir-ImidO**) [44]. It is worth noting that none of the iridium free nanotube and graphene materials showed any catalytic activity (see Supporting Information). Additionally, the nanotube and graphene based catalysts prepared by means of the same procedure but without NHC linkages showed no catalytic activity at all after the first cycle probably due to leaching of the iridium after washing (see Supporting Information).

Taking into account the carbon nanotube-iridium-NHC catalysts, the catalytic activity of the partially reduced materials **TRCNTO-1-Ir** is higher than that of **CNTO-1-Ir**, leading to yields higher than 90% in 100 min instead of 210 min required for the fully oxidized catalyst (conversions determined by GC with

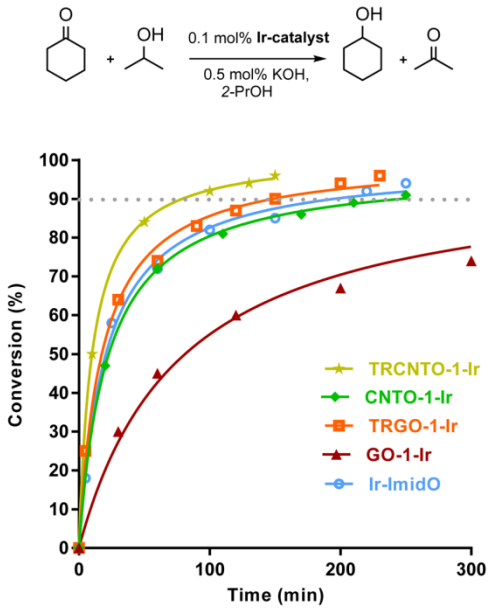

Fig. 3 – Reaction profiles showing the transfer hydrogenation of cyclohexanone by carbon nanotube and graphene based iridium-NHC hybrid catalysts and the related homogeneous molecular catalyst [IrCl(cod)(MeIm(CH_2)$_3$OCOCH_3)] (**Ir-ImidO**).

mesitylene as internal standard). A similar trend was observed for the graphene-based hybrid catalysts, which confirms that for this type of catalytic reactions, a partial reduction of the nano-support has a positive effect on the catalytic activity. Additionally, all iridium-NHC carbon nano-supports can easily recycled by a method consisting on simple centrifugation, washing of the catalysts with fresh 2-propanol (4 x 5 mL) and addition of more cyclohexanone, KOH and 2-propanol. The recycling processes render conversions above 90 % after five catalytic runs with reaction times of 2.5 h for **TRGO-1-Ir** and 13 h for **GO-1-Ir** for each run, while the catalytic reactions take 1.5 h and 4 h for **TRCNTO-1-Ir** and **CNTO-1-Ir**, respectively. All the reaction profiles are similar in the successive experiments, even in the case of the last cycle, where there is no protective atmosphere (see Supporting Information). In addition, ICP-MS measurements of the reused materials after the fifth catalytic runs showed similar iridium content (12.3 and 10.0 wt.% for **CNTO-1-Ir** and **TRCNTO-1-Ir**, respectively) than that of the fresh catalysts (12.5 and 10.1 wt.%, respectively) which reveal no leaching of the iridium on those materials.

Of special interest, however, is the fact that the catalytic activity of all the carbon nanotube-based hybrid catalysts is greater than that of their

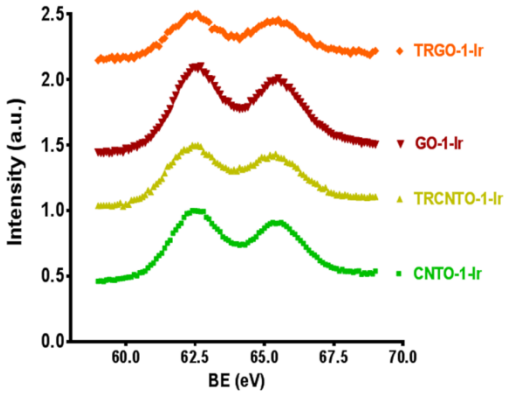

Fig 4. High-resolution Ir4f XPS spectra obtained for the all the hybrid carbon nanotube and graphene based iridium-NHC catalysts.

corresponding graphene material. In this regard it is worth noting that the catalytic activity of **GO-1-Ir** is also lower than that of the homogeneous catalyst. In order to explain these findings, a detailed characterization of the supported catalyst was performed.

3.2 Structural features of the nanotubes and graphene-NHC-Iridium hybrid catalysts

In order to gain an insight into the local structure of the iridium atoms in the hybrid catalysts, XAS measurements were performed at room temperature. All the XANES spectra show similar features (see Supporting Information) and their edge position is equal to that observed in the Ir(I) reference compound, [IrCl(cod)(MeIm $(CH_2)_3OH$)], and therefore intermediate between the metal Ir and IrCl3 indicating a similar state of oxidation of (I) for the Ir atoms in these hybrid catalysts (see Supporting Information). This is in agreement with the high-resolution Ir4f XPS band obtained for all hybrid nanotube and graphene based iridium catalysts (Fig. 4) which shows two peaks (corresponding to $Ir4f_{7/2}$ and $Ir4f_{5/2}$) centered at 62.4 and 65.6 eV, that are characteristic of iridium(I) compounds [57].

Fig. 5a presents the k^2-weighted EXAFS signals for all studied hybrid catalysts and the reference compound [IrCl(cod)(MeIm$(CH_2)_3OH$)] for the sake of comparison. The four hybrid catalysts show similar oscillations in the spectra though a higher damping is observed in the signal of **GO-1-Ir**. However, the signal for the reference compound shows a clear interference at k ~ 8-11 $Å^{-1}$. In order to highlight the differences between the compounds under study, Fig. 5b displays the modulus of the FTs of the previous EXAFS spectra to provide a

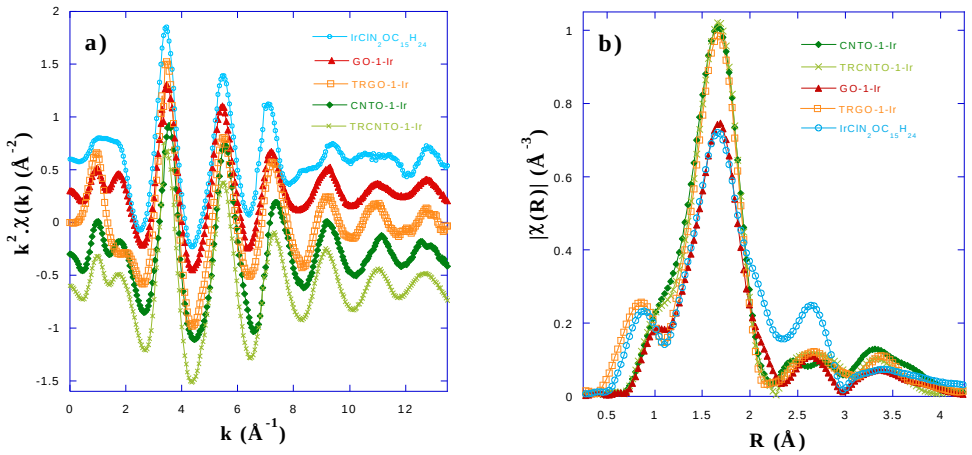

Fig 5. A) k^2-weighted EXAFS spectra for the four hybrid catalysts and the [IrCl(cod)(MeIm$(CH_2)_3$OH)] reference compound ($IrClN_2OC_{15}H_{24}$). Data are shifted in the vertical scale for the sake of comparison. B) Moduli of the FTs of the $k^2\chi(k)$ EXAFS signals for the same samples.

measure of the pseudo radial distribution function around the Ir atom. The hybrid catalysts show a first coordination shell composed by a single peak at R ~ 1.7 Å (without phase shift correction) while a second peak or shoulder is observed in the reference complex close to 2.1 Å (related to the above mentioned interference) that it is ascribed to the Ir-Cl bond. Then, the first main isolated peak in the FTs of the catalysts corresponds to the first-neighbors coordination shell, which is only composed of light elements, likely ascribed to C (and/or some O). The intensity of this peak is significantly smaller for the **GO-1-Ir** samples than in the other three compounds. The decrease in intensity is related to the high damping observed in its EXAFS signal and indicates greater structural disorder. Structures beyond 2.2 Å correspond to mixed contributions from the next-neighbors coordination shells. Although all the samples exhibit different patterns in this range, the signals are significantly weaker and broader, which prevent them from being analyzed. Therefore, EXAFS analysis was limited to the first coordination shell, performing the study between 1.15 and 2.25 Å in the R-space.

In order to obtain an accurate model for the analysis of our EXAFS data, we have drawn on our previous experience [43]. The first coordination shell of the Ir atom in the reference complex, [IrCl(cod)(MeIm$(CH_2)_3$OH)], is composed of a Cl atom, C number 1 (C_1) in the

248hloride248-2-ylidene ring and 4 C atoms of both C=C bonds present in the cyclooctadiene ligand (see Fig. 6a).

The hybrid materials should have, in principle, the IrCl(cod) metal fragment anchored to the carbon matrix (either **CNTO** or **GO**) through the NHC linker (Fig. 1). However, having in mind a possible iridium-support interaction, the ionization of the 248hloride ligand cannot be discarded. Thus, replacement of the Cl by another anion, probably an O atom from the oxidized carbon matrix, could be possible. As shown in Fig. 5, the EXAFS signal rules out the presence of Cl atoms in the first coordination shell of these hybrid catalysts (lack of interference at k ~ 8-11 $Å^{-1}$), as reported in related compounds [35,44]. Therefore, our proposed model for the first coordination shell surrounding Ir atoms inside the catalysts is composed of five Ir-C and one Ir-O contributions. The Ir-C and Ir-O phase shifts and back scattering amplitudes were calculated from the square planar reference compound [Ir($NCCH_3$)(cod)(MeIm$(CH_2)_3$OH][BF_4] and their bond lengths were taken as the starting point (see Fig. 6b). The distances of Ir to the carbons in the diolefin range between R_2 = 2.13 Å and R_3 = 2.19 Å and they are coupled in pairs (2+2). The bond length to the C_1 is R_1~ 2.03 Å and the Ir-O bond length is assumed to be close to this value. As a result, the iridium centre is bonded to six light elements with the following distribution: R_1 (×2), R_2 (×2) and R_3 (×2). A total of 4 parameters are refined, with an average inner potential correction of the threshold (ΔE_0), an average Debye-Waller factor (σ^2) and two distances, R_2 and R_3 are coupled with the same free parameter. The amplitude reduction factor S^2_0 is

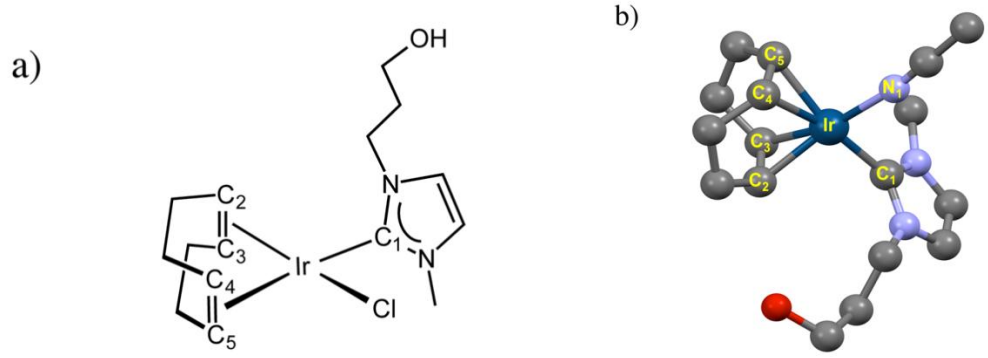

Fig 6. A) Schematic molecular structure of the reference neutral chloride compound [IrCl(cod)(MeIm$(CH_2)_3$OH)]**.** B) Molecular structure of the cation of [Ir($NCCH_3$)(cod)(MeIm$(CH_2)_3$OH)][BF_4] (Hydrogen atoms have been omitted for clarity). Selected bond lengths (Å) and angles (º): Ir–C(1) 2.031(3) , Ir–C(2) 2.127(3), Ir–C(3) 2.134(4), Ir–C(4) 2.199(3), Ir–C(5) 2.186(3), Ir–N(1) 2.032(3), C(1)–Ir–N(1) 92.44(12), C(1)–Ir–C(2) 90.58(13), N(1)–Ir–C(5) 87.55(12), C(2)–Ir–C(4) 90.11(14) [52].

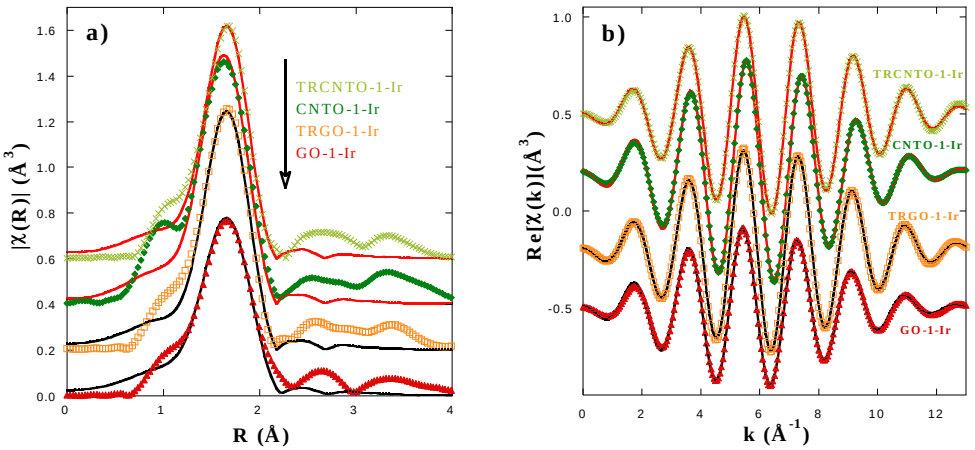

Fig. 7 – Comparison between experimental data (circles) and best fits (solid lines) for the spectra of the hybrid catalyst. A) Moduli of the FTs of the $k^2\chi(k)$ EXAFS signals, and b) real part of the Fourier-filtered spectra in k-space corresponding to the first shell coordination.

fixed to 1 in agreement with the value obtained for the reference compounds. Fig. 7 compares the best fit and experimental spectra corresponding to the moduli of the FTs of the k^2-weighted EXAFS (Fig. 7a) with the corresponding Fourier filtered spectra in k-space (Fig. 7b). There is considerable agreement in spite of the simplicity of our structural model.

The relevant structural parameters obtained for the four hybrid catalysts are summarized in Table 3. The distribution of bond lengths is very similar for the four materials and they are slightly shorter than that of the reference compound. The only significant difference concerns the **GO-1-Ir** compound that exhibits greater local disorder and this is reflected in a larger σ^2–value. This disorder is also reflected in the higher standard deviation of the refined distances and may indicate a broader distribution of Ir-C paths.

If these results are compared with the catalytic activity exhibited by these materials it will be observed that **GO-1-Ir** shows by far the lowest catalytic activity (Fig. 3, Table 2). This reflects the stronger local disorder of the Ir first-neighbors coordination shell in this sample that could be due to the high oxidation degree of this support (Table 1) has a negative effect on the catalytic activity of the compound. The catalytic results are however also determined by the peculiarities of the particular carbon support. It can be inferred from this results that the next-neighbors coordination shells, which are different in all the samples studied,

Table 3 – Best fit structural parameters for the first coordination shell of the hybrid catalysts at the Ir L_3-edge: Average inner potential correction (eV), bond lengths (Å), average Debye-Waller factor ($Å^2$) and a residual factor of the fit.[a]

Sample	ΔEo (eV)	R_1(Å)	R_2(Å)	R_3(Å)	$10^3 \cdot \sigma^2$($Å^2$)	R_F
CNTO-1-Ir	8.3(7)	2.03(2)	2.12(2)	2.18(2)	3.3(4)	0.0029
TRCNTO-1-Ir	7.7(7)	2.02(2)	2.10(2)	2.16(2)	3.0(3)	0.0028
TRGO-1-Ir	8.2(9)	2.02(2)	2.11(2)	2.17(2)	3.6(9)	0.0049
GO-1-Ir	8.5(8)	2.04(4)	2.12(4)	2.18(4)	7.0(22)	0.0085

[a] The residual factor accounts for the misfit between the actual data and the theoretical calculations [58]. Numbers in parentheses are the errors estimated from different analyses to the best significant digit.

also plays a crucial role in the catalytic system. Unfortunately, the strong disorder inferred from the EXAFS spectra prevents an accurate analysis of these coordination shells. Therefore, in order to gain more information about the "local environment" surrounding the active Ir centers in the hybrid catalyst, the XPS C1s analyses of the materials have been closely examined. The results are summarized in Fig. 8.

Similar profiles were obtained for samples **TRCNTO-1-Ir** and **TRGO-1-Ir**, which are also similar to that of **CNTO-1-Ir**. As the first-neighbors coordination shell of the Ir supported on these materials is similar, the differences in the catalytic activity must be related to the differences in the surroundings resulting from the carbon support. Interestingly, the catalytic activity of these three samples, following the order **TRCNTO-1-Ir** > **TRGO-1-Ir** > **CNTO-1-Ir** (Fig. 3), is enhanced with the increase in the amount of Csp^2 bonds and the decrease in functional groups in the supports, which suggests that, for the catalysts with similar first-neighbors coordination shells, a more aromatic support with fewer defects would be favorable for the catalyst performance in the process under study. On the other hand, **GO-1-Ir** also shows the highest percentage of sp^3 carbon bonds and oxygen functional groups (including the C-O, C=O and COO groups). The poorer catalytic activity of this sample (Fig. 3) is therefore probably related to the strong local disorder in the graphene layer supporting the Ir catalyst. However, the extent of the disorder and its proximity to the Ir (particularly of the C-O and C=O derived functional groups in the basal planes) also seem to affect the first-neighbors coordination shell, (as can be observed

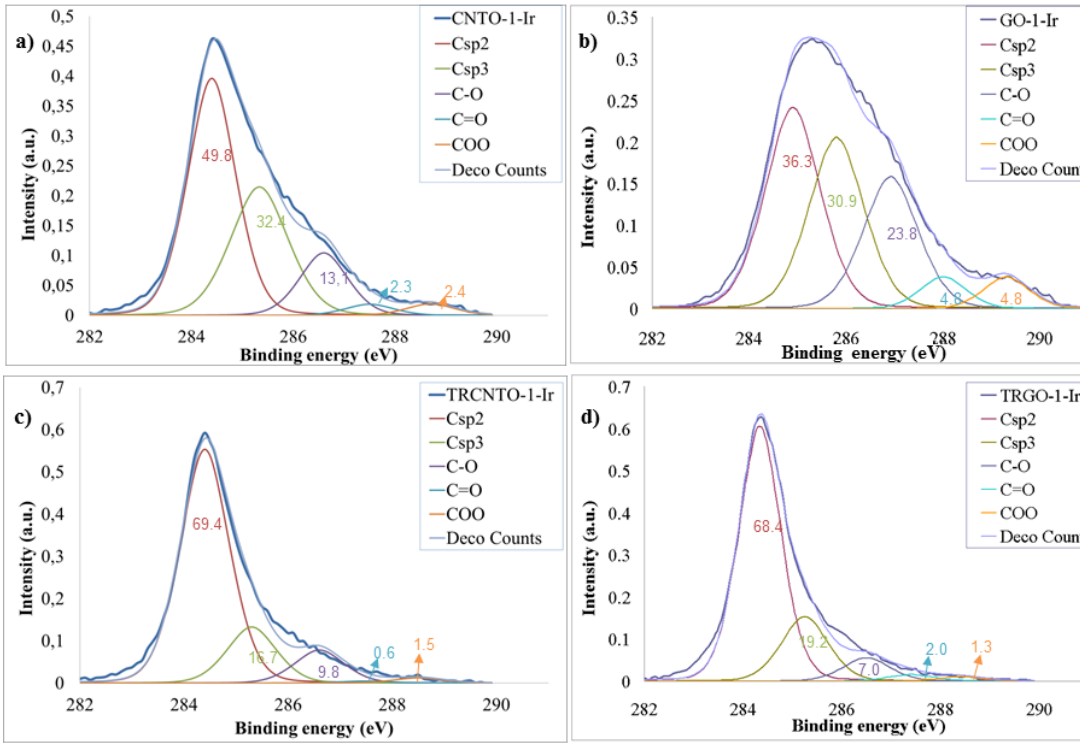

Fig. 8 – Deconvolution results of the XPS C1s curves of a) **CNTO-1-Ir**, b) **GO-1-Ir**, c) **TRCNTO-1-Ir** and d) **TRGO-1-Ir**.

from the EXAFS curves, Fig. 5 and 7) resulting in a drastic decrease in the catalytic activity.

4. Conclusions

The protocol for functionalizing oxidized carbon nanomaterials through their surface OH groups on the basis of the activation with *p*-nitrophenylchloroformate can be successfully applied to oxidized and partially reduced carbon nanotubes in order to immobilize iridium NHC-complexes in their outer and inner walls. The carbon nanotube based iridium-NHC hybrid materials were efficient catalysts for the reduction of cyclohexanone by transfer hydrogenation. These hybrid catalysts have shown a superior catalytic performance than related graphene-based hybrid materials, prepared by the same functionalization strategy, in both the oxidized and thermally reduced graphene supports.

The study of the local structure of the iridium atoms in the hybrid catalyst by EXAFS has revealed the replacement of the 251hloride ligand by an O atom from the oxidized carbon matrix as a

result of the iridium-support interaction, which might be facilitated by the presence of a flexible linker to carbon matrix. On the other hand, as it has been shown by XPS studies, the greater number of structural defects in the graphenic based materials than in their respective nanotubes might explain their different performances. Although the same first-neighbors coordination shell is formed in every hydrid catalyst, the strong structural disorder in this very local environment leads to very poor results, as in the case of the **GO-1-Ir** catalyst. In contrast, the high degree of order in the sp^2 lattice, combined with an appropriate amount of oxygen groups, provides a stability that enhances the catalytic activity, as in the case of **TRCNTO-1-Ir**.

Acknowledgments

The authors thank the Spanish Ministry of Economy and Competitiveness (MINECO/FEDER) (Projects Consolider Ingenio 2010 CSD2009-00050 and CTQ 2013-42532-P), and the Diputación General de Aragón (E07) for their financial support. Dr. P. A. thanks MICINN for a Ramón y Cajal contract. J. F-T. and M. B. acknowledge their fellowships from MINECO and MECD (AP2010-0025).

Appendix A. Supplementary data

Supplementary data associated with this article can be found, in the online version, at http://dx.doi.org/10.1016/xxx.

References

[1] Meyer JC, Geim AK, Katsnelson MI, Novoselov KS, Booth TJ, Roth S. The structure of graphene sheets. Nature 2007;446:60–3.

[2] Novoselov KS, Geim AK, Morozov SV, Jiang D, Zhang Y, Dubonos SV et al. Electric field effect in atomically thin carbon films. Science 2004;306:666–9.

[3] Zhao J, Xie RH. Electronic and photonic properties of doped carbon nanotube. J Nanosci Nanotechno 2003;3:459–78.

[4] Min SK, Kim WY, Cho Y, Kim KS. Fast DNA sequencing with a graphene-based nanochannel device. Nat Nanotechnol 2011;6:162–5.

[5] Liu Z, Bol A, Haensch W. Large-scale graphene transistors with enhanced performance and reliability based on interface engineering by phenylsilane self-assembled monolayers. Nano Lett 2011;11:523–8.

[6] Li J, Lu Y, Ye Q, Cinke M, Han J, Meyyappan M. Carbon nanotube sensors for gas and organic vapor detection. Nano Lett 2003;3:929–33.

[7] Schaetz A, Zeltner M, Stark WJ. Carbon modifications and surfaces for

catalytic organic transformations. ACS Catal 2012;2:1267−84.
[8] Su C, Loh KP. Carbocatalysts: Graphene oxide and its derivatives. Acc Chem Res 2013;10:2275-85.
[9] Sarvari MH, Sharghi H. Simple and improved procedure for the regioselective acylation of aromatic ethers with carboxylic acids on the surface of graphite in the presence of methanesulfonic acid. Synthesis 2004;13:2165–68.
[10] Sarkar S, Niyogi S, Bekyarova E, Haddon RC, Organometallic chemistry of extended periodic π-electron systems: hexahapto-chromium complexes of graphene and single-walled carbon nanotubes. Chem Sci 2011;2:1326–33.
[11] Sabater S, Mata, JA, Peris E. Immobilization of Pyrene-Tagged Palladium and Ruthenium Complexes onto Reduced Graphene Oxide: An Eflicient and Highly Recyclable Catalyst for Hydrodefluorination. Organometallics, 2015;34:1186–90.
[12] Karimi S, Tavasoli A., Mortazavi Y, Karimi A. App. Cat. A-General, 2015;499:188–196.
[13] Wang D, Niu WQ, Tan MH, Wu MB, Zheng XJ, Li YP, et al. Pt Nanocatalysts Supported on Reduced Graphene Oxide for Selective Conversion of Cellulose or Cellobiose to Sorbitol. ChemSusChem, 2014;7:1398–1406.
[14] Zhu, J., Holmen A., Chen D. Carbon Nanomaterials in Catalysis: Proton Affinity, Chemical and Electronic Properties, and their Catalytic Consequences. ChemCatChem,2013;5:378-401.
[15] Castro-Neto AH, Guinea F, Peres NMR, Geim A, Novoselov K. The electronic properties of graphene. Rev Mod Phys 2009;81:109–62.
[16] White CT, Todorov TN. Carbon Nanotubes as long ballistic conductors. Nature 1998;393:240–42.
[17] Baladin AA. Thermal properties of graphene and nanostructured carbon materials. Nat Mater 2011;10:569–81.
[18] Ovid'Ko IA. Mechanical properties of graphene. Rev Adv Mater Sci 2013;34:1–11
[19] Treacy MMJ, Ebbesen TW, Gibson JM. Exceptionally high Young's modulus observed for individual carbon nanotubes. Nature 1996;381:678–80.
[20] Zhang P, Yuan J, Li H, Liu X, Xu X, Antonietti M, et al. Mesoporous nitrogen-doped carbon for copper-mediated Ullmann C-O/-N-S cross-coupling reactions. RSC Adv, 2013;3:1890-5.
[21] Zhang P, Gong Y, Li H, Che Z, Wang Y. Solvent-free aerobic oxidation of hydrocarbons and alcohols with Pd@N-doped carbon from glucose. Nature Commun, 2013;4:1593-5.
[22] Iijima S. Helical microtubes of graphitic carbon. Nature 1991;354:56–8.
[23] Lerf A, He H, Forster M, Klinowski JJ. Structure of graphite oxide revisited. Phys Chem B 1998;102:4477–82.
[24] Dreyer DR, Park S, Bielawski CW, Ruoff RS. The chemistry of graphene oxide. Chem Soc Rev 2010;39:228–40.

[25] Szabo T, Berkesi O, Forgo P, Josepovits K, Sanakis Y, Petridis D, et al. Evolution of surface functional groups in a series of progressively oxidized graphite oxides. Chem Mater 2006;18:2740–9.
[26] Aqel A, Abou El-Nour KMM, Ammar RAA, Al-Warthan A. Carbon nanotubes, science and technology part (I) structure, synthesis and characterization. Arab J Chem 2012;5:1−23.
[27] Sabater S, Mata JA, Peris E. Catalyst enhancement and recyclability by immobilization of metal complexes onto graphene surface by noncovalent interactions. ACS Catal 2014;4:2038−47.
[28] Georgakilas V, Otyepka M, Bourlinos AB, Chandra V, Kim N, Kemp KC et al. Functionalization of graphene: covalent and non-covalent approaches, derivatives and applications. Chem Rev 2012;112:6156–214.
[29] Li F, Zhang B, Li X, Jiang Y, Chen L, Li Y, et al. Highly Efficient oxidation of water by a molecular catalyst immobilized on carbon nanotubes. Angew Chem Int Ed 2011;50:12276–9.
[30] Tasis D, Tagmatarchis N, Bianco A, Prato M. Chemistry of carbon nanotubes. Chem Rev 2006;106:1105–36.
[31] Hamon MA, Chen J, Hu H, Chen YS, Itkis ME, Rao AM et al. Dissolution of single walled carbon nanotubes. Adv Mater 1999;11:834–40.
[32] Shen J, Shi M, Yan B, Ma H, Li N, Hu Y, et al. Covalent attaching protein to graphene oxide via diimide-activated amidation. Colloid Surf B-Biointerfaces 2010;81:434–8.
[33] Chen L, Chai S, Liu K, Ning N, Gao J, Liu Q, et al. Enhanced epoxy/silica composites mechanical properties by introducing graphene oxide to the interface. ACS Appl Mater Interfaces 2012;4:4398–404.
[34] Serp P, Corrias M, Kalck P, Carbon nanotubes and nanofibers in catalysis. Appl Cat A 2003;253:337–58.
[35] Blanco M, Álvarez P, Blanco C, Jiménez MV, Fernández-Tornos J, Pérez-Torrente JJ et al. Graphene–NHC–iridium hybrid catalysts built through –OH covalent linkage. Carbon 2015;83:21-31.
[36] Modugno G, Monney A, Bonchio M, Albrecht M, Carraro M. Transfer hydrogenation catalysis by a N-Heterocyclic carbene iridium complex on a polyoxometalate platform. Eur J Inorg Chem 2014;2356–60.
[37] Azua A, Mata JA, Peris E, Lamaty F, Martínez J, Colacino E. Alternative energy input for transfer hydrogenation using iridium NHC based catalysts in glycerol as hydrogen donor and solvent. Organometallics 2012;31:3911–9.
[38] Diez C, Nagel U. Chiral iridium(I) bis(NHC) complexes as catalysts for asymmetric transfer hydrogenation. App Organomet Chem 2010;24:509–16.
[39] Hahn FE, Holtgrewe C, Pape T, Martin M, Sola E, Oro L A. Iridium complexes with N-Allyl-substituted benzimidazol-2-ylidene ligands and their application in catalytic transfer

hydrogenation. Organometallics 2005;24: 2203–9.
[40] Hillier AC, Lee HM, Stevens ED, Nolan SP. Cationic iridium complexes bearing imidazol-2-ylidene ligands as transfer hydrogenation catalysts. Organometallics 2001;20:4246–52.
[41] Gülcemal S, Gökçe A G, Çetinkaya B. N-benzyl substituted N-heterocyclic carbene complexes of iridium(I): assessment in transfer hydrogenation catalyst. Inorg Chem 2013;52: 10601–9.
[42] Türkmen H, Pape T, Hahn F E, Çetinkaya B. Efficient transfer hydrogenation using iridium and rhodium complexes of benzannulated N-Heterocyclic carbenes. Eur J Inorg Chem 2008;5418–23.
[43] Jiménez MV, Fernández-Tornos J, Pérez-Torrente JJ, Modrego FJ, Winterle S, Cunchillos C, et al. Iridium(I) complexes with hemilabile N-Heterocyclic carbenes: efficient and versatile transfer hydrogenation catalysts. Organometallics 2011;30:5493–508.
[44] Blanco M, Álvarez P, Blanco C, Jiménez MV, Fernández-Tornos J, Pérez-Torrente JJ, et al. Enhanced hydrogen-transfer catalytic activity of iridium N-Heterocyclic carbenes by covalent attachment on carbon nanotubes. ACS Catal 2013;3:1307-17.
[45] Blanco M, Álvarez P, Blanco C, Campos N, Gómez D, Menéndez R. Influence of the alignment degree of CVD-grown carbon nanotubes on their functionalization and adsorption capacity. Diam Relat Mater 2013;37:1–7.
[46] Botas C, Álvarez P, Blanco C, Santamaría R, Granda M, Gutiérrez M D, et al. Critical temperatures in the synthesis of graphene-like materials by thermal exfoliation-reduction of graphite oxide. Carbon 2013;52:476–85.
[47] Bekhouche M, Blum L J, Doumèche B. Ionic liquid-inspired cations covalently bound to FDH improve its stability and activity in IL. ChemCatChem 2011;3:875–82.
[48] Usón R, Oro L A, Cabeza J A. Dinuclear Methoxy, Cyclooctadiene, and Barrelene Complexes of Rhodium(I) and Iridium(I). Inorg Synth 1985;23:126–7.
[49] Sherwood PMA. In Practical Surface Analysis in Auger and X-ray Photoelectron Spectroscopy; Briggs D, Seah M P. Eds.; Wiley: New York, 1990, Vol. 1, pp. 574.
[50] Elgrabli D, Floriani M, Abella-Gallar S, Meunier L, Gamez C, Delalain P, et al. Biodistribution and clearance of instilled carbon nanotubes in rat lung. Part Fibre Toxicol 2008;5:20–33.
[51] Ravel B, Newville M, ATHENA, ARTEMIS, HEPHAESTUS: data analysis for X-ray absorption spectroscopy using IFEFFIT. J Synchrotron Radiat 2005;12:537–41.
[52] Rehr JJ, Albers RC. Theoretical approaches to x-ray absorption fine structure. Rev Mod Phys 2000;72:621–54.
[53] Letsinger R L, Ogilvie K K. Use of p-nitrophenyl chloroformate in blocking hydroxyl groups in nucleosides. J Org Chem 1967;32:296–300.

[54] Oh JK, Drumright R, Siegwart DJ, Matyjaszewski K. The development of microgels/nanogels for drug delivery applications. Prog Polym Sci 2008;33:448–77.
[55] Chiang YC, Lin WH, Chang YC. The influence of treatment duration on multi-walled carbon nanotubes functionalized by H_2SO_4/HNO_3 oxidation. Applied Surface Science 2011;257:2401–10.
[56] Lu J, Serna P, Aydin C, Browning ND, Gates BC. Supported molecular iridium catalysts: Resolving effects of metal nuclearity and supports as ligands. J Am Chem Soc 2011;133:16186–95.
[57] Crotti C, Farnetti E, Filipuzzi S, Stener M, Zangrando E, Moras P. Evaluation of the donor ability of phenanthrolines in iridium complexes by means of synchrotron radiation photoemission spectroscopy and DFT calculations. Dalton Trans 2007;133–42.
[58] The crystal structure resolution for the compound $[Ir(NCCH_3)(cod)(MeIm(CH_2)_3OH)][BF_4]$, with the Formula: C17 H27 Ir1 N3 O1 1+,B1 F4 1-, and the Unit Cell Parameters: a 7.7481(5) b 11.0858(7) c 12.5112(8) P-, has been deposited in the Cambridge Structural Database (CSD) as private communication, and the numbers CCDC 1406120 have been assigned after deposition.

SUPPLEMENTARY DATA

S1. Solvent stability

S2. ^{1}H-NMR spectra of **CNTO-1** and **TRCNTO-1**

S3. FTIR spectra

S4. HRTEM and EDX spectra of nanotube derivatives

S5. XANES curves of hybrids materials

S6. Catalytic activity of iridium-free nanotube/graphene-based materials and nanotube and graphene-based catalyst prepared by means of the same procedure but without NHC linkers.

S1. Solvent stability of CNTs and TRCNTs

CNTO and **TRCNTO** form stable suspensions in water, dichloromethane (DCM) and acetone, for a period of time superior to 2 months (Figure S1, a). The materials having the imidazolium ligand, **CNTO-1** and **TRCNTO-1**, also form stable suspensions but for shorter periods of time (Figure S1, b). **CNTO-1-Ir** and **TRCNTO-1-Ir** do not form stable suspensions in those solvents (Figure S1, c).

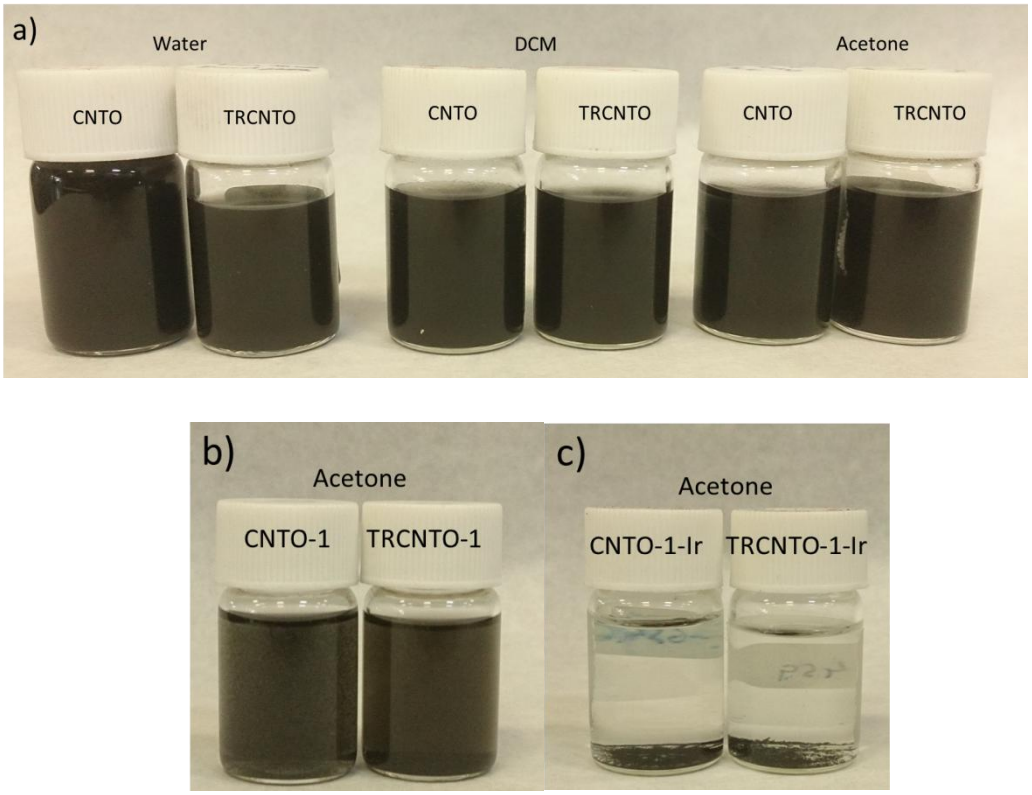

Figure S1. Images of suspensions of materials: a) **CNTO** and **TRCNTO** in water, DCM and acetone, b) **CNTO-1** and **TRCNTO-1** in acetone, c) **CNTO-1-Ir** and **TRCNTO-1-Ir** in acetone

S.2 ^{1}H NMR spectra of CNTO-1 and TRCNTO-1

CNTO-1 and **TRCNTO-1** form stable suspensions in acetone-d_6 which allowed their characterization by ^{1}H NMR. The spectra are depicted in Figure S2.

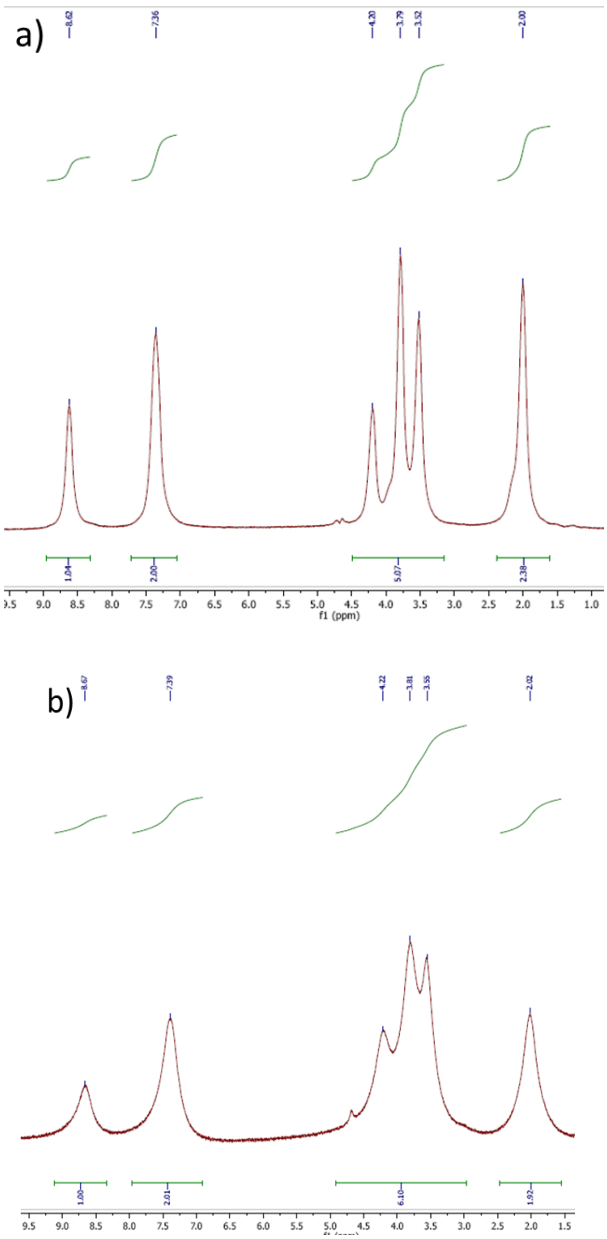

Figure S2. ^{1}H NMR spectra of a) **CNTO-1** and b) **TRCNTO-1**

S.3 FTIR spectra of CNTO and TRCNTO

Fourier transformed infrared (FTIR) spectra were collected on a ThermoFisher Nicolet 8700 FTIR interferometer equipped with a deuterated triglycine sulfate (DFT) detector, working on transmission mode; samples were prepared prior the measurements in KBr pellets. FTIR spectra, Figure S3, of oxidized nanotubes clearly show larger amount of OH groups in **CNTO**.

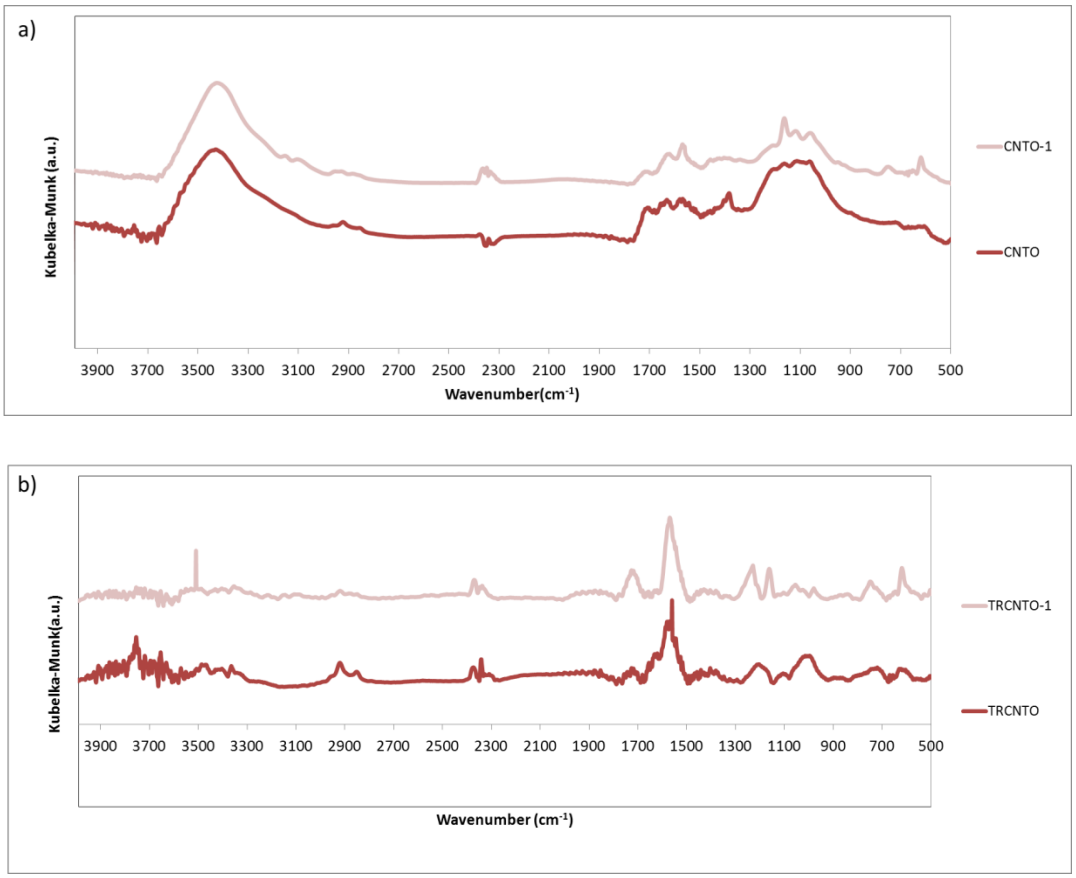

Figure S3. FTIR spectra of a) CNTO-materials and b) TRCNTO-materials

S.4 HRTEM and EDX spectra of nanotube derivatives

EDX spectra obtained from HRTEM measurements of **CNTO-1-Ir** and **TRCNTO-1-Ir** are depicted in Figure S4. Iridium center is clearly detected.

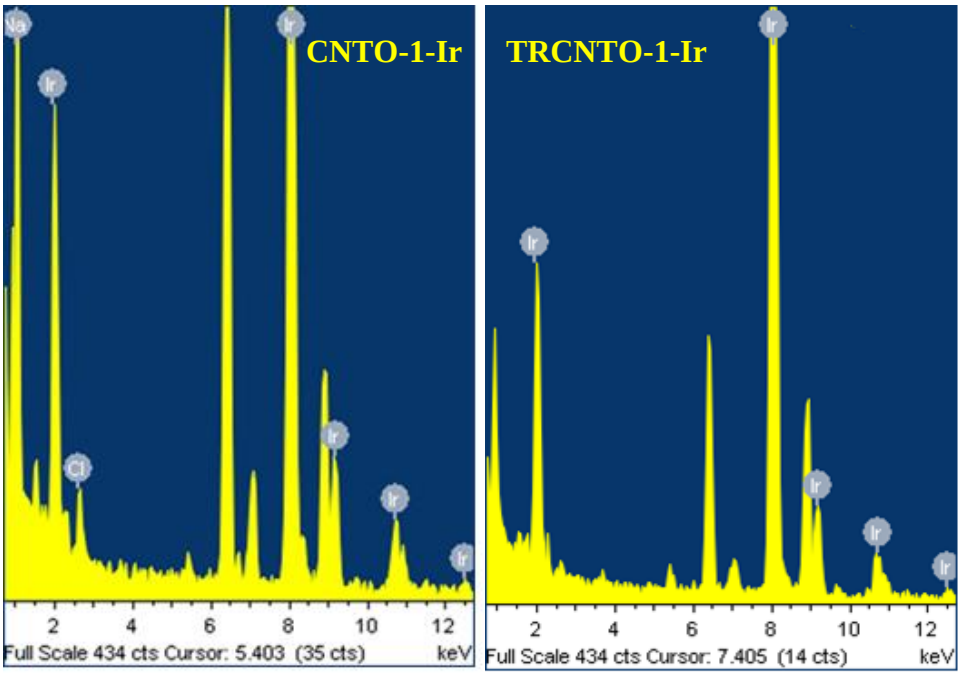

Figure S4. EDX spectra of **CNTO-1-Ir** and **TRCNTO-1-Ir**

HRTEM images of a) **CNTO**, b) **CNTO-1**, c) **TRCNTO** and d) **TRCNTO-1** are shown in Figure S5. No modification of the materials was detected after the functionalization treatment. Also, none of the materials in which the iridium complexes are supported showed any modification compared with parent and imidazolium-decorated materials.

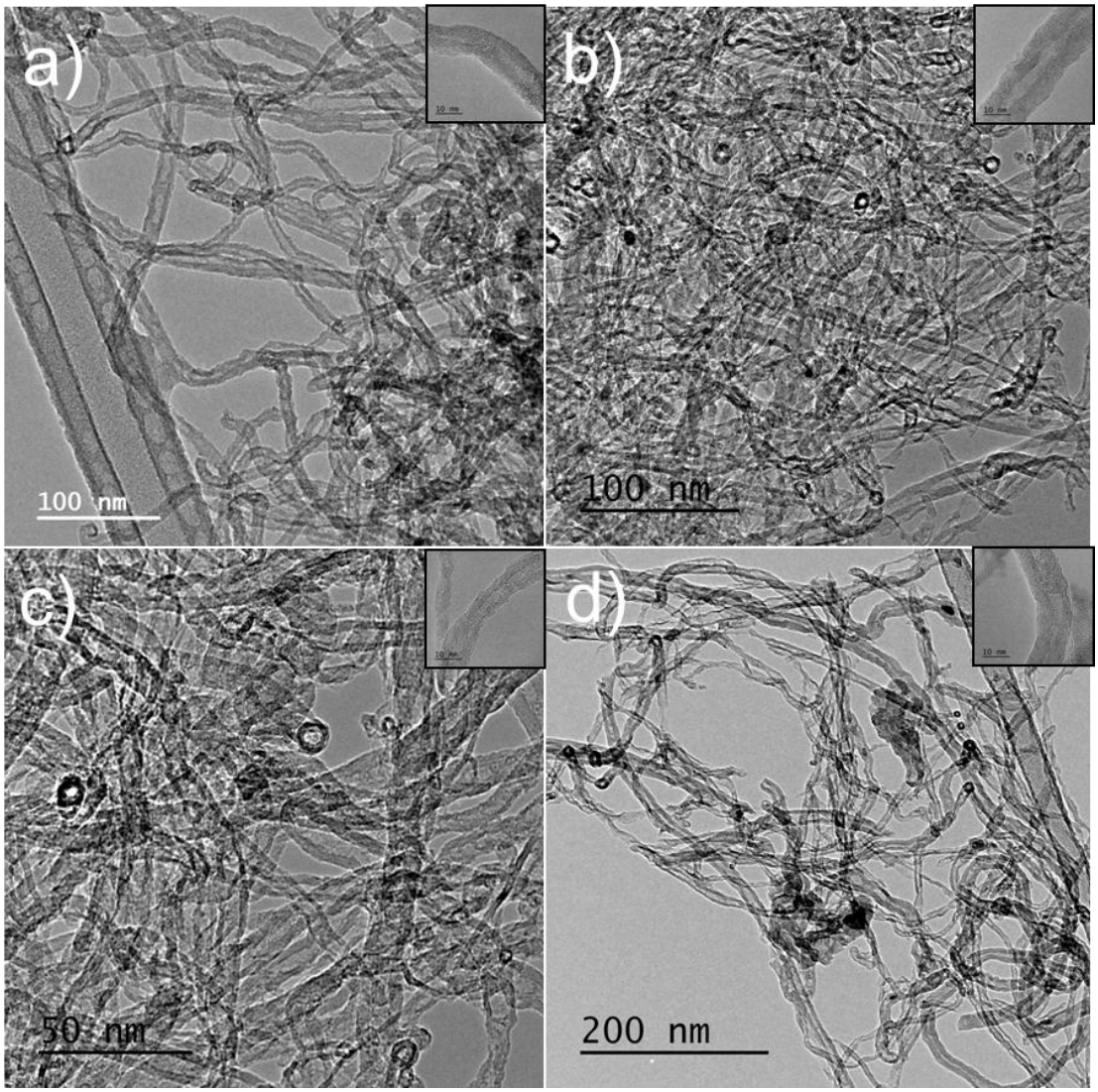

Figure S5. HRTEM images of **CNTO**, **CNTO-1**, **TRCNTO** and **TRCNTO-1.** Insets: magnification of the tubes.

S.5 XANES curves of hybrids materials

The L_{III} – edge, corresponding to the 2p → 5d transition white-line features are represented on figure S6, with the references metallic iridium (0), [IrCl(cod)(MeIm$(CH_2)_3$OH)] (I) and iridium chloride (III). The first peak is called 'white line' and its energy position and intensity give information about the electronic state of the photoabsorber atom. Figure S6.a displays the XANES spectra of the four catalysts and the Ir(I) reference compound showing the same energy position and similar features for the five samples. Figure S6.b shows that the position/energy of one organometallic complex (similar results are obtained for the rest of catalysts) lies between the ones for Ir^0 and $IrCl_3$, indicating an intermedium oxidation state. Both plots agree with Ir(I) for the hybrid catalysts as confirmed in the XPS spectra depicted on the main text.

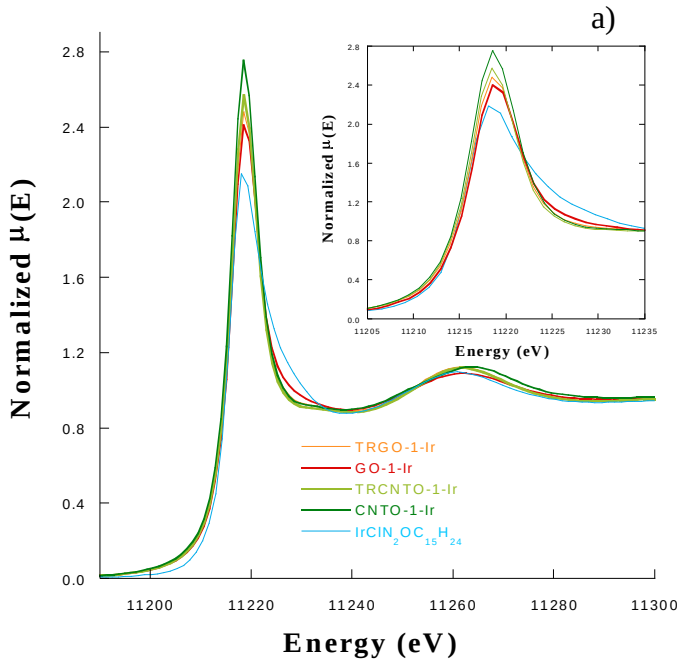

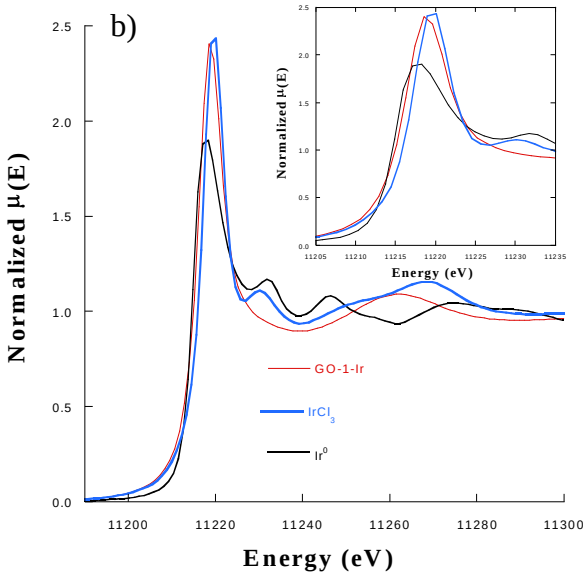

Figure S6. A) XANES spectra for the four hybrid catalysts and [IrCl(cod) (MeIm $(CH_2)_3OH$)]. B) XANES spectra for Ir^0, **GO-1-Ir** and $IrCl_3$ (similar plots are obtained for the rest of catalysts). Insets: magnifications of the white-lines.

S.6 Catalytic activity of iridium-free nanotube/graphene-based materials and nanotube and graphene-based catalyst prepared by means of the same procedure but without NHC linkers.

The catalytic activity of iridium free nanotube/graphene-based materials as well as nanotube and graphene-based catalyst prepared by means of the same procedure lacking NHC linkers is shown in Figure S7.

The iridium-free **CNTO-1**, **TRCNTO-1**, **GO-1** and **TRGO-1** materials showed no catalytic activity. On the other hand, the nanotube/graphene-based catalyst prepared by means of the same procedure but lacking NHC linkers (control samples **CNTO-**

Ir, **TRCNTO-Ir**, **GO-Ir** and **TRGO-Ir**) showed a very limited catalytic activity becoming inactive after the first cycle probably due to leaching of the iridium after washing. However, the NHC-based catalysts achieved complete conversion after 5 cycles, including the final one performed without protective atmosphere.

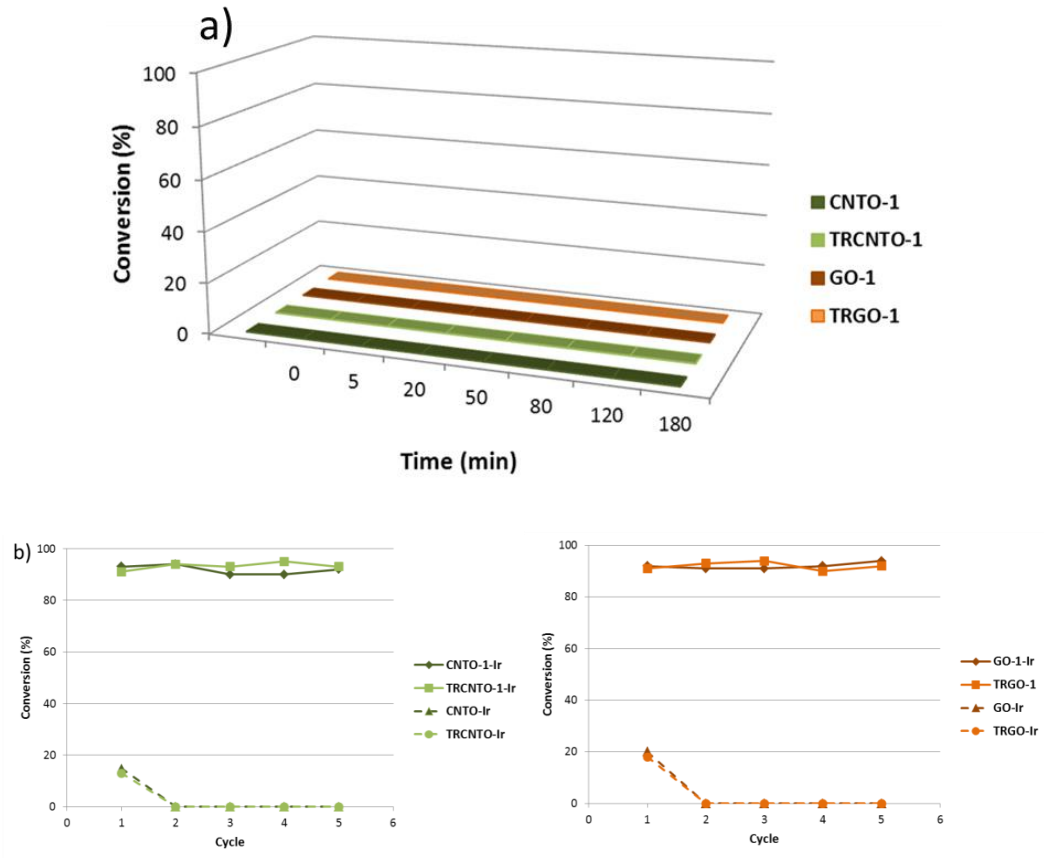

Figure S7. Catalytic activity of: a) iridium-free nanotube/graphene-based materials, and b) nanotube and graphene-based catalyst prepared by means of the same procedure but lacking NHC linkers

5. CONCLUSIONES

CONCLUSIONES

La presente Memoria describe las diferentes metodologías aplicadas a la funcionalización de nanomateriales de carbono, concretamente nanotubos de carbono y materiales grafénicos, con complejos organometálicos de tipo NHC de iridio para su utilización como catalizadores en procesos de reducción de sustratos insaturados a través de transferencia de hidrógeno.

Conforme a todo lo expuesto a lo largo del Trabajo, las principales conclusiones extraídas en esta Tesis Doctoral son las siguientes:

- Diferentes complejos organometálicos NHC de iridio pueden ser introducidos en los grupos funcionales oxigenados superficiales de nanomateriales de carbono, como nanotubos de carbono oxidados y óxido de grafeno. Un adecuado desarrollo de esta química superficial oxigenada es necesario para obtener una buena carga metálica en la superficie del soporte.

- Los complejos organometálicos soportados se comportan como catalizadores activos y estables en procesos de reducción por medio de transferencia de hidrógeno. La actividad catalítica de dichos complejos enlazados al material, a través de los grupos carboxilo o hidroxilo, es

similar o mejor que en el caso de sistemas homogéneos análogos. Además, los catalizadores se vuelven más estables en atmósferas no protegidas, y la heterogenización permite la reutilización de los mismos al obtener conversiones similares en los mismos tiempos tras la realización de varios ciclos sucesivos.

- La reconstrucción estructural al aplicar un proceso de reducción térmica a ambos materiales oxidados hace que el sistema catalítico final, tras las rutas de funcionalización, presente mejores prestaciones que el correspondiente sistema oxidado funcionalizado de idéntico modo.

- El entorno local del metal, junto con la química superficial del material, determina la actividad catalítica del sistema final. Si bien todas las muestras ensayadas que contienen complejos NHC obtuvieron conversiones completas, los catalizadores más rápidos fueron aquellos que presentaron una adecuada cantidad y tipo de grupos funcionales oxigenados y defectos estructurales. Una oxidación excesiva que genere grupos carboxilo libres, o ineficaz, que no aporte el suficiente oxígeno superficial, desemboca en catalizadores menos eficientes.

Además, de los cinco artículos que componen esta Memoria se pueden extraer las siguientes conclusiones específicas, que son las que figuran en los mismos:

<u>En la oxidación de nanotubos de carbono:</u>

El tratamiento aplicado a nanotubos de carbono alineados y tipo ovillo con reactivos de capacidad oxidativa creciente conduce a un incremento proporcional en

los grupos funcionales oxigenados en la superficie y puntas de los nanotubos. Contrariamente a lo publicado con anterioridad, el tratamiento con los agentes menos oxidantes fue más efectivo en los nanotubos alineados, principalmente en forma de grupos COH/C=O, posiblemente debido a sus más homogéneas propiedades superficiales y a su mayor longitud. Únicamente el tratamiento más oxidante introduce más grupos oxigenados en los nanotubos tipo ovillo (menor relación C/O), aunque con una menor cantidad de grupos COOH. Estas observaciones afectan tanto a la capacidad de formar suspensiones estables en agua como la capacidad de adsorción de los nanotubos. Así, en el estudio comparativo de adsorción de benceno, los nanotubos alienados presentaron cinéticas más rápidas y mayores capacidades de adsorción cuando fueron sometidos al tratamiento más severo. Los resultados obtenidos confirman que con el adecuado tratamiento es posible la preparación de nanotubos alineados con el potencial suficiente para convertirse en adsorbentes competitivos de benceno en corrientes industriales de desechos.

En la funcionalización de nanotubos de carbono oxidados a través de sus ácidos carboxílicos:

La funcionalización covalente de tipo éster entre los nanotubos y sales de imidazolio se puede realizar a través de los grupos carboxilo producto del proceso de oxidación. Los materiales modificados con sales de imidazolio son apropiados para la síntesis de catalizadores nanohíbridos que contienen complejos organometálicos de tipo NHC de iridio con gran eficiencia.

Los materiales basados en complejos de NHC de iridio soportados sobre nanotubos son catalizadores activos en la reducción de ciclohexanona a ciclohexanol por procesos de transferencia de hidrógeno usando 2-propanol como fuente de

hidrógeno. Estos materiales mostraron un comportamiento superior al obtener conversiones completas en menores tiempos que sus análogos catalizadores homogéneos con ligandos NHC funcionalizados con grupos acetoxy. No obstante, ambos catalizadores presentan perfiles de reacción similares, lo que sugiere que se rigen por el mismo mecanismo.

Además, se confirmó que los catalizadores soportados pueden ser reusados en ciclos consecutivos sin observar ninguna pérdida de actividad, incluso cuando se realiza la reacción bajo una atmosfera no protectora. El efecto de confinamiento, debido a la porosidad del material, o un efecto de superficie basado en la potencial cooperación de los grupos funcionales hidroxílicos de las paredes del nanotubo podrían explicar el notable incremento observado en la actividad catalítica.

En la funcionalización de nanotubos de carbono con distinto grado de oxidación:

Se realizó la funcionalización covalente de nanotubos de carbono oxidados progresivamente con un carbeno N-Heterocíclico de iridio. La carga del ligando imidazólico así como del iridio metálico en los soportes dependió del grado de oxidación del nanotubo de partida empleado.

La actividad catalítica de los complejos NHC soportados en la transferencia de hidrógeno de ciclohexanona también dependió de la química superficial y del grado de oxidación de los nanotubos en los que están soportados. Como el soporte más oxidado es aquel que consigue la mejor actividad de las muestras estudiadas, es necesaria la correcta cantidad de grupos funcionales y defectos estructurales que permitan una mejor difusión, dispersión y acceso a los centros activos, así como una mejor estabilización del metal para la obtención de buenos resultados catalíticos

En la funcionalización de materiales grafénicos en sus grupos hidroxilos:

El anclaje covalente de una sal de imidazolio se consiguió a través de un intermedio tipo carbonato orgánico lábil preparado a través de reacciones selectivas con los grupos –OH superficiales con *p*-nitrofenil cloroformiato. Los materiales grafénicos funcionalizados con sales de imidazolio fueron usados para la síntesis de materiales híbridos que contuvieran complejos NHC de iridio soportados enlazados mediante estos carbonatos.

Los materiales híbridos grafeno-iridio-NHC se utilizaron como catalizadores en la reducción de ciclohexanona a ciclohexanol mediante transferencia de hidrógeno usando 2-propanol como fuente de hidrógeno. Se consiguió un mejor comportamiento catalítico con el material grafénico parcialmente reducido, incluso ligeramente superior al complejo homogéneo basado en ligandos NHC funcionalizados con grupos acetoxy análogo. Dicha mejora puede ser debida a la reconstrucción parcial de la estructura sp^2 que ejerce un efecto positivo en la actividad

No obstante, la presencia de los grupos funcionales oxigenados en la superficie del material, actuando como centros capaces de promover reacciones secundarias con los complejos precursores de iridio, parecen ser la razón de la baja actividad de los catalizadores híbridos basados en óxido de grafeno sin uniones de tipo NHC con el metal.

También se demostró que los catalizadores heterogéneos de materiales grafénicos pueden ser reutilzados en cinco ciclos consecutivos sin detectar perdida de actividad, incluso cuando la reacción es realizada al aire.

En la comparación de nanotubos de carbono con materiales grafénicos:

El protocolo para la funcionalización de nanomateriales de carbono oxidados a través de sus grupos OH, a través de la activación con p-nitrofenil cloroformiato, se puede aplicar a nanotubos de carbono oxidados y parcialmente reducidos con el objetivo de inmovilizar complejos NHC de iridio tanto en las paredes internas como externas. Los materiales híbridos nanotubo de carbono – complejo NHC de iridio fueron catalizadores activos en la reducción de ciclohexanona por transferencia de hidrógeno, mostrando mayor actividad que sus correspondientes materiales híbridos de grafeno, preparados mediante la misma estrategia, tanto en el caso de soportes oxidados como reducidos.

El estudio de la estructura local de los átomos de iridio en los catalizadores híbridos mediante EXAFS reveló la sustitución del ligando cloruro por un átomo de oxígeno de la matriz de carbono, como resultado de las interacciones iridio-soporte. Por otro lado, los estudios XPS demostraron que el mayor número de defectos estructurales en los catalizadores con materiales grafénicos, comparados con sus análogos nanotubos, podrían ser la causa de las diferentes actividades encontradas. Aunque se forme la misma primera esfera de coordinación en cada catalizador, el mayor desorden estructural que presenta **GO-1-Ir** en este entorno tan localizado conduce a pobres resultados. Sin embargo, el alto grado de orden en la estructura aromática, combinado con la apropiada cantidad de grupos oxigenados proporciona un grado de estabilidad que induce un incremento en la actividad catalítica, como es el caso de **TRCNTO-1-Ir**.

BIBLIOGRAFÍA

BIBLIOGRAFÍA

[1] IUPAC. Compendium of Chemical Terminology, 2nd ed. (the "Gold Book"). Compiled by A. D. McNaught and A. Wilkinson. Blackwell Scientific Publications, Oxford (1997)

[2] R. Dybkaer. *Pure Appl. Chem.* **2001,** 73, 927-932

[3] P. A. Brady, J, K. M. Sanders. *Chem. Soc. Rev.*, **1997**, 26, 327-336

[4] D. D. Vos, I. F. J. Vankelecom, P. A. Jacobs. Eds. "Chiral Catalyst Immobilization and Recycling". Wiley, New York, 11 jul. 2008.

[5] A. Corma. *Chem. Rev*. **1997**, 97, 2373−2419

[6] B. Clapham, T. S. Reger, K. D. Janda. *Tetrahedron* **2001,** 57, 4637–4662

[7] F. Rodríguez-Reinoso. *Carbon* **1998**, 36, 159-175

[8] a) J. P. Cleuziou, W. Wernsdorfer, V. Bouchiat, T. Ondarçuhu, M. Monthioux. *Nat. Nanotechnology* **2006**, 1, 53-59; b) M.I. Katsnelson, K.S. Novoselov. *Solid State Communications*, **2007**, 143, 3-13.

[9] IUPAC Gold Book. International Union of Pure and Applied Chemistry. Blackwell Scientific Publications, Oxford. Retrieved 31 March 2012.

[10] K. S. Novoselov, A. K. Geim, S. V. Morozov, D. Jiang, Y. Zhang, S. V. Dubonos, I. V. Grigorieva1, A. A. Firsov. *Science* **2004**. 306, 666-669

[11] S. Iijima. *Nature* **1991**. 354, 56-58.

[12] K. Tanaka, T. Yamabe, K. Fukui. The Science and Technology of Carbon Nanotubes, First ed. Elsevier, Oxford. 1999

[13] M. Wilson, K. Kannagara, G. Smith, M. Simmons, B. Raguse. "Nanotechnology. Basic Science and Emerging Technologies". CRC Press, London. 2002

[14] a), A.H. Castro-Neto, F. Guinea, N.M.R. Peres, A. Geim, K. Novoselov, *Reviews of Modern Physics* **2009**, 81, 109-162; b) C. T. White, T. N. Todorov. *Nature*, **1998**, 393, 240.

[15] a) A.A. Baladin. *Nat. Mater*. **2011,** 10, 569-581; b) J. P. Lu. *Physical Review Letters*, **1997,** 79, 1297.

[16] a) I.A. Ovid'Ko. *Rev. Adv. Mater. Sci*. **2013**, 34, 1-11; b) J. Zhao, R. H. Xie. *Journal of Nanoscience and Nanotechnology*, **2003**, 3, 459.

[17] E. L. Evans, J. D López-González, A. Martín-Rodríguez, F. Rodríguez-Reinoso *Carbon* **1976**, 13, 461-464.

[18] a) Y. Dong, J. Shao, C. Chen, H. Li, R. Wang, Y. Chi, X. Lin, G. Chen, *Carbon* **2012,** 50, 4738-4743; b) O. Akhavan, E. Ghaderi, *ACS Nano*, **2010**, 4, 5731–5736; c) J. E. Riggs, Z. Guo, D. L. Carroll, Y. P. Sun. *J. Am. Chem. Soc*. **2000**, 122, 5879-5880; d) C. D. Vecitis, M. H. Schnoor, S. Rahaman, J. D. Schiffman , M. Elimelech. *Environ. Sci. Technol*., **2011**, 45, 3672–3679

[19] N. Karousis, N. Tagmatarchis, D. Tasis. *Chem. Rev*. **2010**, 110, 5366–5397

[20] A. Schaetz, M. Zeltner, W. J. Stark. *ACS Catal*. **2012**, 2, 1267−1284

[21] Z. Jin, G. Q. Xu, S. H. Goh, *Carbon* **2000,** 38, 1135-1139.

[22] A. A. A. El-Nour, K. M. M., Ammar, R. A. A., Al-Warthan, A. *Arab. J. Chem*. **2012**, 5, 1−23

[23] F. Avilés, J. V. Cauich-Rodríguez, L. Moo-Tah, A. May-Pat, R. Vargas-Coronado. *Carbon* **2009**, 47, 2970-2976.

[24] H. He, J. Klinowski, M. Forster, A. Lerf. *Chemical Physics Letters* **1998**, 287, 53-56.

[25] B. Machado, P. Serp. *Catal. Sci. Technol.* **2012**, 2, 54–75

[26] M. Kakran, G. N. Sahoo, H. Bao, Y. Pan, L. Li. *Curr Med Chem* **2011,** 18,4503–4512.

[27] C. Xu, X. Wang, J. Wang, H. Hu, L. Wan. *Chem Phys Lett* **2010,** 498, 162–167.

[28] N. Karousis, S. P. Economopoulos, E. Sarantopoulou, N. Tagmatarchis. *Carbon* **2010**, 48, 854–860.

[29] a) Z. Liu, J. T. Robinson, X. Sun and H. Dai, *J. Am. Chem. Soc*. **2008**, 130, 10876–10877; b) L. M. Veca, F. Lu, M. J. Meziani, L. Cao, P. Zhang, G. Qi, L. Qu, M. Shrestha and Y.-P. Sun, *Chem. Commun*. **2009**, 2565–2567.

[30] G. Gabriel, G. Sauthier, J. Fraxedas, M. Moreno-Mañas, M. T. Martínez, C. Miravitlles, J. Casabó. *Carbon* **2006**, 44, 1891-1897

[31] L. Chen, S. Chai, K. Liu, N. Ning, J. Gao, Q. Liu, F. Chen, Q. Fu. *ACS Appl Mater. Interfaces* **2012**, 4, 4398–4404.

[32] a) M. H. Sarvari, H. Sharghi, *Synthesis*, **2004**, 2165-2168, b) John W. Larsen, Michael Freund, Kwang Y. Kim, Matthew Sidovar, John L. Stuart, *Carbon* **2000,** 38,

655-661; c) B. Garrigues, R. Laurent, C. Laporte, A. Laporterie, J. Dubac, *Liebigs. Ann*. **1996**, 743–744.

[33] S. Sarkar, S. Niyogi, E. Bekyarova, R. C. Haddon. *Chem. Sci.*, **2011**, 2, 1326-1333.

[34] a) H. Yu, F. Peng, J. Tan, X. W. Hu, H. J. Wang, J. A. Yang, W. X. Zheng. *Angew. Chem., Int. Ed*. **2011**, 50, 3978–3982. b) N. F. Goldshleger, *Fullerene Sci. Technol.*, **2001**, 9, 255-280

[35] A. V. Kumar, K. R. Rao. *Tetrahedron Lett.* **2011**, 52, 5188–5191

[36] D. R. Dreyer, K. A. Jarvis, P. J. Ferreira, C. W. Bielawski. *Polym. Chem*. **2012**, 3, 757–766.

[37] a) D. R. Dreyer, H. P. Jia, C. W. Bielawski. *Angew. Chem., Int. Ed*. **2010**, 49, 6813– 6816. b) H. P. Jia, D. R. Dreyer, C. W. Bielawski. *Tetrahedron* **2011**, 67, 4431–4434.

[38] H. B. Wang, T. Maiyalagan, X. Wang. *ACS Catal*. **2012**, 2, 781–794.

[39] Y. J. Gao, D. Ma, C. L. Wang, J. Guan, X. H. Bao. *Chem. Commun*. **2011**, 47, 2432–2434.

[40] C. Su, K.P. Loh. *Acc. Chem. Res*. **2013,** 10, 2275-2285.

[41] H. García. *Advances in Chemistry* **2014**. DOI: http://dx.doi.org/10.1155/2014/906781

[42] a) G. M. Scheuermann, L. Rumi, P. Steurer, W. Bannwarth, R. Mülhaupt. *J. Am. Chem. Soc.*, **2009**, 131, 8262-8270; b) Y. Li, X. Fan, J. Qi, J. Ji, S. Wang, G. Zhang and F. Zhang. *Nano Res*., **2010**, 3, 429-437.

[43] M. Stein, J. Wieland, P. Steurer, F. Tölle, R. Mülhaupt, B. Breit. *Adv. Synth. Cat*. **2013**. 353, 523-527

[44] A.O. Biying, V.R. Vangala, C. S. Chen, L. P. Stubs, N. S. Hosmane, Z. Yinghuai. *Dalton Trans.*, **2014**, 43, 5014–5020

[45] R. Gao, C. D. Tan, R. T. K. Baker, *Catal. Today* **2001,** 65, 19-29.

[46] J. P. Tessonnier, L. Pesant, G. Ehret, M. J. Ledoux, C. PhamHuu. *Appl. Catal., A* **2005**, 288, 203-210.

[47] a) Q. Zhao, C. Bai, W. Zhang, Y. Li, G. Zhang, F. Zhang, X. Fan. *Ind. Eng. Chem. Res*. **2014**, 53, 4232−4238; b) Z. Li, S. Wu, H. Ding, D. Zheng, J. Hu, X. Wang, Q. Huo, J. Guan, Q. Kan. *New J. Chem.*, **2013**, 37, 1561-1568; c) G. Xie, K. Zhang, B. Guo, Q. Liu, L Fang, J. R. Gong. *Adv. Mater*. **2013**, 25, 3820–3839.

[48] Q. Zhao, Y. Li, R. Liu, A. Chen, G. Zhang, F. Zhang, X. Fan. *J. Mater. Chem. A* **2013**, 1, 15039–15045.

[49] T. Xue, S. Jiang, Y. Qu, Q. Su, R. Cheng, S. Dubin, C. Y. Chiu, R. Kaner, Y. Huang, X. Duan. *Angew. Chem.*, **2012**, 124, 3888–3891.

[50] Y. Zhang, H. B. Zhang, G. D. Lin, P. Chen, Y. Z. Yuan, K.R. Tsai, *Appl. Catal. A: Gen*. **1999,** 187, 213-224.

[51] M. Pérez-Cadenas, L. J. Lemús-Yegres, M. C. Román-Martínez, C. Salinas-Martínez de Lecea. *Appl. Catal. A* **2011**, 402, 132−138; b) L. J. Lemus-Yegres, M.

C. Román-Martínez, I. Such-Basáñez, C. Salinas-Martínez de Lecea, *Microporous Mesoporous Mater*. **2008**, 109, 305−316.

[52] G. Liu, B. Wu, J. Zhang, X. Wang, M. Shao, J. Wang. *Inorg.Chem.* **2009**, 48, 2383-2390

[53] Y. Si, E. T. Samulski. *Chem. Mater*. **2008**, 20, 6792-6797.

[54] N. Zhang, Y. Zhang, Y.J. Xu. *Nanoscale*, **2012**, 4, 5792–5813

[55] R.H. Crabtree. The Organometallic Chemistry of the Transition Metals (4th ed.). New Jersey: Wiley-Interscience. 2005

[56] A. J. Arduengo, R. L. Harlow, M. Kline. *J. Am. Chem. Soc.* **1991**, 113, 361–363

[57] M. N. Hopkinson, C. Richter, M. Schedler. F. Glorius. *Nature* **2014,** 510 485-495

[58] J. Fernández. Tesis Doctoral, Universidad de Zaragoza. 2013

[59] C. W. Bielawski, R. H. Grubbs. *Angew. Chem., Int. Ed.* **2000**, *39*, 2903

[60] A. C. Hillier, H. M. Lee, E. D. Stevens, S. P. Nolan. *Organometallics* **2001**, 20, 4246-4252

[61] K. Muñiz. *Angew. Chem. Int. Ed.* **2005**, 44, 6622-6627

[62] J. R. Miecznikowski, R. H. Crabtree. *Organometallics* **2004**, *23*, 629-631

[63] M. Bekhouche, L. J. Blum, B. Doumèche. *ChemCatChem* **2011**, 3, 875−882.

[64] H. Glas, E. Herdtweck, M. Spiegler, A. K. Pleier, W. R. J. Thiel. *Organomet. Chem.* **2001**, 626, 100−105.

[65] R. Usón, L. A. Oro, J. A. Cabeza. *Inorg. Synth*. **1985**, 23, 126−127.

[66] C. Botas, P. Álvarez, C. Blanco, R. Santamaría, M. Granda, M. D. Gutiérrez, F. Rodríguez-Reinoso, R. Menéndez. *Carbon* **2013,** 52, 476–485.

[67] L. Ulmer, J. Mattay, H. G. Torres-García, H. Luftmann. *Eur. J. Mass Spectrom*. **2000**, 6, 49−52.

[68] E.G. Hernández. *J. Nanoc. Moletrón* **2012**, 10, 1845-1856

[69] M. Inagaki, Y. A. Kim, M. Endo. *J. Mater. Chem.* **2011**, 21, 3280-3294

[70] V. Datsyuk, M. Kalyva, K. Papagelis, J. Partheniosa, D. Tasis, A. Siokou, I Kallitsis, C. Galiotis. *Carbon* **2008**, 46, 833-840

[71] B. Ravel, M. Newville. *J. Synchrotron Radiat*. **2005**, 12, 537-541

[72] J. J. Rehr, R. C. Albers, *Rev. Mod. Phys*. **2000,** 72, 621.

[73] D. Baskaran, J. W. Mays, M. S. Bratcher. *Angew. Chem., Int. Ed*. **2004**, 43, 2138−2142.

[74] J. L. Figueiredo, M. F. R. Pereira, M. M. A. Freitas, J. M. M. Órfão. *Ind. Eng. Chem. Res*. **2007**, 46, 4110−4115.

[75] D. Elgrabli, M. Floriani, S. Abella-Gallar, L. Meunier, C. Gamez, P. Delalain, F. Rogerieux, J. Boczkowski, G. Lacroix. *Part. Fibre Toxicol*. **2008**, 5, 20−33.

[76] S. Brunauer, P. H. Emmett, E. J. Teller. *J. Am. Chem Soc.* **1938**. 60, 309-319.

[77] M. M. Dubinin. Progress in Surface and Membrane Science. Vol. 9. Academic Press, London. 1975.

[78] M. M. Dubinin. Chemistry and Physics of Carbon. Vol. 2. Marcel Dekker Inc., New York. 1966

[79] N. G. Asenjo, P. Álvarez, M. Granda, C. Blanco, R. Santamaría, R. Menéndez. *Journal of Hazardous Materials* **2011,** 192, 1525-1532.

[80] M. V. Jiménez, J. Fernández-Tornos, J. J. Pérez-Torrente, F. J. Modrego, S. Winterle, C. Cunchillos, F. J. Lahoz, L. A. Oro. *Organometallics* **2011**, 30, 5493−5508.

ANEXO

CONTRIBUCIONES A CONGRESOS

ImagineNano 2011, Bilbao (España), Abril 11-14 2011.

Optimization of CVD processes for the growth of carbon nanotubes with applications in the development of novel polymeric nanocomposites and water purification concepts. Nuria Campos, David Gómez, Matías Blanco, Patricia Álvarez

Presentación: Póster

Carbon 2011, Shanghai (China). Julio 24-29, 2011

Selective oxidation of forest-like carbon nanotubes obtained by CVD and applications in the elimination of contaminants in industrial wastewater. M. Blanco, R.Menéndez, P. Álvarez, N. Campos, D. Gómez, R.Santamaría, C. Blanco, M. Granda

Presentación: Póster

XI Reunión del Grupo Español del Carbón, Badajoz (España), Octubre 24-26, 2011

Oxidación selectiva de nanotubos de carbono tipo césped obtenidos por CVD y aplicaciones en la eliminación de contaminantes en aguas industriales. Matías Blanco, Rosa Menéndez, Patricia Alvarez, Nuria Campos, David Gómez, Ricardo Santamaría, Clara blanco, Marcos granda

Presentación: Póster

XII Congreso Nacional de Materiales, Alicante (España). 30 Mayo – 1 Julio 2012.

Funcionalización covalente de óxido de grafeno y nanotubos de carbono para su aplicación en catálisis. Matías Blanco, Patricia Álvarez, Clara Blanco, M. Victoria Jiménez, Javier Fernández-Tornos, Jesús J. Pérez-Torrente, Luis A. Oro y Rosa Menéndez

Presentación: Comunicación Oral

Carbon 2012, Krakow (Polonia), Junio 17-22 2012.

Functionalization of carbon nanotubes and graphene oxide for catalysis applications. M. Blanco, P. Álvarez, C. Blanco, M. V. Jiménez, J. Fernández-Tornos, J.J. Pérez-Torrente, L. A. Oro y R. Menéndez

Presentación: Póster

Carbon 2013, Rio de Janeiro, Brasil. Julio 14-19 2013

Functionalized carbon nanotubes as support of iridium-NHC complexes for catalysis applications. M. Blanco, P. Álvarez, C. Blanco, M. V. Jiménez, J. Fernández-Tornos, J. J. Pérez-Torrente, L. A. Oro y R. Menéndez

Presentación: Póster

Covalent functionalization of graphene oxides for catalysis applications. M. Blanco, P. Álvarez, C. Blanco, M. V. Jiménez, J. J. Pérez-Torrente, L. A. Oro y R. Menéndez.

Presentación: Póster

EUROMAT 2013, Sevilla (España), Septiembre 8-13 2013

Covalent functionalization of carbon nanotubes with iridium-NHC complexes for catalysis applications. Matías Blanco, Patricia Álvarez, Clara Blanco, M. Victoria

Jiménez, Javier Fernández-Tornos, Jesús J. Pérez-Torrente, Luis A. Oro y Rosa Menéndez

Presentación: Póster

XXXIV Reunión Bienal de la Real Sociedad de Química Española. Santander (España), Septiembre 15-18 2013

Covalent functionalization of carbon nanotubes with iridium-NHC complexes for catalysis applications. M. V. Jiménez, J. Fernández-Tornos, J. J. Pérez-Torrente, L. A. Oro, M. Blanco, P. Álvarez y R. Menéndez

Presentación: Póster

XII Reunión del Grupo Español del Carbón. Madrid (España), Octubre 20-23 2013

Funcionalización de nanotubos de carbono como soporte de complejos NHC de iridio para su aplicación en catálisis. Matías Blanco, Patricia Álvarez, Clara Blanco, M. Victoria Jiménez, Javier Fernández-Tornos, Jesús J. Pérez-Torrente, Luis A. Oro y Rosa Menéndez.

Presentación: Comunicación Oral

Funcionalización covalente de óxido de grafeno para aplicaciones en catálisis Matías Blanco, Patricia Álvarez, Clara Blanco, M. Victoria Jiménez, Jesús J. Pérez-Torrente, Luis A. Oro y Rosa Menéndez.

Presentación: Póster

Graphene 2014, Toulouse (Francia), Mayo 06-09 2014

Preparation of coke-based graphenes and their application in batteries and catalysis. Uriel Sierra, Zoraida González, Patricia Álvarez, Matías Blanco, Clara Blanco, M. Victoria Jiménez, Javier Fernández-Tornos, Jesús J. Pérez-Torrente, Luis A. Oro, Rosa Menéndez.

Presentación: Póster

Carbon 2014. Jeju (Corea) 29 Junio – 04 Julio 2014

Hydroxylic functionalization of graphene oxides with iridium N-heterocyclic carbenes for catalytic applications. Patricia Álvarez, Matías Blanco, Clara Blanco, M. Victoria Jiménez, Jesús J. Pérez-Torrente, Luis A. Oro, Rosa Menéndez.
Presentación: Póster

CVD Growth OH-Carbon nanotubes as support of Iridium NHC complexes for hydrogen transfer catalytic application. Patricia Álvarez, Matías Blanco, Clara Blanco, M. Victoria Jiménez, Jesús J. Pérez-Torrente, Luis A. Oro, S.M. Vega-Diaz, F. Tristán-López, A.L. Elías, M. Terrones, Rosa Menéndez.
Presentación: Comunicación Oral

IV Hybrid Materials Conference. Sitges (España). Marzo 09-13 2015

Catalytic activity of iridium NHC complexes covalently bonded to carbon nanotubes and graphene oxide. Matías Blanco, Patricia Álvarez Clara Blanco, M. Victoria Jiménez, Jesús J. Pérez-Torrente, Luis A. Oro, Rosa Menéndez.
Presentación: Póster

ImagineNano 2015. Bilbao (España). Marzo 10-13 2015

Catalytic activity of iridium NHC complexes covalently bonded to carbon nanotubes and graphene oxide. Matías Blanco, Patricia Álvarez Clara Blanco, M. Victoria Jiménez, Jesús J. Pérez-Torrente, Luis A. Oro, Rosa Menéndez.
Presentación: Póster

Carbon 2015. Dresden (Alemania), Julio 12-17 2015

Catalytic activity of iridium NHC complexes covalently bonded to carbon nanotubes and graphene oxide. Matías Blanco, Patricia Álvarez, Zoraida González, Clara Blanco, M. Victoria Jiménez, Javier Fernández-Tornos, Jesús J. Pérez-Torrente, Luis A. Oro y Rosa Menéndez.

Presentación. Comunicación Oral

XAFS16, Karlsruhe (Alemania), Agosto 23-28 2015

XAFS study of Iridium organometallic catalysts covalently bonded to carbon nanotubes. Javier Blasco, Vera Cuartero, Gloria Subías, M. Victoria Jiménez, Jesús J. Pérez-Torrente, Luis A. Oro, Matías Blanco, Patricia Álvarez, Clara Blanco y Rosa Menéndez.

Presentación. Póster

XAFS study of graphene-Iridium hybrid catalysts. Javier Blasco, Gloria Subías, Vera Cuartero, M. Victoria Jiménez, Matías Blanco, Jesús J. Pérez-Torrente, Luis A. Oro, Patricia Álvarez, Clara Blanco y Rosa Menéndez.

Presentación. Póster

XIII Reunión del Grupo Español del Carbón. Alicante (España), Octubre 18-22 2015

Efecto del soporte en la actividad catalítica de complejos NHC de iridio en nanotubos de carbono y grafeno. Matías Blanco, Patricia Álvarez, Clara Blanco, M. Victoria Jiménez, Javier Fernández-Tornos, Jesús J. Pérez-Torrente, Luis A. Oro y Rosa Menéndez.

Presentación: Póster

Funcionalización covalente de materiales grafénicos reducidos a altas temperaturas con aplicaciones catalíticas. M. Blanco, P. Álvarez, C. Blanco, A. Criado, T. Da Ros, M. Prato y R. Menéndez.

Presentación. Comunicación Oral

OTRAS PUBLICACIONES

J Blasco[1], V Cuartero[2], G Subías[1], M V Jiménez[3], J J Pérez-Torrente[3], L A Oro[3], M Blanco[4], P Álvarez[4], C Blanco[4] and R Menéndez[4]. J. Phys Conf. Ser. 2015. Enviado

Local structure of Iridium organometallic catalysts covalently bonded to carbon nanotubes.

J Blasco[1], V Cuartero[2], G Subias[1], M V Jiménez[3], J J Pérez-Torrente[3], L A Oro[3], M Blanco[4], P Álvarez[4], C Blanco[4] and R Menéndez[4]

[1]Instituto de Ciencia de Materiales de Aragón, Departamento de Física de la Materia Condensada, CSIC-Universidad de Zaragoza, C/ Pedro Cerbuna 12, 50009 Zaragoza (Spain)
[2]ESRF-The European Synchrotron, 71, Avenue des Martyrs, Grenoble (France)
[3]Departamento de Química Inorgánica, Instituto de Síntesis Química y Catálisis Homogéneas-ISQCH, Universidad de Zaragoza-CSIC, C/ Pedro Cerbuna 12, 50009 Zaragoza (Spain)
[4]Instituto Nacional del Carbon, CSIC, P.O. Box 73, 33080 Oviedo (Spain)

E-mail: jbc@unizar.es

Abstract. Hybrid catalysts based on Iridium N-heterocyclic carbenes anchored to carbon nanotubes (CNT) have been studied by XAFS spectroscopy. Oxidation of CNT yields a large amount of functional groups, mainly hydroxyl groups at the walls and carboxylic groups at the tips, defects and edges. Different kinds of esterification reactions were performed to functionalize oxidized CNT with imidazolium salts. Then, the resulting products were reacted with an Ir organometallic compound to form hybrid catalysts efficient in hydrogen transfer processes. XANES spectroscopy agree with the presence of Ir(I) in these catalysts and the EXAFS spectra detected differences in the local structure of Ir atoms between the initial Ir organometallic compound and the Ir complexes anchored to the CNT. Our results confirm that the halide atom, present in the Ir precursor, was replaced by oxygen from –OH groups at the CNT wall in the first coordination shell of Ir. The lability of this group accounts for the good recyclability and the good efficiency shown by these hybrid catalysts.

1. Introduction

Carbon nanotubes (CNT) can be considered as a versatil matrix to develop heterogeneous catalysts with improved activity [1]. Here we report a thorough characterization by X-ray absorption fine structure spectroscopy (XAFS) of a set of catalysts based on N-heterocyclic carbene iridium complexes covalently bonded to CNT properly functionalized with imidazolium salts. These materials showed catalityc activity in hydrogen transfer processes and they were tested in the hydrogenation of cyclohexanone with 2 propanol showing both good efficiency and good recyclability [2].

Chemical oxidation of CNT yields different oxo-groups that can be functionalized. Hydroxyl groups are located at the basal planes of CNT walls whereas carboxylic acids mainly lie at the tips, edges and defects of CNT. These oxidized CNT materials can react directly with some methoxo-cylooctadiene iridium dimer complexes, [{Ir(μ-OMe)(cod)}$_2$] (cod=1,5-cyclooctadiene), resulting poor active catalysts [2]. Better results were obtained when oxidized CNT were functionalized with the imidazolium salts (Im) like [MeImH(CH$_2$)$_3$OH]Cl (chloride of 3-methyl-1-(3-hydroxypropil)- imidazolium, hereafter denoted as Im-1) or [MeImH(1-cyclohexyl-2-ol]I (iodide of 3-methyl-1-(1- cyclohexyl-2-ol)-imidazolium (denoted as Im-2) rendering functionalized *f*-CNT supports for NHC carbene iridium complexes synthesis by simple reaction with [{Ir(μ-OMe)(cod)}$_2$]. Two ways to functionalize CNT were tested, either esterification reactions of –COOH groups with Im-1 or Im-2 (denoted as CNT-1 and CNT-2, respectively) and activation of –OH groups with *p*-nitrophenylchloroformate followed by the reaction with Im-1 (denoted as CNT-pNPh-1). Both functionalized CNT were then reacted with [{Ir(μ-OMe)(cod)}$_2$] to yield the hybrid catalysts: CNT-1-Ir, CNT-2-Ir and CNT-pNPh-1-Ir. In the latter case, the Ir complex can be also anchored to the reactive –COOH groups. In order to discriminate activities obtained from those different anchoring points, some CNT were thermally reduced at 400ºC in inert atmosphere to remove –COOH groups. The resulting product was functionalized in the same way as CNT-pNPh-1-Ir and then reacted with the Ir precursor, resulting in a supported NHC complex without secondary products, which was named CNT-T400-pNPh-1-Ir. Figure 1 shows the proposed final structure for the hybrid catalysts synthesized.

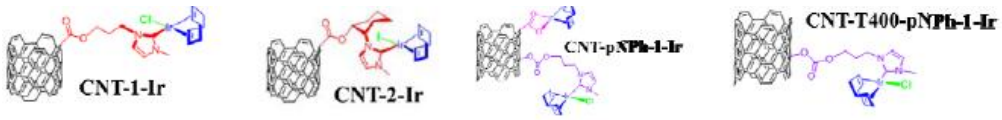

Figure 1. *Presumed structures for the hybrid catalysts after the synthesis route.*

The local iridium structure is unknown but the halide ligand is proposed to remain in the first coordination shell of the Ir atom and the output of this anion from the coordination sphere of the metal is suggested as the initiation of the catalysis mechanism [2]. In order to verify it, XAFS spectroscopy has been used with the aim of studying both the electronic state of Ir atoms and its local environment in these hybrid catalysts.

2. Experimental section

XAFS spectra at the Ir L_3-edge were recorded at the BL22-Claess (Alba) and at the BM23 (ESRF) beamlines. The measurements were carried out in transmission mode at room temperature on pellets of the materials mixed with cellulose if necessary. The beam was monochromatized by a fixed-exit Si (111) double crystal and harmonic rejection better than 10^{-5} was achieved by using the Si mirror coating of the double flat mirror installed after the monochromator. Energy resolution was estimated to be ~8×10^{-5} at the Ir L_3-edge and a pellet of Ir metal with cellulose was simultaneously measured for energy calibration. The XANES spectra were normalized to the high energy part of each spectrum at ~100 eV. We have also recorded spectra of Ir-metal, IrCl(cod)[MeIm$(CH_2)_3$OH] and $IrCl_3$ as references for Ir^0 , Ir^+ and Ir^{3+} respectively. The second compound is labelled as Ir(I)-reference and its structure can be seen in the inset of the figure 2.

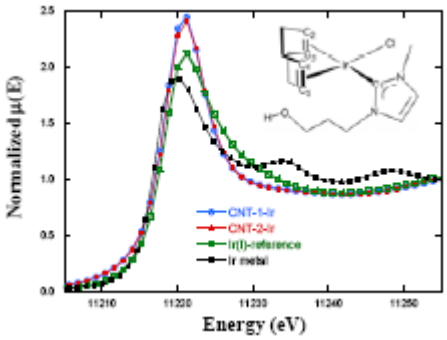

Figure 2. *XANES spectra at the Ir L_3-edge for CNT-1-Ir, CNT-2-Ir, Ir(I)-reference and metal Ir. Inset: Structure of the Ir(I)-reference compound. The XANES spectra of the other two CNT-catalysts display similar features to the ones shown in this figure.*

EXAFS signal extraction and background removal were carried out using Athena software [3] and the EXAFS structural analysis was performed using the ARTEMIS program [3] which makes use of theoretical scattering amplitudes and phases calculated from FEFF6 code [4] for the several single and multiple scattering paths. The fits were carried out in the R-space using a Hanning window in the region 1.1-2.3 Å which only include contributions from the first coordination shell as it is correlated to the main differences in the local environment of Ir atoms.

3. Results and conclusions

Figure 2 shows Ir L_3-edge XANES spectra of representative catalysts compared to the ones for Ir^0 and the Ir(I)- reference. All catalysts exhibit similar spectra with a strong peak (white line) centered at 11220.5 eV. The edge position of CNT-catalysts agree with Ir(I)-reference suggesting a similar oxidation state for the Ir atoms at CNT-catalysts. However, the white line is broader and asymmetric for the Ir(I)-reference.

The extracted EXAFS signals at room temperature for all studied samples are compared in Figure 3(a) for the sake of comparison. CNT-based catalysts exhibit similar EXAFS oscillations but the Ir(I)-reference has noticeable differences in the $8Å^{-1} \leq k \leq 12Å^{-1}$ range. Figure 3(b) shows the Fourier transform (FT) of the k_2-weighted EXAFS spectra, calculated between 2.75 and 14 $Å^{-1}$ using a Hanning window.

All CNT-based catalysts show a strong peak at 1.67 Å (without phase shift correction) corresponding to the first coordination shell. This distance agrees with the expected one for Ir-C bond length. The Ir(I)-reference shows the same peak but with less intensity which can be ascribed either to a higher disorder or fewer Ir-C paths respect to the Ir in hybrid catalysts. In addition, the FT of Ir(I)-reference displays a shoulder at ~2.0 Å ascribed to the Ir-Cl bond length that is lacked in the CNT-based catalysts.

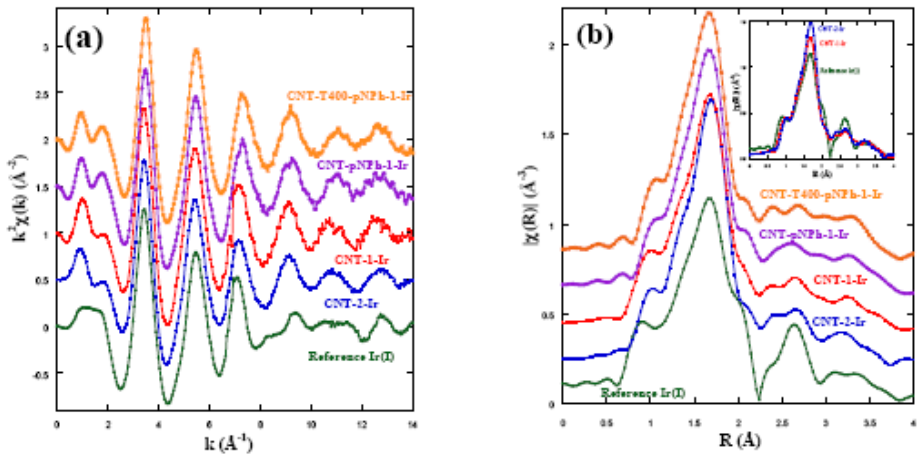

Figure 3. *(a) EXAFS spectra, $k^2 \times \chi(k)$, at the Ir L_3-edge for the indicated CNT-based catalysts and the Ir(I)-reference at room temperature. (b) Modulus of the Fourier transforms extracted from the curves of Fig. 3(a).*

The structural analysis was carried out as indicated in the experimental section. We have considered contributions from single scattering paths, Ir-C, Ir-O and Ir-Cl. The representative best fits corresponding to backward Fourier filtered EXAFS spectra of the first coordination sphere are shown in the figure 4. The Ir(I)-reference was analysed using the local environment indicated in the figure 2 and the fit agrees with a first coordination shell composed by 5 Ir-C paths and an additional Ir-Cl contribution with the following bond lengths: Ir-C1= 2.03(1) Å, Ir-C2(C3)= 2.11(1) Å, Ir-C4(C5)=2.19(1) Å and Ir-Cl= 2.43(1) Å in agreement with reported structural data in related compounds [5]. However, this environment failed to fit the EXAFS signal of CNT-based catalysts. Preliminary fits clearly showed the absence of Cl paths in the CNT-1-based catalysts (or I in the CNT-2-compound) as the resulting bond length was unphysical long and the fit was very poor. Hence, the logical hypothesis is that chloride (or iodide) has been displaced by another nucleophile and the most logical candidate was the –OH groups from the CNT wall. Therefore, we replaced the Ir-Cl path by an Ir-O one and the fit converged to yield an Ir-O distance similar to the previous Ir-C1. Therefore, we performed the structural analysis using this model and some constrains were imposed to avoid over-parametrization.

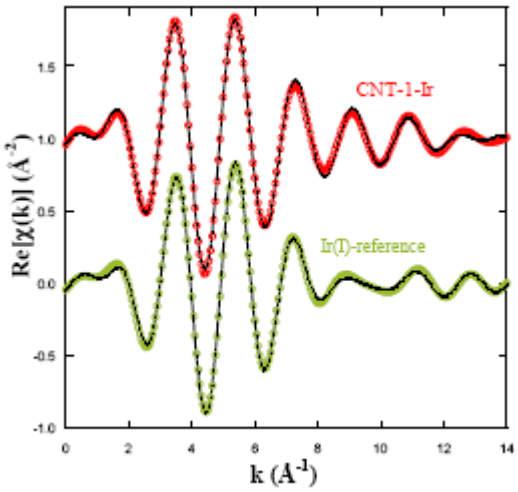

Figure 4. *Experimental k_2-weighted filtered EXAFS signal (real part) for the first shell of the indicated samples (circles) and the best fits (lines) to their respective structural models.*

Table 1. Best fit parameters (inner potential, bond lengths, average Debye-Waller factor and reliability factors [3]) obtained from the fitting of EXAFS data in the R-space mode. Numbers in parentheses refer to standard deviation of the last significant digits

Sample	ΔE_0 (eV)	R_1(Å)	R_2(Å)	R_3(Å)	σ^2(Å^2) ×10^{-3}	R_F
CNT-1-Ir	3.9(9)	2.035(19)	2.107(26)	2.186(24)	4.3(19)	0.0043
CNT-2-Ir	3.9(7)	2.029(21)	2.101(14)	2.186(20)	1.7(14)	0.0028
CNT-pNph-1-Ir	3.6(8)	2.029(21)	2.083(34)	2.172(32)	3.1(19)	0.0038
CNT-pNph-1-T400-Ir	3.3(9)	2.024(37)	2.090(28)	2.158(37)	2.9(22)	0.0049

Summarizing, XAFS spectroscopy resulted very useful to discern the local structure around Ir atoms in CNT-based hybrid catalysts. Halide ions (Cl in CNT-1 or I in CNT-2) are lost during the synthesis process to obtain the hybrid catalysts. They are likely replaced by –OH groups from the CNT wall. The lability of these –OH groups explains the good recyclability shown by these catalysts [2,7].

Acknowledgments

Authors acknowledge the financial support from Mineco/FEDER CTQ2010-15221, MAT2012-38213- C02-01, and DGA E07 and E69 projects. They also thank

Alba and ESRF for granting beam time and the kind assistance of Claess staff. M. Blanco thanks MECD for his FPU grant (AP2010-0025).

References

[1] Schaetz A, Zeltner M and Stark W J 2012 ACS Catal. 2 1267.

[2] Blanco M et al. 2013 ACS Catal. 3 1307.

[3] Ravel B and Newville M 2005 J. Synchrotron Radiat. 12 537.

[4] Rehr J J and Albers R C 2000 Rev. Mod. Phys. 72 621.

[5] Jiménez M V et al. 2011 Organometallics 30 5493.

[6] Roy M, Gurman S J and van Dorssen G 1997 J. Phys. IV 7 151.

[7] Blanco M et al. 2015 Carbon submitted.